COMPACT HIGH ORDER COMPUTATION OF COMPLEX HEAT AND MASS TRANSFER PROBLEMS ON NONUNIFORM GRIDS

by

Sailen Dutta

DEPARTMENT OF MECHANICAL ENGINEERING
INDIAN INSTITUTE OF TECHNOLOGY GUWAHATI
GUWAHATI-781039, INDIA
OCTOBER, 2021

COMPACT HIGH ORDER COMPUTATION OF COMPLEX HEAT AND MASS TRANSFER PROBLEMS ON NONUNIFORM GRIDS

A thesis submitted

in partial fulfillment of the requirements

for the degree of

DOCTOR OF PHILOSOPHY

by

Sailen Dutta

(Roll Number: 136103001)

DEPARTMENT OF MECHANICAL ENGINEERING
INDIAN INSTITUTE OF TECHNOLOGY GUWAHATI
GUWAHATI-781039, INDIA
October, 2021

Declaration

I hereby declare that the work contained in the thesis entitled **"Compact high order computation of complex heat and mass transfer problems on nonuniform grids"** has been done by me, under the guidance of **Dr. Anoop K. Dass**, Professor, Department of Mechanical Engineering & **Dr. Jiten C. Kalita**, Professor, Department of Mathematics, Indian Institute of Technology Guwahati, for the award of the degree of Doctor of Philosophy and this work has not been submitted elsewhere for a degree.

Guwahati
October 2021.

Sailen Dutta
Roll No: 136103001
Department of Mechanical Engineering
Indian Institute of Technology Guwahati
Guwahati-781039, India


भारतीय प्रौद्योगिकी संस्थान गुवाहाटी
Indian Institute of Technology Guwahati

Certificate

We hereby declare that the work contained in the thesis entitled **"Compact high order computation of complex heat and mass transfer problems on nonuniform grids"** has been done by **Mr. Sailen Dutta**, a student of the Department of Mechanical Engineering, Indian Institute of Technology Guwahati, for the award of the degree of Doctor of Philosophy has been carried out under our supervision and this work has not been submitted elsewhere for a degree.

Guwahati
October 2021

Prof. Anoop K. Dass
Department of Mechanical Engineering
Indian Institute of Technology Guwahati
Guwahati-781039, India

Prof. Jiten C. Kalita
Department of Mathematics
Indian Institute of Technology Guwahati
Guwahati-781039, India

Dedicated

To

Ma and Deuta

Acknowledgements

When I joined the PhD program at the Department of Mechanical Engineering at IIT Guwahati, I could not have imagined a more different journey. It sounds like a cliché, but it has been a roller-coaster ride. I could not made it this far without the help and guidance of my superiors, friends, and family. I would like to take this opportunity to express my gratitude for their support.

Firstly, I would like to express my sincere gratitude to my supervisors Prof. Jiten C. Kalita and Prof. Anoop K. Dass for the continuous support of my research journey. Prof. Kalita has been a mentor not only in the academic aspects of my PhD, but also in the bigger stage of life. The cynic in me is constantly amazed at his positive attitude. I thank him for providing the much needed lifeline at a critical time in my PhD journey. Prof. Dass has provided a steady support throughout, and I thank him for his patience and immense knowledge.

Besides my advisors, I would like to thank the rest of my doctoral committee members: Prof. Manmohan Pandey, Prof. Amaresh Dalal, and Dr. Suresh A. Kartha, for their insightful comments and encouragement, which motivated me to widen my research from various perspectives.

My sincere thanks also goes to Prof. Praveen Chandrashekar of TIFR CAM for his help and support during my brief stay at IIT Delhi.

I am also grateful to all the staff members of the Department of Mathematics and Mechanical Engineering for their assistance in various ways during my research period.

I would like to thank my friends and colleagues Pankaj, Devanand, Raghav, Kamaljyoti and many others for all their encouragement and support during this period. I express my sincere thanks to Pankaj on whose coattails I have ridden for a long time, and to my childhood friend Dorsana for being a source of constant support even at my lowest.

Last but not the least, I am extremely grateful to my parents. My father could not be with me to the end of this journey, but I hope I have made him proud. I also thank my extended family for their unconditional love and support.

Finally, I would like to acknowledge everybody who is important to the successful completion of the thesis as well as express my apology that I could not mention each of them individually.

And above all, I thank the Gods for their blessings.

October, 2021 **Sailen Dutta**

Abstract

This work is concerned with the application of compact and higher order compact (HOC) finite difference schemes to complex heat and mass transfer problems on nonuniform grids, which have been used overwhelmingly for fluid flow problems, and the handful of works dealing with heat and mass transfer problems have used grid transformation when dealing with non-rectangular geometries, which in turn leads to increased computational time and complexity, and numerical errors. This work uses a combination of two recently developed schemes for the streamfunction-velocity (ψ-v) form of the Navier-Stokes (N-S) equations, and existing HOC schemes for the temperature equation, in addition to using body fitted Cartesian grids when dealing with non-rectangular geometries. Using this approach four different problems of heat and mass transfer have been tackled viz. natural convection around heated bodies (a circular, and a diamond cylinder respectively) placed in a square enclosure, double diffusive natural convection in a porous annulus, conjugate heat transfer (CHT) in suddenly expanding flow, and forced convection over a heated diamond cylinder in uniform flow. The numerical approach has been shown to work remarkably well for the range of Rayleigh numbers ($10^3 \leq Ra \leq 10^7$) considered. A comprehensive analysis of flow physics has been provided, and for the first time, secondary corner vortices have been shown to exist for certain parameters. A reconstructed HOC scheme was applied to study the double diffusive natural convection in a porous annulus. This study was focused on teasing out general heat and mass transfer characteristics for all the parameters considered, and studying transient flow behavior for a particular set of parameters. While investigating CHT in suddenly expanding flows, new benchmark results have been provided for the backward facing step (BFS) geometry, and new insights into the heat transfer phenomena have been provided for flow in a suddenly expanding channel with large expansion ratios. Finally, comprehensive computations were carried out to investigate forced convection over a heated diamond cylinder in uniform flow. The use of body fitted Cartesian grids was demonstrated again, and an insightful picture of the heat transfer phenomena was provided. In all the cases, present numerical results are in excellent agreement with well established results in the literature.

LIST OF FIGURES

LIST OF TABLES

CONTENTS

CHAPTER 1

INTRODUCTION

1.1 Background

Computational Fluid Dynamics (CFD) at its core involves the solution of partial differential equations (PDEs) via an appropriate numerical method, as the equations governing the fluid flow and heat transfer phenomena lack analytical solutions. The most widely used methods are the finite difference (FD) [144], finite volume (FV) [156], and finite element (FE) [131] methods, which are all techniques used to derive discrete representations of the partial derivatives. The simplest and historically oldest method is the finite difference method, which involves setting up a grid and approximating the derivatives appearing in the governing equations by finite difference approximations. This, in turn, results in a large but finite algebraic system of equations which can be solved in a computer.

The most commonly used finite difference representation of the partial derivatives is based on Taylor series expansion of the variables at the grid points. The order of accuracy of the scheme is determined by the leading term in truncation error (TE) of the Taylor series expansion. A scheme is said to be of order of accuracy m, or simply $\mathcal{O}(h^m)$, h being the distance between two successive grid points, if the TE is asymptotically proportional to h^m. Schemes which are $\mathcal{O}(h^2)$ accurate (central difference schemes) found widespread application to linear PDEs on account of their simplicity. However, such schemes, when applied to computing fluid-flow problems governed by the Navier-Stokes (N-S) equations, cause spurious oscillations to appear in the solution, unless the grid is sufficiently refined.

Grid refinement, on the other hand, inevitably increases the computational cost and time. Such handicaps led to the emergence of higher order compact (HOC) schemes, which have found successful application in the field of CFD over the years.

A compact stencil is identified as one in which the grid are points located only directly adjacent to the node about which differences are taken. A finite difference scheme which utilizes these grid points only is termed a compact FD scheme, and in addition if the scheme has an order of accuracy greater than two, then it is termed a higher order compact scheme. Higher order compactness of finite difference schemes can be achieved in several ways. The schemes used in this work have utilized the idea of using the original differential equation to substitute for the leading TE terms of the standard central difference approximation. This idea was first used by Lax and Wendroff for the time dependent hyperbolic PDEs [99].

In the computation of fluid flow problems, the streamfunction-vorticity (ψ-ω) formulation of the Navier-Stokes (N-S) equations has found much traction among researchers, as it circumvents the need to solve the pressure Poisson equation of the conventional primitive variable formulation. Researchers over the years have developed HOC schemes for the ψ-ω form of the N-S equations, and used them to successfully simulate fluid flow problems of varying degrees of complexity. Schemes developed on both uniform ([54, 66, 76–78, 108, 150, 173]) and non-uniform ([25, 29, 80, 81, 130, 148]) grids have gained popularity over the years. However, a disadvantage of using the ψ-ω form is that vorticity is not specified at the boundaries. Considering this, the pure streamfunction formulations ([19, 20, 98, 155]), and streamfunction-velocity formulation (ψ-v) ([55, 82]) that use the biharmonic form of the N-S equations have emerged as an attractive alternative approach of solving the N-S equations. This approach eliminates the need to compute pressure and vorticity as a part of the computational process and therefore computationally much efficient than the primitive variable and ψ-ω formulations. The main advantages of the pure streamfunction formulation are:

1. Avoids difficulties associated with primitive variables such as computing the pressure.

2. Avoids use of artificial vorticity boundary conditions.

3. Iterations involve only a single variable.

The pioneering work on the development of compact schemes for the pure stream-function formulation of the incompressible viscous N-S equations was carried out by Kupferman [98] in 2001. Researchers since then have developed various compact schemes for the ψ-v formulation for the 2D N–S equations. The schemes developed by Gupta and Kalita [55, 56], Kalita and Gupta [82], Ben-Artzi et.al. [19] were based on uniform grids. Thus they could not accomplish the benefits associated with non-uniform grids, especially, in regions of the physical domain where large gradient of flow variables are prevalent. Clustering the grids in regions of high gradient and spreading it out in small gradient regions is one of the better ways of efficient computation. Apart from accurately resolving smaller scales, it brings savings in computational time. The use of nonuniform grids is quite common in the finite volume or finite element setup, where the physical and the computational domain remain the same. In the finite difference setup, however, most of the works using nonuniform grids involved transforming the governing equations from the physical domain onto the computational domain embedded with uniform grid. The equations are first solved on the computational space before mapping this solution back onto the physical space (see Pandit [118], Sen et.al. [142], Sen and Kalita [141]).

Recently, however, Kumar and Kalita [94] have developed and employed a methodology of using body fitted Cartesian grids in a finite difference setup for fluid flow problems involving non-rectangular geometries, thereby forgoing the process of aforementioned grid transformation. They developed a compact FD scheme for the ψ-v form of the N-S equations, first for the steady [94] and later for the unsteady [95] version and tackled problems of varying complexity to great success.

1.2 Motivation

A careful review of the works discussed so far reveals a couple of serious issues regarding the application of compact and HOC schemes. Firstly, the overwhelming majority of the works have focused only on fluid flow problems, thus ignoring heat and mass transfer phenomena, especially convection - both natural and forced, which are abundantly prevalent in engineering applications. Secondly, the approach of using grid transformation while employing nonuniform grids has certain disadvantages:

1. The number of terms to be discretized in the transformed equations increases, thereby increasing the computational time ([11, 74, 81, 154]).
2. Increase in computational complexity due to the appearance of cross derivative terms for most cases ([61, 119, 120, 140]).
3. In case the transformation is not explicitly known, it has to go through a series of numerical approximations, leading to additional errors creeping in([140, 154]).
4. The overall solution process turns complicated and is prone to errors ([74,119,120]).

Many natural phenomena, as well as engineering applications, involve heat and mass transfer along with fluid flow. Simulating such phenomena involving complicated geometries using the simplest of numerical methods available viz. the finite difference method, presents unique challenges to the CFD community. Meanwhile, we are also presented with an opportunity of using nonuniform grids without resorting to grid transformation. This work is an attempt towards meeting those challenges, and advancing the application of compact & HOC schemes on nonuniform grids without transformation to heat and mass transfer problems.

1.3 Objectives

The objectives of the work are as follows:

1. To apply high order compact schemes on non-uniform grids for the pure streamfunction form (or ψ-v form) of the Navier - Stokes (N-S) equations to heat and mass transfer problems of varying complexity.
2. To use higher order compact (HOC) schemes to solve for temperature wherever applicable.
3. To demonstrate the use of body fitted Cartesian grids as a viable (possibly better) alternative for tackling flows over different geometries.
4. To gain new insights into the fluid flow and heat transfer problems considered.

1.4 The work

First, we derive the biharmonic form of N-S equations for problems involving steady state natural convection. We then apply the compact scheme developed by Kumar and Kalita [94] for the aforementioned equations, along with an HOC scheme developed by Kalita et.al. [80] for the temperature equations. The problem of natural convection in a differentially heated square cavity is taken up as a code validation exercise. Then, we simulate natural convection around a heated circular, and diamond cylinder respectively placed in a square enclosure. For these two cases, we demonstrate the use of Cartesian body fitted non-uniform grids [86], thus eliminating the need for grid transformation as resorted to in earlier works. The combined schemes are shown to be capable of handling higher Rayleigh numbers in all three cases. Also, for the first time we observe the formation of some secondary corner vortices for the circular cylinder case.

Next, we reconstruct an HOC scheme on nonuniform grids developed by Kalita et.al. [81] an apply it to the problem of double diffusive natural convection in a vertical porous annulus. In the process we also propose a novel way of explicitly calculating the velocities. Particular attention was paid to slender cavities, and influence of all non-dimensional parameters on heat and mass transfer characteristics was investigated. In this process, we have brought out a general pattern of heat and mass transfer characteristics as well. While earlier studies focused only on steady state results, we have also investigated transient flow behavior for certain parameters.

The problem of steady state conjugate heat transfer in suddenly expanding flows is considered next. Two different geometries have been considered - the backward facing step, and a symmetric channel with large expansion ratios. As in the case of natural convection, a combination two different schemes ([80, 94]) has been used to solve for streamfunction (ψ) and temperature (T). In addition to providing new insights into the flow physics and heat transfer phenomena, we have also established new benchmark results for the case of conjugate heat transfer in backward facing step flow. New insights for the heat transfer phenomena in symmetric channel is also arrived at. Also, properties of the recirculation eddies for both values of expansion ratios have been tabulated for the first time. To the best of our knowledge, this is the only work to have applied a ψ-v approach to simulating conjugate heat transfer.

Finally, we have tackled the problem of forced convection over a heated diamond cylinder in uniform flow. Three values of Reynolds number were considered viz. $Re = 80$, 100, and 120, and the working fluid was taken to be air. A combination of two schemes ([81, 95]) has been used to solve for ψ and T, while vorticity was calculated in post-processing. To validate the code, we carried out computations for forced convection over a circular cylinder for $15 \leq Re \leq 40$, and compared our results with well established results in the literature. As in the case of natural convection over heated bodies, we have used body fitted Cartesian grids for this problem too. Results were presented in terms of streamlines, isotherms, and vorticity contours. Interesting observations have been arrived at via Fast Fourier Transform (FFT) plot, as well as the variation of surface average Nusselt number.

1.5 Organization of the thesis

The current dissertation is organized into seven chapters. Chapter 2 briefly describes the different compact and HOC schemes used in this work. In Chapter 3, we apply the schemes discussed in chapter 2 to simulate natural convection around heated bodies placed in a square enclosure. Chapter 4 discusses the heat and mass transfer characteristics of double diffusive natural convection a vertical porous annulus. Chapter 5 deals with steady state conjugate heat transfer in suddenly expanding flow. In Chapter 6, we simulate forced convection over a diamond cylinder in uniform flow. Finally, chapter 7 concludes the whole work and discusses the scope for future work.

CHAPTER 2

COMPACT FINITE DIFFERENCE SCHEMES - A BRIEF DESCRIPTION

2.1 Introduction

In this chapter we briefly describe the various compact schemes used in this work. It is worthwhile to note that all the schemes used in this work are applied on a 9 point compact stencil. Figure 2.1 shows such a stencil with non-uniform spacing.

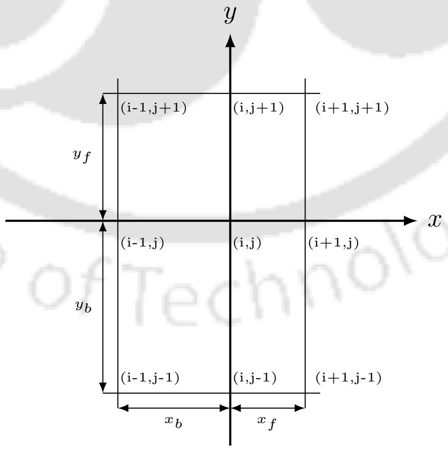

Figure 2.1: A compact finite difference stencil

Consider a rectangular domain $[a_1, a_2] \times [b_1, b_2]$ in the xy-plane. The interval $[a_1, a_2]$ is divided into m sub-intervals, not necessarily of equal lengths, by the points $a_1 = x_0, x_1, x_2, x_3, \ldots, x_{m-1}, x_m = a_2$ and similarly $[b_1, b_2]$ into n subintervals by the points

$b_1 = y_0, y_1, y_2, y_3, \ldots, y_{n-1}, y_n = b_2$.

In the x-direction, we define the forward and backward step-lengths x_f, x_b at the $(i,j)^{\text{th}}$ point (see figure 2.1) of the problem domain as,

$$x_f = (x_{i+1,j} - x_{i,j})$$
$$x_b = (x_{i,j} - x_{i-1,j}).$$

Likewise, in the y-direction,

$$y_f = (y_{i,j+1} - y_{i,j})$$
$$y_b = (y_{i,j} - y_{i,j-1}).$$

There exist compact schemes which do not utilize a 9 point stencil, rather they exclude the four corner points i.e., the grid points $(i-1, j+1)$, $(i+1, j+1)$, $(i-1, j-1)$, and $(i+1, j-1)$ (Figure 2.1). The resulting scheme is called a 5 point compact scheme. In case of compact/HOC schemes for transient state equations, some schemes make use of 9 grid points in the n^{th} time level and 5 grid points in the $(n+1)^{th}$ time level. These are called $(9,5)$ compact/HOC schemes. Notable examples include the works of Kalita et.al. [78], Kalita and Chhabra [76], Kalita and Sen [83] etc. Similarly, we have $(5,5)$ schemes (Sen [139], Deka and Sen [38]), and $(9,9)$ schemes (Kalita et.al. [81], Kumar and Kalita [95]). In case of steady-state problems, the use of schemes based on 5 point compact stencil may lead to errors, as shown by Kumar and Kalita [94]. In the present work, we have used a combination of two different schemes, except for the work detailed in chapter 4, which uses a single $(9,9)$ HOC scheme. Note that the compact scheme used for the biharmonic form of the N-S equations, and the HOC scheme used to solve for temperature are all based on a 9 point stencil.

2.2 HOC scheme for convection-diffusion type equations

Consider the following 2D convection-diffusion type equation for a flow variable ϕ:

$$b\frac{\partial \phi}{\partial t} - \nabla^2\phi + c(x,y,t)\frac{\partial \phi}{\partial x} + d(x,y,t)\frac{\partial \phi}{\partial y} = f(x,y,t) \tag{2.1}$$

where $b > 0$ is a constant, $c(x,y,t)$ and $d(x,y,t)$ are convection coefficients in the x- and y- directions respectively and $f(x,y,t)$ is a forcing function.

Kalita et.al. [81] had developed an HOC scheme on non-uniform Cartesian grids for (2.1), which, for a grid point (i,j), can be written as follows:

$$\begin{aligned}
& b[1 + (H_1 + H_2c)\delta_x + (K_1 + K_2d)\delta_y + \{H_2 - 0.5(x_f - x_b)(H_1 + H_2c)\}\delta_x^2 \\
& \quad + \{K_2 - 0.5(y_f - y_b)(K_1 + K_2d)\}\delta_y^2]\delta_t^+\phi_{ij}^n \\
& \quad + [-A_{ij}\delta_x^2 - B_{ij}\delta_y^2 + C_{ij}\delta_x + D_{ij}\delta_y + G_{ij}\delta_x\delta_y - H_{ij}\delta_x\delta_y^2 - K_{ij}\delta_x^2\delta_y - L_{ij}\delta_x^2\delta_y^2]\phi_{ij}^n \\
& \quad = F_{ij}
\end{aligned} \tag{2.2}$$

where δ_t^+ denotes the forward difference operator for time with uniform time step Δt and n represents the time level. Here, δ_x and δ_y are the first and δ_x^2 and δ_y^2 are the second order central difference operators along the x and y directions respectively.

The expressions for the finite difference operators appearing in equation (2.2) are given below:

$$\delta_t^+\phi_{ij}^n = \frac{\phi_{ij}^{n+1} - \phi_{ij}^n}{\Delta t} \tag{2.3}$$

$$\delta_x\phi_{ij} = \frac{\phi_{i+1,j} - \phi_{i-1,j}}{x_f + x_b} \quad \text{and} \quad \delta_y\phi_{ij} = \frac{\phi_{i,j+1} - \phi_{i,j-1}}{y_f + y_b} \tag{2.4}$$

$$\delta_x^2\phi_{ij} = \frac{2}{(x_f + x_b)}\left[\frac{\phi_{i+1,j}}{x_f} - \left(\frac{1}{x_f} + \frac{1}{x_b}\right)\phi_{i,j} + \frac{\phi_{i-1,j}}{x_b}\right] \tag{2.5}$$

$$\delta_y^2\phi_{ij} = \frac{2}{(y_f + y_b)}\left[\frac{\phi_{i,j+1}}{y_f} - \left(\frac{1}{y_f} + \frac{1}{y_b}\right)\phi_{i,j} + \frac{\phi_{i,j-1}}{y_b}\right]. \tag{2.6}$$

$$\begin{aligned}
\delta_x\delta_y^2\phi_{ij} = & \frac{1}{2hk}\left[\frac{1}{y_f}\Big(\phi_{i+1,j+1} - \phi_{i-1,j+1}\Big) - \left(\frac{1}{y_f} + \frac{1}{y_b}\right)\Big(\phi_{i+1,j} - \phi_{i-1,j}\Big)\right. \\
& \left. + \frac{1}{y_b}\Big(\phi_{i+1,j-1} - \phi_{i-1,j-1}\Big)\right]
\end{aligned} \tag{2.7}$$

$$\begin{aligned}\delta_x^2\delta_y\phi_{ij} =& \frac{1}{2hk}\left[\frac{1}{x_f}\left(\phi_{i+1,j+1}-\phi_{i+1,j-1}\right) - \left(\frac{1}{x_f}+\frac{1}{x_b}\right)\left(\phi_{i,j+1}-\phi_{i,j-1}\right)\right. \\ &\left. + \frac{1}{x_b}\left(\phi_{i-1,j+1}-\phi_{i-1,j-1}\right)\right]\end{aligned} \tag{2.8}$$

$$\begin{aligned}\delta_x^2\delta_y^2\phi_{ij} = \frac{1}{hk}&\left[\frac{\phi_{i+1,j+1}}{x_f y_f}+\frac{\phi_{i-1,j+1}}{x_b y_f}-\left(\frac{1}{x_f y_f}+\frac{1}{x_b y_f}\right)\phi_{i,j+1}-\left(\frac{1}{x_f y_f}+\frac{1}{x_f y_b}\right)\phi_{i+1,j}\right. \\ &+\left(\frac{1}{x_f y_f}+\frac{1}{x_f y_b}+\frac{1}{x_b y_f}+\frac{1}{x_b y_b}\right)\phi_{i,j}-\left(\frac{1}{x_f y_b}+\frac{1}{x_b y_b}\right)\phi_{i,j-1} \\ &\left.-\left(\frac{1}{x_b y_f}+\frac{1}{x_b y_b}\right)\phi_{i-1,j}+\frac{\phi_{i+1,j-1}}{x_f y_b}+\frac{\phi_{i-1,j-1}}{x_b y_b}\right]\end{aligned} \tag{2.9}$$

The coefficients C_{ij}, D_{ij}, A_{ij}, B_{ij}, G_{ij}, H_{ij}, K_{ij}, L_{ij} and F_{ij} are to be evaluated at the n^{th} time level. These are given by

$$\begin{aligned}C_{ij} =& [1+(H_1+H_2c)\delta_x+(K_1+K_2d)\delta_y+\{H_2-0.5(x_f-x_b)(H_1+H_2c)\}\delta_x^2 \\ &+\{K_2-0.5(y_f-y_b)(K_1+K_2d)\}\delta_y^2]c\end{aligned} \tag{2.10}$$

$$\begin{aligned}D_{ij} =& [1+(H_1+H_2c)\delta_x+(K_1+K_2d)\delta_y+\{H_2-0.5(x_f-x_b)(H_1+H_2c)\}\delta_x^2 \\ &+\{K_2-0.5(y_f-y_b)(K_1+K_2d)\}\delta_y^2]d\end{aligned} \tag{2.11}$$

$$A_{ij} = 1-[(H_1+H_2c)+2H_2\{\delta_x c-0.5(x_f-x_b)\delta_x^2 c\}]+0.5(x_f-x_b)C_{ij} \tag{2.12}$$

$$B_{ij} = 1-[(K_1+K_2c)+2K_2\{\delta_y d-0.5(y_f-y_b)\delta_y^2 d\}]+0.5(y_f-y_b)D_{ij} \tag{2.13}$$

$$\begin{aligned}G_{ij} =& (H_1+H_2c)d+(K_1+K_2d)c+2H_2\delta_x d+2K_2\delta_y c \\ &-\{H_2(x_f-x_b)\delta_x^2 d+K_2(y_f-y_b)\delta_y^2 c\}\end{aligned} \tag{2.14}$$

$$H_{ij} = H_1+H_2c-K_2c \tag{2.15}$$

$$K_{ij} = K_1+K_2d-H_2d \tag{2.16}$$

$$L_{ij} = H_2+K_2 \tag{2.17}$$

$$\begin{aligned}F_{ij} = [1 &+ (H_1 + H_2c)\delta_x + (K_1 + K_2d)\delta_y + \{H_2 - 0.5(x_f - x_b)(H_1 + H_2c)\}\delta_x^2 \\ &+ \{K_2 - 0.5(y_f - y_b)(K_1 + K_2d)\}\delta_y^2]f_{ij}\end{aligned} \tag{2.18}$$

with

$$H_1 = \frac{1}{6}\{2(x_f - x_b) - cx_fx_b\}, \qquad H_2 = \frac{1}{12}\{x_f^2 + x_b^2 - x_fx_b\}$$

and

$$K_1 = \frac{1}{6}\{2(y_f - y_b) - dy_fy_b\}, \qquad K_2 = \frac{1}{12}\{y_f^2 + y_b^2 - y_fy_b\}$$

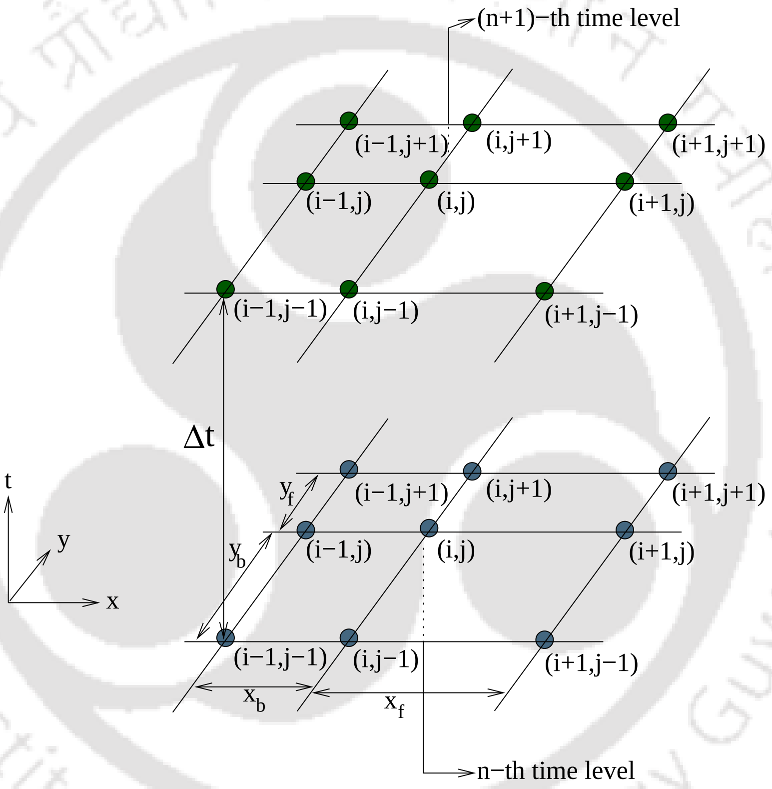

Figure 2.2: The unsteady (9,9) stencil used in the present work.

We now introduce a weighted average parameter μ through the approximation of the time derivative $\dfrac{\partial \phi}{\partial t}$ such that

$$t_\mu = (1 - \mu)t^{(n)} + \mu t^{(n+1)}, \qquad 0 \leq \mu \leq 1$$

Varying μ yields different schemes of different time accuracies. Varying μ yields different schemes of different time accuracies. For $\mu = 0$, the computational stencil requires nine points at the n^{th} and five points at $(n+1)^{th}$ time level resulting in a $(9,5)$ scheme. Similarly $\mu = 0.5$ and $\mu = 1$ yields a $(9,9)$ (see the corresponding stencil in figure 2.2) and a $(5,9)$ scheme, respectively. The temporal order of accuracy is two for the $(9,9)$ scheme, which is of Crank-Nicolson type, and one for the other two. With these, Eq.(2.2) can be put in the form

$$\sum_{k_1=-1}^{1}\sum_{k_2=-1}^{1} w_{i+k_1,j+k_2}\phi^{(n+1)}_{i+k_1,j+k_2} = \sum_{k_1=-1}^{1}\sum_{k_2=-1}^{1} w'_{i+k_1,j+k_2}\phi^{(n)}_{i+k_1,j+k_2} + (\mu F^{(n+1)}_{ij} + (1-\mu)F^{(n)}_{ij})\Delta t \tag{2.19}$$

where,

$$w_{i+k_1,j+k_2} = -\mu\Delta t\, p_{i+k_1,j+k_2} + q_{i+k_1,j+k_2} \quad \text{and} \quad w'_{i+k_1,j+k_2} = (1-\mu)\Delta t\, p_{i+k_1,j+k_2} + q_{i+k_1,j+k_2}$$

with,

$$p_{i-1,j-1} = -\frac{G_{ij}}{4hk} - \frac{H_{ij}}{2hky_b} - \frac{K_{ij}}{2hkx_b} + \frac{L_{ij}}{hkx_by_b}$$

$$p_{i-1,j+1} = \frac{G_{ij}}{4hk} - \frac{H_{ij}}{2hky_f} + \frac{K_{ij}}{2hkx_b} + \frac{L_{ij}}{hkx_by_f}$$

$$p_{i+1,j-1} = \frac{G_{ij}}{4hk} + \frac{H_{ij}}{2hky_b} - \frac{K_{ij}}{2hkx_f} + \frac{L_{ij}}{hkx_fy_b}$$

$$p_{i+1,j+1} = -\frac{G_{ij}}{4hk} + \frac{H_{ij}}{2hky_f} + \frac{K_{ij}}{2hkx_f} + \frac{L_{ij}}{hkx_fy_f}$$

$$p_{i,j-1} = \frac{B_{ij}}{ky_b} + \frac{D_{ij}}{2k} + \frac{K_{ij}}{2hk}\left(\frac{1}{x_f} + \frac{1}{x_b}\right) - \frac{L_{ij}}{hk}\left(\frac{1}{x_fy_b} + \frac{1}{x_by_b}\right)$$

$$p_{i,j+1} = \frac{B_{ij}}{ky_f} - \frac{D_{ij}}{2k} - \frac{K_{ij}}{2hk}\left(\frac{1}{x_f} + \frac{1}{x_b}\right) - \frac{L_{ij}}{hk}\left(\frac{1}{x_by_f} + \frac{1}{x_fy_f}\right)$$

$$p_{i-1,j} = \frac{A_{ij}}{hx_b} + \frac{C_{ij}}{2h} + \frac{H_{ij}}{2hk}\left(\frac{1}{y_f} + \frac{1}{y_b}\right) - \frac{L_{ij}}{hk}\left(\frac{1}{x_by_f} + \frac{1}{x_by_b}\right)$$

$$p_{i+1,j} = \frac{A_{ij}}{hx_f} - \frac{C_{ij}}{2h} + \frac{H_{ij}}{2hk}\left(\frac{1}{y_f} + \frac{1}{y_b}\right) - \frac{L_{ij}}{hk}\left(\frac{1}{x_fy_b} + \frac{1}{x_fy_f}\right)$$

$$p_{i,j} = -\frac{A_{ij}}{h}\left(\frac{1}{x_f} + \frac{1}{x_b}\right) - \frac{B_{ij}}{k}\left(\frac{1}{y_f} + \frac{1}{y_b}\right) + \frac{L_{ij}}{hk}\left(\frac{1}{x_fy_f} + \frac{1}{x_fy_b} + \frac{1}{x_by_f} + \frac{1}{x_by_b}\right)$$

$$q_{i-1,j-1} = 0$$

$$q_{i-1,j+1} = 0$$

$$q_{i+1,j-1} = 0$$

$$q_{i+1,j+1} = 0$$

$$q_{i,j-1} = -\frac{b}{2k}(K_1 + K_2 d) + \frac{b}{ky_b}\{K_2 - 0.5(K_1 + K_2 d)(y_f - y_b)\}$$

$$q_{i,j+1} = \frac{b}{2k}(K_1 + K_2 d) + \frac{b}{ky_f}\{K_2 - 0.5(K_1 + K_2 d)(y_f - y_b)\}$$

$$q_{i-1,j} = -\frac{b}{2h}(H_1 + H_2 c) + \frac{b}{hx_b}\{H_2 - 0.5(H_1 + H_2 c)(x_f - x_b)\}$$

$$q_{i+1,j} = \frac{b}{2h}(H_1 + H_2 c) + \frac{b}{hx_f}\{H_2 - 0.5(H_1 + H_2 c)(x_f - x_b)\}$$

$$q_{i,j} = b - \frac{b}{h}\left(\frac{1}{x_f} + \frac{1}{x_b}\right)\{H_2 - 0.5(H_1 + H_2 c)(x_f - x_b)\} - \frac{b}{k}\left(\frac{1}{y_f} + \frac{1}{y_b}\right)\{K_2 - 0.5(K_1 + K_2 d)(y_f - y_b)\}$$

The detailed derivation of the scheme can be found in the work of Kalita et.al. [81]. Note that the steady state version of equation (2.1) is given by -

$$-\nabla^2\phi + c(x,y)\frac{\partial\phi}{\partial x} + d(x,y)\frac{\partial\phi}{\partial y} = f(x,y) \tag{2.20}$$

The HOC scheme developed by Kalita et.al. [80] for equation (2.20) on a grid point (i,j) is given by -

$$[-A_{ij}\delta_x^2 - B_{ij}\delta_y^2 + C_{ij}\delta_x + D_{ij}\delta_y + G_{ij}\delta_x\delta_y - H_{ij}\delta_x\delta_y^2 - K_{ij}\delta_x^2\delta_y - L_{ij}\delta_x^2\delta_y^2]\phi_{ij} = F_{ij} \tag{2.21}$$

The expressions for the coefficients C_{ij}, D_{ij}, A_{ij}, B_{ij}, G_{ij}, H_{ij}, K_{ij}, L_{ij} and F_{ij} have been detailed above.

2.3 Compact high order scheme for the biharmonic form of the N-S equation

The equations governing the conservation of mass and momentum for a 2D incompressible, viscous fluid in non-dimensional form are given by:

$$\frac{\partial u}{\partial x}+\frac{\partial v}{\partial y}=0 \tag{2.22}$$

$$\frac{\partial u}{\partial t}+u\frac{\partial u}{\partial x}+v\frac{\partial u}{\partial y}=-\frac{\partial p}{\partial x}+\frac{1}{Re}\left(\frac{\partial^2 u}{\partial x^2}+\frac{\partial^2 u}{\partial y^2}\right) \tag{2.23}$$

$$\frac{\partial v}{\partial t}+u\frac{\partial v}{\partial x}+v\frac{\partial v}{\partial y}=-\frac{\partial p}{\partial y}+\frac{1}{Re}\left(\frac{\partial^2 v}{\partial x^2}+\frac{\partial^2 v}{\partial y^2}\right) \tag{2.24}$$

Now introducing dimensionless vorticity ω and stream-function ψ, defined by

$$\omega=\frac{\partial v}{\partial x}-\frac{\partial u}{\partial y} \tag{2.25}$$

and

$$u=\frac{\partial \psi}{\partial y}, \quad v=-\frac{\partial \psi}{\partial x} \tag{2.26}$$

the equations (2.22) - (2.24) can be written as

$$\frac{\partial \omega}{\partial t}+u\frac{\partial \omega}{\partial x}+v\frac{\partial \omega}{\partial y}=\frac{1}{Re}\left(\frac{\partial^2 \omega}{\partial x^2}+\frac{\partial^2 \omega}{\partial y^2}\right) \tag{2.27}$$

$$\frac{\partial^2 \psi}{\partial x^2}+\frac{\partial^2 \psi}{\partial y^2}=-\omega \tag{2.28}$$

Substituting (2.26) back into (2.27), we obtain

$$Re\left[\frac{\partial}{\partial t}(\nabla^2\psi)\right]+Re\left[\frac{\partial \psi}{\partial y}\left(\frac{\partial^3 \psi}{\partial x^3}+\frac{\partial^3 \psi}{\partial x\partial y^2}\right)-\frac{\partial \psi}{\partial x}\left(\frac{\partial^3 \psi}{\partial x^2\partial y}+\frac{\partial^3 \psi}{\partial y^3}\right)\right]=\frac{\partial^4 \psi}{\partial x^4}+2\frac{\partial^4 \psi}{\partial x^2\partial y^2}+\frac{\partial^4 \psi}{\partial y^4} \tag{2.29}$$

Equation (2.29) is variously referred to as the biharmonic or pure streamfunction or

ψ - v form of the N-S equations. It is a fourth-order partial differential equation in streamfunction (ψ). Kumar and Kalita [94] first developed a compact high order scheme on nonuniform grids for the steady version of equation (2.29), which, for a grid point (i,j) is given by

$$A\psi_{i+1,j+1}+B\psi_{i,j+1}+C\psi_{i-1,j+1}+D\psi_{i+1,j}+E\psi_{i,j}+F\psi_{i-1,j}+G\psi_{i+1,j-1}+H\psi_{i,j-1}+I\psi_{i-1,j-1}=f_{i,j} \tag{2.30}$$

The details of the coefficients A,B,C,D,E,F,G,H,I and f_{ij} can be found in the work of Kumar and Kalita [94]. This second order accurate 9-point scheme was applied to various fluid flow problems, and the computed results were found to be in excellent agreement with available numerical and experimental results in the literature.

The superiority of using a 9-point compact stencil over a 5-point compact stencil has been demonstrated by Kumar and Kalita [94]. They have considered the well-known problem of flow in a lid driven cavity for Reynolds number $Re = 7500$ and compared their results with the results obtained by Yu and Tian [174] who had used a 5-point compact stencil. These computations have revealed that the scheme of Yu and Tian [174] produced prominent wiggles in streamline contours at the top right corner for uniform grid. While these wiggles could be removed to a certain extent by using a clustering parameter of 0.5, the scheme of Kumar and Kalita [94] removed the wiggles completely. Moreover, the scheme of Yu and Tian [174] could handle moderate clustering parameters only, whereas the scheme of Kumar and Kalita [94] can handle extreme clustering ($= 0.99$).

In a subsequent work Kumar and Kalita [95] developed a compact finite difference scheme on nonuniform grids for equation (2.29) which was second order accurate in space and time. The scheme was specifically designed for flow past bluff bodies and was found to perform remarkably well for a variety of problems such as flow over bluff bodies (flat plate, circular cylinder, and inclined square cylinder) in uniform and accelerated flow, and flow past a mounted wedge.

The compact scheme for equation 2.29 on a grid point (i,j) is given by

$$\begin{aligned}
Re\delta_t^+\left(\nabla^2\psi\right) = {} & p\delta_x^4\psi + 2\delta_x^2\delta_y^2\psi + q\delta_y^4\psi - Re\left\{v\left(\delta_x^2 u + \delta_y^2 u\right) - u\left(\delta_x^2 v + \delta_y^2 v\right)\right\} \\
& + \frac{6p(3x_f^2 + 3x_b^2 - x_f x_b)(x_f - x_b)}{x_f x_b(2x_f^2 + 2x_b^2 - x_f x_b)}\delta_x^2 v - \frac{36p(x_f^2 + x_b^2 - x_f x_b)}{x_f x_b(2x_f^2 + 2x_b^2 - x_f x_b)}\delta_x v \\
& + \frac{72p(x_f^2 + x_b^2)(x_f - x_b)}{x_f^2 x_b^2(2x_f^2 + 2x_b^2 - x_f x_b)}v - \frac{6q(3y_f^2 + 3y_b^2 - y_f y_b)(y_f - y_b)}{y_f y_b(2y_f^2 + 2y_b^2 - y_f y_b)}\delta_y^2 u \\
& + \frac{36q(y_f^2 + y_b^2 - y_f y_b)}{y_f y_b(2y_f^2 + 2y_b^2 - y_f y_b)}\delta_y u - \frac{72q(y_f^2 + y_b^2)(y_f - y_b)}{y_f^2 y_b^2(2y_f^2 + 2y_b^2 - y_f y_b)}u \qquad (2.31) \\
& - Re.v\frac{(x_f - x_b)}{3}\delta_x^2\delta_y v + Re.u\frac{(y_f - y_b)}{3}\delta_x\delta_y^2 u + \frac{2(x_f - x_b)}{3}\delta_x^2\delta_y^2 v - \frac{2(y_f - y_b)}{3}\delta_x^2\delta_y^2 u \\
& + O\Bigg(\frac{x_f^2 x_b^2}{(2x_f^2 + 2x_b^2 - x_f x_b)}, (x_f - x_b)(y_f - y_b), \frac{y_f^2 y_b^2}{(2y_f^2 + 2y_b^2 - y_f y_b)}, \\
& \qquad (x_f^2 + x_b^2 - x_f x_b), (y_f^2 + y_b^2 - y_f y_b), \Delta t\Bigg)
\end{aligned}$$

A general formulation is obtained by using a weighted time average parameter μ by employing a uniform time step Δt and making use of the approximations for the finite difference operators. With this, (2.31) can be discretized compactly on the nonuniform nine-point stencil as

$$\begin{aligned}
& \frac{1}{h}\left[\frac{\psi_{i+1,j}^{n+1}}{x_f} + \frac{\psi_{i-1,j}^{n+1}}{x_b} - \left(\frac{1}{x_f} + \frac{1}{x_b}\right)\psi_{i,j}^{n+1}\right] + \frac{1}{k}\left[\frac{\psi_{i,j+1}^{n+1}}{y_f} + \frac{\psi_{i,j-1}^{n+1}}{y_b} - \left(\frac{1}{y_f} + \frac{1}{y_b}\right)\psi_{i,j}^{n+1}\right] \\
& = \frac{\mu\Delta t}{Re}\Big\{\Big(A\psi_{i+1,j+1}^n + B\psi_{i,j+1}^n + C\psi_{i-1,j+1}^n + D\psi_{i+1,j}^n + E\psi_{i,j}^n + F\psi_{i-1,j}^n + G\psi_{i+1,j-1}^n \\
& \qquad + H\psi_{i,j-1}^n + I\psi_{i-1,j-1}^n\Big) - \phi_{i,j}^n\Big\} \\
& + \frac{(1-\mu)\Delta t}{Re}\Big\{\Big(A\psi_{i+1,j+1}^{n+1} + B\psi_{i,j+1}^{n+1} + C\psi_{i-1,j+1}^{n+1} + D\psi_{i+1,j}^{n+1} + E\psi_{i,j}^{n+1} + F\psi_{i-1,j}^{n+1} + G\psi_{i+1,j-1}^{n+1} \\
& \qquad + H\psi_{i,j-1}^{n+1} + I\psi_{i-1,j-1}^{n+1}\Big) - \phi_{i,j}^{n+1}\Big\} \qquad (2.32) \\
& + \frac{1}{h}\left[\frac{\psi_{i+1,j}^n}{x_f} + \frac{\psi_{i-1,j}^n}{x_b} - \left(\frac{1}{x_f} + \frac{1}{x_b}\right)\psi_{i,j}^n\right] + \frac{1}{k}\left[\frac{\psi_{i,j+1}^n}{y_f} + \frac{\psi_{i,j-1}^n}{y_b} - \left(\frac{1}{y_f} + \frac{1}{y_b}\right)\psi_{i,j}^n\right] \\
& + \frac{x_f - x_b}{2h}\left[\frac{v_{i+1,j}^n}{x_f} + \frac{v_{i-1,j}^n}{x_b} - \left(\frac{1}{x_f} + \frac{1}{x_b}\right)v_{i,j}^n\right] - \frac{y_f - y_b}{2k}\left[\frac{u_{i,j+1}^n}{y_f} + \frac{u_{i,j-1}^n}{y_b} - \left(\frac{1}{y_f} + \frac{1}{y_b}\right)u_{i,j}^n\right] \\
& + \frac{x_f - x_b}{2h}\left[\frac{v_{i+1,j}^{n+1}}{x_f} + \frac{v_{i-1,j}^{n+1}}{x_b} - \left(\frac{1}{x_f} + \frac{1}{x_b}\right)v_{i,j}^{n+1}\right] - \frac{y_f - y_b}{2k}\left[\frac{u_{i,j+1}^{n+1}}{y_f} + \frac{u_{i,j-1}^{n+1}}{y_b} - \left(\frac{1}{y_f} + \frac{1}{y_b}\right)u_{i,j}^{n+1}\right]
\end{aligned}$$

The details of all the coefficients above can be found in the work of Kumar and Kalita [95]. As mentioned in section 2.2, choosing $\mu = 0.5$ results in a $(9,9)$ scheme which is second order accurate in time.

A note on the solution of algebraic system of equations: The application of schemes (2.21), (2.2), (2.30) to specific fluid flow and heat transfer problems give rise to a system of equations which can be written in matrix form as

$$A\boldsymbol{\phi} = \boldsymbol{b} \tag{2.33}$$

where $\boldsymbol{\phi}$ is the flow variable (either streamfunction ψ, temperature T, or concentration S), and A is an asymmetric matrix of order mn on a grid of size $m \times n$. Although the solution procedure for equations of the type (2.33) remains same for all the problems considered in this work, there are subtle differences in the overall solution procedure. Thus, at the risk of sounding repetitive, the solution procedure for the algebraic system of equations are detailed in every chapter henceforth.

CHAPTER 3

NATURAL CONVECTION AROUND HEATED BODIES PLACED IN A SQUARE ENCLOSURE

3.1 Introduction

Natural convection in an enclosure is relevant to many industrial and environmental applications such as heat exchangers, nuclear and chemical reactors, cooling of electronic equipment, and stratified atmospheric boundary layers. In engineering applications, the geometries that arise, however, are more complicated than a simple enclosure filled with a convective fluid. Therefore, studies on geometric configuration with the presence of bodies embedded within the enclosure have, of late, generated much interest among scientists.

Moukalled and Acharya [115] studied the change of the thermo-flow field between the low temperature outer square enclosure and high temperature inner circular cylinder by varying the radius of the inner circular cylinder. They considered the primitive variable form of the N-S equations, and used the Finite Volume method along with grid transformation to curvilinear coordinates for the computations.

De and Dalal [36] considered the problem of natural convection around a square, horizontal, heated cylinder placed inside an enclosure in the range of $10^3 \leq Ra \leq 10^6$. They used the streamfunction-vorticity (ψ-ω) form of the N-S equations, and general curvilinear body fitted grids for the computations. To generate the curvilinear grid, two Poisson equations had to be solved, thus introducing additional computational complexities.

Kim et.al. [89] studied the problem of natural convection around a heated circular cylinder within a cooled square enclosure. The location of the cylinder was varied along the vertical centerline of the square enclosure. They considered the primitive variable form of the N-S equations in conjunction with the immersed boundary method for the computations. Yoon et.al. [172] investigated the effect of the position of a circular cylinder in a square enclosure on natural convection at Rayleigh number of 10^7.

Recently, Kumar and Kalita [94] developed a second order accurate compact finite difference scheme for the biharmonic form of the steady-state N-S equations on nonuniform Cartesian grids without transformation. Contrary to the schemes developed on rectangular Cartesian grids for N-S equations that could handle only rectangular boundaries, the proposed scheme can easily accommodate bluff bodies with curved boundary. The scheme was shown to handle the boundary of an immersed body not necessarily aligned to the grid lines for one of the problems, and for another, it tackled a curved boundary on Cartesian grid without the need for roping in any immersed interface in the process.

In the present work, we tackle three different problems of natural convection[1] using a combination of: 1. A reconstructed form of the scheme developed by Kumar and Kalita [94] for the biharmonic form of the steady-state N-S equations, and 2. A compact finite difference scheme developed by Kalita et.al. [80] for the temperature equation. Firstly, we tackle the problem of a buoyancy driven square cavity with adiabatic top and bottom walls, and differentially heated vertical walls as a validation exercise. Next, we study the natural convection around a circular, horizontal, heated cylinder placed in an enclosure. And lastly, we compute the natural convection around a diamond shaped horizontal, heated cylinder placed in an enclosure. For the last two cases, we demonstrate the use of Cartesian body fitted non-uniform grids [86], thus eliminating the need for grid transformation as resorted to in earlier works. For all the three problems, we demonstrate the capability of the scheme to handle higher Rayleigh numbers. We also observe the formation of some secondary corner vortices for the second problem not reported earlier, thus showing the robustness and versatility of the scheme.

The outline of this chapter is as follows. In section 3.2, we present the governing equations of the problems to be tackled, and a derivation of the biharmonic form for

---

[1] Part of this study has been published in [45]

problems governing natural convection. In sections 3.3 and 3.4, we briefly discuss the discretization and numerical procedure. In the next section (3.5), we take up the problem of natural convection in a differentially heated square cavity as a validation exercise of our code. In the subsection 3.5.2, we compare the values of various parameters with well established results. In section 3.6 we present the results of the simulation of natural convection around a circular, horizontal, heated cylinder placed in an enclosure. The next section, i.e., section 3.7 deals with the problem of natural convection around a diamond, horizontal, heated cylinder placed in an enclosure. Much like the previous section, we briefly describe the problem in section 3.7 before discussing the results in subsections 3.7.1 and 3.7.2. A brief comparative exercise is undertaken in subsection 3.7.3. Finally in the last section (3.8) we present our conclusions for this chapter.

3.2 Governing Equations - The bi-harmonic form

The governing equations of mass, momentum, and energy for steady state N-S equations in primitive variable form in two-dimension (2D), after invoking the Boussinesq approximation, are given by:

$$\frac{\partial u}{\partial x}+\frac{\partial v}{\partial y}=0 \tag{3.1}$$

$$u\frac{\partial u}{\partial x}+v\frac{\partial u}{\partial y}=-\frac{1}{\rho}\frac{\partial p}{\partial x}+\nu\nabla^2 u \tag{3.2}$$

$$u\frac{\partial v}{\partial x}+v\frac{\partial v}{\partial y}=-\frac{1}{\rho}\frac{\partial p}{\partial y}+g\beta_T(T-T_0)+\nu\nabla^2 v \tag{3.3}$$

$$u\frac{\partial T}{\partial x}+v\frac{\partial T}{\partial y}=\alpha\nabla^2 T \tag{3.4}$$

where $u, v, p, g, T, \rho, \nu, \beta_T$, and α are the x- and y- velocities, pressure, gravitational acceleration, temperature, dynamic viscosity, coefficient of thermal expansion, and thermal diffusivity of the fluid respectively.

Introducing the following non-dimensional variables:

$$x^*=\frac{x}{H},\ y^*=\frac{y}{H},\ u^*=\frac{uH}{\alpha},\ v^*=\frac{vH}{\alpha},\ \theta=\frac{T-T_0}{T_h-T_c},\ \text{and}\ p^*=\frac{pH^2}{\rho\alpha^2} \tag{3.5}$$

Here, H is a characteristic length, T_h and T_c are the hot and cold temperatures respectively

$(T_h > T_c)$, and T_0 is a reference temperature. In all the cases considered in this chapter, the colder temperature T_c is taken as the reference temperature $(T_0 = T_c)$

The non-dimensional form of the equations (3.1) - (3.4) on dropping the asterisks become,

$$\frac{\partial u}{\partial x} + \frac{\partial v}{\partial y} = 0 \tag{3.6}$$

$$u\frac{\partial u}{\partial x} + v\frac{\partial u}{\partial y} = -\frac{\partial p}{\partial x} + Pr\nabla^2 u \tag{3.7}$$

$$u\frac{\partial v}{\partial x} + v\frac{\partial v}{\partial y} = -\frac{\partial p}{\partial y} + Ra\,Pr\,\theta + Pr\nabla^2 v \tag{3.8}$$

$$u\frac{\partial \theta}{\partial x} + v\frac{\partial \theta}{\partial y} = \nabla^2 \theta \tag{3.9}$$

where $Pr = \dfrac{\nu}{\alpha}$, and $Ra = \dfrac{g\beta_T H^3 (T - T_0)}{\nu\alpha}$ are the Prandtl and Rayleigh numbers respectively.

Following the procedure outlined in section 2.3 of the previous chapter, we obtain the biharmonic form for the equations governing natural convection, which is given by

$$\frac{\partial^4 \psi}{\partial x^4} + 2\frac{\partial^4 \psi}{\partial x^2 \partial y^2} + \frac{\partial^4 \psi}{\partial y^4} = \frac{1}{Pr}\left[u\left(\frac{\partial^3 \psi}{\partial x^3} + \frac{\partial^3 \psi}{\partial x \partial y^2}\right) + v\left(\frac{\partial^3 \psi}{\partial x^2 \partial y} + \frac{\partial^3 \psi}{\partial y^3}\right)\right] + Ra\frac{\partial \theta}{\partial x} \tag{3.10}$$

3.3 Discretization and Numerical Procedure

Recall from section 2.3 of chapter 2 that Kumar and Kalita [94] have developed a compact finite difference scheme on nonuniform grids for the biharmonic form of the N-S equations. For the present case, the term $Ra\dfrac{\partial \theta}{\partial x}$ is added to f_{ij} and Re is replaced by $\dfrac{1}{Pr}$, and the scheme given by (2.30) is used to solve for ψ. Additionally, equation (3.9) is discretized using the HOC scheme given by (2.21) of Kalita et.al. [80].

The velocities u and v can be calculated as:

$$\begin{aligned}u_{i,j} =& \frac{\partial \psi}{\partial y} \\ =& \delta_y \psi_{i,j} - \frac{1}{2}(y_f - y_b)\delta_y^2 \psi_{i,j} - \frac{y_f y_b}{6}\frac{\partial^3 \psi}{\partial y^3} \\ =& \delta_y \psi_{i,j} - \frac{1}{2}(y_f - y_b)\delta_y^2 \psi_{i,j} - \frac{y_f y_b}{6}\frac{\partial^2 u}{\partial y^2}\end{aligned}$$

Making use of the formulas for the first and second order central difference operators and rearranging, this reduces to

$$\begin{aligned}\frac{y_b}{6k}u_{i,j+1} - \left(1 - \frac{y_f + y_b}{6k}\right) u_{i,j} + \frac{y_f}{6k}u_{i,j-1} =& \frac{(\psi_{i,j+1} - \psi_{i.j-1})}{2k} \\ &- \frac{(y_f - y_b)}{2k}\left[\frac{\psi_{i,j+1}}{y_f} + \frac{\psi_{i,j-1}}{y_b} - (\frac{1}{y_f} + \frac{1}{y_b})\psi_{i,j}\right]\end{aligned} \tag{3.11}$$

Similarly, v can be obtained from the following equation

$$\begin{aligned}\frac{x_b}{6h}v_{i+1,j} - \left(1 - \frac{x_f + x_b}{6h}\right) v_{i,j} + \frac{x_f}{6h}v_{i-1,j} =& \frac{(\psi_{i-1,j} - \psi_{i+1,j})}{2h} \\ &+ \frac{(x_f - x_b)}{2h}\left[\frac{\psi_{i+1,j}}{x_f} + \frac{\psi_{i-1,j}}{x_b} - (\frac{1}{x_f} + \frac{1}{x_b})\psi_{i,j}\right].\end{aligned} \tag{3.12}$$

The expressions for u and v in the form of equations (3.11) and (3.12) facilitate the use of Tridiagonal solvers for computing them.

3.4 Solution of algebraic systems

We now discuss the solution of algebraic systems resulting from the discretization of equations (3.9) and (3.10). The system of equations formed by applying (2.30) and (2.21) can be written in matrix form as

$$A_1 \boldsymbol{\psi} = \boldsymbol{f}(\boldsymbol{Ra}, \boldsymbol{u}, \boldsymbol{v}, \boldsymbol{\theta}) \tag{3.13}$$

$$A_2 \boldsymbol{\theta} = \boldsymbol{b} \tag{3.14}$$

where for a grid of size $m \times n$, the coefficient matrices A_1, A_2 are non symmetric matrices of order mn, the non-symmetry being rendered by the non-uniformity of the grid under consideration.

The computation of the steady-state solutions of fluid flow problems governed by equations (3.9) and (3.10) involves an outer–inner iteration procedure. After initializing u, v, ψ, and θ along with appropriate boundary conditions, (3.13) is solved for ψ. Next, u and v are computed from equations (3.11) and (3.12) by employing Thomas algorithm [10] for tridiagonal system of equations. Then, θ is computed by solving (3.14). This constitutes one outer iteration. Making use of the updated values of u, v, ψ and θ on the right hand side of (3.13), ψ is computed again. This process is repeated till maximum ψ-error (defined as the difference between ψ values of the current and previous outer iterations) reaches 0.5×10^{-8}, at which juncture we assume the solution to have reached steady-state.

The inner iterations involve solving the matrix equations (3.13)-(3.14) at each outer iteration by iterative solvers. We have used biconjugate gradient stabilized method (BiCGStab) [143] with preconditioning, where Incomplete LU decomposition is used as a preconditioner. Preconditioning was particularly useful for high Rayleigh numbers where we have used the Lis library [105]. The inner iterations were stopped when the Euclidean norms of the residual vectors $\boldsymbol{r}_1 = \boldsymbol{f} - A_1\boldsymbol{\psi}$ and $\boldsymbol{r}_2 = \boldsymbol{b} - A_2\boldsymbol{\theta}$ arising out of equations (3.13)-(3.14) fell below 0.5×10^{-8}. We have used a relaxation parameter λ for both inner and outer iteration cycles. Larger the value of Rayleigh number, smaller is the value of λ. All of our computations were carried out on an Intel core i7 based PC with 16 GB RAM.

3.5 Validation of Code - Natural Convection in a differentially heated square cavity

The scheme developed for the present study is first validated for the problem of natural convection in a differentially heated square cavity. Consider the 2D incompressible steady-state flow of a Boussinesq fluid of Prandtl number (Pr) 0.71 in an upright square cavity of side H (figure 3.1). The vertical walls are both isothermal; the left wall at temperature T_h is hotter than the right wall at temperature T_c ($T_h > T_c$). The horizontal walls are both insulated. Natural convection starts owing to the temperature difference between the left and right walls. Body forces are present in the form of gravitational force that acts in the negative y direction.

The governing equations for this problem are Eq. (3.9) and Eq. (3.10). The non-dimensional boundary conditions are as follows:

$$\begin{aligned}
&\psi = u = v = 0, \quad \theta = 1 \quad \text{at } x = 0\,(0 \le y \le 1),\\
&\psi = u = v = 0, \quad \theta = 0 \quad \text{at } x = 1\,(0 \le y \le 1),\\
&\psi = u = v = 0, \quad \frac{\partial \theta}{\partial y} = 0 \quad \text{at } y = 0\,(0 \le x \le 1),\\
&\psi = u = v = 0, \quad \frac{\partial \theta}{\partial y} = 0 \quad \text{at } y = 1\,(0 \le x \le 1)
\end{aligned} \tag{3.15}$$

The Nusselt number characterizes the rate of heat transfer across the cavity. The local Nusselt number in the horizontal direction at any point in the cavity is

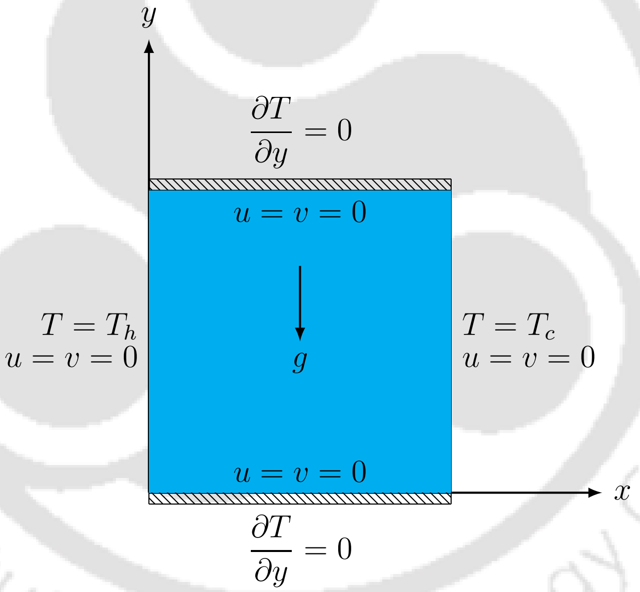

Figure 3.1: Schematic view of the differentially heated square cavity.

$$Q(x, y) = u\theta - \frac{\partial \theta}{\partial x} \tag{3.16}$$

Through any line parallel to the $y-$ axis, this is given by

$$Nu_x = \int_0^1 Q(x, y)\, dy \tag{3.17}$$

Finally, integrating Nu_x along the horizontal direction, the average Nusselt number is given by

$$\overline{Nu} = \int_0^1 Nu_x \, dx \tag{3.18}$$

In order to perform integration for equations (3.17) and (3.18), we employ Simpson's one-third rule on nonuniform grids.

Note: Simpson's $1/3^{rd}$ rule for integrating a function $f(x)$ between the limits x_i and x_{i+2} using non-uniform integration intervals is given by

$$\begin{aligned}\int_{x_i}^{x_{i+2}} f(x)\,dx \approx \frac{1}{6}\Bigg[&\frac{(h_{i+1}+h_{i+2})(2h_{i+1}-h_{i+2})}{h_{i+1}} f_i + \frac{(h_{i+1}+h_{i+2})^3}{h_{i+1}\,h_{i+2}} f_{i+1} \\ &+ \frac{(h_{i+1}+h_{i+2})(2h_{i+2}-h_{i+1})}{h_{i+2}} f_{i+2}\Bigg]\end{aligned} \tag{3.19}$$

Here,

$$h_{i+1} = x_{i+1} - x_i, \qquad h_{i+2} = x_{i+2} - x_{i+1} \qquad \text{and} \qquad f_i = f(x_i)$$

3.5.1 Grid Generation

To generate a centro-symmetric grid with clustering near the walls, we use the stretching function [81]

$$x_i = \frac{i}{i_{max}} - \frac{\eta_1}{2\pi}\sin\left(\frac{2\pi\, i}{i_{max}}\right), \quad 0 \le \eta_1 < 1 \quad \text{in the } x\text{-direction} \tag{3.20}$$

$$y_j = \frac{j}{j_{max}} - \frac{\eta_2}{2\pi}\sin\left(\frac{2\pi\, j}{j_{max}}\right), \quad 0 \le \eta_2 < 1 \quad \text{in the } y\text{-direction} \tag{3.21}$$

Here, i_{max} is the number of grid points in the x - direction, and j_{max} the number of grid points in the y - direction. For all the computations carried out in this section $\eta_1 = \eta_2 = 0.99$ has been used.

3.5.2 Results and Comparison

First we present the horizontal velocity at the vertical mid-plane u, and the vertical velocity at the horizontal mid-plane v, and for $Ra = 10^5$ in different grid sizes (Figures 3.2(a) and (b)). The overlapping of the graphs for grids of sizes 81 × 81, 161 × 161, and 321×321 clearly indicates the grid independence of our results. Computations were carried out for different values of Rayleigh number viz. $Ra = 10^3$, 10^4, 10^5, 10^6, 10^7 and 10^8. The results of the present computations are presented through a table. Table 3.1 compares the computed values of the absolute value of ψ at the mid-point of the cavity $|\psi_{mid}|$, the average Nusselt number Nu_0 at the hot wall, the maximum value of Nu_0 on the hot wall, the maximum vertical velocity at the horizontal mid-plane v_{max}, and the maximum horizontal velocity respectively with some well established results and the agreement with most of them is found to be excellent.

Figures 3.3, and 3.4 show the isotherms and streamlines respectively for different values of Ra. The computations were carried out on 81×81 grid for $Ra = 10^3, 10^4, 10^5$, and 10^6, and 129×129 grid for $Ra = 10^7$ and 10^8. From figures 3.3(a)-(f), one can clearly see gradual thinning of the thermal boundary layers with increasing Ra at the hot and cold walls. The same can be seen for the hydrodynamic boundary layers in figures 3.4(a)-(f). The single cellular structures for lower Ra's giving away to multicellular structures for larger Ra's can also be seen from these figures. Once again our qualitative results are very close to those of [30, 37, 101, 174].

We also compute the rate of convergence of our computed data by defining the order of accuracy $O(A)$ as [66]

$$O(A) = \frac{ln(E_c/E_f)}{ln\, 2} \tag{3.22}$$

where E_f and E_c are the relative errors based on root mean square (RMS) on a fine and a coarse grid respectively. The coarse grid has half of the numbers of points in each direction than the finer one. Due to the non-existence of analytical solution for the problem, the numerical solution obtained on the finest grid, viz., 321×321 is treated as a reference analytical solution. These errors are presented in table 3.2. As can be seen from the table, the errors decay with a convergence rate slightly higher than the theoretical rate of the scheme in [94].

Table 3.1: Comparison of present results with established numerical results.

Reference	$\lvert\psi_{mid}\rvert$	Nu_0	$Nu_{0\max}$	u_{max}	v_{max}
		$Ra = 10^3$			
De Vahl Davis [37]	1.174	1.117	1.505	3.649	3.697
Chenoweth and Paolucci [30]	–	1.118	–	3.565	3.687
Denis and Hudson [40]	1.1747	1.1176	1.5058	3.6497	3.6977
Kalita *et. al.* [77]	1.175	1.118	1.505	3.650	3.697
Yu and Tian [174]	1.1749	1.1178	1.5062	3.6501	3.6976
Present	1.1741	1.11538	1.5029	3.6479	3.69249
		$Ra = 10^4$			
De Vahl Davis [37]	5.071	2.238	3.528	16.178	19.617
Chenoweth and Paolucci [30]	–	2.246	–	15.89	19.58
Denis and Hudson [40]	5.0735	2.2396	3.5193	16.1829	19.6293
Kalita *et. al.* [77]	5.080	2.243	3.526	16.203	19.613
Yu and Tian [174]	5.0721	2.2450	3.5314	16.1756	19.6233
Present	5.0745	2.2379	3.5209	16.1797	19.6192
		$Ra = 10^5$			
De Vahl Davis [37]	9.111	4.509	7.717	34.73	68.59
Chenoweth and Paolucci [30]	–	4.531	–	34.23	68.37
Denis and Hudson [40]	9.1126	4.4959	7.6830	34.716	68.6837
Kalita *et. al.* [77]	9.123	4.512	7.670	34.825	68.606
Yu and Tian [174]	9.1093	4.5226	7.7212	34.6856	68.5748
Present	9.1011	4.4898	7.6833	34.6623	67.8331
		$Ra = 10^6$			
De Vahl Davis [37]	16.32	8.817	17.925	64.63	219.36
Chenoweth and Paolucci [30]	–	8.874	–	63.76	218.8
Le Quéré [101]	16.3864	8.8252	17.536	64.8344	220.559
Kalita *et. al.* [77]	16.42	8.763	17.018	65.332	221.658
Yu and Tian [174]	16.3657	8.235	17.5035	64.7187	220.377
Present	16.3409	8.7721	17.5494	64.4527	217.442
		$Ra = 10^7$			
Chenoweth and Paolucci [30]	–	16.82	–	146	699
Le Quéré [101]	29.361	16.523	39.3947	148.59	699.17
Kalita *et. al.* [77]	29.382	16.075	34.925	155.82	696.238
Yu and Tian [174]	29.3126	16.489	38.7386	147.6246	696.857
Xu *et. al.* [167]	29.36267	16.52229	39.40215	148.57189	699.33944
Present	29.06041	16.2525	39.4272	144.406	672.739
		$Ra = 10^8$			
Le Quéré [101]	52.3223	30.255	87.2335	321.878	2222.39
Xu *et. al.* [167]	52.32652	30.2265	87.49182	320.98831	2223.46603
Present	50.7929	29.9898	87.663	304.344	2184.62

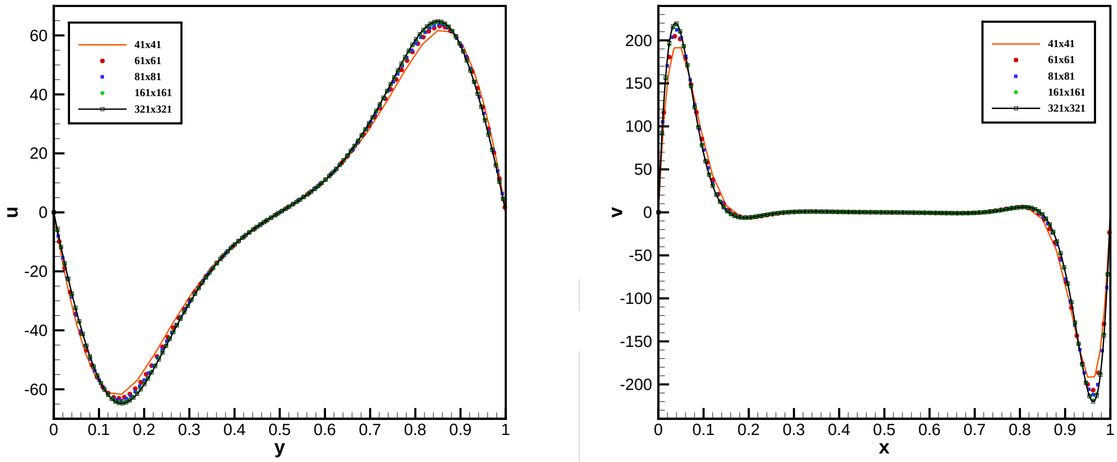

(a) u vs. y

(b) v vs. x

Figure 3.2: Grid independence for $Ra = 10^6$ using five different grids.

Table 3.2: Root Mean Square (RMS) error for u, v, ψ, and T and rate of convergence for $Ra = 10^5, 10^6$ in three different grids.

Ra	Variable	RMS error(41×41)	Rate	RMS error(81×81)	Rate	RMS error(161×161)
10^5	u	2.604041×10^{-2}	1.96	6.687827×10^{-3}	2.25	1.404634×10^{-3}
	v	4.559169×10^{-2}	1.98	1.149601×10^{-2}	2.38	2.203620×10^{-3}
	ψ	1.995389×10^{-2}	1.99	5.020825×10^{-3}	2.41	9.477741×10^{-4}
	T	4.188191×10^{-3}	2.03	1.023991×10^{-3}	2.43	1.851134×10^{-4}
10^6	u	9.437819×10^{-2}	1.71	2.870804×10^{-2}	2.23	6.149545×10^{-3}
	v	1.88046×10^{-1}	1.79	3.420254×10^{-2}	2.24	7.205754×10^{-3}
	ψ	5.993817×10^{-2}	1.79	1.735417×10^{-2}	2.24	3.650825×10^{-3}
	T	1.134107×10^{-2}	1.85	3.147893×10^{-3}	2.28	6.487190×10^{-4}

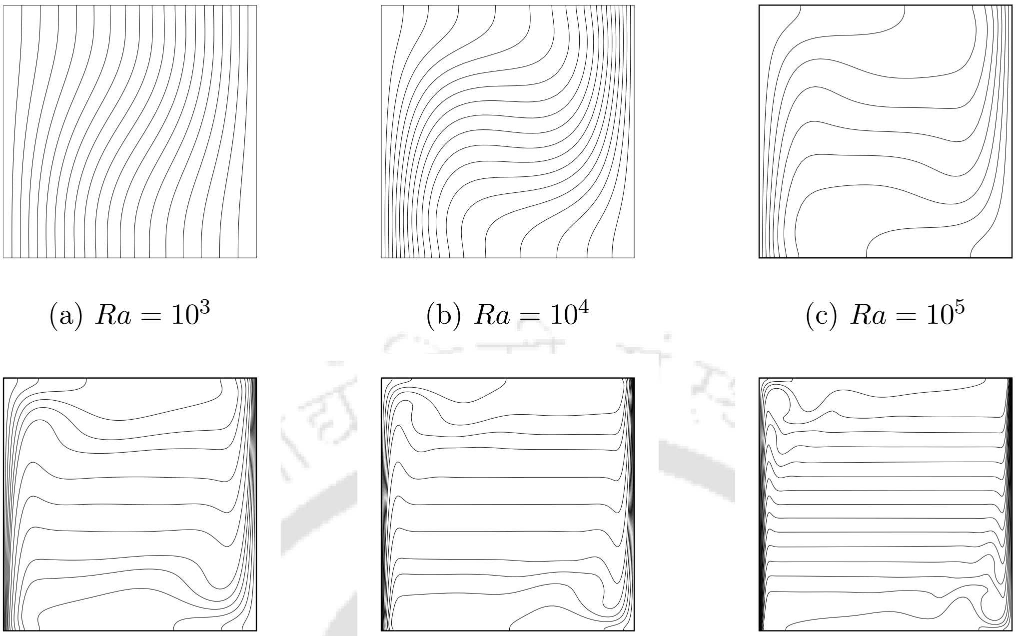

(a) $Ra = 10^3$ (b) $Ra = 10^4$ (c) $Ra = 10^5$

(d) $Ra = 10^6$ (e) $Ra = 10^7$ (f) $Ra = 10^8$

Figure 3.3: Isotherms for different values of Ra.

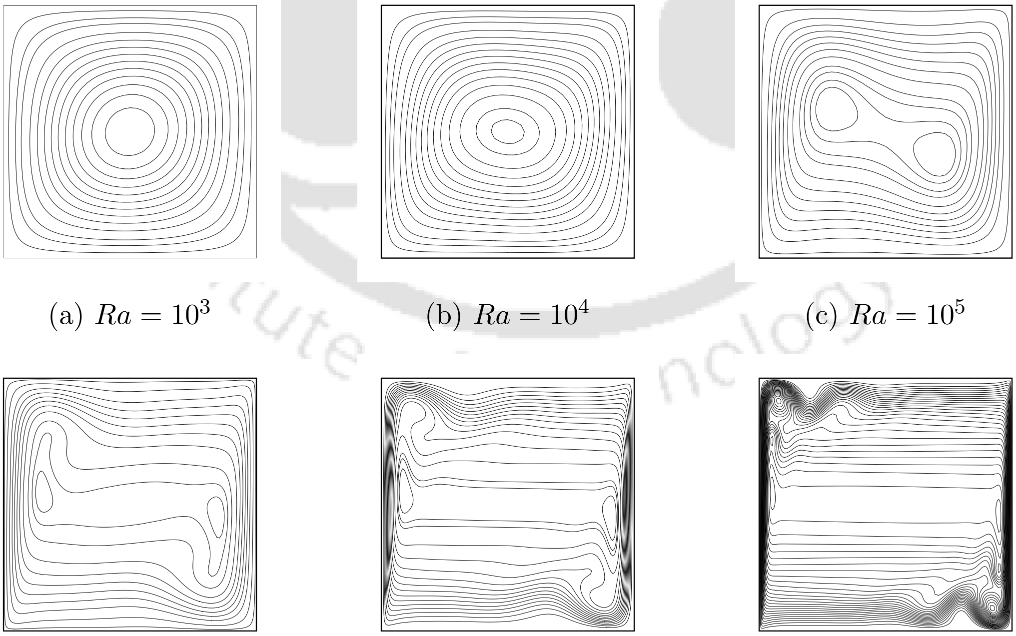

(a) $Ra = 10^3$ (b) $Ra = 10^4$ (c) $Ra = 10^5$

(d) $Ra = 10^6$ (e) $Ra = 10^7$ (f) $Ra = 10^8$

Figure 3.4: Streamlines for different values of Ra.

3.6 Natural convection around a horizontal, heated, circular cylinder placed in an enclosure

A schematic of the system considered in the present study is shown in figure 3.5. The system consists of a square enclosure with sides of length L, within which a circular cylinder with a radius $R(= 0.2L)$ is located and moves along the vertical centerline in the range from $-0.25L$ to $0.25L$. The walls of the square enclosure is kept at a constant low temperature of T_c , whereas the cylinder is kept at a constant high temperature of T_h . In this study, we assume that the radiation effects are negligible. The fluid properties are also assumed to be constant, except for the density in the buoyancy term, which follows the Boussinesq approximation. The gravitational acceleration acts in the negative y-direction.

In the simulations to be reported here, the Prandtl number Pr is taken to be 0.71 (corresponding to that of air) and $r(= R/L) = 0.2$. No-slip and impermeability boundary conditions are imposed on the walls, i.e., $\psi = 0$ on the walls and on the circular cylinder. The hot and cold wall temperatures of $\theta = 0$ and $\theta = 1$ are imposed on the walls of the enclosure and on the surface of the cylinder, respectively.

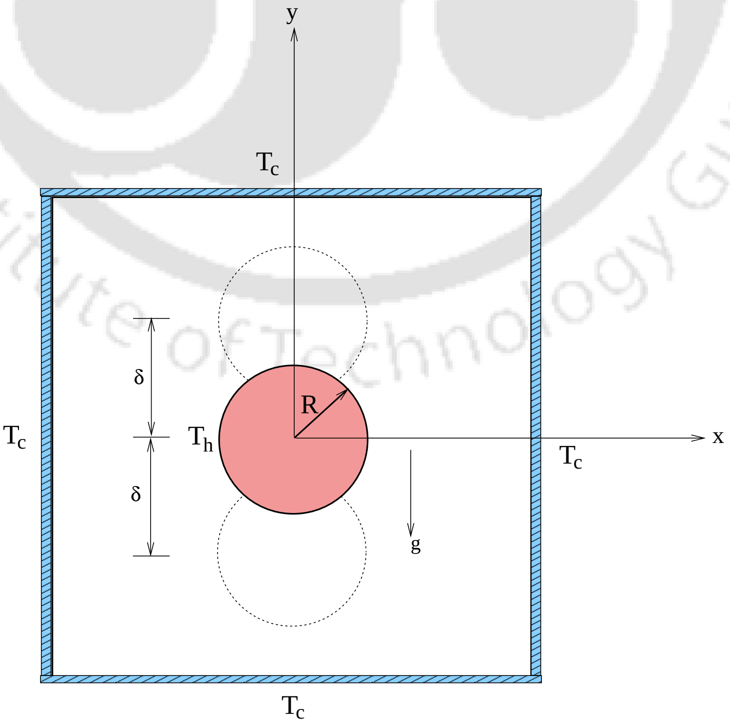

Figure 3.5: Schematic view of a heated circular cylinder enclosed inside a square cavity.

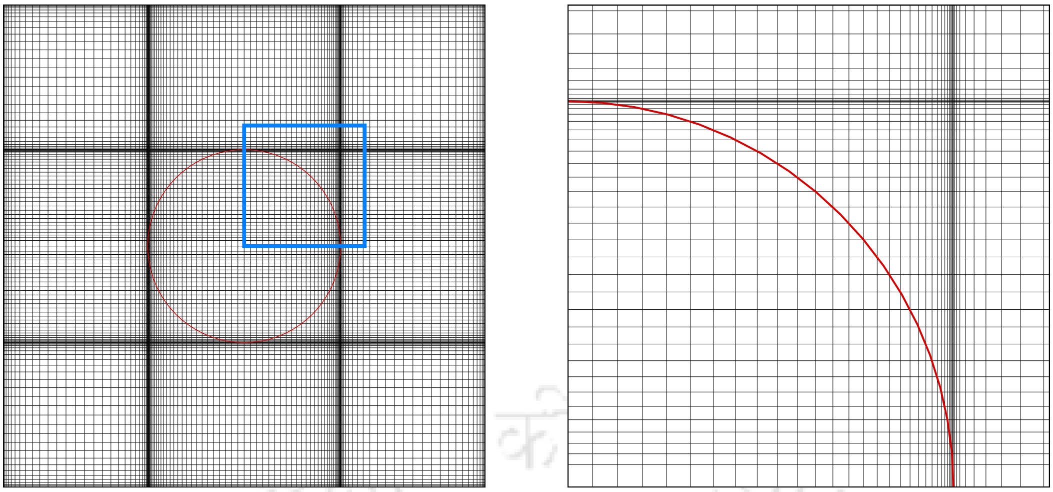

(a) Representative grid. (b) Close-up view inside the blue box.

Figure 3.6: Representative grid and close-up view of a part of the grid.

Figure3.6 (a) shows the computational geometry in the xy- plane with a body-fitted non-uniform grid distribution. A grid resolution of 121×121 along horizontal (x) and vertical (y) directions was employed in computations to be reported in this section. The grid points are densely distributed in the vicinity of the cylinder and the walls in order to account for the high gradients. Note that the grid has been generated in such a way that the circular geometry passes through the grid points as seen in fig. 3.6 (b).

3.6.1 Grid Independence of the computed data

In order to establish grid independence of the computed data, we present streamlines and isotherms on three different grids of sizes 121×121, 161×161 and 241×241 in figure 3.7 for the highest value of Rayleigh number considered in the current study, viz., $Ra = 10^7$ corresponding to $\delta = 0$. The overlapping of the contours shown in these figures clearly demonstrates the grid independence of the simulated data. Further, we have also exhibited the surface Nusselt number distribution corresponding to the same grids in figure 3.8 and once again a close match is observed.

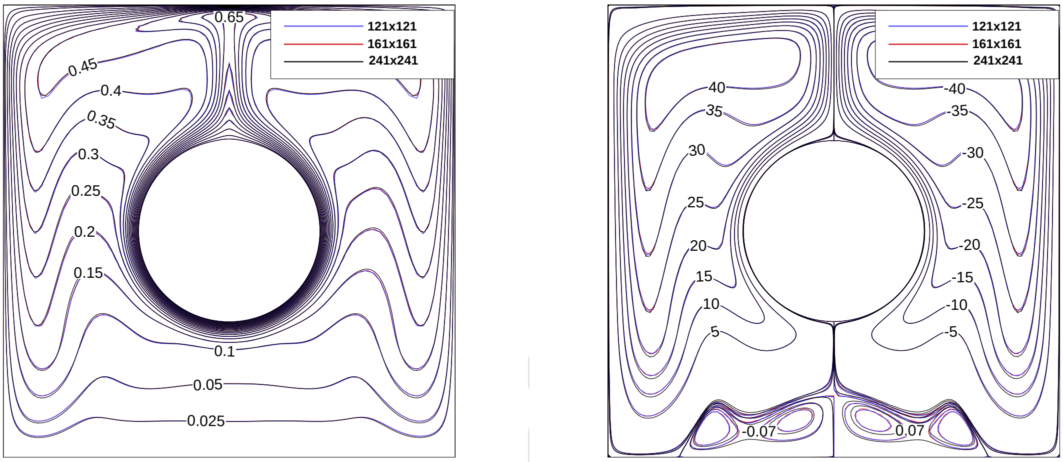

(a) Isotherms.

(b) Streamlines.

Figure 3.7: Isotherms and Streamlines for $Ra = 10^7$ with $\delta = 0$ on three different grids.

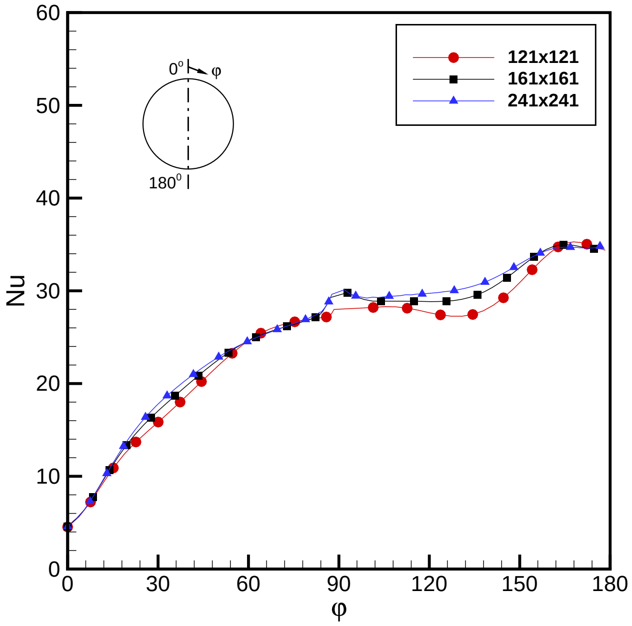

Figure 3.8: Variation of local Nusselt number (Nu) along the surface of the cylinder for $Ra = 10^7$ on three different grids.

3.6.2 Results and discussion

Flow and thermal fields when $\delta = 0$

Figs. 3.9 and 3.10 show the isotherms and streamlines respectively for different Rayleigh Numbers when the cylinder is located at the center of the enclosure which corresponds to $\delta = 0$. For all Rayleigh numbers considered in this study, the flow and thermal fields eventually reach steady state with the symmetric shape about the vertical centerline through the center of the inner circular cylinder.

In general, the heated lighter fluid is lifted and moves upward along the hot surface of the inner cylinder and the vertical symmetry line until it encounters the cold top wall. Then the fluid becomes gradually colder and denser while it moves horizontally outward in contact with the cold top wall. Consequently, the cooled denser fluid descends along the cold side walls.

For $Ra = 10^3$, the heat transfer in the enclosure is mainly dominated by conduction. The circulation of the flow shows two overall rotating symmetric eddies with two inner vortices respectively as shown in figure 3.10(a). At $Ra = 10^4$, the patterns of the isotherms and streamlines are about the same as those for $Ra = 10^3$. A careful observation reveals that the thermal boundary layer on the bottom part of cylinder is thinner than its top counterpart and the inner lower vortex slightly becomes smaller in size and weaker in strength compared with the upper one, because the effect of convection on heat transfer and flow increases with an increase in the Rayleigh number.

At $Ra = 10^5$, the role of convection in heat transfer is significant and consequently the thermal boundary layer on the surface of the cylinder becomes thinner. Also, a plume starts to appear on the top of the cylinder and as a result the isotherms move upward, giving rise to a stronger thermal gradient in the upper part of the enclosure and a much lower thermal gradient in the lower part. Thus, the dominant flow is in the upper half of the enclosure, and correspondingly the core of the recirculating eddies is located only in the upper half (Figure 3.10(a)).

At $Ra = 10^6$, heat transfer in the enclosure is mainly governed by convection. Since the convection velocity significantly increases with increasing Rayleigh number, the boundary layer behavior can be clearly observed in regions of the lower part of cylinder and the upper part of the enclosure as shown in figure 3.9(b). The thermal boundary layer separates from the surface near the top of the cylinder and as a result a strong plume appears. As a result, the flow impinges on the top of the enclosure, which also leads to the formation of a thinner thermal boundary layer in this region and enhances the heat transfer. Tiny symmetric vortices appear in the vicinity of the bottom wall of the enclosure owing to the separation of the boundary layer by strong convective flow (Figure 3.10(b)).

At $Ra = 10^7$ convective heat transfer is much more pronounced. As seen from figure 3.9(c), the thermal boundary layer that forms on the inner cylinder is thinner than that at $Ra = 10^6$, and the isotherms become flatter at the bottom half of the enclosure. Also, the plume that appears on the top of the cylinder becomes sharper and impinges strongly on the top of the enclosure. The tiny vortices that appeared in the lower region of the enclosure at $Ra = 10^6$ becomes larger and splits into two.

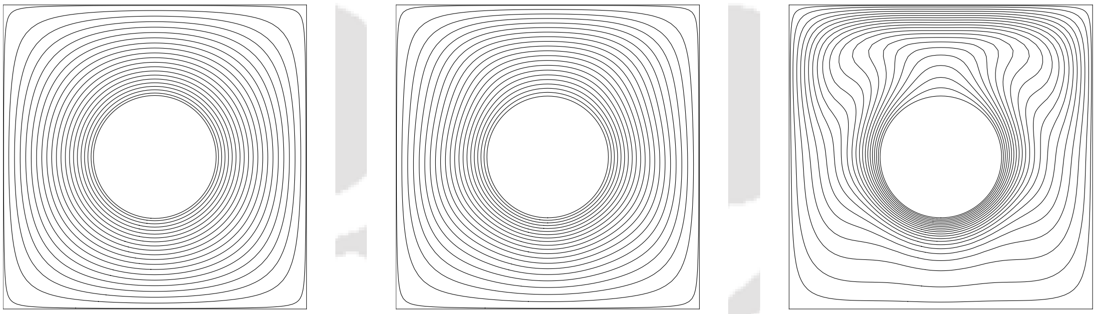

(a) $Ra = 10^3$ (b) $Ra = 10^4$ (c) $Ra = 10^5$

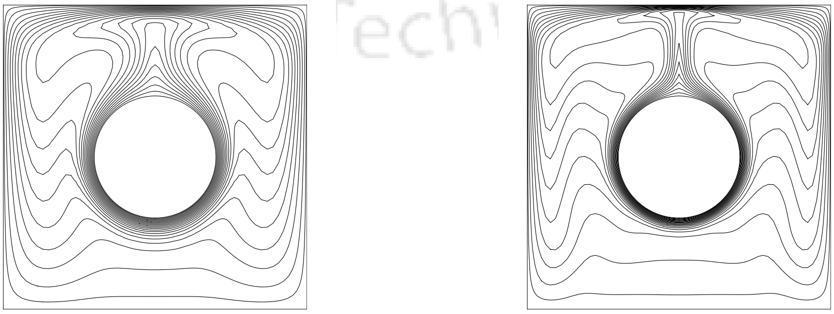

(d) $Ra = 10^6$ (e) $Ra = 10^7$

Figure 3.9: Isotherms for different values of Ra with $\delta = 0$.

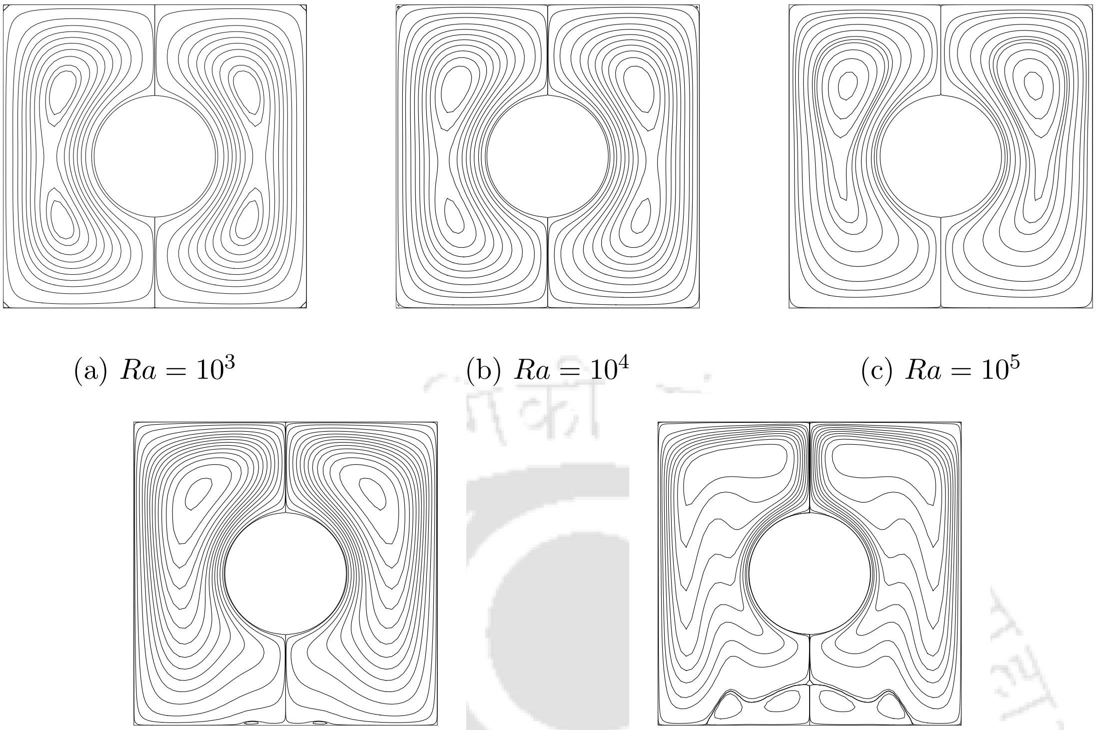

(a) $Ra = 10^3$ (b) $Ra = 10^4$ (c) $Ra = 10^5$

(d) $Ra = 10^6$ (e) $Ra = 10^7$

Figure 3.10: Streamlines for different values of Ra with $\delta = 0$.

Flow and thermal fields as a function of δ

We now discuss the flow structure when the cylinder is displaced from the center of the square. The displacement of the cylinder can be controlled through the parameter δ: a positive value indicating a displacement upwards through a distance δ and likewise a negative value of δ indicates a displacement downwards through the same distance.

(a) $Ra = 10^3$ We can observe the dependence of flow and thermal fields on δ in the plots of isotherms and streamlines for different δ's at $Ra = 10^3$ in Figs. 3.11 and 3.12 respectively. Figs. 3.11 (a) - (j) show the isotherms and Figs. 3.12 (a) - (j) show the streamlines when the inner cylinder moves upward and downward at the same intervals of 0.05, respectively. Regardless of the variation in δ, the solutions have a two-fold symmetry about the vertical center line. When the cylinder moves downward, the size of the lower inner vortex is reduced gradually and the two inner vortices merge into a single one at $\delta = -0.15$ (Figure3.12 (f)) because the space between the cylinder and the bottom wall of the enclosure decreases. On the other hand, the size of the upper inner vortex increases and its core moves toward the center of the enclosure. As the magnitude of δ increases, the isotherms become denser between the lower part of the inner cylinder and the bottom wall, whereas they become coarser in the opposite region. As the cylinder moves upward, we can observe the same patterns of isotherms and streamlines as when the cylinder moves downwards, but in the opposite sense.

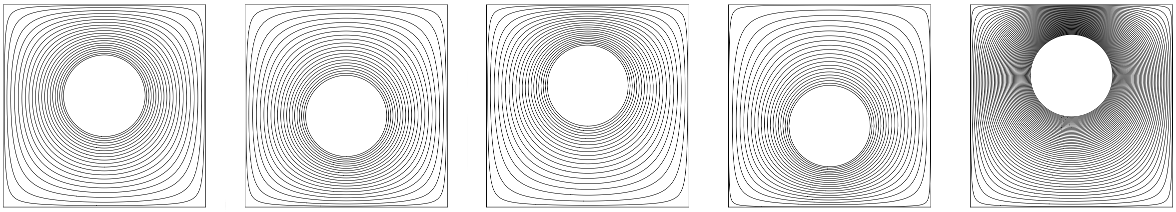

(a) $\delta = 0.05$ (b) $\delta = -0.05$ (c) $\delta = 0.1$ (d) $\delta = -0.1$ (e) $\delta = 0.15$

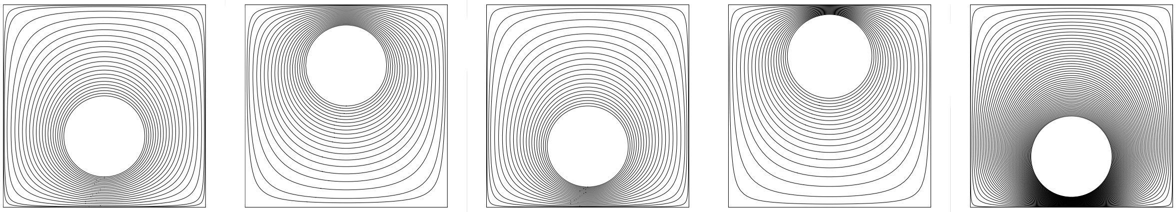

(f) $\delta = -0.15$ (g) $\delta = 0.2$ (h) $\delta = -0.2$ (i) $\delta = 0.25$ (j) $\delta = -0.25$

Figure 3.11: Isotherms for $Ra = 10^3$ different values of δ.

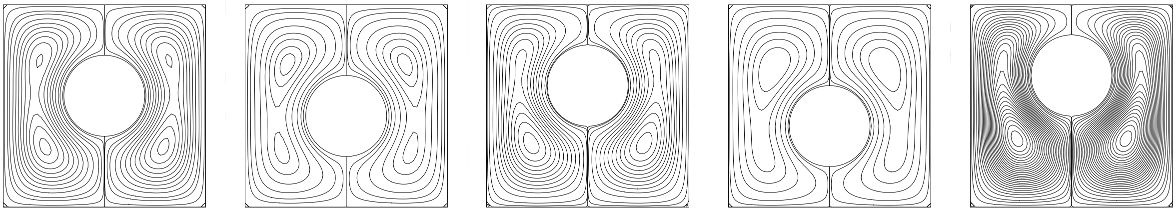

(a) $\delta = 0.05$ (b) $\delta = -0.05$ (c) $\delta = 0.1$ (d) $\delta = -0.1$ (e) $\delta = 0.15$

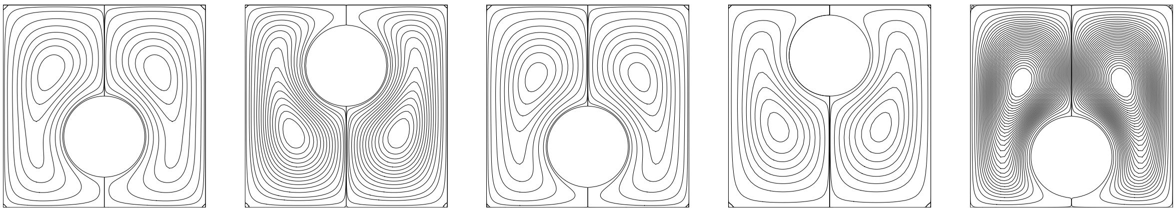

(f) $\delta = -0.15$ (g) $\delta = 0.2$ (h) $\delta = -0.2$ (i) $\delta = 0.25$ (j) $\delta = -0.25$

Figure 3.12: Streamlines for $Ra = 10^3$ different values of δ.

(b) $Ra = 10^4$ Figs. 3.13 and 3.14 show the isotherms and streamlines, respectively, for different δ's when $Ra = 10^4$. As Ra increases to 10^4, the effect of convective heat transfer becomes more pronounced than at $Ra = 10^3$. When the cylinder moves downward, the two inner vortices merge into a single vortex at $\delta = -0.1$, which is earlier than $\delta = -0.15$ at $Ra = 10^3$. With increase in the magnitude of δ, the isotherms gradually become distorted and the size of the thermal plumes formed on the top of the inner cylinder becomes larger. When the cylinder moves upward, the bifurcation from inner bi-cellular vortices to uni-cellular vortex occurs at $\delta = 0.15$, which is later than that for the case when the cylinder moves downward. This is because of the existence of a stronger convective flow in the region between the hot inner cylinder and top wall of the enclosure. When we increase δ further, the centers of the two vortices move closer to the center of the enclosure. The switch from bi-cellular to uni-cellular structure as one moves from a lower Ra to a higher one as seen corresponding to $\delta = 0$ (Figure3.14), can also be seen here.

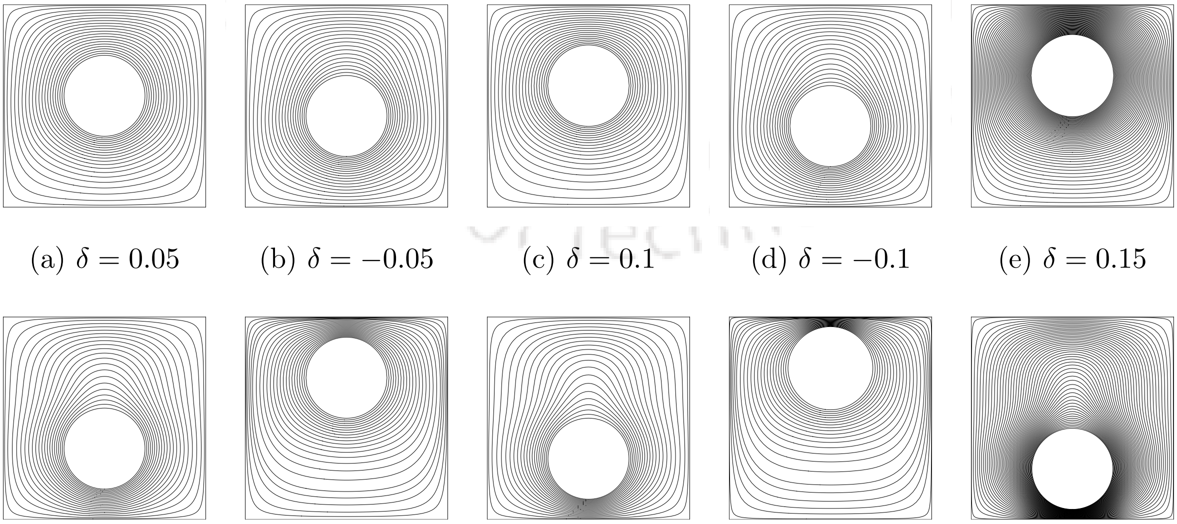

(a) $\delta = 0.05$ (b) $\delta = -0.05$ (c) $\delta = 0.1$ (d) $\delta = -0.1$ (e) $\delta = 0.15$

(f) $\delta = -0.15$ (g) $\delta = 0.2$ (h) $\delta = -0.2$ (i) $\delta = 0.25$ (j) $\delta = -0.25$

Figure 3.13: Isotherms for $Ra = 10^4$ different values of δ.

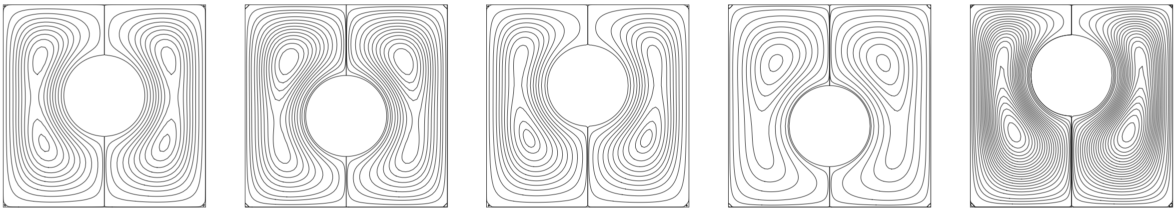

(a) $\delta = 0.05$ (b) $\delta = -0.05$ (c) $\delta = 0.1$ (d) $\delta = -0.1$ (e) $\delta = 0.15$

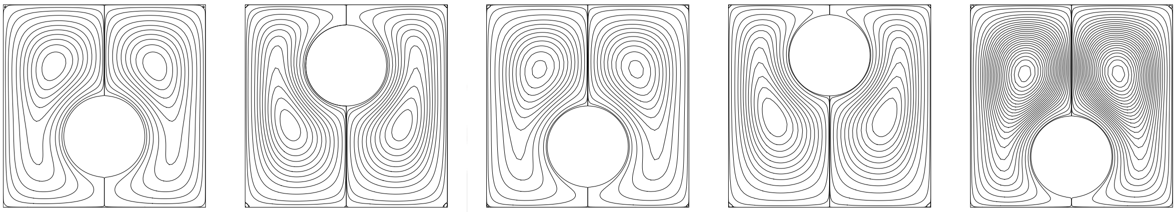

(f) $\delta = -0.15$ (g) $\delta = 0.2$ (h) $\delta = -0.2$ (i) $\delta = 0.25$ (j) $\delta = -0.25$

Figure 3.14: Streamlines for $Ra = 10^4$ different values of δ.

(c) $Ra = 10^5$ Figs. 3.15 and 3.16 show the isotherms and streamlines, respectively, for different δ's when $Ra = 10^5$. When the inner cylinder is placed at the center (Figure 3.9), the flow pattern is unicellular. When the inner cylinder moves vertically on either direction at $Ra = 10^5$, the pattern of major vortices formed in the enclosure is also unicelluar as shown in figure 3.16. The pattern of isotherms at $Ra = 10^5$ are so because buoyancy induced convection becomes more dominant than conduction.

When the inner cylinder moves upward, the pattern of isotherms and streamlines is much different from that when the cylinder moves downward. At $\delta = 0.05$, when the cylinder is located slightly above the center of the enclosure, isotherms at the upper half of the enclosure are slightly squeezed and the temperature value at the vertical center line is lower than that at the same elevation close to the vertical centerline. Thus, at $\delta = 0.05$, the plume that we see in figure 3.9(a) for $\delta = 0.0$ is divided into three plumes as shown in figure 3.15(a). Two upward plumes appear on the top of the cylinder at about ±20° from the vertical centerline. A third plume appears above the top of the inner circular cylinder with reverse direction owing to the two secondary vortices newly generated over the upper part of the inner circular cylinder (Figure 3.16 (a)). As we increase δ further, the reduced space above the top of inner cylinder confines the vertical motion of flow and consequently heat conduction is dominant over convective heat transfer locally in this space. Thus, the two secondary vortices over the top of the cylinder decreases in size and finally disappears at $\delta = 0.2$, and accordingly no third plume is found at this position. The primary symmetric eddies are squeezed and elongated vertically as the inner cylinder moves upward, which can be compared with the cases of the cylinder moving downward.

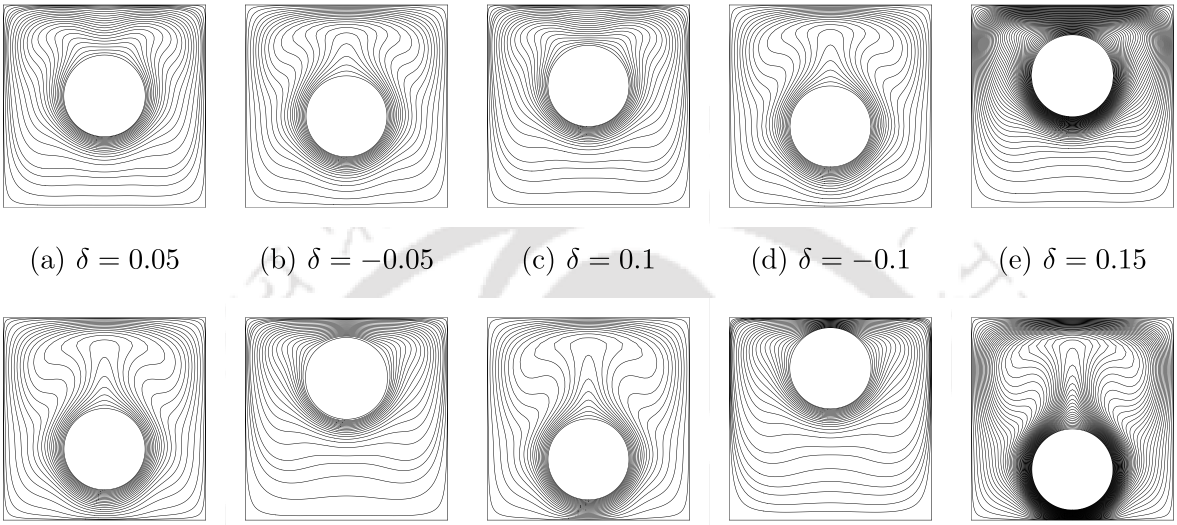
(a) $\delta = 0.05$ (b) $\delta = -0.05$ (c) $\delta = 0.1$ (d) $\delta = -0.1$ (e) $\delta = 0.15$

(f) $\delta = -0.15$ (g) $\delta = 0.2$ (h) $\delta = -0.2$ (i) $\delta = 0.25$ (j) $\delta = -0.25$

Figure 3.15: Isotherms for $Ra = 10^5$ different values of δ.

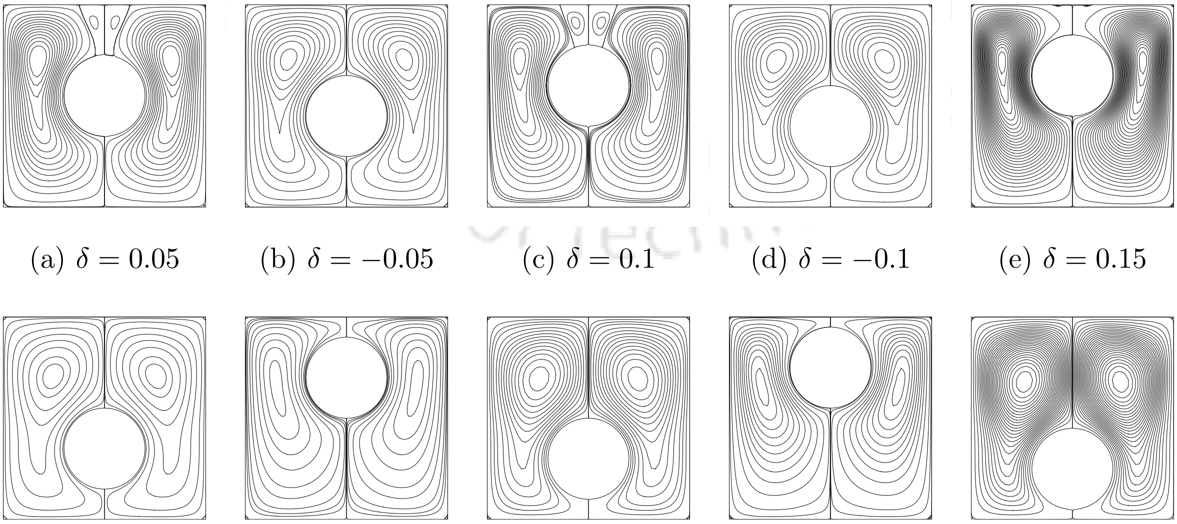
(a) $\delta = 0.05$ (b) $\delta = -0.05$ (c) $\delta = 0.1$ (d) $\delta = -0.1$ (e) $\delta = 0.15$

(f) $\delta = -0.15$ (g) $\delta = 0.2$ (h) $\delta = -0.2$ (i) $\delta = 0.25$ (j) $\delta = -0.25$

Figure 3.16: Streamlines for $Ra = 10^5$ different values of δ.

(d) $Ra = 10^6$ Figs. 3.17 and 3.18 show the isotherms and streamlines for different δ's when $Ra = 10^6$. When the Rayleigh number increases to 10^6, the magnitude of the velocity circulating in the enclosure increases and the isotherms are distorted more due to the stronger convection effects, leading to the stable stratification of the isotherms. As a result the thickness of the thermal boundary layer formed on the surface of the cylinder and the enclosure reduces further and the thermal gradients on the walls become larger.

When the center of inner cylinder is placed below the center of the enclosure ($\delta < 0$), the distribution of the isotherms and streamlines for different δ's shows a similar pattern with the large upwelling plumes on the top of the cylinder and the two main rotating symmetric eddies whose core is located at the upper half of the enclosure. When $\delta < 0$, this feature at $Ra = 10^6$ is very similar to that at $Ra = 10^5$, except that the temperature gradients formed on the surfaces of the cylinder and enclosure when $Ra = 10^6$ are sharper than those when $Ra = 10^5$. When $\delta < 0$, the vortices which exist around the center of the bottom wall when $\delta \geq 0$, disappear as the space decreases between the cylinder and the bottom wall. When the cylinder moves upward, secondary vortices are formed on the top surface of the cylinder in addition to the main vortices, similar to the case of $Ra = 10^5$. The size of the secondary vortices is larger than that at $Ra = 10^5$ because of the stronger convection effects.

When $\delta = 0.05$, we can observe the descending plume on the top surface of the inner cylinder and two ascending plumes on the upper part of the cylinder at approximately 30^0 from the vertical centerline (Figure 3.17(a)), corresponding to the secondary vortices formed on the upper surface of the cylinder. When $\delta = 0.05$, the size of the secondary vortices and the distance from the vertical centerline to the ascending plume becomes larger, compared to those at $Ra = 10^5$, due to the increasing convection effects with the increasing Rayleigh number. When $\delta = 0.05$, we can also observe the formation of additional vortices on the bottom wall of the enclosure, which is not present when $\delta < 0$ at the same Rayleigh number. The size of the vortices formed on the bottom wall and the distance from the center to the separation point at $\delta = 0.05$ becomes larger, compared to those at $\delta = 0$.

When δ increases further to 0.1 (Fig 3.17(c)) and 0.15 (Figure 3.17(e)), the isotherms are a little squeezed as the space between the cylinder and the top wall of the enclosure decreases, but the shapes of the isotherms and streamlines are generally similar to those at $\delta = 0.05$. The size of the secondary vortices formed on the upper surface of the inner cylinder at $\delta = 0.1$ (Figure 3.18(c)) and 0.15 (Figure 3.18(e)) is smaller than that at $\delta = 0.05$, whereas the size of the additional vortices formed on the bottom wall becomes larger, compared to those at $\delta = 0.05$.

At $\delta = 0.2$, for $Ra = 10^5$, the secondary vortices on the upper surface of the cylinder disappear as shown in Fig. 3.16(g). However, as the Rayleigh number increases to 10^6, tertiary vortices are formed on the top surface of the cylinder in addition to the secondary vortices (Figure 3.18(g)) with the presence of three upward and two downward plumes on the upper surface of the cylinder (Figure 3.17(g)), even though the space between the cylinder and thetop wall of the enclosure becomes smaller. The additional vortices which are present on the bottom wall at $0 \leq \delta \leq 0.15$ disappear at $\delta = 0.2$, because the convective flow is not strong enough to penetrate the increased space below the bottom of the cylinder. As a result the separation of the boundary layer on the bottom wall doesn't occur.

When $\delta = 0.25$, the space between the cylinder and the top wall of the enclosure is very small. As a result the two pairs of the vortices formed on the upper surface of the cylinder at $\delta = 0.2$ merge into a pair of secondary vortices. Thus there is a single downward and two upward plumes on the upper surface of the cylinder. The shape of the main vortices at $\delta = 0.25$ is similar to that at $\delta = 0.2$.

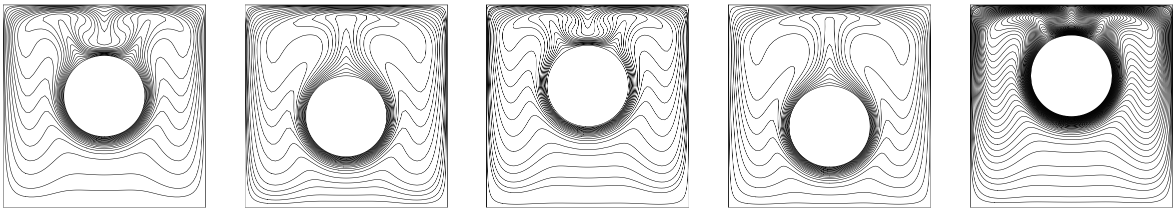

(a) $\delta = 0.05$ (b) $\delta = -0.05$ (c) $\delta = 0.1$ (d) $\delta = -0.1$ (e) $\delta = 0.15$

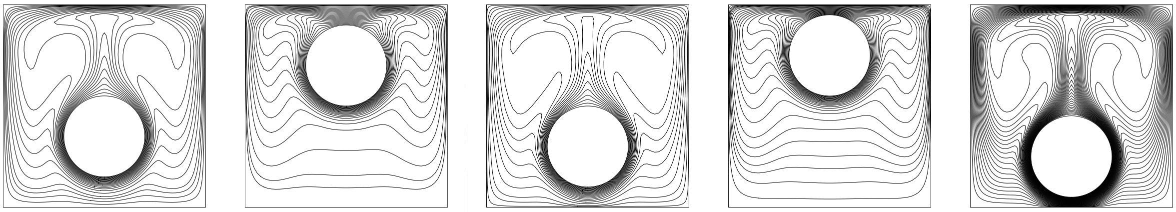

(f) $\delta = -0.15$ (g) $\delta = 0.2$ (h) $\delta = -0.2$ (i) $\delta = 0.25$ (j) $\delta = -0.25$

Figure 3.17: Isotherms for $Ra = 10^6$ different values of δ.

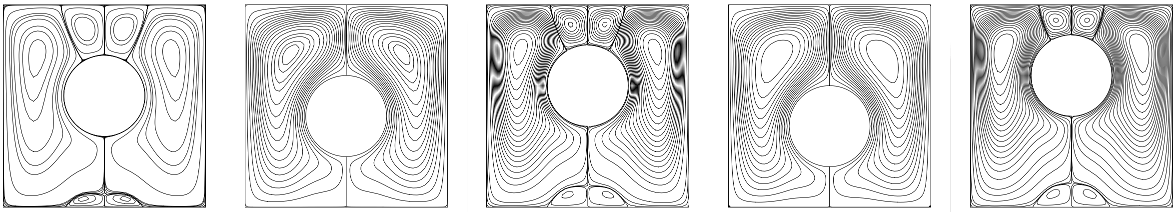

(a) $\delta = 0.05$ (b) $\delta = -0.05$ (c) $\delta = 0.1$ (d) $\delta = -0.1$ (e) $\delta = 0.15$

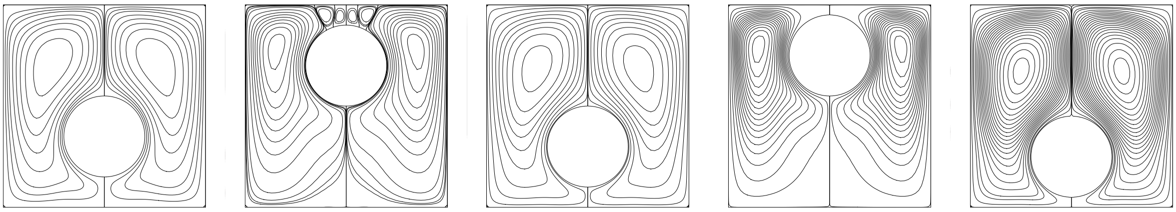

(f) $\delta = -0.15$ (g) $\delta = 0.2$ (h) $\delta = -0.2$ (i) $\delta = 0.25$ (j) $\delta = -0.25$

Figure 3.18: Streamlines for $Ra = 10^6$ different values of δ.

(e) $Ra = 10^7$ Figs. 3.19 and 3.20 show the isotherms and streamlines for different δ's when $Ra = 10^7$. At $Ra = 10^7$, steady state could not be obtained for the whole range $-0.25 \leq \delta \leq 0.25$ considered earlier for $Ra = 10^5, 10^6$. Yoon *et. al.* [172] had shown that steady state existed for $0.05 \leq \delta \leq 0.18$. Thus we consider only those values of δ here. When the cylinder was too close to either the top or bottom walls, the residual set for obtaining steady state solution (section 3.4) was seen to diverge.

At $\delta = 0.05$, the descending plume that existed for $Ra = 10^6$ disappears, and only a sharp upward plume is noticed (Figure 3.19(a)) with a thinning of the thermal boundary layer on the surface of the cylinder, with the flow structure becoming chaotic (Figure 3.20(a)).

At $\delta = 0.1$, the space between the top surface of the cylinder and the upper part of the enclosure decreases, but the pattern of the thermal plume that impinges on the top surface of the enclosure remains same as at $\delta = 0.05$. The flow structure at $\delta = 0.05$ and $\delta = 0.1$ are almost similar.

When $\delta = 0.15$, we observe a descending plume on the top surface of the cylinder and two ascending plumes at approximately 20° from the vertical centerline (Figure 3.19(c)), corresponding to the two secondary vortices that appear on the top surface of the cylinder (Figure3.20(c)). This pattern can be seen again at $\delta = 0.18$ (Figure 3.19(d)). The secondary vortices appearing on the top surface of the cylinder at $\delta = 0.15$ are reduced in size as the space between the top of the cylinder and the upper wall of the enclosure decreases.

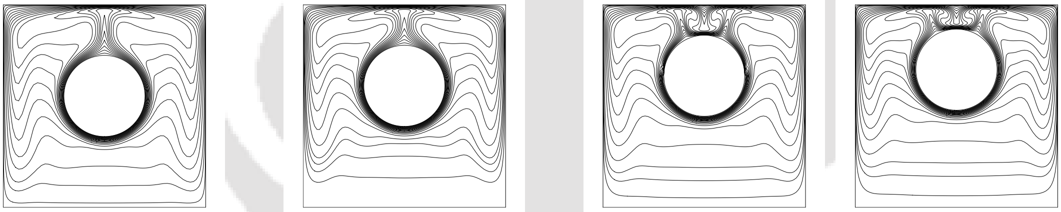

(a) $\delta = 0.05$ (b) $\delta = 0.1$ (c) $\delta = 0.15$ (d) $\delta = 0.18$

Figure 3.19: Isotherms for $Ra = 10^7$ different values of δ.

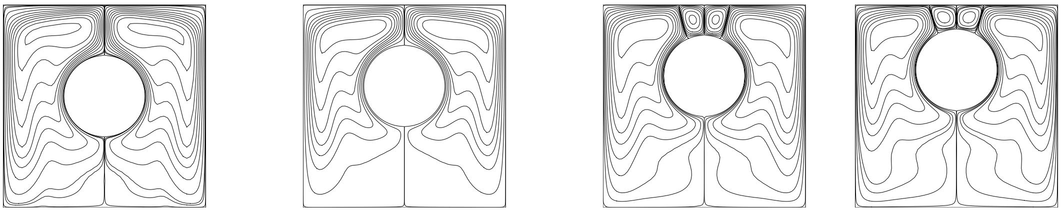

(a) $\delta = 0.05$ (b) $\delta = 0.1$ (c) $\delta = 0.15$ (d) $\delta = 0.18$

Figure 3.20: Streamlines for $Ra = 10^7$ different values of δ.

Formation of secondary corner vortices

At all positions of the cylinder, we can see the formation of secondary vortices at the four corners of the enclosure for $10^3 \leq Ra \leq 10^6$. The strength of the vortices at their centers as well the coordinates of the centers are tabulated in Tables 3.3 and 3.4. Figs. 3.21a, 3.21b, 3.21c, and 3.21d show the details of the corner vortices for four different configurations. For the sake of brevity, we are limiting ourselves to showing four figures rather than the full range of configurations. In these figures, 'LP' denotes Left Primary, 'TL' denotes Top Left, 'RP' denotes Right Primary, 'BR' denotes Bottom Right, and 'BL' denotes Bottom Left.

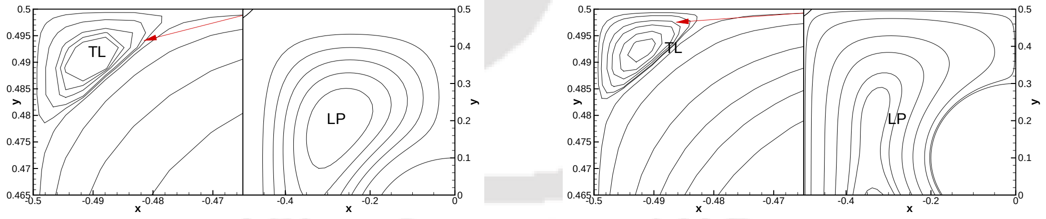

(a) Top left corner, $Ra = 10^3$ and $\delta = -0.1$ (b) Top left corner, $Ra = 10^3$ and $\delta = 0.1$

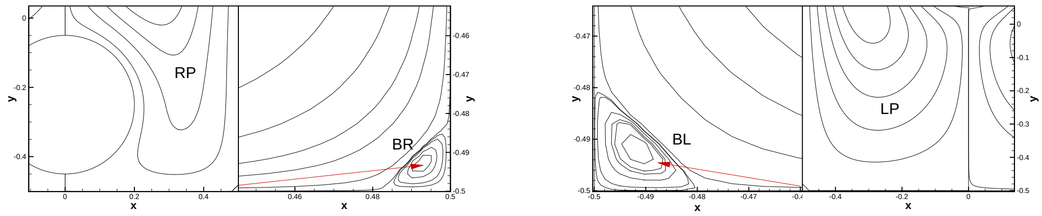

(c) Bottom right corner, $Ra = 10^3$ and $\delta = 0.1$ (d) Bottom left corner, $Ra = 10^5$ and $\delta = 0.25$

Figure 3.21: Secondary corner vortices at different corners of the cavity for different Ra and δ.

Table 3.3: Details of corner vortices - I.

δ	Ra	Top Left		Top Right	
		ψ_{mid}	(x, y)	ψ_{mid}	(x, y)
0	10^3	-6.239e-7	(-0.4937,0.4892)	6.295e-7	(0.4892,0.4937)
	10^4	-6.818e-6	(-0.4892,-0.4937)	6.818e-6	(0.4892,0.4937)
	10^5	-2.864e-5	(-0.4937,-0.4937)	2.664e-5	(0.4937,0.4937)
	10^6	-1.356e-5	(-0.4966,0.4966)	1.356e-5	(0.4966,0.4966)
0.05	10^3	-5.793e-7	(-0.4937,0.4910)	5.793e-7	(0.4937,0.4910)
	10^4	-6.145e-6	(-0.4937,0.4910)	6.145e-6	(0.4937,0.4910)
	10^5	-2.493e-5	(-0.4937,0.4947)	2.493e-5	(0.4937,0.4947)
	10^6	-1.491e-5	(-0.4966,0.4972)	1.491e-5	(0.4966,0.4972)
0.1	10^3	-4.991e-7	(-0.4937,0.4928)	4.991e-7	(0.4937, 0.4928)
	10^4	-5.273e-6	(-0.4937,0.4928)	5.273e-6	(0.4937, 0.4928)
	10^5	-2.204e-5	(-0.4937,0.4958)	2.204e-5	(0.4937,0.4958)
	10^6	-1.852e-5	(-0.4966,0.4977)	1.852e-5	(0.4966,0.4977)
0.15	10^3	-4.193e-7	(-0.4897,0.4948)	4.267e-7	(0.4949,0.4920)
	10^4	-4.448e-6	(-0.4949,0.4920)	4.448e-6	(0.4949,0.4920)
	10^5	-2.395e-5	(-0.4949,0.4948)	2.395e-5	(0.4949,0.4948)
	10^6	-1.347e-5	(-0.4949,0.4974)	1.347e-5	(0.4949,0.4974)
0.2	10^3	-4.522e-7	(-0.4937,0.4917)	4.522e-7	(0.4937,0.4917)
	10^4	-4.382e-6	(-0.4937,0.4917)	4.382e-6	(0.4937,0.4917)
	10^5	-1.826e-6	(-0.4937,0.4964)	1.826e-5	(0.4937,0.4964)
	10^6	-2.125e-5	(-0.4966,0.4964)	2.125e-5	(0.4966,0.4964)
0.25	10^3	-4.093e-7	(-0.4937,0.4921)	4.093e-7	(0.4937,0.4921)
	10^4	-4.099e-6	(-0.4937,0.4921)	4.099e-6	(0.4937,0.4921)
	10^5	-1.884e-5	(-0.4937,0.4958)	1.884e-5	(0.4937,0.4958)
	10^6	-2.336e-5	(-0.4966,0.4971)	2.336e-5	(0.4966,0.4971)
-0.05	10^3	-7.717e-7	(-0.4892,0.4926)	7.717e-7	(0.4892,0.4926)
	10^4	-8.851e-6	(-0.4892,0.4926)	8.851e-6	(0.4892,0.4926)
	10^5	-2.830e-6	(-0.4937,0.4926)	2.830e-6	(0.4937,0.4926)
	10^6	-1.024e-5	(-0.4966,0.4961)	1.024e-5	(0.4966,0.4961)
-0.1	10^3	-7.882e-7	(-0.4897,0.4932)	7.882e-7	(0.4897,0.4932)
	10^4	-1.005e-5	(-0.4897,0.4932)	1.005e-5	(0.4897,0.4932)
	10^5	-2.954e-5	(-0.4949,0.4932)	2.954e-5	(0.4949,0.4932)
	10^6	-8.967e-6	(-0.4966,0.4979)	8.967e-6	(0.4966,0.4979)
-0.15	10^3	-9.652e-7	(-0.4879,0.4918)	9.652e-7	(0.4879,0.4918)
	10^4	-1.269e-5	(-4916,0.4875)	1.297e-5	(0.4879,0.4918)
	10^5	-3.021e-5	(-0.4945,0.4918)	3.021e-5	(0.4945,0.4918)
	10^6	-1.008e-5	(-0.4966,0.4971)	-1.008e-5	(0.4966,0.4971)
-0.2	10^3	-1.084e-6	(-0.4879,0.4909)	1.084e-6	(0.4879,0.4909)
	10^4	-1.597e-5	(-0.4892,0.4895)	1.597e-5	(0.4892,0.4895)
	10^5	-3.110e-5	(-0.4937,0.4944)	3.110e-5	(0.4937,0.4944)
	10^6	-9.239e-6	(-0.4966,0.4974)	9.239e-6	(0.4966,0.4974)
-0.25	10^3	-1.186e-6	(-0.4892,0.4884)	1.186e-6	(0.4892,0.4884)
	10^4	-1.726e-5	(-0.4892,0.4884)	1.726e-5	(0.4892,0.4884)
	10^5	-3.433e-5	(-0.4937,0.4938)	3.433e-5	(0.4937,0.4938)
	10^6	-9.196e-6	(-0.4966,0.4971)	9.196e-6	(0.4966,0.4971)

Table 3.4: Details of corner vortices - II.

δ	Ra	Bottom Left		Bottom Right	
		ψ_{mid}	(x, y)	ψ_{mid}	(x, y)
0	10^3	-6.146e-7	(-0.4892,-0.4937)	6.146e-7	(0.4892,-0.4937)
	10^4	-5.449e-6	(-0.4892,-0.4937)	5.449e-6	(0.4892,-0.4937)
	10^5	-1.770e-5	(-0.4892,-0.4937)	1.770e-5	(0.4892,-0.4937)
	10^6	-1.294e-5	(-0.4937,-0.4966)	1.294e-5	(0.4937,-0.4966)
0.05	10^3	-7.407e-7	(-0.4892,-0.4926)	7.407e-7	(0.4892,-0.4926)
	10^4	-6.141e-6	(-0.4892,-0.4926)	6.141e-6	(0.4892,-0.4926)
	10^5	-1.450e-5	(-0.4892,-0.4926)	1.450e-5	(-0.4892,-0.4926)
	10^6	-1.085e-5	(-0.4937,-0.4961)	1.085e-5	(0.4937,-0.4961)
0.1	10^3	-8.540e-7	(-0.4892,-0.4916)	8.540e-7	(0.4892,-0.4916)
	10^4	-6.492e-6	(-0.4892,-0.4916)	6.4924e-6	(0.4892,-0.4916)
	10^5	-1.102e-5	(-0.4937,-0.4916)	1.1029e-5	(0.4892,-0.4916)
	10^6	-8.258e-6	(-0.4966,-0.4955)	8.258e-6	(0.4966,-0.4955)
0.15	10^3	-8.297e-7	(-0.489,-0.4924)	8.297e-7	(0.4897,-0.4924)
	10^4	-5.781e-6	(-0.4897,-0.4924)	5.781e-6	(0.4897,-0.4924)
	10^5	-9.957e-6	(-0.4897,-0.4924)	9.957e-6	(0.4897,-0.4924)
	10^6	-3.009e-7	(-0.4949,-0.4924)	3.009e-7	(0.4949,-0.4924)
0.2	10^3	-9.970e-7	(-0.4892,-0.4895)	9.970e-7	(0.4892,-0.4895)
	10^4	-6.183e-6	(-0.4892,-0.4895)	6.183e-6	(0.4892,-0.4895)
	10^5	-6.804e-6	(-0.4937,-0.4895)	6.804e-6	(0.4937,-0.4895)
	10^6	-5.047e-6	(-0.4966,-0.4944)	5.047e-6	(0.4966,-0.4944)
0.25	10^3	-1.012e-6	(-0.4892,-0.4884)	1.012e-6	(0.4892,-0.4884)
	10^4	-5.654e-6	(-0.4892,-0.4884)	5.654e-6	(0.4892,-0.4884)
	10^5	-5.406e-6	(-0.4892,-0.4938)	5.406e-6	(0.4892,-0.4938)
	10^6	-4.121e-6	(-0.4966,-0.4938)	4.121e-6	(0.4966,-0.4938)
-0.05	10^3	-5.695e-7	(-0.4937,-0.4910)	5.695e-7	(0.4937,-0.4910)
	10^4	-5.212e-6	(-0.4937,-0.4910)	5.212e-6	(0.4937,-0.4910)
	10^5	-2.141e-5	(-0.4937,-0.4910)	2.141e-5	(0.4937,-0.4910)
	10^6	-1.642e-5	(-0.4966,-0.4947)	1.325e-5	(0.4937,-0.4972)
-0.1	10^3	-5.291e-7	(-0.489,-0.4931)	5.291e-7	(0.4897,-0.4931)
	10^4	-5.218e-6	(-0.4897,-0.4931)	5.218e-6	(0.4897,-0.4931)
	10^5	-2.548e-5	(-0.4897,-0.4931)	2.548e-5	(0.4897,-0.4931)
	10^6	-1.670e-5	(-0.4966,-0.4958)	1.670e-5	(0.4966,-0.4958)
-0.15	10^3	-4.886e-7	(-0.4916,-0.4939)	4.886e-7	(0.4916,-0.4939)
	10^4	-4.896e-6	(-0.4916,-0.4915)	4.896e-6	(0.4916,-0.4915)
	10^5	-2.761e-5	(-0.4916,-0.4915)	2.761e-5	(0.4916,-0.4915)
	10^6	-1.836e-5	(-0.4945,-0.4958)	1.836e-5	(0.4945,-0.4958)
-0.2	10^3	-4.391e-7	(-0.4916,-0.4924)	4.3915e-7	(0.4916,-0.4924)
	10^4	-4.504e-6	(-0.4937,-0.4917)	4.504e-6	(0.4937,-0.4917)
	10^5	-2.519e-5	(-0.4937,-0.4917)	2.519e-5	(0.4937,-0.4917)
	10^6	-1.741e-5	(-0.4966,-0.4943)	1.741e-5	(0.4966,-0.4943)
-0.25	10^3	-4.152e-7	(-0.4937,-0.4921)	4.152e-7	(0.4937,-0.4921)
	10^4	-4.318e-6	(-0.4937,-0.4921)	4.318e-6	(0.4937,-0.4921)
	10^5	-2.422e-5	(-0.4937,-0.4921)	2.422e-5	(0.4937,-0.4921)
	10^6	-1.648e-5	(-0.4966,-0.4958)	1.648e-5	(0.4966,-0.4958)

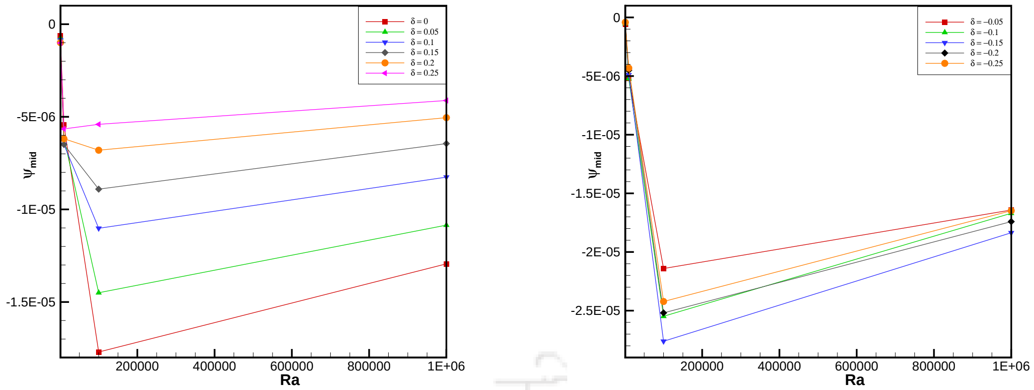

(a) Bottom left corner, $\delta \geq 0$ (b) Bottom left corner, $\delta < 0$

Figure 3.22: Variation of ψ_{mid} with Ra for different values of δ

Figures 3.6.2 (a) and 3.6.2 (b) show the variation of ψ_{mid} with Ra for $\delta \geq 0$ and $\delta < 0$ respectively. As the secondary corner vortices are symmetric, the variation of ψ_{mid} in only one side is shown. One can see that the value of ψ_{mid} varies in a similar pattern for both positive and negative values of δ. As Ra increases from 10^3 to 10^5, the value of ψ_{mid} decreases fro every δ, and on further increasing Ra to 10^6, ψ_{mid} increases. A close look at figure 3.6.2 (a) reveals that the change in the value of ψ_{mid} is steeper for lower values of δ, i.e., further away the cylinder is from the top wall, steeper is the increase in ψ_{mid} as Ra is increased from 10^5 to 10^6. However, there is a small change this pattern as the cylinder is moved towards the bottom wall (figure 3.6.2 (b)). Although the general pattern of the variation of ψ_{mid} remains similar, it does not follow the same trajectory as for $\delta \geq 0$.

A similar pattern of variation of ψ_{mid} with Ra can be plotted for the secondary vortices in the top left corner as well as the top right corner. To avoid being repetitive, only the plot for secondary vortices in the bottom left corner are shown.

Verification by pressure gradient observation

By the use of no-slip condition and the appropriate temperature on the walls, the x- and y- momentum equations (3.7) and (3.8) reduce to,

$$\frac{\partial p}{\partial x} = Pr\frac{\partial^2 u}{\partial y^2} \tag{3.23}$$

$$\frac{\partial p}{\partial y} = Pr \frac{\partial^2 v}{\partial x^2} \tag{3.24}$$

We use a one-sided first-order finite difference formula to discretize equations (3.23) and (3.24). For the left and bottom walls we have used forward difference formula, and for the right and top walls we have used backward difference formula.

$$\text{For left wall: } \left.\frac{\partial p}{\partial y}\right|_{0,j} = 2\,Pr\left[\frac{x_2 v_{1,j} - x_1 v_{2,j} + (x_2 - x_1) v_{0,j}}{x_1 x_2 (x_1 - x_2)}\right] \tag{3.25}$$

$$\text{For right wall: } \left.\frac{\partial p}{\partial y}\right|_{i_{max},j} = 2\,Pr\left[\frac{x_2 v_{i_{max}-1,j} - x_1 v_{i_{max}-2,j} + (x_2 - x_1) v_{i_{max},j}}{x_1 x_2 (x_1 - x_2)}\right] \tag{3.26}$$

where, $x_1 = \Delta x_1$ and $x_2 = \Delta x_1 + \Delta x_2$ ($\Delta x_i = x_{i+1} - x_i$, x_i being the i^{th} point along the x direction)

$$\text{For bottom wall: } \left.\frac{\partial p}{\partial x}\right|_{i,0} = 2\,Pr\left[\frac{y_2 u_{i,1} - y_1 u_{i,2} + (y_2 - y_1) u_{i,0}}{y_1 y_2 (y_1 - y_2)}\right] \tag{3.27}$$

$$\text{For top wall: } \left.\frac{\partial p}{\partial x}\right|_{i,j_{max}} = 2\,Pr\left[\frac{y_2 u_{i,j_{max}-1} - y_1 u_{i,j_{max}-2} + (y_2 - y_1) u_{i,j_{max}}}{y_1 y_2 (y_1 - y_2)}\right] \tag{3.28}$$

where, $y_1 = \Delta y_1$ and $y_2 = \Delta y_1 + \Delta y_2$ ($\Delta y_j = y_{j+1} - y_j$, y_j being the j^{th} point along the y direction)

It is well known that whenever the pressure gradient changes its sign, separation in the flow takes place paving the way for the creation of a vortex [52, 164]. As such, the number of eddies will depend on the total number of changes of sign in pressure gradient. To illustrate this, we consider the configuration of the cylinder placed at $\delta = 0.2$ and $Ra = 10^6$. We plot the normalized pressure gradient p_x along the top wall. From the figures 3.23 (a) and (b), we can see that the number of vortices for this particular configuration equals the number of sign changes of the pressure gradient along the top wall, i.e., the x - direction. Note that the vortices numbered 1 and 7 denote the secondary corner vortices discussed in 3.6.2.

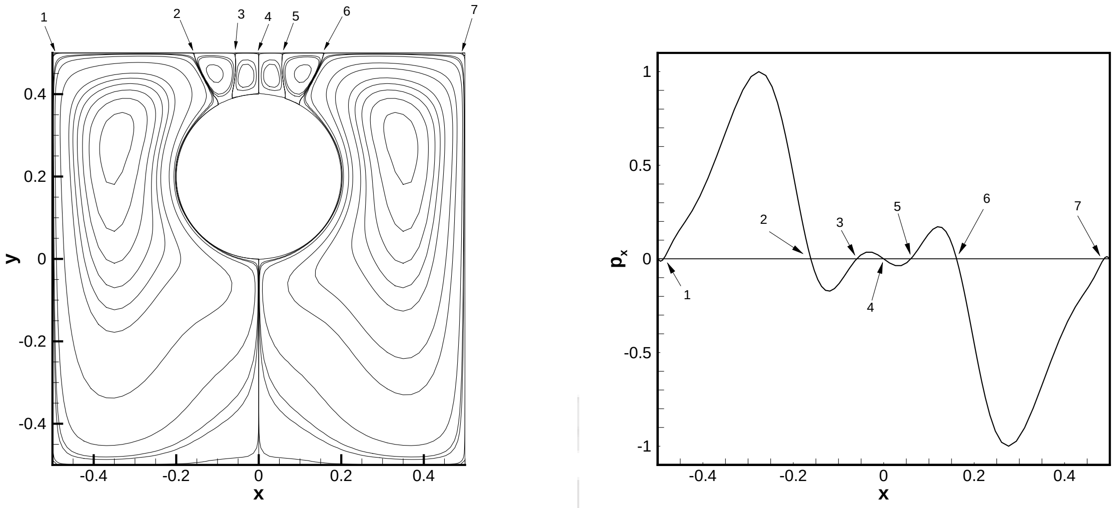

(a) $\delta = 0.2$ and $Ra = 10^6$.

(b) p_x vs. x for the top wall.

Figure 3.23: Points of separation on the top wall for $\delta = 0.2$ and $Ra = 10^6$.

Surface-averaged Nusselt number

The local, and surface-averaged Nusselt numbers are defined as

$$Nu = \frac{\partial \theta}{\partial n}, \quad \overline{Nu} = \frac{1}{W}\int_0^W Nu\, dS \tag{3.29}$$

where n is the normal direction with respect to the walls, and W is the surface area of the walls.

Figure 3.24(a) shows the surface-averaged Nusselt number at the top wall of the enclosure, $\overline{Nu_T}$, as a function of δ for different Rayleigh numbers. $\overline{Nu_T}$ generally increases with increasing Ra due to the increasing effect of convection.

When δ increases from -0.25 to -0.05 at $Ra = 10^5$, $\overline{Nu_T}$ increases slowly due to the slight increase in thermal gradient on the top wall of the enclosure with decreasing distance between the inner cylinder and the top wall. The dependence of $\overline{Nu_T}$ on δ is very low in this region. However, when δ increases to 0 and 0.05 at $Ra = 10^5$, the strength of the rising thermal plume formed around the top surface of the inner cylinder decreases and secondary vortices are formed on the top surface of the inner cylinder. As a result $\overline{Nu_T}$ decreases slightly when $\delta = 0$ and 0.05 at $Ra = 10^5$. If δ increases further to values larger than 0.1, the effect of δ becomes more dominant even though secondary vortices exist on the upper surface of the inner cylinder and as a result $\overline{Nu_T}$ increases again rapidly with increasing δ.

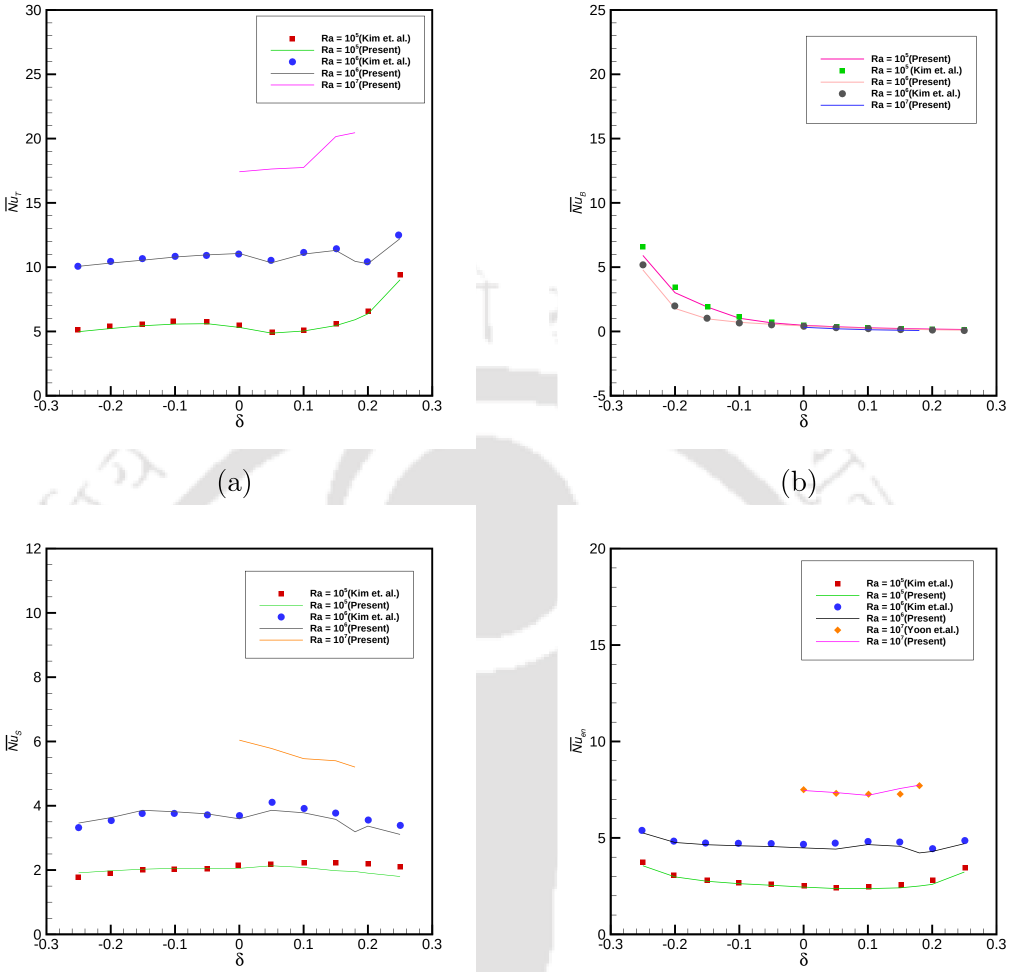

(a) (b)

(c) (d)

Figure 3.24: Average Nusselt numbers of (a) Top wall, (b) Bottom wall, (c) Side walls, and (d) The enclosure.

When $Ra = 10^3$, $\overline{Nu_T}$ depends on the variation of δ very much and increases very rapidly with increasing δ. When the inner cylinder is placed at the lower half of the enclosure ($\delta < 0$) at $Ra = 10^4$, $\overline{Nu_T}$ increases very slowly with increasing δ. However, when $\delta > 0$ at $Ra = 10^4$, $\overline{Nu_T}$ increases very rapidly due to the increasing effect of δ. Thus, if the distance from the inner cylinder to the top wall decreases, the difference in the value of $\overline{Nu_T}$ between $Ra = 10^3$ and 10^4 decreases and $\overline{Nu_T}$ at $Ra = 10^4$ is almost the same as that at $Ra = 10^3$ when $\delta = 0.2$ and 0.25.

The variation of $\overline{Nu_T}$ at $Ra = 10^6$ is generally similar to that at $Ra = 10^5$. When δ

increases at $Ra = 10^6$, $\overline{Nu}_T$ increases slowly for $-0.25 \leq \delta \leq 0$, decreases at $\delta = 0.05$ due to the presence of the strong secondary vortices on the upper surface of the inner cylinder, and increases again at $0.05 \leq \delta \leq 0.15$ due to the increasing effect of the distance between the inner cylinder and the top wall of the enclosure in presence of the secondary vortices. When $\delta = 0.2$ at $Ra = 10^6$, $\overline{Nu}_T$ decreases again because the presence of secondary and tertiary vortices on the upper surface of the inner cylinder has a more dominant effect on $\overline{Nu}_T$ than δ. When $\delta = 0.25$ at $Ra = 10^6$, $\overline{Nu}_T$ increases to the maximum value because the distance between the inner cylinder and the top wall of the enclosure is smallest in addition to the absence of secondary and tertiary vortices.

The variation of $\overline{Nu}_T$ at $Ra = 10^7$ for $0 \leq \delta \leq 0.1$ is similar to that at $Ra = 10^6$. However, between $\delta = 0.1$ and 0.15, there is a steep increase in the value of $\overline{Nu}_T$, as the distance between the top wall and the upper surface of the cylinder increases in addition to the appearance of secondary vortices on the upper surface of the cylinder.

Figure 3.24 (b) shows the surface-averaged Nusselt number at the bottom wall of the enclosure, $\overline{Nu}_B$, as a function of δ for different Ra. $\overline{Nu}_B$ generally decreases with increasing Ra number due to the increasing effect of convection. When the distance between the inner cylinder and the bottom wall of the enclosure increases with increasing δ, $\overline{Nu}_B$ decreases due to the decreasing thermal gradient on the bottom wall. When $-0.25 \leq \delta \leq 0$, $\overline{Nu}_B$ decreases very rapidly with increasing δ, showing a significant dependence of $\overline{Nu}_B$ on δ in this region. However, when $0 \leq \delta \leq 0.25$, $\overline{Nu}_B$ decreases slowly with increasing δ. The presence of secondary and tertiary vortices on the upper surface of the inner cylinder has some influence on the distribution of isotherms and their corresponding variation of $\overline{Nu}_T$. However, the effect of the presence of additional vortices on the bottom wall on the distribution of isotherms and their corresponding variation of $\overline{Nu}_B$ is very small.

Figure 3.24(c) shows the surface-averaged Nusselt number at the side wall of the enclosure, $\overline{Nu}_S$, as a function of δ for different Ra. $\overline{Nu}_S$ also generally increases with increasing Ra due to the increasing effect of convection. However, the effect of δ on $\overline{Nu}_S$ is small whereas the effect of Ra on $\overline{Nu}_S$ is large.

Figs. 3.24(d) and 3.25 shows the total surfaces-averaged Nusselt number of the enclosure, $\overline{Nu}_{en}$, and the surface-averaged Nusselt number of the inner cylinder, $\overline{Nu}_C$, as a function of δ for different Ra's. $\overline{Nu}_{en}$ represents the surface- averaged sum of $\overline{Nu}_T$, $\overline{Nu}_B$ and $\overline{Nu}_S$.

When $Ra = 10^3$ and 10^4, $\overline{Nu}_{en}$ has a parabolic profile with a minimum value at $\delta = 0$. The value of $\overline{Nu}_{en}$ at $Ra = 10^4$ is almost the same as that at $Ra = 10^3$.

When $Ra = 10^5$, $\overline{Nu}_{en}$ has a minimum value at $\delta = 0.05$, due to the presence of secondary vortices on the upper surface of the inner cylinder. The value of $\overline{Nu}_{en}$ at $\delta = 0.25$ is smaller than that at $\delta = -0.25$, because the stagnant region at $\delta = 0.25$ is larger than that $\delta = -0.25$.

For $-0.25 \leq \delta \leq 0$ at $Ra = 10^6$, $\overline{Nu}_{en}$ decreases with increasing δ, similar to when $Ra = 10^5$. However, for $0 \leq \delta \leq 0.25$ at $Ra = 10^6$, the variation of $\overline{Nu}_{en}$ w.r.t δ is different from that at $Ra = 10^5$, due to the combined effect of the secondary and tertiary vortices, and the distance between the inner cylinder and top and bottom walls of the enclosure. With increasing δ, $\overline{Nu}_{en}$ increases at $0 \leq \delta \leq 0.15$, decreases at $\delta = 0.2$ and increases again at $\delta = 0.25$.

When $Ra = 10^7$, $\overline{Nu}_{en}$ decreases for $0 \leq \delta \leq 0.1$, increases sharply at $\delta = 0.1$ to $\delta = 0.18$.

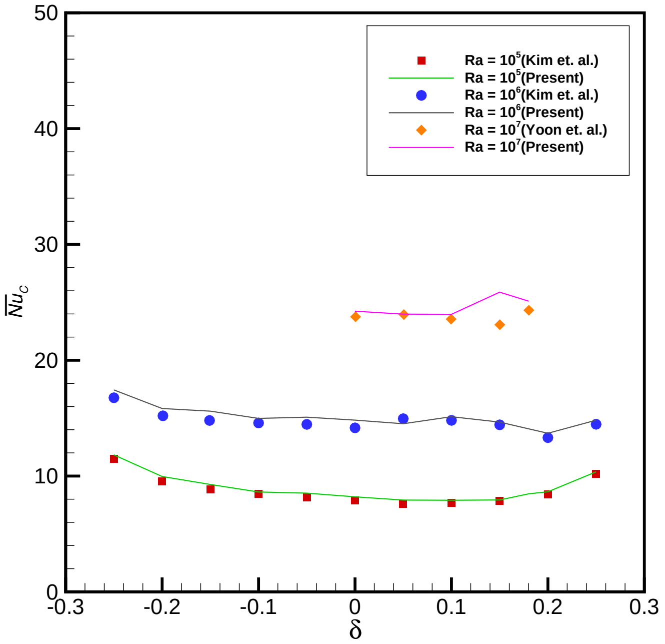

Figure 3.25: Surface-averaged Nusselt number, $\overline{Nu}_C$ of the inner cylinder w.r.t δ for different Rayleigh numbers.

Figure 3.25 shows the surface-averaged Nusselt number of the inner cylinder, $\overline{Nu}_C$, as a function of δ for different Rayleigh numbers. The pattern of $\overline{Nu}_C$ vs δ is similar to that of $\overline{Nu}_{en}$. However, the magnitude of $\overline{Nu}_C$ is larger than that of $\overline{Nu}_{en}$ for all different cylinder positions because the isotherms are formed more densely on the surface of the inner cylinder than that on the surfaces of the enclosure. In both figures 3.24 and 3.25, we have compared the Nusselt numbers from our computations with those of Kim et al. [89] and Yoon et al. [172]; it is heartening to note that our coarse grid (computed on grid of size 121×121) results are extremely close to the fine grid computations of [89] and [172] (201×201).

3.7 Natural convection around a horizontal, heated, diamond cylinder placed in an enclosure

Figure 3.26(a) shows the geometry in which natural convective heat transfer is studied in the present section. It consists of an enclosure having insulated horizontal and cold vertical walls containing air (Pr $= 0.71$) as working fluid. A heated cylinder of side $a = 0.2\sqrt{2}$, maintained at a temperature of T_h, is placed at the center of the enclosure in a prismatic orientation. The vertical walls are maintained at a uniform temperature of T_c, and the horizontal walls are adiabatic $(\dfrac{\partial T}{\partial y} = 0)$. This configuration is different from the heated horizontal circular cylinder due to the following reasons:

1. The top and bottom walls are adiabatic rather than isothermal.
2. The more streamlined shape of the cylinder favours the development of the boundary layer and its interaction with the core fluid.

Figure 3.27 (a) shows the computational geometry in the xy- plane with a body-fitted non-uniform grid distribution. A grid resolution of 121×121 along horizontal (x) and vertical (y) directions was employed in computations to be reported in this section. Similar to the grid generated for the circular cylinder, the grid has been generated in such a way that the diamond geometry passes through the grid points as seen in fig. 3.27 (b).

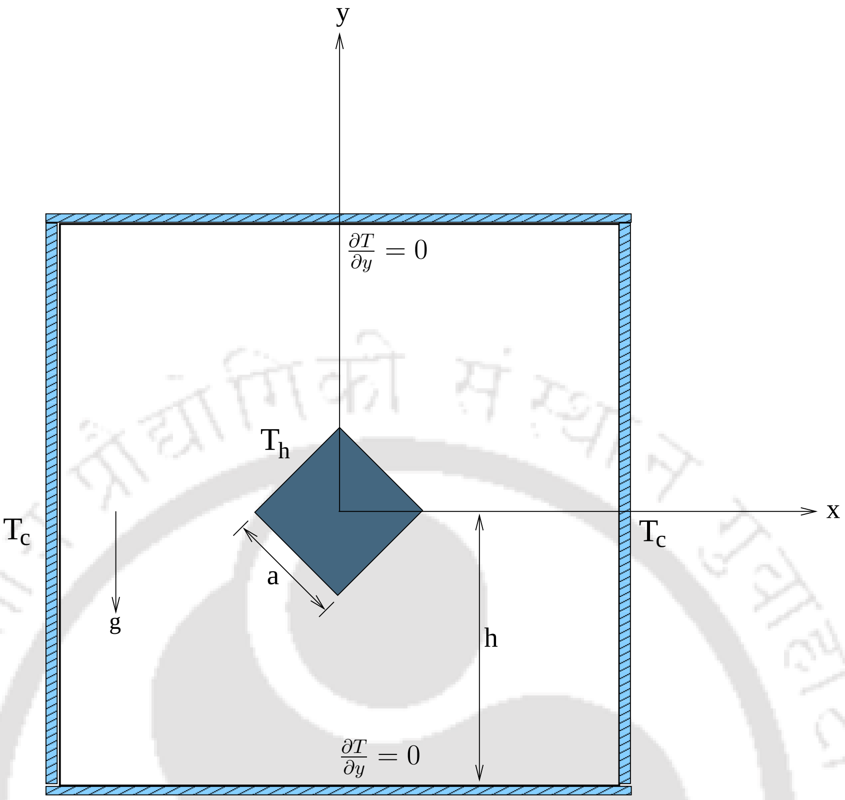

Figure 3.26: Schematic view of a heated circular cylinder enclosed inside a square cavity.

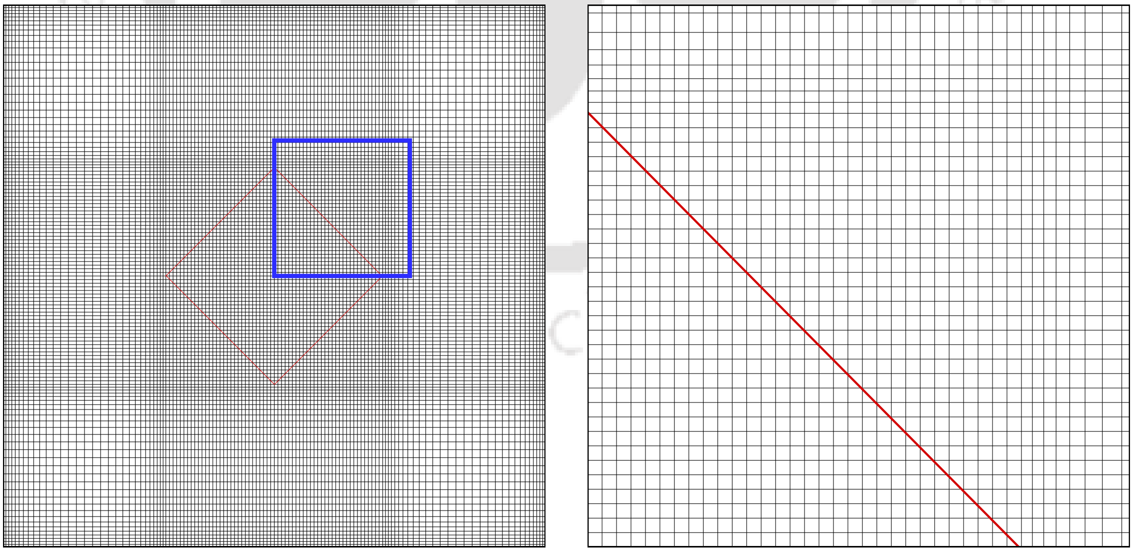

(a) Representative grid.

(b) Close-up view inside the blue box.

Figure 3.27: Representative grid for the case of diamond cylinder and close-up view of a part of the grid.

3.7.1 Results and Discussion

A previous study by De and Dalal [36] has shown that steady state exists for the problem for $10^3 \leq Ra \leq 10^6$. In this study we have carried out computations for $10^5 \leq Ra \leq 10^7$. As in the circular cylinder case, we have used the recent scheme developed by Kumar and Kalita [94], and the fourth order compact scheme developed by Kalita et.al. [80] for our computations. A grid resolution of 121×121 has been used for the computations carried out in this section.

The isotherms at different Rayleigh numbers ($10^5 \leq Ra \leq 10^7$) for different positions of the inner cylinder ($h = 0.5, 0.75, 0.25$) are shown in Figs. 3.28, 3.30, and 3.32, whereas the streamlines are shown in Figs. 3.29, 3.31, and 3.33. As in the case of circular cylinder, for all Rayleigh numbers considered in this study, the flow and thermal fields eventually reach steady state with the symmetric shape about the vertical centerline through the center of the inner cylinder.

In general, since the cylinder is kept heated, the hot fluid pumped in by the cylinder rises upward near the vertical mid plane of the enclosure due to thermal expansion. This hot fluid moves horizontally toward corners after impinging on the roof. Finally, the colder and thus denser fluid descends along the cold side walls as it comes in contact with cooled fluid away from the cylinder. We can see that the isotherms get distorted as the Rayleigh number increases, and the formation of thermal boundary layer on the cylinder surface from its bottom to its top and on the enclosure-side wall from its top to its bottom is prominent. This feature is identical for all the positions of the cylinder and leads to a stable stratification at the core of the enclosure at high Rayleigh numbers.

A close look at the isotherms obtained in the previous case of circular cylinder and the current problem would reveal a marked absence of thermal boundary layers at the top and bottom walls. This is because of the different thermal boundary conditions imposed thereat. As in the case of natural convection in a square cavity in section 3.5, the insulated walls prevented the formation of thermal boundary layer in the present case.

The denser streamlines near the enclosure wall and the cylinder indicate stronger convective flow at higher Rayleigh numbers. The flow pattern changes from bi-cellular to uni-cellular form at high Rayleigh number for $h = 0.5$ in each half. However, no such behavior is found for the other two positions of the cylinder. For $h = 0.75$, flow is primarily confined to the upper half of the enclosure leaving cold fluid at the bottom half showing poorer mixing compared to the other two cases. Also, the adiabatic boundary conditions at the top and bottom walls prevented the formation of secondary vortices at the top and bottom walls, which could be observed in the circular cylinder case, being facilitated by the isothermal boundary conditions.

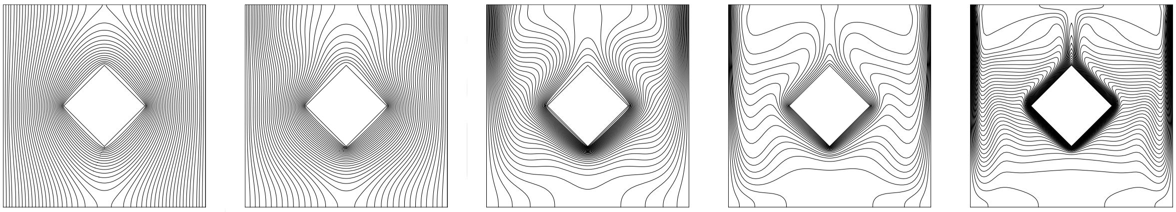

(a) $Ra = 10^3$ (b) $Ra = 10^4$ (c) $Ra = 10^5$ (d) $Ra = 10^6$ (e) $Ra = 10^7$

Figure 3.28: Isotherms for different values of Ra with $h = 0.5$.

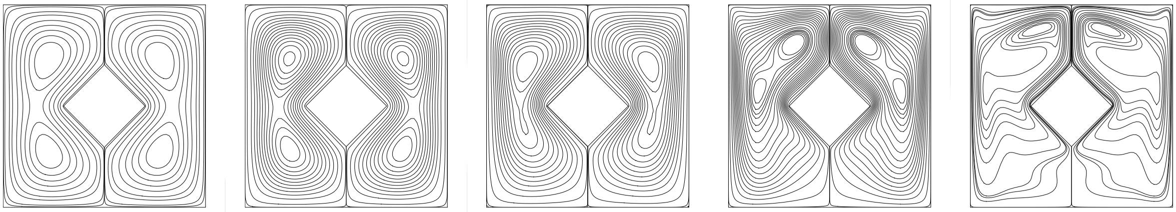

(a) $Ra = 10^3$ (b) $Ra = 10^4$ (c) $Ra = 10^5$ (d) $Ra = 10^6$ (e) $Ra = 10^7$

Figure 3.29: Streamlines for different values of Ra with $h = 0.5$.

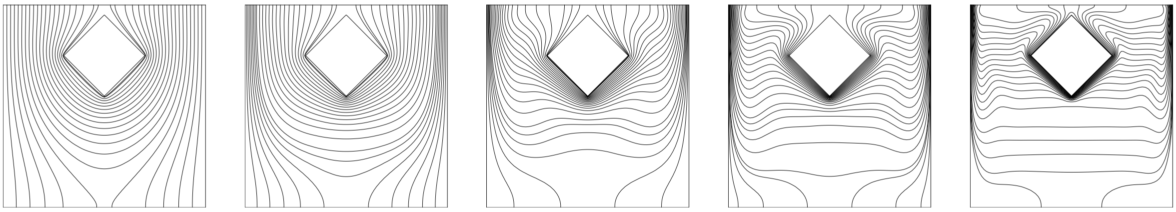

(a) $Ra = 10^3$ (b) $Ra = 10^4$ (c) $Ra = 10^5$ (d) $Ra = 10^6$ (e) $Ra = 10^7$

Figure 3.30: Isotherms for different values of Ra with $h = 0.75$.

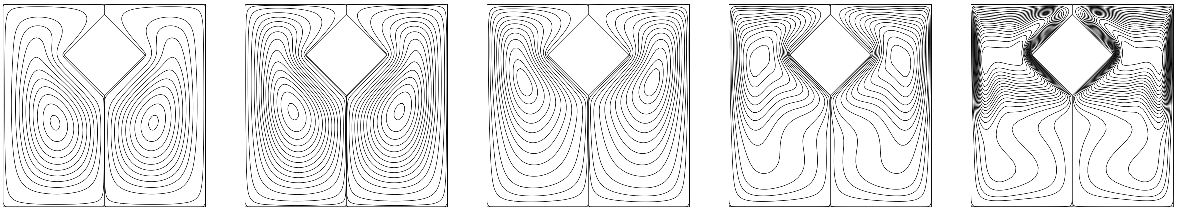
(a) $Ra = 10^3$ (b) $Ra = 10^4$ (c) $Ra = 10^5$ (d) $Ra = 10^6$ (e) $Ra = 10^7$

Figure 3.31: Streamlines for different values of Ra with $h = 0.75$.

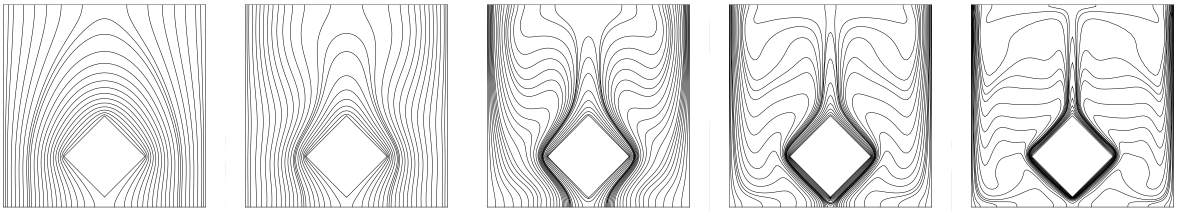
(a) $Ra = 10^3$ (b) $Ra = 10^4$ (c) $Ra = 10^5$ (d) $Ra = 10^6$ (e) $Ra = 10^7$

Figure 3.32: Isotherms for different values of Ra with $h = 0.25$.

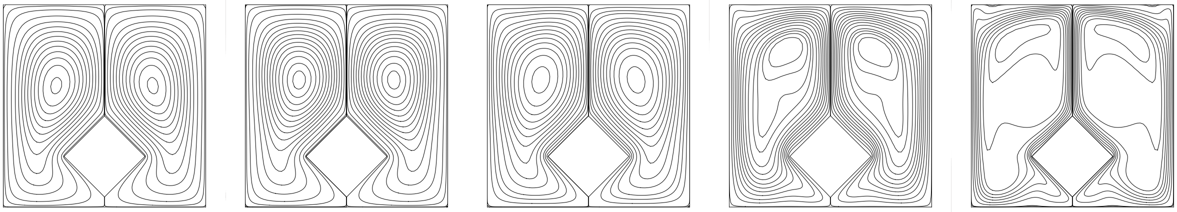
(a) $Ra = 10^3$ (b) $Ra = 10^4$ (c) $Ra = 10^5$ (d) $Ra = 10^6$ (e) $Ra = 10^7$

Figure 3.33: Streamlines for different values of Ra with $h = 0.25$.

3.7.2 A brief Nusselt Number analysis

Average Nusselt numbers are calculated from Eq. (3.29). The average Nusselt number on the cylinder and the side wall are plotted against Rayleigh number for different cylinder positions in Figs. 3.34 (a) and (b) respectively. Heat exchange between fluid and the walls enhances for the higher Rayleigh numbers as absolute value of $\overline{Nu_S}$ increases with Ra. $\overline{Nu_S}$ for $h = 0.75$ is quantitatively lesser compared to $h = 0.25$ and 0.5 owing to poor mixing and heat transfer from the isothermal walls.

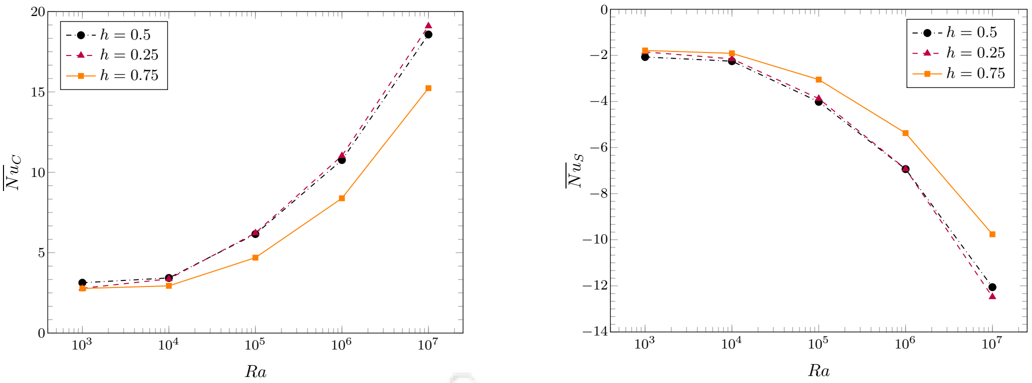

(a) (b)

1 1

Figure 3.34: Average Nusselt number (a) on the cylinder $\overline{Nu}_C$, and (b) on the side walls $\overline{Nu}_S$ with respect to different Ra

Although the dimensions of the cylinder in this section differs from that used by De and Dalal [36] by a tiny margin, the patterns of the isotherms and streamlines bear a close resemblance with their results. The patterns observed in the plots of average Nusselt numbers are also a good match with their results. A quantitative comparison of the present results with that of De and Dalal [36] is provided in table 3.5.

Table 3.5: Comparison of present $\overline{Nu}_C$ and $\overline{Nu}_S$ ($a = 0.2\sqrt{2}$) with that of De and Dalal [36] ($a = 0.25$).

Ra	h	$\overline{Nu}_C$ [36]	$\overline{Nu}_C$ (Present)	$\overline{Nu}_S$ [36]	$\overline{Nu}_S$(Present)
10^3	0.75	3.48656	2.775168	-1.68474	-1.788439
	0.5	3.86628	3.132637	-1.91981	-2.070811
	0.25	3.52276	2.788178	-1.68474	-1.850455
10^4	0.75	3.69818	2.938833	-1.78965	-1.910826
	0.5	4.25875	3.430067	-2.10306	-2.252017
	0.25	4.15026	3.370568	-1.93654	-2.151184
10^5	0.75	6.002212	4.690783	-2.92292	-3.050904
	0.5	7.681415	6.160439	-3.82404	-4.0152
	0.25	7.93584	6.226221	-3.75545	-3.87508
10^6	0.75	10.59882	8.386305	-5.23158	-5.372246
	0.5	13.21091	10.763285	-6.67141	-6.933543
	0.25	13.99115	11.026578	-6.77918	-6.928305
10^7	0.75	__	15.234441	__	-9.762051
	0.5	__	18.572522	__	-12.056118
	0.25	__	19.098155	__	-12.47799

3.7.3 Comparison with the circular cylinder case

Although there is no connection between the two cases of circular and diamond cylinders having different boundary conditions, it will still be interesting to visualize the flow pattern for both the cases under the same boundary conditions. Keeping that in mind, we have computed the flow for the specific case of the circular cylinder being located at the center of the enclosure under the same boundary conditions imposed for the diamond cylinder. In the following figures 3.35 and 3.36, we present the streamlines and isotherms for $Ra = 10^5$, 10^6 and 10^7. A close look at these and figures 3.28 and 3.29 reveal that apart from slight curvature effect on the isotherms and the streamlines, the patterns are almost the same for both the geometries. Table 3.6 also corroborates this fact where the strengths and centers of the vortices have been tabulated. Remarkably, the vertical heights of the vortex centers for respective Rayleigh numbers remains the same in all the three cases.

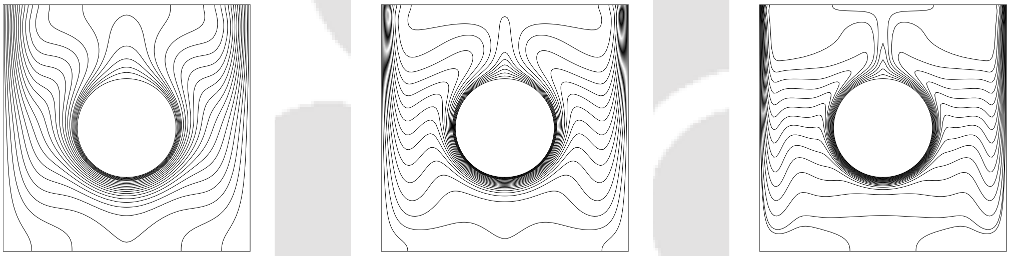

(a) $Ra = 10^5$ (b) $Ra = 10^6$ (c) $Ra = 10^7$

Figure 3.35: Isotherms for different values of Ra at $h = 0.5$.

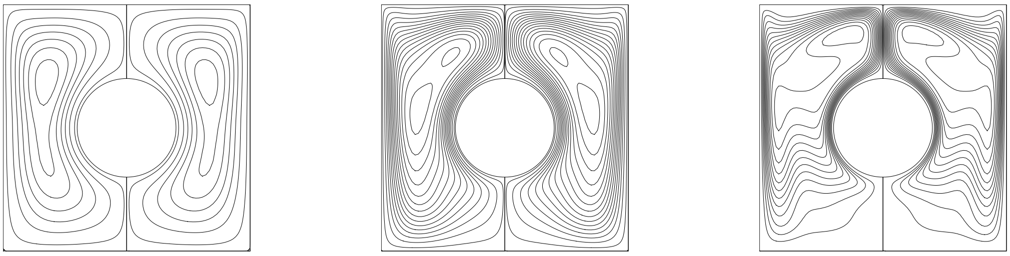

(a) $Ra = 10^5$ (b) $Ra = 10^6$ (c) $Ra = 10^7$

Figure 3.36: Isotherms for different values of Ra at $h = 0.5$.

Table 3.6: Comparison between circular and diamond cylinders.

Ra	Geometry	ψ_{mid}	(x, y)	$\overline{Nu}_C$
10^5	Circle	± 6.60316	$(\mp 0.32, 0.199)$	7.207555
	Diamond	± 6.9618	$(\mp 0.305, 0.199)$	6.160439
10^6	Circle	± 14.1776	$(\mp 0.21, 0.31)$	12.895667
	Diamond	± 14.5157	$(\mp 0.17, 0.31)$	10.763285
10^7	Circle	± 27.2091	$(\mp 0.14, 0.38)$	22.069077
	Diamond	± 28.2084	$(\mp 0.17, 0.38)$	19.098155

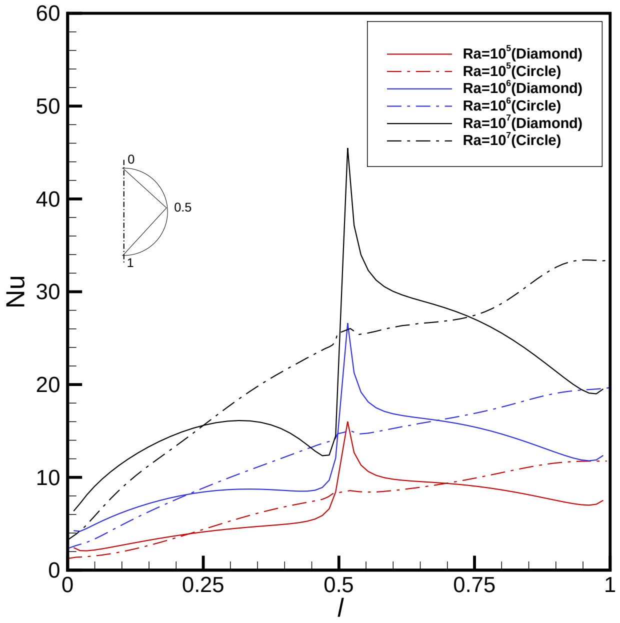

Figure 3.37: Comparison of the variation of surface Nu for diamond and circular cylinders.

In figure 3.37, we present the variation of local Nusselt numbers along the surfaces of the circular and diamond cylinders in the right half of the physical domain. Here the horizontal axis represents the normalized length along the perimeter of the two objects spanning from the point $(0.0, 0.2)$ (the top corner) to $(0.2, 0.0)$ (the right corner) and then to $(0.0, -0.2)$ (the bottom corner). One can clearly see that while the local Nusselt number increases monotonically for the circular cylinder, it has a distinct spike at the right corner for the diamond cylinder reflecting the curvature effect. Also at the bottom of the objects, the convective heat transfer is much stronger for the circular cylinder, whereas, at the top, it is slightly lower than diamond cylinder. As Rayleigh number increases, convective heat transfer also itensifies as expected which can also be seen from the average Nu values in table 6. Note that this Nu distribution is symmetric about the vertical centerline.

3.8 Conclusions

In this chapter, we have taken up the study of natural convection around heated bodies of different shapes embedded in a square enclosure using the ψ-v form of the N-S equations. We reconstructed a recent scheme developed by Kumar and Kalita [94], and a fourth order compact scheme [80] for the energy equation. Probably for the first time, a body fitted cartesian grid has been used for the computations for such studies, thus avoiding the need for grid transformation and also gaining significant computational simplicity.

First, we validated the reconstructed scheme by applying it to the classic problem of natural convection in a differentially heated square cavity. Apart from establishing grid independence for our computed solutions, they were found to be in excellent agreement with well established results in the literature.

Next, we took up the problem of natural convection around a heated circular cylinder embedded in a square enclosure. We studied the characteristics of the flow for $10^5 \leq Ra \leq 10^7$, and different vertical positions (δ) of the inner circular cylinder. In the process, we have also carried out a grid convergence study for the highest Rayleigh number considered in the study. We showed that steady state existed for $Ra = 10^7$ for the range $0 \leq \delta \leq 0.18$. We further established the existence of secondary vortices at the four corners of the enclosure for $10^3 \leq Ra \leq 10^6$, and at all positions of the cylinder. We verified that these secondary corner vortices as well as other vortices reported in the literature are non-spurious by observing the changes in sign of the pressure gradient along the surfaces. Note that these secondary corner vortices have not been reported in any previous study in the literature. The intensity of the vortices at their centers as well as the coordinates of the centers have been tabulated for further perusal by the scientific community. Further, we have compared our results with well-known results in literature and our results on relatively coarser grid was found to be close match with those.

We then studied the problem of natural convection around a diamond cylinder embedded in a square enclosure. Unlike the previous problem, the top and bottom walls were adiabatic. The streamlined nature of the body favoured the formation of boundary layers, and its interaction with the fluid. We performed simulations for three different vertical positions of the cylinder. At all the positions, steady state was found to exist for $10^5 \leq Ra \leq 10^7$. Moreover, the location of the cylinder was seen to have very little influence on the heat transfer pattern as confirmed by the average Nusselt numbers. Lastly, we have provided a brief comparison of the flow structure and heat transfer characteristics on a circular cylinder vis a vis its diamond cylinder counterpart under the same conditions prescribed on the boundaries.

CHAPTER 4

DOUBLE DIFFUSIVE NATURAL CONVECTION IN A VERTICAL POROUS ANNULUS

4.1 Introduction

Natural convection which results from the combined effects of both temperature and concentration gradients is known as double-diffusive natural convection (DDNC), or simply double diffusive convection. Over the years, this phenomenon of DDNC in fluid saturated porous medium has been investigated extensively, due to its importance in numerous applications [111]. Some notable examples are flow through packed beds, the dispersion of chemical contaminants through water-saturated soil, the migration of moisture through the air contained in fibrous insulation and grain storage installations, the extraction of energy from geothermal reservoirs, and in chemical reactors for the separation or purification of mixtures. DDNC flows in porous media are also of significance in the fields of geophysics, electrochemistry, metallurgy etc. [62,117,159]. These factors have encouraged theoretical, experimental, and numerical studies on this phenomenon.

Most early studies of DDNC in porous media were concerned with square and rectangular cavities. Early numerical and analytical studies carried out by Trevisan and Bejan [157, 158], Lin [103], Alavyoon [2], Alavyoon et. al. [3], Kalla et. al. [84] paved the way for further investigations into the intricacies of flow phenomena in rectangular and square porous cavities. Other notable works include that of Mamou et. al. [109] who had numerically demonstrated that multiple convection patterns existed in the transition regime of approximately equal and opposite thermal and concentration buoyancy forces, the analytical and numerical investigation of Amahmid et. al. [9] who showed that the boundary layer regimes which were attained for $N < 0$ differed significantly from $N > 0$ of previous studies, and the numerical investigation by Bourich et. al. [26] of DDNC in a square porous cavity subjected to cross gradients of temperature and concentration. Bourich et. al. [27] also numerically investigated DDNC in a square porous cavity, the bottom of which was partially heated and differentially salted. They explored the multiplicity of solutions and proved that asymmetric bicellular flow existed when the heated element was moved towards a vertical wall. Further, they [28] reported a scale analysis of 2D DDNC in a square porous cavity with a heated bottom wall and a cooled top wall, whereas a horizontal concentration gradient was imposed on the vertical walls. Kramer et.al. [91] presented a boundary domain integral method (BDIM) to analyse DDNC in a square porous cavity. Zhao et. al. numerically studied DDNC in a vertical porous enclosure with localized heating and salting from one side [178], and DDNC of a binary mixture in a square porous enclosure which was subjected to partial heating and salting on the right wall respectively [179]. They [180] further reported numerical results for DDNC in a rectangular porous enclosure where discrete moisture and heat sources were attached to the bottom wall. On the other hand Alloui et. al. [5] numerically investigated DDNC within a square porous enclosure with localized heating and salting from below. They demonstrated that multiple steady state solutions existed corresponding to the use of appropriate initial perturbations. Benissaad and Ouazaa [21] reported a numerical as well as analytical study of DDNC in a 2D rectangular cavity of a porous medium saturated with a binary fluid mixture. Altawallbeh et. al. [8] numerically studied DDNC in a square porous enclosure when the bottom wall was partially heated and the right wall was partially salted. They [7] also numerically investigated the effect of magnetic field on 2D DDNC in a square porous cavity, the top wall of which was colder than the bottom wall, and the right wall maintained at a higher concentration than the left wall. Mondal and Sibanda [112] used a finite-difference method based on staggered grid to study the effects of buoyancy ratio on unsteady DDNC in a square cavity filled with porous medium subjected to non-uniform boundary conditions. Xu et.al. [169] used lattice Boltzmann method (LBM) to numerically investigate DDNC around a heated cylinder placed in a square porous enclosure. In [168] Xu et.al. included Soret and Dufour effects as well.

In more practical applications, however, DDNC takes place in the annular space between two concentric cylinders. Much work has been done for this particular geometry over the years. Marcoux et.al. [110] analytically and numerically studied DDNC through a fluid-saturated, vertical porous annulus (homogeneous) the sides of which were subjected to uniform heat and mass fluxes. Particular attention was paid to the numerical investigation of the influence of curvature on HMT characteristics. An analytical solution for steady state stratified flow in slender enclosures was also presented. Beji et.al. [18] conducted a numerical study of DDNC occurring in a concentric vertical porous annulus. This study was done based on a finite volume pressure-velocity formulation on non-uniform grids, and the influences of Ra, N, Le, and κ on the HMT characteristics were discussed. Benzeghiba et.al. [22] numerically studied DDNC in a vertical concentric cavity partly filled with a porous medium. Bahloul et.al. [15] reported a numerical and analytical study of DDNC (including Soret effect) through a binary fluid saturating a vertical porous annulus. They derived a parallel flow approximation based analytical solution for tall enclosures ($A >> 1$). Kalita and Dass [79] numerically studied the problem of DDNC in a concentric vertical porous annulus. They presented steady-state results for a variety of configurations obtained via an unsteady HOC scheme for the convection-diffusion equation on uniform grids.Venkatachalappa et.al. [160] numerically investigated the effect of axial or radial magnetic field on DDNC in a vertical cylindrical annulus. They found that the double-diffusive convection is suppressed by the magnetic field for only small values of buoyancy ratios, whereas it is quite effective in suppressing the thermal flow for larger values of buoyancy ratios. Sankar et.al. [137] numerically studied double-diffusive convection in a fluid-saturated vertical porous annulus subjected to discrete heat and mass fluxes from a portion of the inner wall. They found that the location of heat and solute source had a significant influence on the flow pattern, heat and mass transfer rates (HMTR) in the porous annulus. Ja and Cheddadi [63] numerically investigated the effect of cooperating and opposite buoyancy forces on the flow structure and the HMTR in a horizontal annular space of radius ratio $R = 2$, filled with a porous medium saturated by a binary fluid. Himrane et.al. [60] numerically investigated unsteady DDNC in vertical open ended cylinder filled with a porous medium, where a sinusoidal variation of temperature was imposed on the vertical walls. They reported three types of flow and observed that the heat transfer rate was significantly affected by Ra, N, and non-dimensional amplitude.

To the best of our knowledge only Kalita and Dass [79] have applied an HOC scheme to numerically investigate DDNC in a vertical porous annulus. Previous studies for various cylindrical configurations [2, 3, 18, 79, 110] have shown the appearance of thermal and solutal boundary layers in regions (especially near the walls) with steep gradients in temperature and concentration, especially for slender cavities ($A >> 1$). To resolve the boundary layers accurately, a comparatively greater number of grid points are required near the walls where the temperature and solutal gradients are steeper than at regions with low temperature and concentration gradients. It is seen that use of uniform grid [79] results in an increase of grid points both near the walls and at regions with low temperature and concentration gradients. However, use of non-uniform grid provides a means of increasing the number of grid points in high temperature and concentration gradient regions, without a corresponding increase at the low gradient regions. Thus, with the same number of grid points as in uniform grid, greater accuracy is achieved with non-uniform grid.

In the present chapter an existing HOC streamfunction-vorticity formulation on non-uniform grids is reconstructed for the simulation of DDNC in a vertical porous annulus. Particular attention is paid to slender cavities ($A >> 1$), and investigation is carried out to study the influence of aspect ratio (A), radius ratio (κ), Lewis number (Le), buoyancy ratio (N), and thermal Rayleigh number (Ra) on the flow. In this process a general pattern of heat and mass transfer (HMT) characteristics is sought. Note that while Kalita and Dass [79] reported only steady state results, the current study also investigates the transient behaviour of the flow phenomena. [1]

This chapter is organized as: In section 4.2 the problem schematic along and the governing equations both in dimensional and non-dimensional form is presented. Section 4.3 provides details of the discretization procedure, the scheme used (developed by Kalita et.al. [81]), the derivation of HOC Neumann boundary conditions (4.3.1), and a novel way to calculate velocities (4.3.2). Section 4.4 briefly describes the grid generation procedure. In section 4.5 the algorithm for solving the system of equations resulting from

---

[1] Part of this study has been published in [44]

the discretization of the non-dimensional governing equations is detailed. In section 4.6 algorithm and code are validated against available results in the literature. In section 4.7 results are presented and finally, the conclusions of this chapter are summarized in section 4.8.

4.2 The problem

Consider a fluid-saturated porous medium sandwiched in the annular region of two vertical, concentric cylinders of height H (Figure 4.1). The radii of the inner and outer cylinder are r_i and r_o respectively. Uniform temperature and concentration boundary conditions are imposed on the impermeable inner and outer walls of the annulus. The temperature and concentration of the inner wall are T_h and S_h respectively, whereas that on the outer wall are T_c and S_c respectively ($T_h > T_c$, $S_h > S_c$). Further, the top and bottom boundaries of the cavity are adiabatic and impermeable.

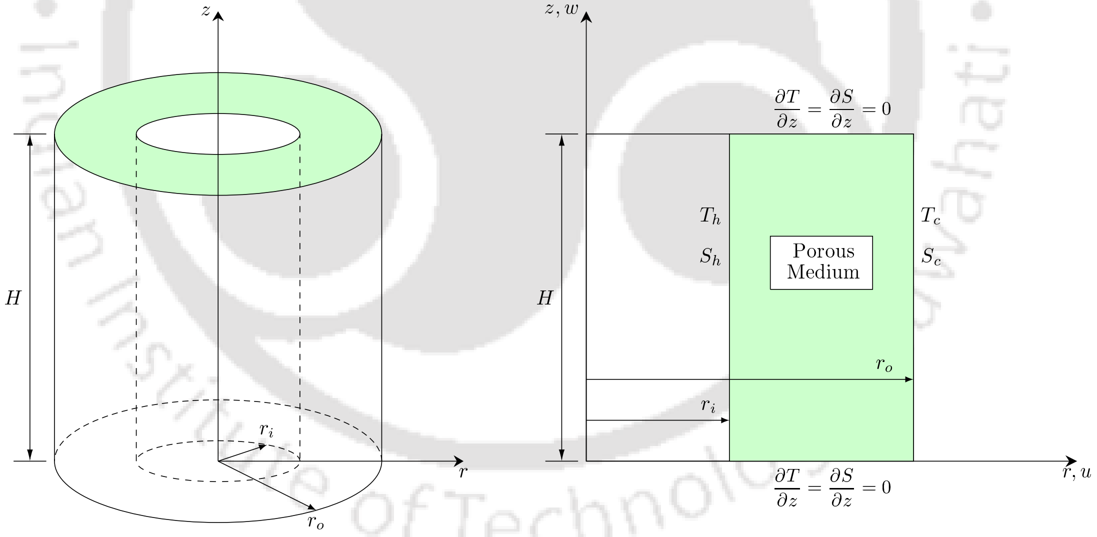

(a) (b)

Figure 4.1: Schematic view of vertical porous annulus.

The following assumptions hold for this study:

1. Darcy's law is applicable in the porous medium.

2. The porous matrix is uniform and in equilibrium with the fluid.

3. The thermo-physical properties are constant.
4. The flow is laminar and incompressible.
5. Soret and Dufour effects are ignored.
6. Boussinesq approximation is used for the fluid. Thus the density of the mixture can be written as

$$\rho(T,S) = \rho_r[1 - \beta_T(T - T_r) - \beta_S(S - S_r)] \tag{4.1}$$

where ρ_r is the density at $T = T_r$, $S = S_r$, β_T is the thermal expansion coefficient, β_S is the solutal expansion coefficient.

Under these assumptions, the equations governing the conservation of mass, momentum, heat, and concentration in vector form can be written as [2]

$$\nabla \cdot \mathbf{V} = 0 \tag{4.2}$$

$$\frac{\mu}{K}\mathbf{V} = -\nabla p - \rho g \mathbf{e}_z \tag{4.3}$$

$$\sigma \frac{\partial T}{\partial t} + \mathbf{V} \cdot \nabla T = \alpha \nabla^2 T \tag{4.4}$$

$$\epsilon \frac{\partial S}{\partial t} + \mathbf{V} \cdot \nabla S = D \nabla^2 S \tag{4.5}$$

where $\mathbf{V}(r,z) = u(r,z)\mathbf{e}_r + w(r,z)\mathbf{e}_z$, u and w being the r and z components of Darcy velocity, T and S are the temperature and concentration respectively, K is the permeability of the porous medium, μ is the fluid's viscosity, p is the pressure, g is the acceleration due to gravity, α is the fluid's thermal diffusivity, D is the solutal diffusivity, and ϵ is the porosity of the porous medium. The heat capacity σ is given by

$$\sigma = \frac{\epsilon(\rho C)_f + (1 - \epsilon)(\rho C)_p}{(\rho C)_f} \tag{4.6}$$

where $(\rho C)_f$ is the heat capacity of the fluid, and $(\rho C)_p$ is the heat capacity of the saturated porous medium.

The boundary conditions are given by

$$T = T_h, \quad S = S_h, \quad u = 0 \quad \text{at} \quad r = r_i \tag{4.7}$$

$$T = T_c, \quad S = S_c, \quad u = 0 \quad \text{at} \quad r = r_o \tag{4.8}$$

$$\frac{\partial T}{\partial z} = \frac{\partial S}{\partial z} = 0, \quad w = 0, \quad \text{at} \quad z = 0, H \tag{4.9}$$

We now introduce the following non-dimensional variables

$$r^* = \frac{r}{H}, \; z^* = \frac{z}{H}, \; u^* = \frac{uH}{\alpha}, \; w^* = \frac{wH}{\alpha}, \; t^* = \frac{t\alpha}{H^2\sigma}, \; p^* = \frac{pH^2}{\rho\alpha^2}$$

Making use of these dimensionless variables, equations (4.2) - (4.5), on dropping the asterisks, become

$$\nabla \cdot \mathbf{V} = 0 \tag{4.10}$$

$$\mathbf{V} = -\nabla p + Ra(T + NS)\mathbf{e}_z \tag{4.11}$$

$$\frac{\partial T}{\partial t} + (\mathbf{V} \cdot \nabla)T = \nabla^2 T \tag{4.12}$$

$$\epsilon_1 \frac{\partial S}{\partial t} + (\mathbf{V} \cdot \nabla)S = \frac{1}{Le}\nabla^2 S \tag{4.13}$$

The non-dimensional parameters that appear in equations (4.11) - (4.13) are the thermal Rayleigh number $Ra = \dfrac{Kg\beta_T \Delta T H}{\nu\alpha}$, the buoyancy ratio $N = \dfrac{\beta_S \Delta S}{\beta_T \Delta T}$, the Lewis number $Le = \dfrac{\alpha}{D}$, and the normalized porosity $\epsilon_1 = \dfrac{\epsilon}{\sigma}$. Here, $\nabla^2 = \dfrac{1}{r}\dfrac{\partial}{\partial r}\left(r\dfrac{\partial}{\partial r}\right) + \dfrac{\partial^2}{\partial z^2}$.

The dimensionless boundary conditions are given by

$$T = S = 0.5, \quad u = 0 \quad \text{at} \quad r = \frac{1}{A(\kappa - 1)} \tag{4.14}$$

$$T = S = -0.5, \quad u = 0 \quad \text{at} \quad r = \frac{\kappa}{A(\kappa - 1)} \tag{4.15}$$

$$\frac{\partial T}{\partial z} = \frac{\partial S}{\partial z} = 0, \quad w = 0 \quad \text{at} \quad z = 0,\, 1 \tag{4.16}$$

where $A = \dfrac{H}{r_o - r_i}$ is the aspect ratio, and $\kappa = \dfrac{r_o}{r_i}$ is the radius ratio of the cavity.

The dimensionless streamfunction ψ is defined as [18]

$$u = -\frac{1}{r}\frac{\partial \psi}{\partial z}, \qquad w = \frac{1}{r}\frac{\partial \psi}{\partial r} \tag{4.17}$$

Making use of (4.17), and expanding the ∇ and ∇^2 operators, equations (4.10) and (4.11) can be combined to a single equation given by

$$\frac{\partial^2 \psi}{\partial r^2} - \frac{1}{r}\frac{\partial \psi}{\partial r} + \frac{\partial^2 \psi}{\partial z^2} = rRa\left(\frac{\partial T}{\partial r} + N\frac{\partial S}{\partial r}\right) \tag{4.18}$$

with $\psi = 0$ on all the boundaries. Thus, the governing equations for the present problem are equations (4.12), (4.13), and (4.18), while the boundary conditions are given by equations (4.14) - (4.16).

A note on the assumptions: Since Darcy's law is assumed to hold true, the slip boundary conditions prevail at the walls. Also, the Darcy velocity $\mathbf{V}$ is sufficiently small. Darcy's law has been verified by the results of many experiments, and theoretical backing for it has been obtained in various ways, with the aid of either deterministic or statistical models [117].

The Soret effect refers to the mass flux produced by temperature gradient, and the Dufour effect refers to the heat flux produced by concentration gradient. Soret and Dufour effects are usually minor and can be neglected in most cases. However, when they are not negligible, equations (4.4) and (4.5) become respectively,

$$\frac{(\rho C)_p}{(\rho C)_f}\frac{\partial T}{\partial t} + \mathbf{V}\cdot\nabla T = \nabla\cdot\left(\alpha\nabla T + D_{TS}\nabla S\right) \tag{4.19}$$

$$\epsilon\frac{\partial S}{\partial t} + \mathbf{V}\cdot\nabla S = \nabla\cdot\left(D\nabla S + D_{ST}\nabla T\right) \tag{4.20}$$

where $\dfrac{D_{TS}}{\alpha}$ is the Dufour coefficient, and $\dfrac{D_{ST}}{D}$ is the Soret coefficient of the porous medium.

Also, the variation of density with temperature and concentration gives rise to a combined buoyancy force, proportional to $\beta_T(T - T_0) + \beta_S(S - S_0)$. The fact that the coefficients of equation (4.19) differ from those of equation (4.20) leads to interesting effects, such as flows oscillating in time in the presence of steady boundary conditions [117].

Additionally, the Boussinesq approximation is applied to simplify the analysis. This approximation is valid provided the density changes $\Delta\rho$ remain small in comparison with ρ_r throughout the flow region and provided that temperature variations are insufficient to cause the various properties of the medium (fluid and solid) to vary significantly from their mean values. [117]. The validity of the Boussinesq approximation was discussed by Johannsen [69] for the case of a benchmark problem known as the Elder problem.

4.3 Discretization of the governing equations

For the present problem, we utilize the HOC scheme of Kalita et.al. [81] described in chapter 2. Although the governing equations (4.10) - (4.13) are in cylindrical polar co-ordinates, and the scheme was developed for 2D convection-diffusion type equations on Cartesian grids, a minor restructuring of the governing equations allow the use of the HOC scheme (2.2).

Equations (4.12), (4.13), and (4.18), after expanding the ∇ and ∇^2 operators, can respectively be re-written as

$$\frac{\partial T}{\partial t} - \nabla^2 T + \left(u - \frac{1}{r}\right)\frac{\partial T}{\partial r} + w\frac{\partial T}{\partial z} = 0 \tag{4.21}$$

$$\epsilon Le\frac{\partial S}{\partial t} - \nabla^2 S + \left(Le\, u - \frac{1}{r}\right)\frac{\partial S}{\partial r} + Le\, w\frac{\partial S}{\partial z} = 0 \tag{4.22}$$

$$-\nabla^2\psi + \frac{1}{r}\frac{\partial \psi}{\partial r} = -rRa\left(\frac{\partial T}{\partial r} + N\frac{\partial S}{\partial r}\right) \tag{4.23}$$

Note that for equations (4.21) - (4.23) $\nabla^2 = \dfrac{\partial^2}{\partial r^2} + \dfrac{\partial^2}{\partial z^2}$

Firstly, Eq.(4.21) is solved with $c = u - \dfrac{1}{r}$, $d = w$, and $f = 0$. Then, Eq.(4.22) is solved with $b = \epsilon Le$, $c = Le\,u - \dfrac{1}{r}$, $d = Le\,w$ and $f = 0$. Finally Eq.(4.23) is solved with $c = \dfrac{1}{r}$, $d = 0$, and $f = -rRa\left(\dfrac{\partial T}{\partial r} + N\dfrac{\partial S}{\partial r}\right)$.

4.3.1 HOC Neumann Boundary Conditions

The Neumann boundary conditions at the top and bottom can be approximated as follows. At the top boundary ($z = b_0$), a Taylor series expansion for ϕ at $z = b_0 - H_j$ (j being the index along the vertical axis), viz. the j^{th} point away from the top boundary, about $z = b_0$ is given by

$$\phi_{i,b_0-j} = \phi(b_0 - H_j) = \phi(b_0) - H_j\left.\frac{\partial\phi}{\partial z}\right|_{i,b_0} + \frac{H_j^2}{2}\left.\frac{\partial^2\phi}{\partial z^2}\right|_{i,b_0} - \frac{H_j^3}{6}\left.\frac{\partial^3\phi}{\partial z^3}\right|_{i,b_0} + O(H_j^4), j = 1,2,3$$

Here H_1, H_2 and H_3 are the distances of the first, second and third grid points away from the boundary. Performing some simple mathematical operations on the three equations above to eliminate second and third order derivatives, a third order accurate approximation of the Neumann boundary condition is obtained as

$$\left.\frac{\partial\phi}{\partial x}\right|_{i,b_0} = -\frac{A\phi(b_0 - H_1) + B\phi(b_0 - H_2) + C\phi(b_0 - H_3) - (A + B + C)\phi(b_0)}{AH_1 + BH_2 + CH_3}$$

resulting in

$$A\phi_{i,b_0-1} + B\phi_{i,b_0-2} + C\phi_{i,b_0-3} - (A + B + C)\phi_{b_0,j} = 0, \tag{4.24}$$

where $A = H_2^2H_3^2(H_2 - H_3)$, $B = H_3^2H_1^2(H_3 - H_1)$ and $C = H_1^2H_2^2(H_1 - H_2)$. Here ϕ stands for either T or S.

4.3.2 Calculation of velocities

Eq. (4.23) can be re-written as

$$\nabla^2\psi = \frac{1}{r}\frac{\partial\psi}{\partial r} + rRa\left(\frac{\partial T}{\partial r} + N\frac{\partial S}{\partial r}\right) \tag{4.25}$$

Analogous to the ψ-ω form of the N-S equations $\nabla^2\psi = -\omega$, it can be assumed for the present situation that $\omega = -\left[\frac{1}{r}\frac{\partial\psi}{\partial r} + rRa\left(\frac{\partial T}{\partial r} + N\frac{\partial S}{\partial r}\right)\right]$. Utilizing this fact, explicit expressions for both u and w can be obtained.

$$
\begin{aligned}
u_{ij} &= -\frac{1}{r_{ij}}\frac{\partial\psi}{\partial z}\bigg|_{ij} \\
&= -\frac{1}{r_{ij}}\left[\delta_z\psi_{ij} - \frac{(z_f - z_b)}{2}\delta_z^2\psi_{ij} - \frac{z_f z_b}{6}\frac{\partial^3\psi}{\partial z^3}\bigg|_{ij}\right] \\
&= -\frac{1}{r_{ij}}\left[\delta_z\psi_{ij} - \frac{(z_f - z_b)}{2}\delta_z^2\psi_{ij} - \frac{z_f z_b}{6}\frac{\partial}{\partial z}\left(\frac{\partial^2\psi}{\partial z^2}\right)\right] \\
&= -\frac{1}{r_{ij}}\left[\delta_z\psi_{ij} - \frac{(z_f - z_b)}{2}\delta_z^2\psi_{ij} - \frac{z_f z_b}{6}\frac{\partial}{\partial z}\left(-\omega - \frac{\partial^2\psi}{\partial r^2}\right)\right] \\
&= -\frac{1}{r_{ij}}\left[\delta_z\psi_{ij} - \frac{(z_f - z_b)}{2}\delta_z^2\psi_{ij} + \frac{z_f z_b}{6}\frac{\partial\omega}{\partial z}\bigg|_{ij} + \frac{z_f z_b}{6}\frac{\partial^3\psi}{\partial z\,\partial r^2}\bigg|_{ij}\right]
\end{aligned}
$$

Substituting the approximations for $\frac{\partial\omega}{\partial z}\Big|_{ij}$ and $\frac{\partial^3\psi}{\partial z\,\partial r^2}\Big|_{ij}$, and simplifying,

$$
u_{ij} = -\frac{1}{r_{ij}}\left[\delta_z\psi_{ij} - \frac{(z_f - z_b)}{2}\delta_z^2\psi_{ij} + \frac{z_f z_b}{6}\delta_z\omega_{ij} - \frac{z_f z_b(z_f - z_b)}{12}\delta_z^2\omega_{ij} + \frac{z_f z_b}{6}\delta_z\delta_r^2\psi_{ij}\right] \tag{4.26}
$$

Similarly,

$$
w_{ij} = \frac{1}{r_{ij}}\left[\delta_r\psi_{ij} - \frac{r_f - r_b}{2}\delta_r^2\psi_{ij} + \frac{r_f r_b}{6}\delta_r\omega_{ij} - \frac{r_f r_b(r_f - r_b)}{12}\delta_r^2\omega_{ij}\frac{r_f r_b}{6}\delta_r\delta_z^2\psi_{ij}\right] \tag{4.27}
$$

A note on the numerical approach: As mentioned in section 4.1, steady state results for this problem was reported by Kalita and Dass [79]. They used an HOC scheme which was based on uniform grids. The use of non-uniform grids in this chapter provides us a flexibility over uniform grids. In addition, this work also makes use of HOC Neumann boundary conditions as described in section 4.3.1.

4.3.3 Nusselt and Sherwood number

In most applications, the Nusselt (Nu) and Sherwood number (Sh) provide a summary of the overall HMT characteristics respectively. The local Nusselt and Sherwood numbers along the inner (hotter) wall are given by

$$Nu_i = \left.\frac{\partial T}{\partial r}\right|_{r=\frac{1}{A(\kappa-1)}} \tag{4.28}$$

$$Sh_i = \left.\frac{\partial S}{\partial r}\right|_{r=\frac{1}{A(\kappa-1)}} \tag{4.29}$$

To obtain the average Nusselt ($\overline{Nu}$) and Sherwood ($\overline{Sh}$) numbers, (4.28) and (4.29) are integrated along the inner (hotter) wall

$$\overline{Nu_i} = \int_0^1 Nu_i\, dz \tag{4.30}$$

$$\overline{Sh_i} = \int_0^1 Sh_i\, dz \tag{4.31}$$

The derivatives of T and S appearing in (4.28) and (4.29) respectively have been approximated using the formula derived in section 4.3.1, and numerical integration for (4.30) and (4.31) have been carried out using Simpson's $\frac{1}{3}rd$ rule in non-uniform grids.

4.4 Grid Generation

Previous studies [18, 79] have shown that high gradients of temperature and concentration occur near the walls. To capture these high gradients, more grid points are required in the vicinity of the walls relative to the center of the cavity. To generate such a grid which has a higher concentration of grid points near the walls relative to the center, following equations [81] are used

$$x_i = \frac{i}{i_{max}} - \frac{\mu_1}{2\pi}\sin\left(\frac{2\pi\, i}{i_{max}}\right), \quad 0 \leq \mu_1 < 1 \quad \text{in the } x\text{-direction} \tag{4.32}$$

$$y_j = \frac{j}{j_{max}} - \frac{\mu_2}{2\pi}\sin\left(\frac{2\pi\, j}{j_{max}}\right), \quad 0 \leq \mu_2 < 1 \quad \text{in the } y\text{-direction} \tag{4.33}$$

The clustering parameters μ_1 and μ_2 control the intensity of clustering along the walls; larger the value of μ_i, greater is the intensity of clustering. For all the computations carried out in this work, we have set $\mu_1 = \mu_2$. The value of the clustering parameter, however, depends on the parameters considered.

4.5 Iterative solution procedure of the discrete equations

After discretizing (4.21) and (4.22) by employing the scheme given by (2.2), equations (4.21) and (4.22) reduce to the matrix form

$$A\boldsymbol{\phi}^{(n+1)} = \boldsymbol{B} \tag{4.34}$$

In (4.34), the coefficient matrix A is a nona-diagonal sparse matrix with each row containing a maximum of nine non-zero entries sitting on those diagonals. For a rectangular grid having p points in the x- and q points in the y- direction, the coefficient matrix A is of size p^2q^2. The non-uniformity of the grid render asymmetry to this matrix A. $\boldsymbol{\phi}^{(n+1)}$ is the unknown vector sought, representing the values of T or S at $(n+1)^{th}$ time level with information available at the n^{th} time level from vector $\boldsymbol{B}$; both $\boldsymbol{\phi}^{(n+1)}$ and $\boldsymbol{B}$ has length pq.

In order to compute ψ from (4.23), which does not involve any time-derivative term, the scheme developed by Kalita et.al. [80] for the steady N-S equations is used. Once ψ is known, the velocities u and w are computed using the procedure described in section 4.3.2. Then T and S are computed utilizing (4.34), where BiCGStab [143] with LU decomposition as the pre-conditioner is used. Note that we have employed the Lis library [105] for this purpose and pre-conditioning was seen to be extremely useful in tackling high Rayleigh number flow.

The solution procedure of the matrix equation (4.34) described above at a particular time-step n may be defined as the inner iterations which was stopped once the l_2 norm of the residual fell below 0.5×10^{-9}, i.e., $\|\boldsymbol{B} - A\boldsymbol{\phi}^{(n+1)}\|_2 < 0.5 \times 10^{-9}$. The flow is assumed to reach steady state when $max\ |\boldsymbol{\psi}^{(n+1)} - \boldsymbol{\psi}^{(n)}| < 0.5 \times 10^{-7}$.

4.6 Validation of algorithm and code

In this section the code and algorithm are validated against results which are well established in the literature.

The parameters chosen for this validation exercise are $Ra = 500$, $N = 0$, $Le = 10$, $A = 1$, and $\kappa = 1$ and 5, representing two different cases. The clustering parameter is taken to be 0.4 (Fig. 4.2). To demonstrate grid independence results of the present code, comparison exercise is carried out for the value of the maximum streamfunction (ψ_{max}) with those of Beji et.al. [18], and Kalita and Dass [79] in Table 4.1. The corresponding isotherms, isoconcentrates, and streamlines are shown in Fig. 4.3. These results are qualitatively and quantitatively very similar to those reported by Beji et.al. [18], and Kalita and Dass [79].

Table 4.1: Grid independence study for $A = 1$, $Le = 10$, $N = 0$, and $Ra = 500$.

κ	Reference	Grid	ψ_{max}
1	Beji et.al. [18]	- - -	1359.00
	Kalita and Dass [79]	21 × 21	1381.63
		41 × 41	1364.39
		81 × 81	1363.24
	Present	61 × 61	1337.01
		81 × 81	1347.64
		121 × 121	1355.28
5	Beji et.al. [18]	- - -	7.6310
	Kalita and Dass [79]	21 × 21	7.9893
		41 × 41	7.8539
		81 × 81	7.8160
	Present	61 × 61	7.7114
		81 × 81	7.7457
		121 × 121	7.7701

4.7 Results and discussion

Computations were carried out to investigate the influence of the non-dimensional parameters appearing in (4.21) - (4.23) viz. A, κ, Le, N, and Ra. The normalised porosity ϵ is set to unity. In each subsection four parameters are kept fixed and the remaining parameter is varied to study its influence on the flow.

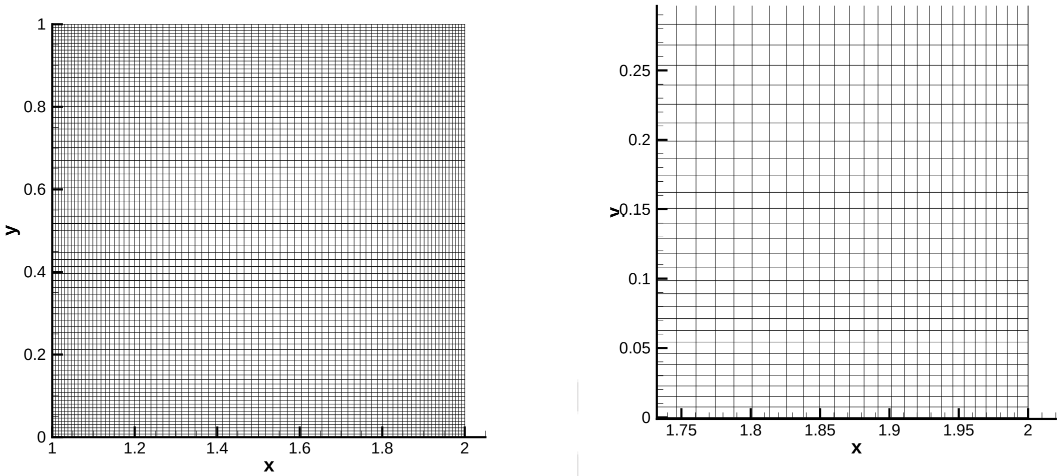

(a) Grid used for $A = 1$.

(b) Magnified portion of the bottom right corner of the grid.

Figure 4.2: Grid used for $A = 1$, with $\mu = 0.4$ in both x- and y- directions.

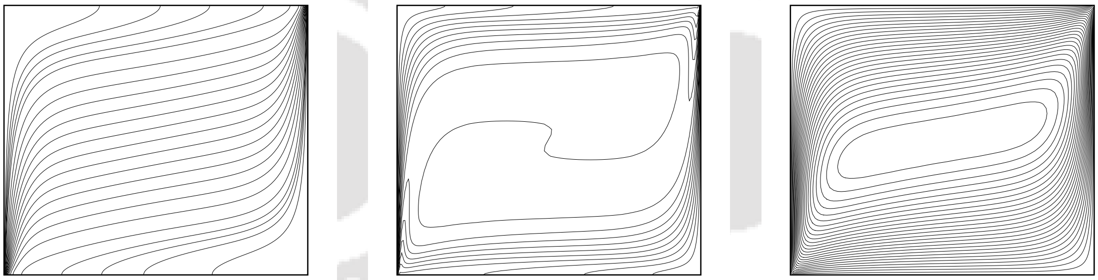

(a) Isotherms. (b) Isoconcentrates. (c) Streamlines.

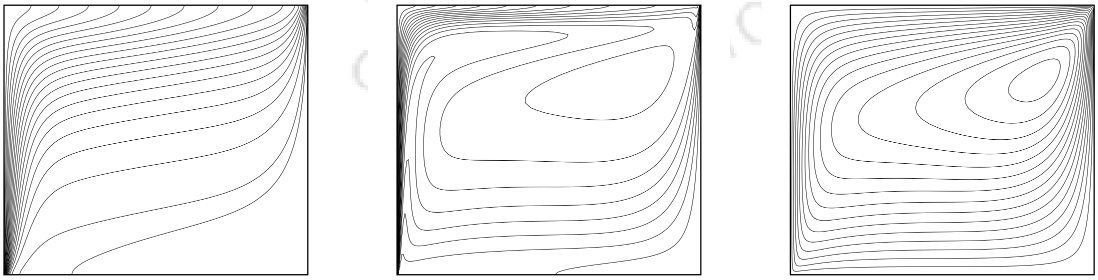

(d) Isotherms. (e) Isoconcentrates. (f) Streamlines.

Figure 4.3: Isotherms, isoconcentrates and the streamlines for $N = 0$, $A = 1$, $Ra = 500$, $Le = 10$ and $\kappa = 1$((a)-(c)) and $\kappa = 5$ ((d)-(e)).

4.7.1 Influence of Aspect Ratio

Here, simulations are carried out to investigate the influence of aspect ratio in the range $1 \leq A \leq 10$ while keeping the other parameters fixed viz. $Ra = 500$, $\kappa = 2$, $Le = 3$ and $N = 2$. The value of N chosen here suggests that moderate gradients of concentration drive the flow. For $A = 1$, 2 the isoconcentrates are uniform at the center of the cavity and solutal gradients are sharper at the top and bottom walls [Fig. 4.5 (a)]. One can observe that the flow becomes stratified with the increase in A [Fig. 4.5]. Further, as A increases, the isotherms settle into an approximately diagonal shape, while also becoming more and more vertical [Fig. 4.4]. At higher values of A viz. at $A = 8$ and 10, in the horizontal direction there is an almost linear variation of temperature at the core of the cavity. [Fig. 4.4(e), 4.4(f)]. It is also observed that as A increases, the hydrodynamic boundary layers at the top and bottom walls of the cavity become thicker and there is a slight shift of the vortex center upwards [figures 4.6 (a) - (f)].

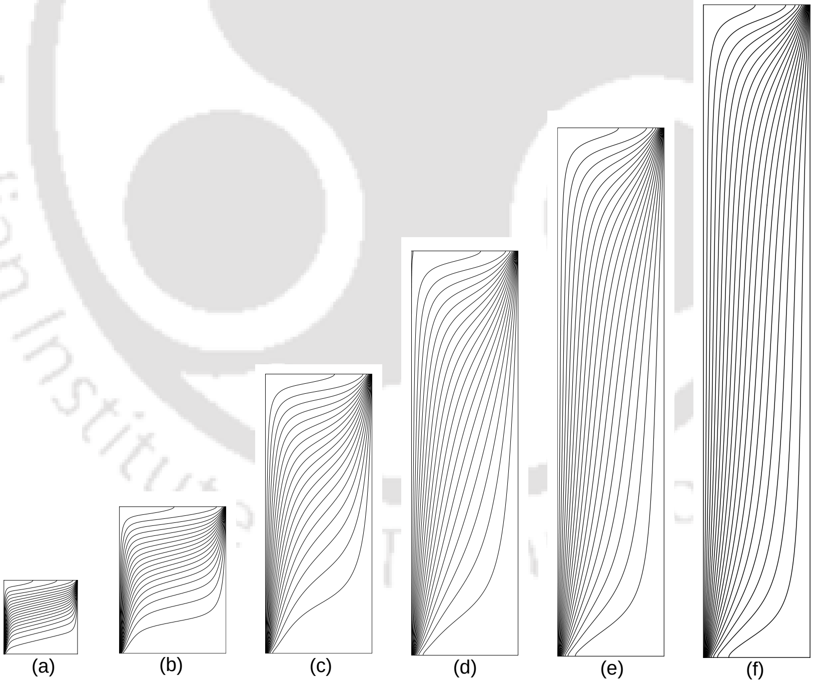

Figure 4.4: Temperature contours for $N = 2$, $\kappa = 2$, $Le = 3$, $Ra = 500$, and various values of $A = 1, 2, 4, 6, 8,$ and 10.

To discern a pattern of HMT characteristics, the variation of $\overline{Nu_i}$ (Fig.4.7 (a)) and $\overline{Sh_i}$ (Fig.4.7 (b)) are plotted for different values of N $(-4 \leq N \leq 4)$ while keeping the other parameters fixed. The plots reveal a marginal increase in $\overline{Nu_i}$ for some cases ($N = -2$,

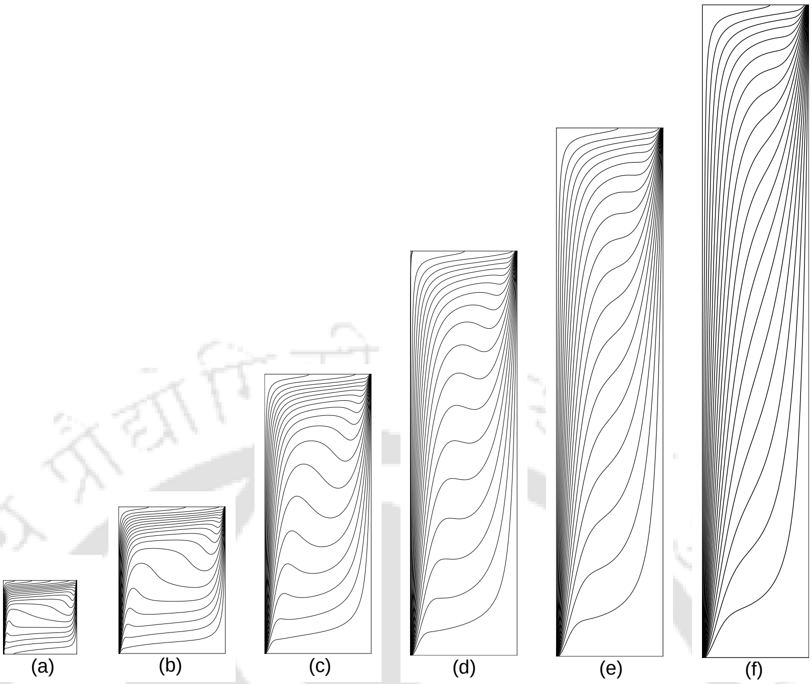

Figure 4.5: Concentration contours for $N = 2$, $\kappa = 2$, $Le = 3$, $Ra = 500$, and various values of $A = 1, 2, 4, 6, 8$, and 10.

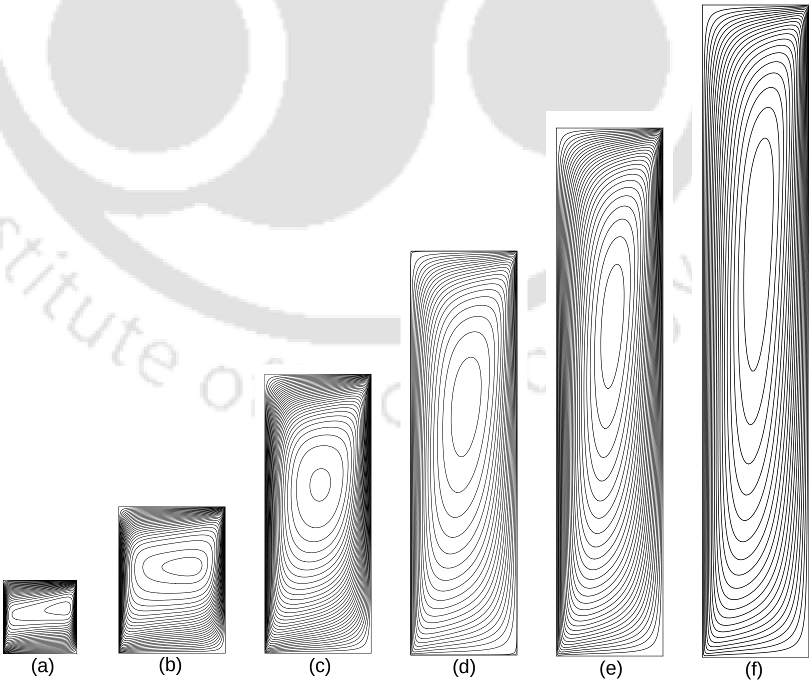

Figure 4.6: Streamfunction contours for $N = 2$, $\kappa = 2$, $Le = 3$, $Ra = 500$, and various values of $A = 1, 2, 4, 6, 8$, and 10.

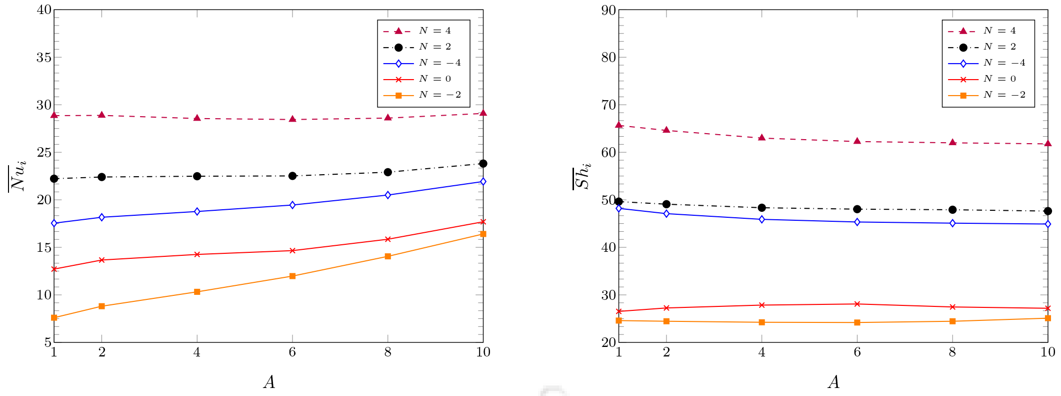

(a) (b)

Figure 4.7: Variation of (a) $\overline{Nu_i}$ and (b) $\overline{Sh_i}$ with aspect ratio A for different values of N.

0) but almost no variation with aspect ratio (A) for the remaining values of N. Similarly, there is a subtle drop in Sherwood number ($\overline{Sh_i}$) when the aspect ratio is increased. Thus, there is no significant change in either $\overline{Nu_i}$ or $\overline{Sh_i}$ with aspect ratio.

4.7.2 Influence of Radius Ratio

Here, the effect of radius ratio (κ) is investigated by carrying out computations for $A = 5, N = -2, Le = 10, Ra = 500$, and $\kappa = 1, 2, 5, 10, 20$, and 50.

Figures. 4.8 and 4.9 show the streamline contours at different instants of non-dimensional time for different values of κ. Figures 4.10 and 4.11 show the steady state isotherms and isoconcentrates respectively. Figures. 4.8(h), 4.8(p), 4.8(x), 4.9(h), 4.9(p), and 4.9(x) show the steady-state streamline contours for $\kappa = 1, 2, 5, 10, 20$, and 50 respectively. As a result of the boundary conditions imposed on temperature and concentration, the direction of the flow driven by temperature is clockwise and the direction of the flow driven by concentration is counterclockwise.

As seen in figures. 4.8 and 4.9, the time required to reach steady-state for $\kappa = 1$ is much greater than what is required for the other values of κ. For $\kappa = 1$, two clockwise rotating thermal vortices are seen to form at the top and bottom of the enclosure at $t = 0.011$. These thermal vortices steadily grow in size, as the solute driven flow at the middle of the enclosure reaches a steady state. When the radius ratio is increased, the top thermal vortex appears earlier than $\kappa = 1$ (Figures. 4.8(i), 4.8(q), 4.9(a), 4.9(i), 4.9(q)) and grows in size and intensity till steady state is reached. This thermal driven flow occupies a greater part of the enclosure than the solute driven flow for $\kappa = 10, 20$, and 50 (Fig. 4.9). The bottom thermal vortex for $\kappa = 2$ appears at a later time than for $\kappa = 1$ (Fig. 4.8(k)) and grows in size till steady state is reached. However, it is of a smaller size than for $\kappa = 1$.

For $\kappa = 5$ the bottom thermal vortex appears in the beginning (Figures. 4.8(s)-(u)), but disappears fairly quickly, and there is no trace of it when the flow becomes steady (Fig. 4.8(x)). For $\kappa = 10, 20$, the bottom thermal vortex is barely discernible in the beginning (Figures. 4.9(c), 4.9(d), 4.9(k)), and disappears completely before reaching steady state. For $\kappa = 50$, there is no bottom thermal vortex at any stage of the flow. However, the top thermal vortex appears to be more chaotic in nature in the earlier stages of the flow (Fig 4.9(q)-(s)).

The flow is solute dominated in the early stages for all κ. With time, the appearance of the thermal vortices causes the clockwise rotating solutal vortex to be sandwiched between the two thermal vortices. The solutal flow occupies most of the enclosure for $\kappa = 1, 2$. However, the size of the solutal vortex reduces when $\kappa = 2$, and its center shifts towards the bottom right of the enclosure. For $\kappa \geq 2$, with the disappearance of the bottom thermal vortex, the enclosure is occupied by one thermal vortex and one solutal vortex. The size of the solutal vortex decreases as κ increases, until $\kappa = 50$ when the thermal vortex occupies most of the enclosure. The center of the solutal also vortex keeps moving to the bottom right of the enclosure with an increase in κ.

The variation of average Nusselt and Sherwood numbers with radius ratio (κ) is shown in figures 4.12 (a) and (b). Similar to the previous section (section 4.7.1), we have carried out computations with different values of N ($-5 \leq N \leq 5$) while keeping the other parameters fixed to arrive at a general picture of HMT characteristics. There is a parabolic increase in $\overline{Nu_i}$ and $\overline{Sh_i}$ for $\kappa \leq 10$ and a linear increase for $\kappa > 10$. However, the variation of $\overline{Nu_i}$ is steeper than that of $\overline{Sh_i}$. The increase in HMTR with κ can be attributed to the corresponding increase in volume of the cavity. Note that the computed values of $\overline{Nu_i}$ and $\overline{Sh_i}$ for $N = 0$ are a close match with that computed by Beji et.al. [18].

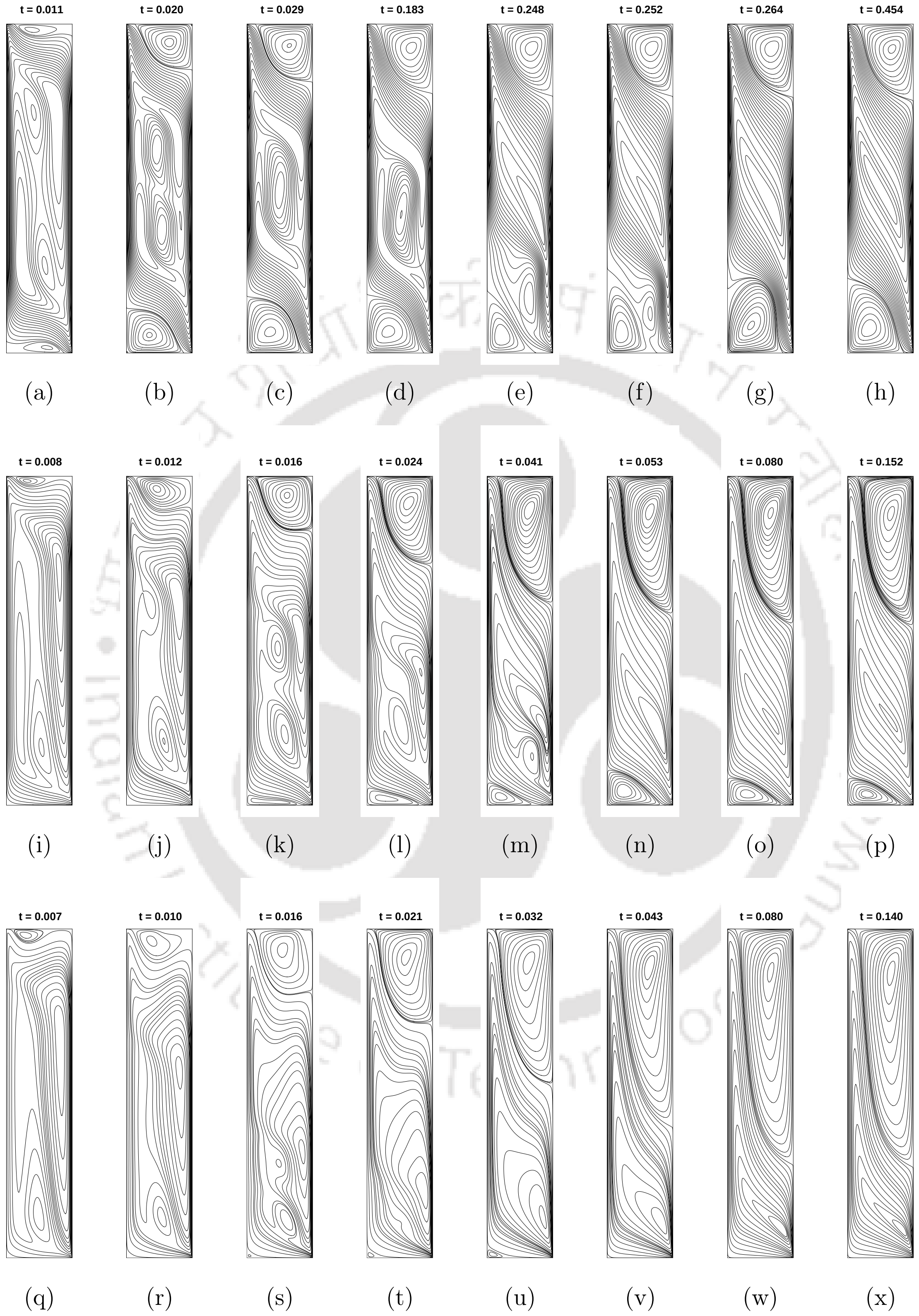

(a) (b) (c) (d) (e) (f) (g) (h)

(i) (j) (k) (l) (m) (n) (o) (p)

(q) (r) (s) (t) (u) (v) (w) (x)

Figure 4.8: Streamlines at different times for $A = 5, N = -2, Ra = 500, Le = 10$ and $\kappa = 1$((a)-(h)),2((i)-(p)), 5((q)-(x)).

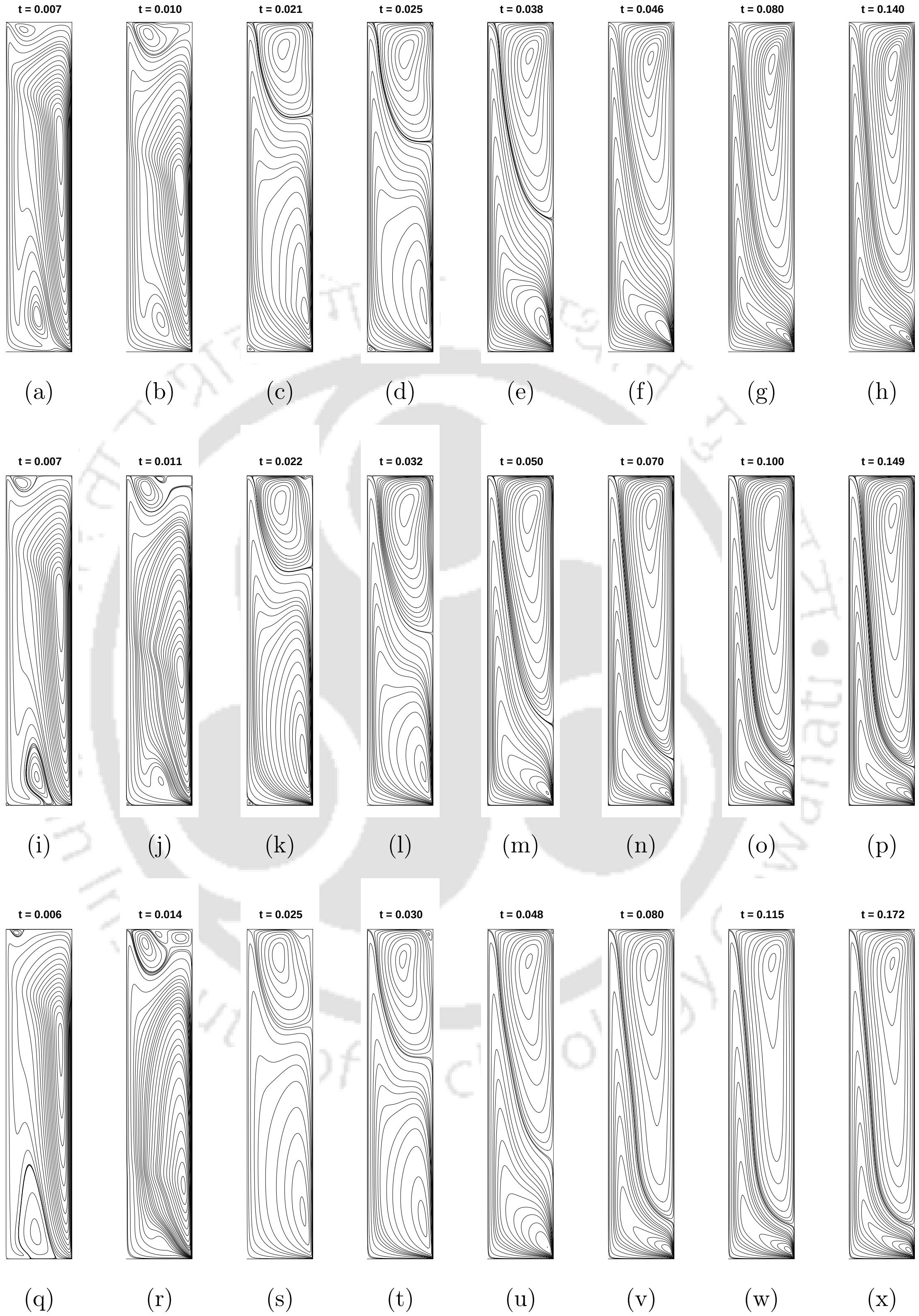

(a) (b) (c) (d) (e) (f) (g) (h)

(i) (j) (k) (l) (m) (n) (o) (p)

(q) (r) (s) (t) (u) (v) (w) (x)

Figure 4.9: Streamlines at different times for $A = 5, N = -2, Ra = 500, Le = 10$ and $\kappa = 10$((a)-(h)),20((i)-(p)), 50((q)-(x)).

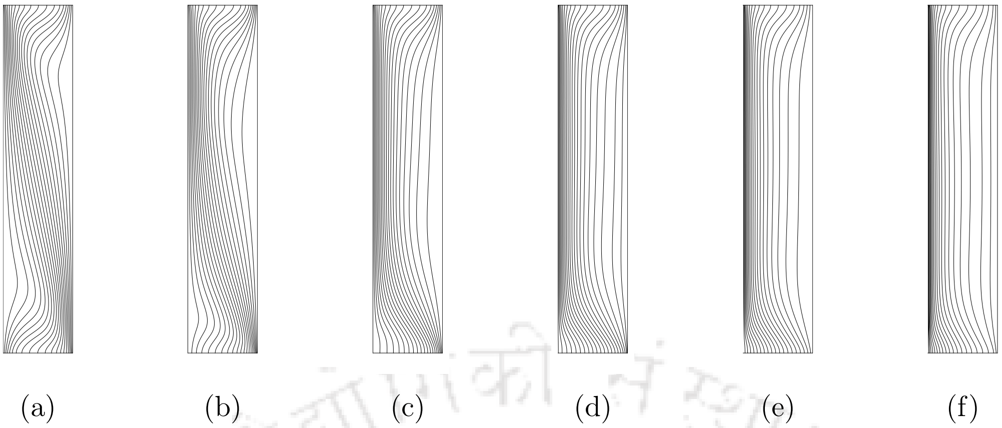

Figure 4.10: Steady state isotherms for $A = 5, Le = 10, N = -2, Ra = 500$, and $\kappa = 1, 2, 5, 10, 20,$ and 50 respectively.

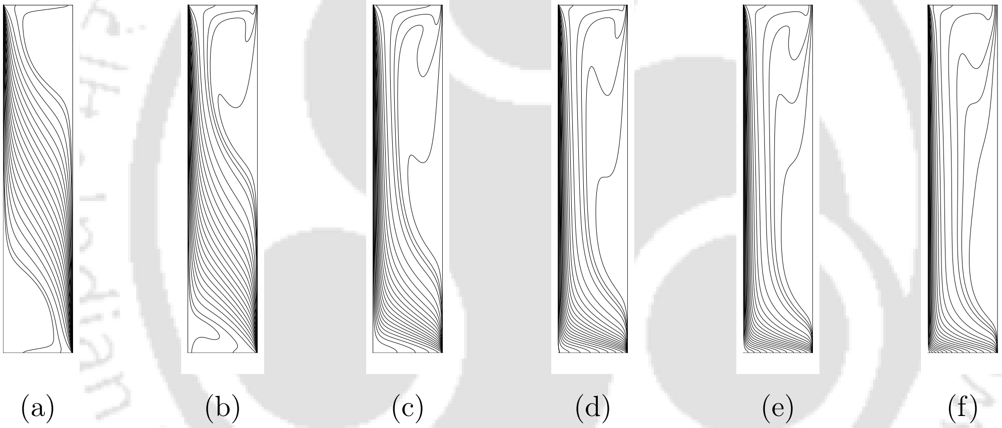

Figure 4.11: Steady state isoconcentrates for $A = 5, Le = 10, N = -2, Ra = 500$, and $\kappa = 1, 2, 5, 10, 20,$ and 50 respectively.

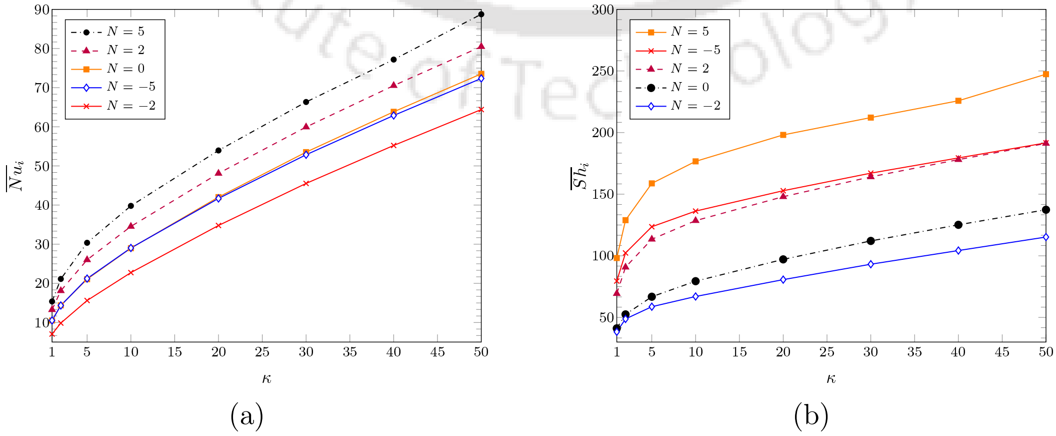

Figure 4.12: Variation of (a) $\overline{Nu_i}$ and (b) $\overline{Sh_i}$ with radius ratio κ for different values of N.

4.7.3 Influence of Lewis number

Here, computations are carried out for $1 \leq Le \leq 200$ while keeping the other parameters fixed at $A = 5$, $N = 1$, $Ra = 500$, and $\kappa = 2$.

The Lewis number (Le) is the ratio of thermal and solutal diffusivities, and it characterizes solute transport relative to thermal diffusion [110]. Thus, for $Le = 1$, as the values of thermal and solutal diffusion are same ($\alpha = D$) the temperature and concentration contours at steady state are identical (Figures. 4.13(a) and 4.14(a)). As Le increases, concentration boundary layers on the hot and cold walls become sharper whereas there is little change in the isotherm patterns. At high Le's, as $D << \alpha$, the horizontal intrusion layers of concentration at the top and bottom walls are significantly sharper than their thermal counterpart. Consequently, at higher Le's, the core of the concentration field is in a state of near uniform concentration. Also, with increase in Le, the center of the vortex shifts towards the cold (inner) wall and hydrodynamic boundary layers become thinner on the cold (inner) wall and thicker at the hot (outer) wall (Fig. 4.15). Note that the contour plots shown here as well as the computed values of Nusselt and Sherwood numbers are in close agreement with those of Kalita and Dass [79]. A plot of average Nusselt and Sherwood numbers (Fig. 4.16) shows that $\overline{Nu_i}$ decreases while $\overline{Sh_i}$ increases with Le.

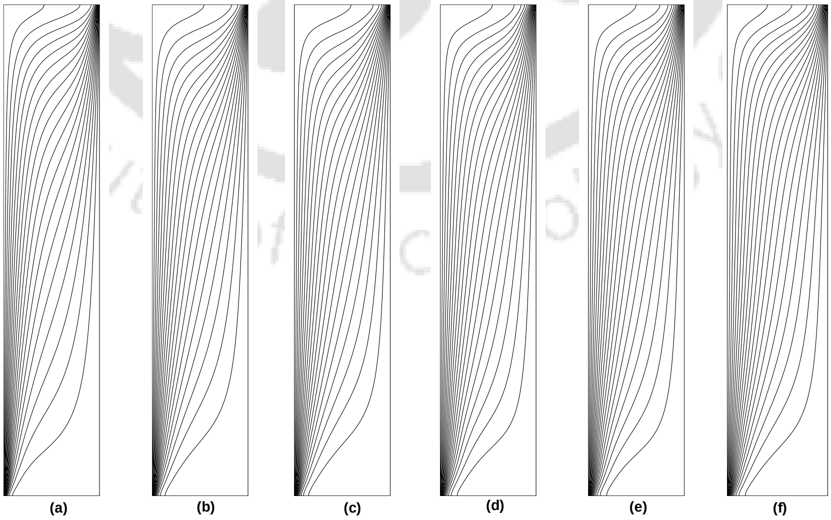

Figure 4.13: Isotherms for $A = 5$, $\kappa = 2$, $Ra = 500$, $N = 1$, and various values of $Le = 1, 5, 10, 50, 100$, and 200 (from left to right in that order).

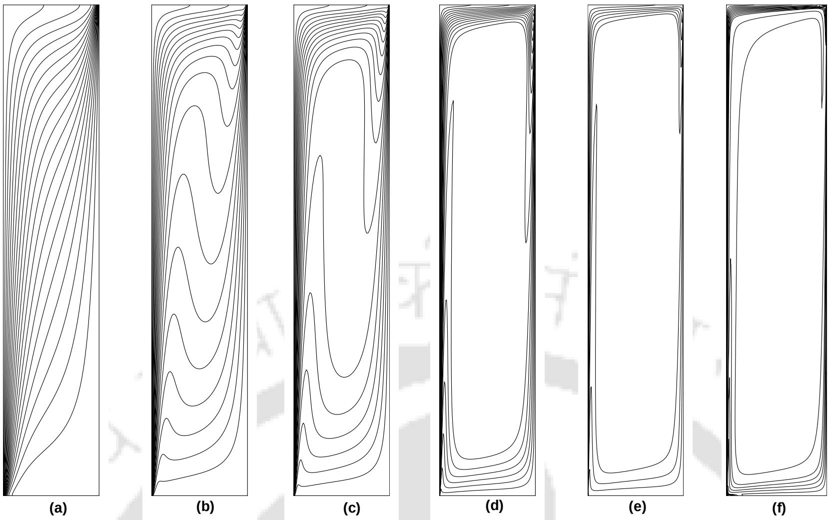

Figure 4.14: Isoconcentrates for $A = 5$, $\kappa = 2$, $Ra = 500$, $N = 1$, and various values of $Le = 1, 5, 10, 50, 100,$ and 200 (from left to right in that order).

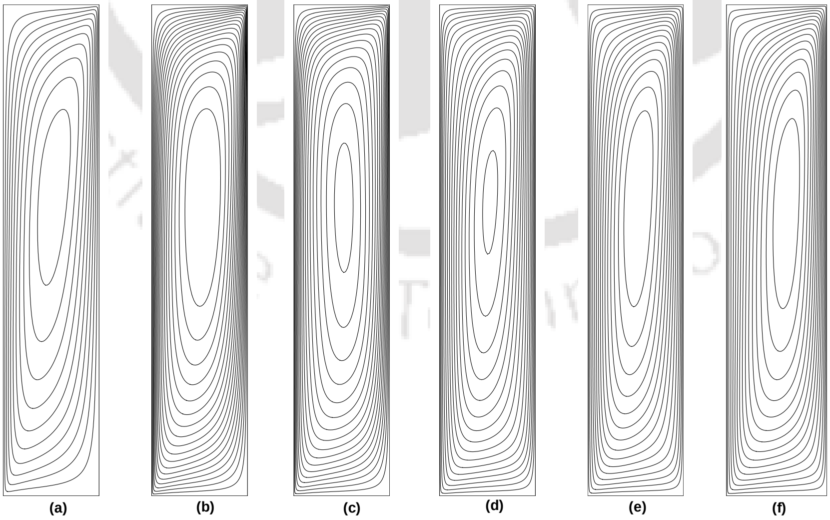

Figure 4.15: Streamlines for $A = 5$, $\kappa = 2$, $Ra = 500$, $N = 1$, and various values of $Le = 1, 5, 10, 50, 100,$ and 200 (from left to right in that order).

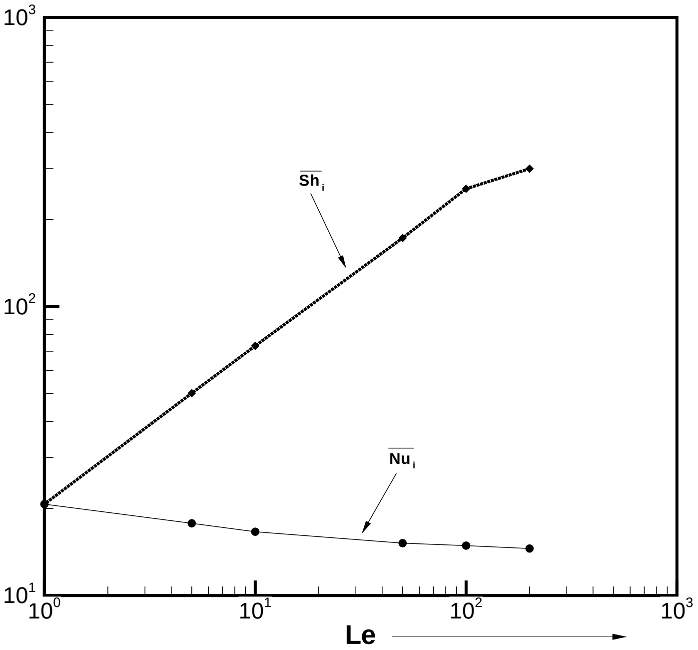

Figure 4.16: Variation of $\overline{Nu_i}$ and $\overline{Sh_i}$ with respect to Le for $A = 5$, $\kappa = 2$, $Ra = 500$, and $N = 1$.

4.7.4 Influence of Buoyancy Ratio

Here, the influence of buoyancy ratio N is studied by varying it in the range $-40 \leq N \leq 40$, while keeping the other parameters fixed at $A = 5$, $Ra = 500$, $\kappa = 2$, and $Le = 5$.

The buoyancy ratio $N = \dfrac{\beta_S \Delta S'}{\beta_T \Delta T'}$ characterizes the ratio of solutal and thermal buoyancy forces. For most fluids at ordinary temperature and pressure, β_T is positive ($\beta_T > 0$), β_S can be negative as well.

Note that as a result of the particular boundary conditions imposed, the thermal flow is in clockwise direction, whereas the direction of the solutal flow depends on the sign of β_s, so that for $N > 0$ it is clockwise and for $N < 0$ it is anticlockwise. For $N \geq 0$, Figures 4.17, 4.18, 4.19 (f) - (k) respectively show the steady state isotherms, isoconcentrates and streamlines for mutually cooperating effects of both the temperature and concentration gradients. When $N << 1$, the solutal contribution to the buoyancy forces that drives the fluid motion is negligible and the flow is driven mainly by gradients of temperature; for $N = 0$, there is no diffusion of species and hence the flow pattern that results is that of heat transfer only. For $N > 0$, the mass species and thermal buoyancy forces are augmented and the flow is simultaneously accelerated clockwise.

The typical features of opposing double-diffusive flow can now be seen from Figures 4.17, 4.18, 4.19 (a) - (e). For $N = -2$, one solute-driven rotating anticlockwise vortex in the core region and one clockwise thermal-driven vortex develop on the top of the cavity (Fig. 4.19 (e)). When N is decreased to -5 (Fig. 4.19 (d)), the upper clockwise vortex is destroyed. With N decreasing further, only the anticlockwise vortex remains with boundary layers becoming thinner on the vertical walls.

Fig. 4.20 shows the variation of $\overline{Nu_i}$ and $\overline{Sh_i}$ with N for different values of aspect ratio. The vertical dashed lines demarcate the aiding and opposing flow regimes. The effect of aiding and opposing flows on convective HMT is evident from the values of $\overline{Nu_i}$ and $\overline{Sh_i}$ for the same $|N|$. It is clearly seen that $\overline{Nu_i}\big|_{(N=2)} > \overline{Nu_i}\big|_{(N=-2)}$, $\overline{Nu_i}\big|_{(N=5)} > \overline{Nu_i}\big|_{(N=-5)}$, and so on. Similar is the case for $\overline{Sh_i}$. The overlapping plots for $A = 5, 6, 7$ (Fig. 4.20(a)) shows that there is little variation in $\overline{Nu_i}$ when aspect ratio increases. For $A = 10$, $\overline{Nu_i}$ increases only for $-10 \leq N \leq 5$. Similar pattern of overlap is observed in the variation of $\overline{Sh_i}$ for $-10 \leq N \leq 10$. For larger values of $|N|$, Sherwood number decreases marginally with increase in aspect ratio. This is consistent with the observations in section 4.7.1

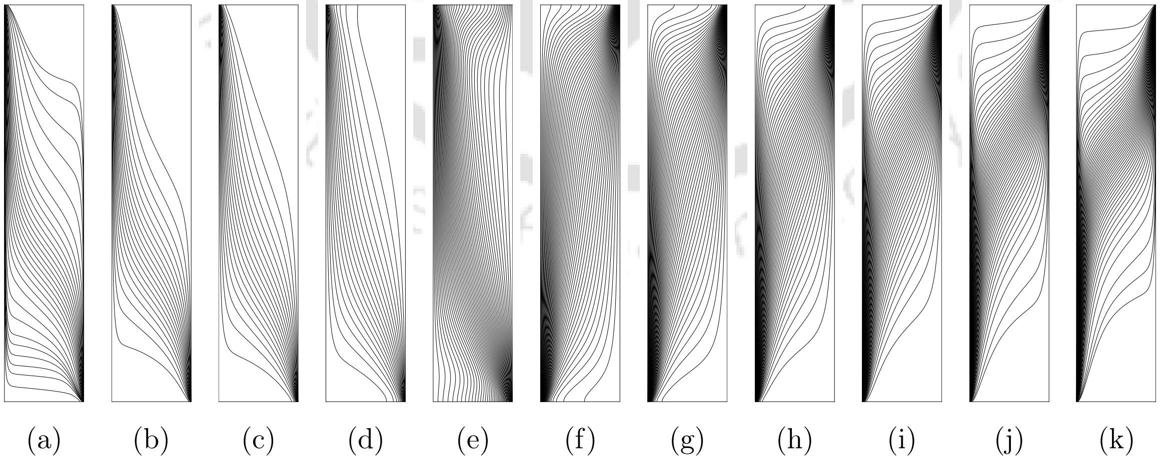

Figure 4.17: Steady state isotherms for $A = 5, Le = 5, \kappa = 2, Ra = 500$, and $N = -40, -20, -10, -5, -2, 0, 2, 5, 10, 20,$ and 40 respectively.

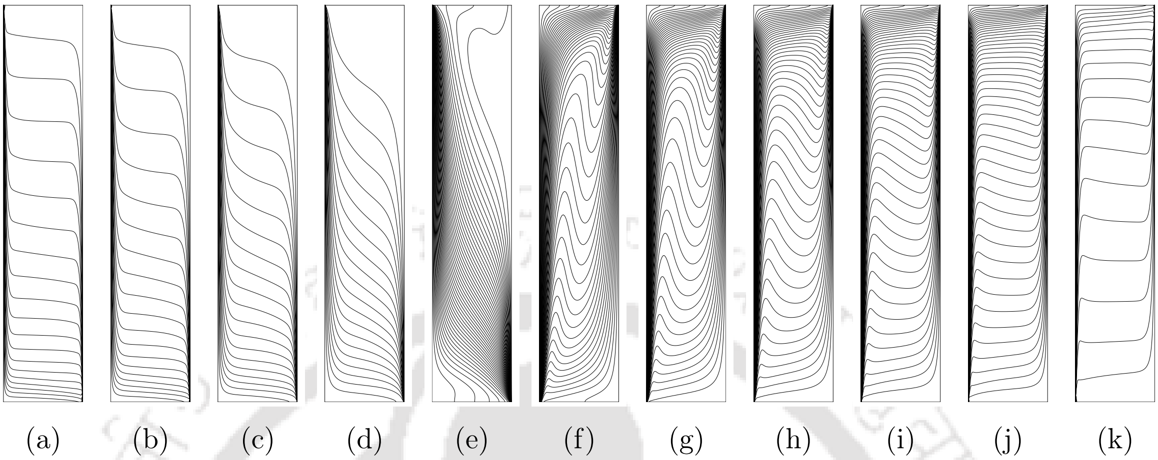

Figure 4.18: Steady state isoconcentrates for $A = 5, Le = 5, \kappa = 2, Ra = 500$, and $N = -40, -20, -10, -5, -2, 0, 2, 5, 10, 20$, and 40 respectively.

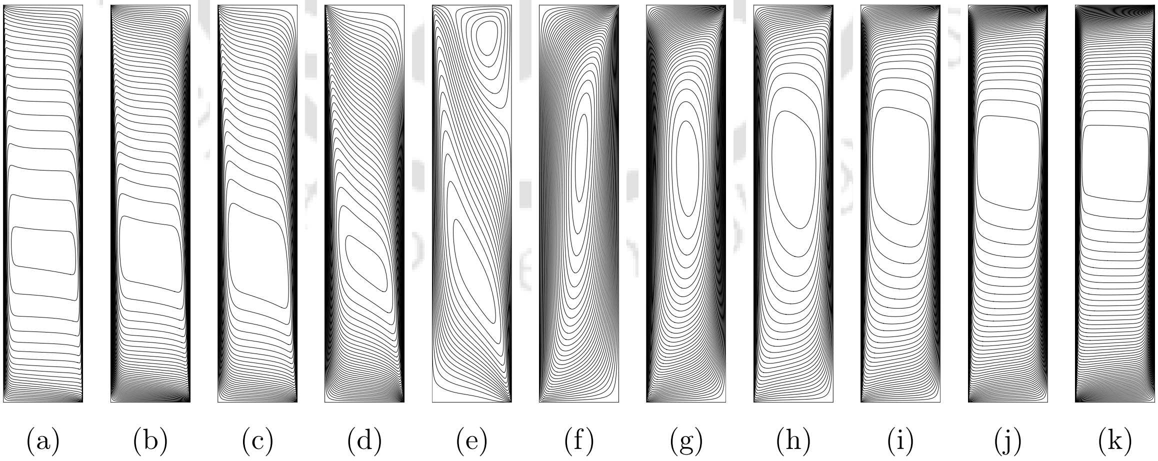

Figure 4.19: Steady state streamlines for $A = 5, Le = 5, \kappa = 2, Ra = 500$, and $N = -40, -20, -10, -5, -2, 0, 2, 5, 10, 20$, and 40 respectively.

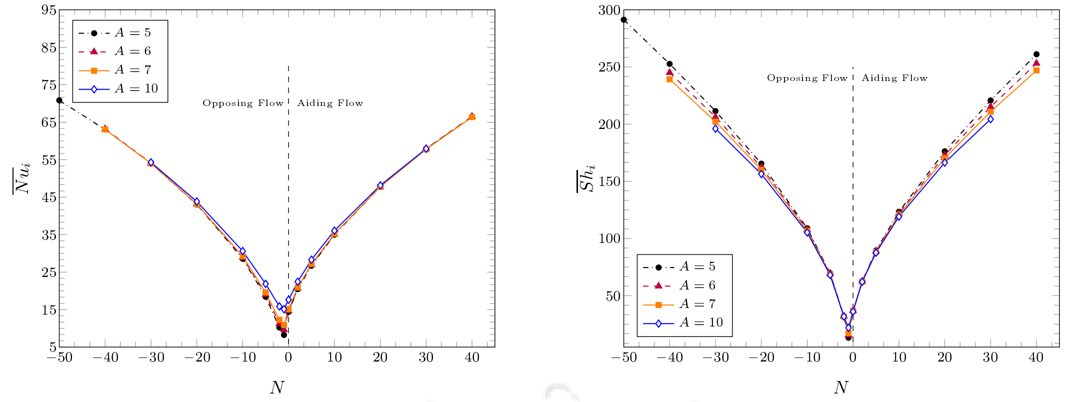

(a) (b)

Figure 4.20: Variation of (a) $\overline{Nu_i}$ and (b) $\overline{Sh_i}$ with buoyancy ratio N for different values of A ($Ra = 500$, $Le = 5$, $\kappa = 2$).

4.7.5 Influence of Thermal Rayleigh Number

Here, the influence of thermal Rayleigh number (Ra) is studied by varying it in the range $20 \leq Ra \leq 2000$ and keeping the other parameters fixed at $A = 5$, $\kappa = 2$, $Le = 10$, and $N = -2$.

Figures 4.21, 4.22, and Figure 4.23 show the the steady state isotherms, isoconcentrates and streamlines respectively. Due to the particular values of Le and N chosen, for $Ra > 20$ a counterclockwise rotating solute-driven vortex is sandwiched between two thermal-driven clockwise rotating vortices (4.23(b)-(h)). As the Ra increases, the strength and size of the top and bottom vortices increase. Consequently, the center of the top vortex moves downwards, and the center of the bottom vortex moves upwards. Similarly, the core solute-driven vortex increases in intensity but not in size. Also its center shifts a little upwards with increasing Ra. The strength of the vortices at their centers as well as their coordinates are tabulated in table 4.2. That convective HMT increases with Ra is clear from the isotherms and isoconcentrates shown in figures 4.21 and 4.22, as well from the variation of $\overline{Nu_i}$ and $\overline{Sh_i}$ shown in figure 4.24. Fig. 4.24 also shows the variation of $\overline{Nu_i}$ and $\overline{Sh_i}$ w.r.t Ra for different values of N and $\kappa = 2$. Not only does convective HMT increase with increasing Ra, it also increases with N, which is consistent with our observation in section 4.7.4. Fig. 4.25 shows the variation of $\overline{Nu_i}$ and $\overline{Sh_i}$ w.r.t Ra for different values of N and $\kappa = 5$, which reinforces the observations in section 4.7.2 that convective HMT increases with radius ratio (κ).

Table 4.2: ψ_{mid} values and their locations for $A = 5, , \kappa = 2, Le = 10, N = -2$ and various values of Ra.

Ra	ψ_{mid} (r, z)		
	Solutal	Thermal	
		Top Right	Bottom Left
20	-0.138116 (0.30638,0.34902)	8.48164×10^{-4} (0.384125,0.983748)	1.05474×10^{-4} (0.205868,0.0064156)
50	-0.309042 (0.30957,0.31645)	0.022518 (0.358164,0.953528)	0.0033866 (0.220503,0.0183579)
100	-0.506729 (0.30957,0.306053)	0.11497 (0.34271,0.93357)	0.01385 (0.22893,0.02484)
200	-0.76590 (0.31275,0.29197)	0.37326 (0.33707,0.91509)	0.041216 (0.23950,0.02843)
500	-1.2330 (0.33707,0.24631)	1.05046 (0.33122,0.88753)	0.140566 (0.25728,0.03211)
1000	-1.7243 (0.35328,0.22366)	1.87439 (0.32823,0.87380)	0.29234 (0.28097,0.033985)
1500	-2.08177 (0.36433,0.21330)	2.50403 (0.32561,0.86889)	0.42191 (0.29027,0.03524)
2000	-2.38457 (0.36706,0.20681)	3.01205 (0.32520,0.86658)	0.50406 (0.30957,0.03118)

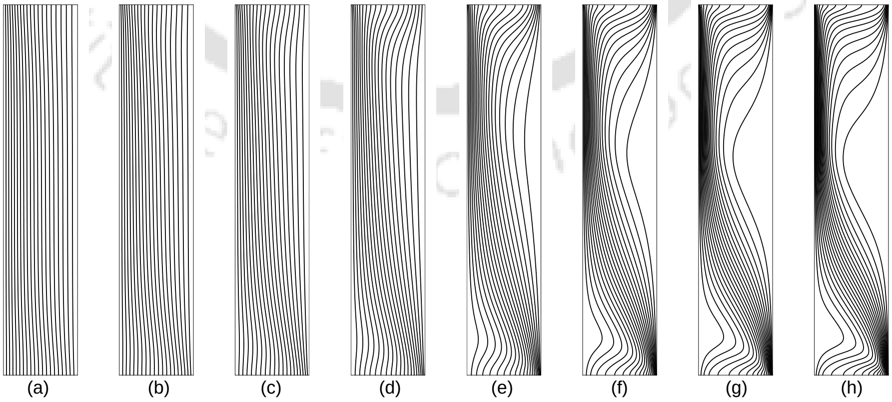
(a) (b) (c) (d) (e) (f) (g) (h)

Figure 4.21: Isotherms for $A = 5$, $Le = 10$, $\kappa = 2$, $N = -2$, and various values of $Ra = 20, 50, 100, 200, 500, 1000, 1500,$ and 2000 (from left to right in that order).

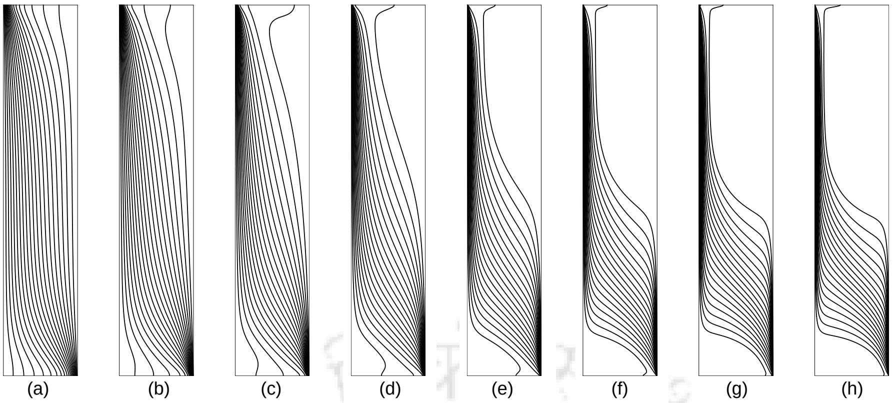

Figure 4.22: Isoconcentrates for $A = 5$, $Le = 10$, $\kappa = 2$, $N = -2$, and various values of $Ra = 20, 50, 100, 200, 500, 1000, 1500,$ and 2000 (from left to right in that order).

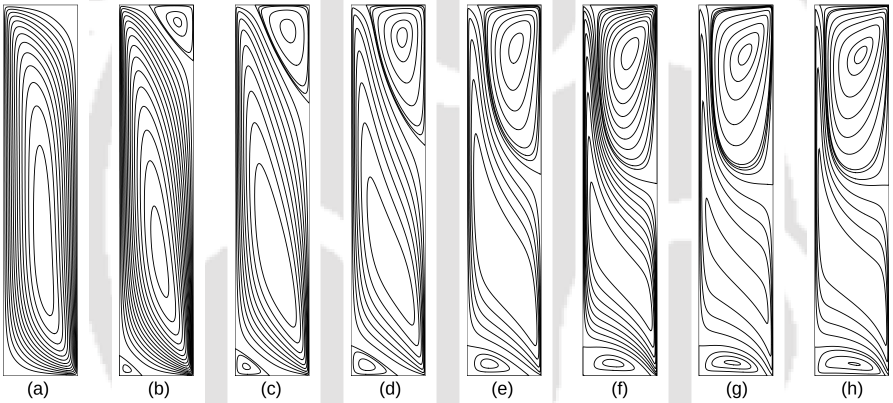

Figure 4.23: Streamlines contours for $A = 5$, $Le = 10$, $\kappa = 2$, $N = -2$, and various values of $Ra = 20, 50, 100, 200, 500, 1000, 1500,$ and 2000 (from left to right in that order).

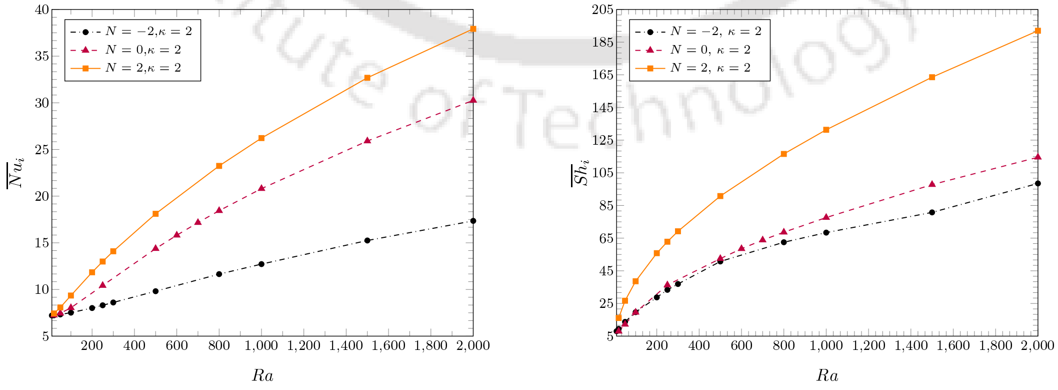

(a) (b)

Figure 4.24: Variation of (a) $\overline{Nu_i}$ and (b) $\overline{Sh_i}$ with Rayleigh number Ra for different values of N, and $A = 5$, $Le = 10$, $\kappa = 2$.

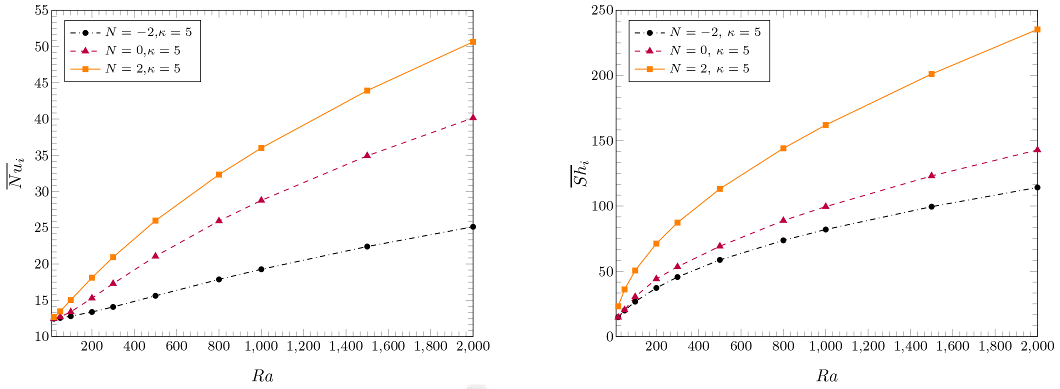

(a) (b)

Figure 4.25: Variation of (a) $\overline{Nu_i}$ and (b) $\overline{Sh_i}$ with Rayleigh number Ra for different values of N, and $A = 5$, $Le = 10$, $\kappa = 5$.

4.8 Conclusions

In this chapter we have numerically investigated the problem of double diffusive natural convection in a vertical porous annulus by applying a reconstructed compact HOC scheme on nonuniform grids. In the process, we also proposed a novel approach to explicitly calculate the velocities. Using the Darcy model, the influence of aspect ratio (A), radius ratio (κ), Lewis number (Le), buoyancy ratio (N), and thermal Rayleigh number (Ra) on the flow were studied. Note that for the range of parameters for which numerical results are available, our simulations are extremely close both in terms of contour plots and the values of Nusselt and Sherwood numbers. While earlier studies concentrated on the description of the steady-state flow, for a certain range of parameters we have reported the transient flow as well. Extensive simulations for various parameters were carried out to discern a clearer picture of heat and mass transfer characteristics. We found that aspect ratio has little influence on the heat and mass transfer rates, whereas radius ratio plays a greater role in enhancing the heat and mass transfer rates. While studying the influence of radius ratio (κ), we showed the time evolution of the flow for $N = -2$. Influence of Lewis number was studied for the range $1 \leq Le \leq 200$, and we found that while Sherwood number increases with Le, Nusselt number decreases with Le. Influence of buoyancy ratio was studied in the range $-40 \leq N \leq 40$. Flow description was provided for a particular configuration of $A = 5$, $\kappa = 2$, $Ra = 500$, and $Le = 10$. While studying the heat and mass transfer characteristics, we found that heat and mass transfer rates are greater for a positive value of N than the corresponding negative value. Finally, we studied the influence of thermal Rayleigh number by varying it in the range $10 \leq Ra \leq 2000$. Flow details was provided for a particular configuration viz. $A = 5$, $N = -2$, $\kappa = 2$, and $Le = 10$. We demonstrated that flow strength increased with Ra by tabulating the strength of the vortices formed. From the plots of Nusselt and Sherwood numbers, we also showed that convective heat and mass transfer rates increase with Ra not only for $N = -2$, but for other values of N as well.

CHAPTER 5

CONJUGATE HEAT TRANSFER IN SUDDENLY EXPANDING FLOW

5.1 Introduction

Conjugate heat transfer (CHT) refers to the phenomenon of heat transfer which occurs as a result of the coupled thermal dynamics in the fluid regime and a solid of finite thickness. This phenomenon is significant in numerous engineering and scientific applications, chief among them are cooling of turbine blades [107], electronic equipments [49], heat exchangers [151], and chemical and nuclear reactors [70]. Thus, over the years numerous analytical, numerical, and experimental studies in the field of CHT have taken place.

The term 'conjugate heat transfer' was first introduced by Perelman [124], who solved heat conduction equations in common with a heat generating body surrounded by a flowing fluid, and provided asymptotic solutions of integral equations for two different cases. Many studies of CHT since then have focused on the case of 2D laminar flow over a flat plate [33,57,65,73,85,87,88,100,104,106,114,125,162,163]. Chiu et.al. [34] carried out a detailed numerical and experimental study of CHT in horizontal channels with a heated section. They demonstrated that different materials of the channel walls had remarkably different effects on the heat transfer characteristics, thus emphasizing the need for proper treatment of conjugate effects while designing channel walls. Jilani et.al. [68] used a finite difference scheme to numerically investigate the effect of various conduction-convection, heat generating parameters and length to diameter ratio for a fluid of Prandtl number 0.005 on steady state CHT for a vertical cylinder. Juncu [71] numerically investigated unsteady CHT for a circular cylinder at low Reynolds numbers ($Re = 2, 20$). He [72] also presented a numerical study of steady state CHT from a circular cylinder with a heat source embedded at the center of the cylinder. Li et. al. [102] presented an experimental quantification of the effects of boundary conditions, both conjugate as well as convective, on heat transfer characteristics for the case of pin fin channel in trailing edge of gas turbine blade. Significant work has been done for CHT involving jet flows, for instance the works of Kanna and Das [126], Mondal et.al. [113], and Paulraj et.al. [123]. In recent years, the lattice Boltzmann method (LBM) has also been applied to problems of CHT, most notably by Seddiq et.al. [138], Pareschi et.al. [121], Patel et.al. [122] etc.

Sudden expansion flows are encountered in many industrial applications such as ejector systems [14], gas turbine combustors [50, 133], heat exchangers, and cooling of electronic equipments [134]. The fundamental nature of the flow physics encountered in the process of flow separation and reattachment makes it an invaluable topic of research. The addition of CHT introduces another layer of computational complexity to relatively simple geometries. In this chapter, we consider two commonly encountered geometries in suddenly expanding flows viz. flow over a backward facing step (BFS), and suddenly expanding flow in a symmetric channel with large expansion ratios.

Kanna and Das [127] first proposed the CHT case for BFS flow as a benchmark problem. They employed an alternate direction implicit (ADI) method in order to obtain steady state results via streamfunction-vorticity (ψ-ω) form of the N-S equations. Their numerical study was focused on investigating the effect of Re, Pr, k, and slab thickness on the heat transfer characteristics. However, subsequent investigations of the same problem by Teruel and Fogliatto [153], and Ramšak [128] revealed discrepancies with the results presented by Kanna and Das [127]. Ramšak [128] remarked that "Professor Kanna has confirmed in personal communication that their results published are probably wrong." The numerical study by Ramšak [128] was also based on the ψ-ω formulation and the solution was obtained using the multidomain Boundary element method. However, both the studies are limited to a single set of parameters. There is a need for an investigation into the influence of all the parameters on the heat transfer characteristics, which we have endeavored to accomplish in this work.

On the other hand, much work has been done in the case of flow in a suddenly expanding symmetric channel. The experimental investigations conducted by Durst et.al. [42], Cherdron et.al. [31], Fearn et.al. [48] demonstrated that the two-dimensional steady state flow phenomena in a suddenly expanding channel at low Reynolds numbers (Re) contains two symmetric recirculation zones equal in size, and the recirculation length increases linearly with Re. These steady symmetric states exist only up to a critical Reynolds number (Re_c). For $Re > Re_c$, the flow, while remaining steady, loses its symmetry and evolves into an asymmetric state with two separation zones of different lengths attached to either walls of the channel. Subsequent numerical investigations of Durst et.al. [43], Alleborn et.al. [4], Battaglia et.al. [17], and Drikakis [41] have also confirmed these experimental findings. At higher Re's the flow becomes time dependent as three-dimensional effects set in [43]. Rusak and Hawa carried out a weakly non-linear analysis of the symmetry breaking pitchfork bifurcation [136]. Hawa and Rusak investigated the effect of slight asymmetry of the channel in flow phenomena [58], and carried out a numerical investigation to study the interaction between effects of viscous dissipation and convection perturbations on the flow stability [59]. Revuelta et.al. [133] investigated the flow of round laminar jets with coaxial confinement when both the jet Re and the expansion ratio are large. Revuelta [132] presented a numerical study of 2D laminar flow of an incompressible viscous jet through a channel with large expansion ratios. It was shown that when the jet Re is sufficiently large, the structure and scale of the resulting flow as well as the critical conditions for asymmetric solutions to appear are determined by the momentum exchange between the incoming jet and the recirculating fluid. This flow behavior in a suddenly expanding channel with large expansion ratio thus presents an opportunity of studying the phenomenon of conjugate heat transfer.

From the preceding literature review, one can distinctly identify the gap in the study of conjugate heat transfer in suddenly expanding flow. Firstly, the results provided by Kanna and Das [127] for the benchmark problem of CHT in BFS flow was found to be erroneous [128]. However, the subsequent study by Ramšak [128] failed to address the physics behind the flow and heat transfer phenomena considering all the parameters involved in the benchmark problem. Additionally, benchmark result was established for one set of parameters only. Secondly, to the best of our knowledge, CHT in a suddenly expanding symmetric channel at low Re's has not been studied in detail previously. In this chapter, we first consider the problem of CHT in BFS flow and explore the physics behind the flow and heat transfer phenomena, in addition to establishing new benchmark results. Next, we study the phenomenon of CHT in a suddenly expanding symmetric channel at low Re's and large expansion ratios. The break in flow symmetry in a suddenly expanding channel is a particularly unique phenomenon, and interesting results are arrived while studying the phenomena of conjugate heat transfer. This chapter is organized as follows: In section 5.2 we simulate CHT in BFS flow. Sections 5.2.2 and 5.2.3 describe in brief the computational grid, and the algorithm for the solution of system of equations respectively. In section 5.2.4 code validation is carried out by comparing the present results with established results in the literature, and section 5.2.5 deals with grid independence of the computed data. The results and discussion for CHT in BFS flow case are presented in section 5.2.6. Next, in section 5.3 we simulate CHT in a suddenly expanding symmetric channel with large expansion ratios. This section follows a similar structure to section 5.2. Finally, in section 5.4 we present our conclusions for this chapter.

5.2 Conjugate heat transfer in backward facing step flow

Consider the flow of a fluid with Prandtl number Pr over a BFS in a channel, which rests over a slab of thickness b (Fig. 5.1). The height of the channel is H, and the step length is $h = H/2$. The downstream length of the channel is taken as 30 times the channel height ($30H$) so that the flow becomes fully developed. At the inlet, we assume a parabolic velocity profile of u, and the streamfunction ψ at inlet is evaluated based on u at inlet. The temperature of the fluid at inlet is uniform. At the outlet, $\dfrac{\partial u}{\partial x} = \dfrac{\partial u}{\partial x} = 0$ (fully developed flow), $\dfrac{\partial \theta}{\partial x} = 0$ (adiabatic boundary condition for temperature). The bottom of the slab is at uniform constant temperature and $\dfrac{\partial \theta}{\partial y} = 0$ for the top wall of the channel (adiabatic). [1]

---

[1] Part of this study has been published in [46]

The steady state non-dimensional governing equation for incompressible laminar flow in streamfunction-velocity form is given as [94]

$$\frac{\partial^4\psi}{\partial x^4}+2\frac{\partial^4\psi}{\partial x^2\partial y^2}+\frac{\partial^4\psi}{\partial y^4}=Re\Big[u\Big(\frac{\partial^3\psi}{\partial x^3}+\frac{\partial^3\psi}{\partial x\partial y^2}\Big)+v\Big(\frac{\partial^3\psi}{\partial x^2\partial y}+\frac{\partial^3\psi}{\partial y^3}\Big)\Big] \tag{5.1}$$

where, $u=\frac{\partial\psi}{\partial y}$, $v=-\frac{\partial\psi}{\partial x}$, and $Re=\frac{U_0H}{\nu}$ is the Reynolds number, and ν is the fluid's kinematic viscosity.

The non-dimensional steady state energy equation in the fluid region is

$$u\frac{\partial\theta_f}{\partial x}+v\frac{\partial\theta_f}{\partial y}=\frac{1}{Re\,Pr}\Big(\frac{\partial^2\theta_f}{\partial x^2}+\frac{\partial^2\theta_f}{\partial y^2}\Big) \tag{5.2}$$

where $Pr=\frac{\nu}{\alpha}$, with α denoting the fluid's thermal diffusivity.

The non-dimensional steady state energy equation in the solid region is given by

$$\frac{\partial^2\theta_s}{\partial x^2}+\frac{\partial^2\theta_s}{\partial y^2}=0 \tag{5.3}$$

Here, the subscripts f and s are used denote the fluid and solid regions respectively.

The non-dimensional quantities are as follows

$$x^*=\frac{x}{H}, y^*=\frac{y}{H},\ u^*=\frac{u}{U_0},\ \theta=\frac{T-T_0}{T_W-T_0} \tag{5.4}$$

where U_0 is the flow velocity at inlet, T_0 is the fluid's temperature at the inlet, and T_W is the temperature of the bottom wall of the slab ($T_W>T_0$). The asterisks have been dropped in equations (5.1) - (5.3) for convenience.

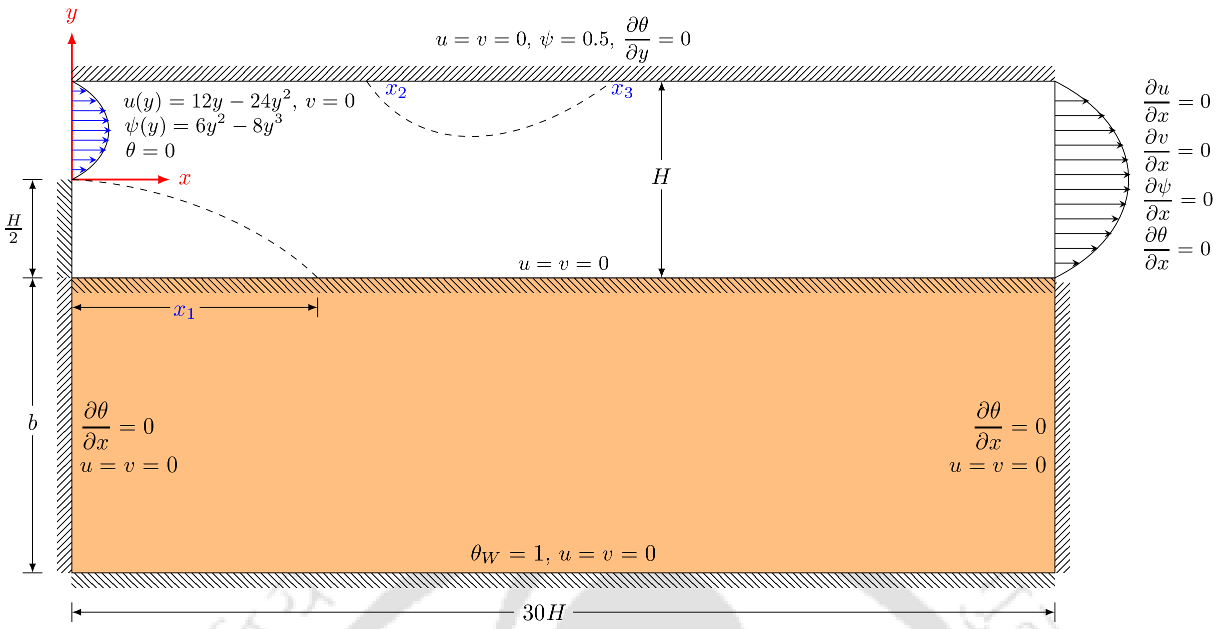

Figure 5.1: Schematic and boundary conditions for conjugate heat transfer on BFS.

At the fluid-solid interface, the continuity in temperatures and heat fluxes are ensured by the following equations

$$\theta_f = \theta_s \tag{5.5}$$

$$k_f\left(\frac{\partial\theta_f}{\partial n}\right)_{wall} = k_s\left(\frac{\partial\theta_s}{\partial n}\right)_{wall} \tag{5.6}$$

where k_f is the thermal conductivity of the fluid, and k_s is the thermal conductivity of the solid.

The local Nusselt number along the fluid-solid interface is given by

$$Nu(x) = -\left.\frac{\partial\theta}{\partial y}\right|_{wall} \tag{5.7}$$

The average Nusselt number is given by

$$\overline{Nu} = \frac{1}{L}\int_0^L Nu(x)dx \tag{5.8}$$

where L is the interface length.

5.2.1 Numerical scheme

The numerical approach used here follows the work described in chapter 3, where steady state natural convection around embedded heated bodies in a square enclosure was investigated using the streamfunction velocity formulation on compact non-uniform Cartesian grids (Fig. 2.1). Equation (5.1) is discretized using the scheme of Kumar and Kalita [94], which is described briefly in section 2.3 of chapter 2. To discretize equations (5.2) and (5.3), we use the HOC scheme of Kalita et.al. [80], which has been briefly described in section 2.2 of chapter 2. Equation (5.2) is discretized with $c = uRePr$, $d = vRePr$, and $f = 0$. Similarly, equation (5.3) is discretized with $c = d = f = 0$.

5.2.2 Grid generation

Previous studies [13,47,51] have shown that a relatively higher number of grid points are required for flow resolution near the step and near the walls. To this end, we use the following stretching functions [81]

$$x_i = \frac{i}{i_{max}} - \frac{\mu_1}{\pi}\sin\left(\frac{\pi i}{i_{max}}\right) \quad 0 \leq \mu_1 < 1 \quad \text{in the } x\text{-direction} \tag{5.9}$$

$$y_j = \frac{j}{j_{max}} - \frac{\mu_2}{2\pi}\sin\left(\frac{2\pi j}{j_{max}}\right) \quad 0 \leq \mu_2 < 1 \quad \text{in the } y\text{-direction} \tag{5.10}$$

where μ_1 is the clustering parameter in the $x-$ direction, and μ_2 the clustering parameter in $y-$ direction; larger the value of μ_i, greater is the intensity of clustering. Here, equation (5.9) is used to gradually increase the density of grid points towards left, and equation (5.10) to generate grid points in a centro-symmetric manner which are clustered near top and bottom walls, and near the interface. Figure 5.2(a) shows a sample grid of size 301 × 201 with $\mu_1 = 0.99$ and $\mu_2 = 0.7$. The magnified view of the grid within the circle is shown in 5.2(b).

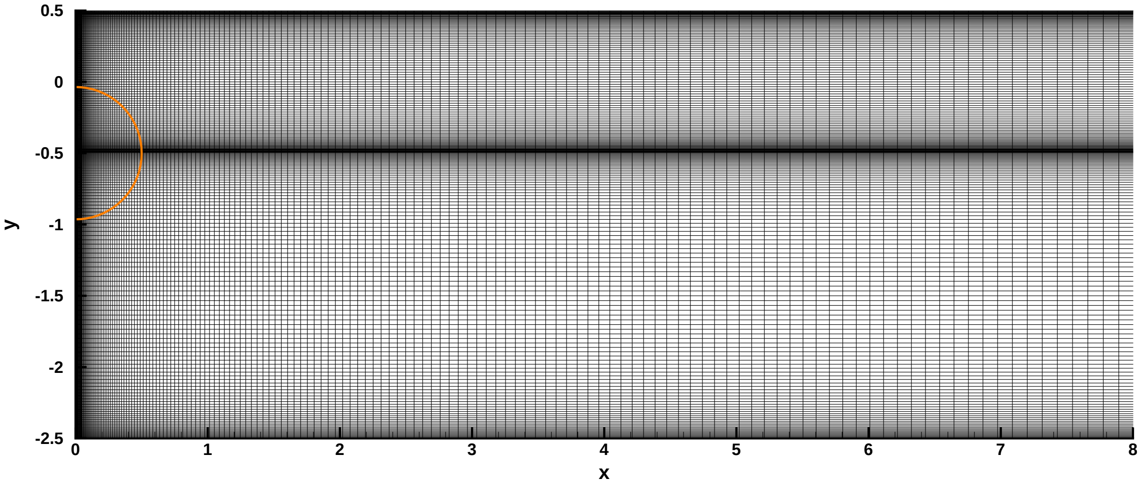

(a) Grid used with $\mu_1 = 0.99$ and $\mu_2 = 0.7$.

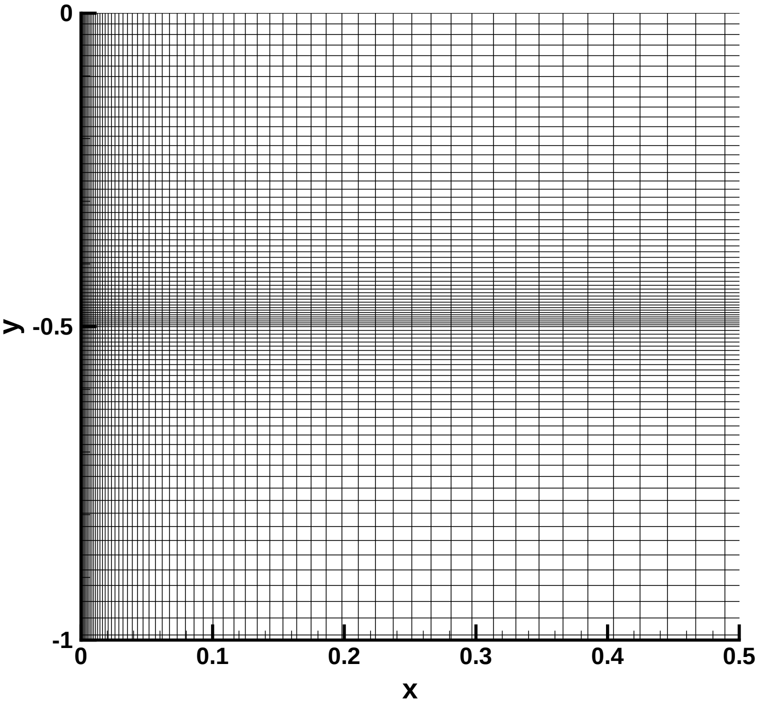

(b) Magnified part of the grid.

Figure 5.2: Mesh distribution.

5.2.3 Solution of system of equations

After discretizing the equations (5.1), (5.2), and (5.3) by applying the schemes (2.30) and (2.21), equations (5.1) - (5.3) reduce to the matrix form as

$$A_1\boldsymbol{\psi} = \boldsymbol{f(Re, Pr, u, v)} \tag{5.11}$$

$$A_2\boldsymbol{\theta} = \boldsymbol{b} \tag{5.12}$$

In (5.11), (5.12) the coefficient matrices A_1, A_2 are nona-diagonal sparse matrices where each row contains a maximum of nine non-zero values sitting on those diagonals. For a rectangular grid having p points in the x- and q points in the y- direction, the coefficient matrices A_1, A_2 are of size p^2q^2. The non-uniformity of the grid render asymmetry to A_1, and A_2.

Computing the solutions of problems governed by equations (5.1), (5.2), and (5.3) involves an outer-inner iteration procedure. This computational algorithm is outlined below:

1. Initialize u, v, ψ, and θ and apply the relevant boundary conditions.

2. Solve (5.11) for ψ.

3. Compute u and v using Thomas algorithm [10, 45, 94].

4. Use (5.12) to compute θ.

   The above steps comprises an outer iteration.

5. Once the values of u, v, ψ and θ are updated, compute ψ again using (5.11) .

6. Repeat the process till the maximum value of ψ-error $(= \psi_{current} - \psi_{previous}) < 0.5 \times 10^{-8}$, solution reaches steady state; stop computation.

The inner iterations consists of solving the matrix equations (5.11)-(5.12) at each outer iteration by iterative solvers. The biconjugate gradient stabilized method (BiCGStab) [143] is used with preconditioning, where the preconditioner used is Incomplete LU decomposition. Preconditioning was found to be extremely effective in tackling flow with high *Re*'s where the Lis library [105] was utilized. The inner iterations were stopped when the the l_2 norm of the residuals from (5.11)-(5.12) fell below 0.5×10^{-9}, i.e., $\|\boldsymbol{f} - A_1\boldsymbol{\psi}\|_2$ & $\|\boldsymbol{f} - A_2\boldsymbol{\theta}\|_2 < 0.5 \times 10^{-9}$. A relaxation parameter λ was used for the inner as well as the outer iteration cycle. Progressively decreasing values of λ were used for increasing values of *Re*. All of our computations were carried out on an Intel core i7 based PC with 16 GB RAM.

5.2.4 Code validation

Two cases are considered in this section for validating the code. Firstly, only the flow over BFS is considered (without the CHT), and results from the present computation are compared against well established results in the literature. In table 5.1 data is presented for the first vortex in the the lower wall for $100 \leq Re \leq 800$ and in table 5.2, the data for the upper wall eddy for $500 \leq Re \leq 800$ is presented. In both the tables, present data is compared with established numerical results and close matches are obtained in all the cases. In figure 5.3, the reattachment length of the primary recirculation region at the step in the Reynolds number range $1 \leq Re \leq 800$ is compared with the experimental results of Armaly et al. [13] and the numerical results of Kim and Moin [90], and Biswas et al. [23]. Note that while the works of Armaly et al. [13], and Biswas et al. [23] used an expansion ratio 1.9428 for the step, for the present work an expansion ratio of 2 has been used. Here also, the results are extremely close to the numerical ones and closer to the experimental results than the other two. The deviation of the numerical results from the experimental ones for $Re > 600$ is attributed to the development of three-dimensionality in the flow for that range. However, the flow still remains steady for $Re \leq 800$ as confirmed by the studies of Biswas et.al. [23], Williams and Baker [165], and Chiang and Sheu [32]. Secondly, the CHT case is considered and computed data is compared with the results presented by Ramšak [128]. The parameters chosen are $Re = 800$, $1 \leq k \leq 1000$, $Pr = 0.71$, and $b = 4h$. As seen from table 5.3 which compares the average Nusselt number $\overline{Nu}$, and figures 5.4 (a) and (b) which compares the plot of temperature along the fluid-solid interface, and local Nusselt number along the interface respectively, the data resulting from the present computation are found to have excellent agreement with the results of Ramšak [128].

Table 5.1: Properties of the lower wall eddy from $Re = 100$ to $Re = 800$.

Re	Eddy Center (x, y)	ψ	Recirculation length
100	(0.5835, −0.1963)	−0.02992	1.623099
200	(0.9756, −0.1963) (0.938, −0.188) [56]	−0.0330 −0.03276 [56]	2.69469 2.633 [56]
300	(1.385, −0.1963) (1.132, −0.188) [56]	−0.0337 −0.03341 [56]	3.60356 3.510 [56] 3.390 [16]
400	(1.750, −0.1963) (1.705, −0.188) [56]	−0.0339 −0.03364 [56]	4.35846 4.239 [56] 4.32 [149]
500	(2.1688, −0.1963)	−0.0340	4.95186 5.16 [16]
600	(2.6947, −0.2112) (2.438, −0.188) [56] (3.350, −0.200) [51]	−0.0341 −0.03375 [56]	5.42004 5.319 [56] 5.495 [16] 5.50 [149]
700	(3.101, −0.2112)	−0.0341 −0.0342 [51]	5.8251 6.5 [53]
800	(3.4742, −0.211) (3.500, −0.219) [56]	−0.0341 −0.03381 [56]	6.15698 6.000 [56] 6.22 [149] 6.10 [51] 5.75 [90] 5.75 [147]

Table 5.2: Properties of the upper wall eddy from $Re = 500$ to $Re = 800$.

Re	Eddy Center (x, y)	ψ	Separation point x_2	Reattachment point x_3
500	(5.499,0.421)	0.5006	4.14	6.844
	(5.438,0.406) [56]	0.5005 [56]	4.309 [56]	6.555 [56]
600	(6.241,0.371)	0.5023	4.358	8.109
	(6.170,0.375) [56]	0.5023 [56]	4.505 [56]	7.908 [56]
			4.13 [16]	7.83 [16]
700	(6.844,0.340)	0.5044	4.577	9.341
	(6.867,0.342) [56]	0.5043 [56]	4.717 [56]	9.127 [56]
800	(7.467,0.318)	0.5064	4.800	10.512
	(7.400,0.300) [51]	0.5064 [51]	4.85 [51]	10.48 [51]
	(7.385,0.313) [56]	0.5066 [56]	4.897 [56]	10.279 [56]
			4.28 [16]	9.28 [16]
			4.70 [147]	9.40 [147]
			5.13 [149]	10.22 [149]

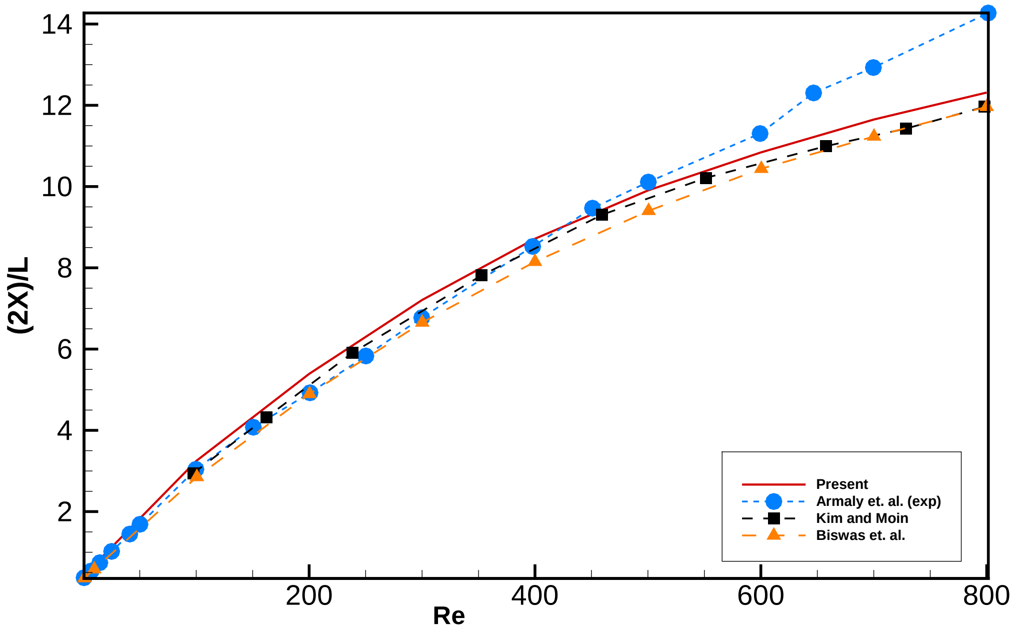

Figure 5.3: The reattachment length as a function of Reynolds number.

Table 5.3: $\overline{Nu}$ (present) compared with the benchmark results of Ramšak [128] ($Re = 800$, $Pr = 0.71$, and $b = 4h$).

	Present	Ramšak [128]	error(%)
$k = 1$	0.425562	0.425	0.132235
$k = 10$	1.79598	1.793	0.166202
$k = 100$	2.609363	2.602	0.282975
$k = 1000$	2.729308	2.722	0.268479

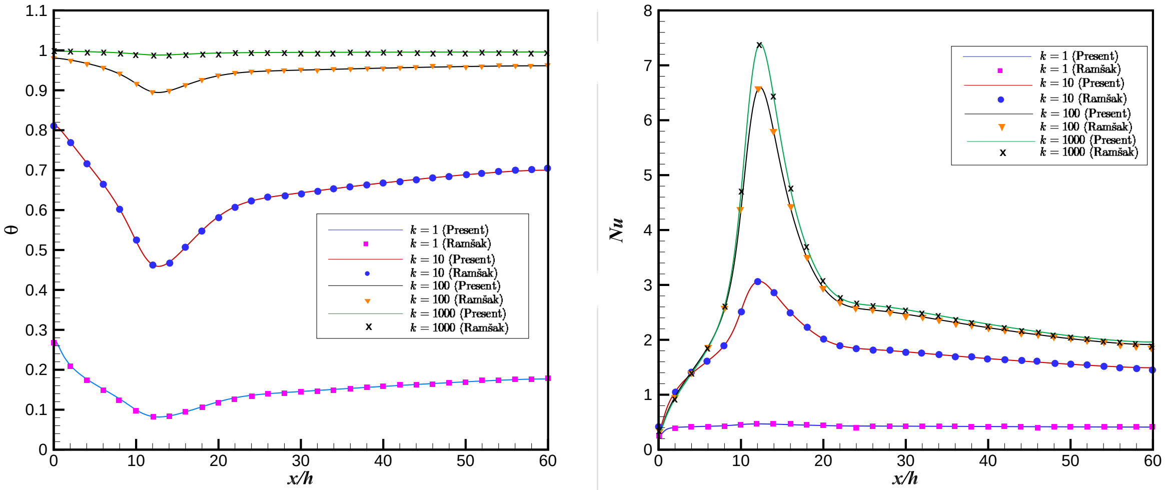

(a) Interface temperature.

(b) Nusselt number.

Figure 5.4: Comparison of present data (interface temperature and Nusselt number) with that of Ramšak [128] ($Re = 800$, $Pr = 0.71$, and $b = 4h$).

5.2.5 Grid Independence

To demonstrate grid independence of the presently computed data, we first plot u vs. y and v vs. y along the vertical line passing through the center of the eddy formed at the lower wall at $Re = 800$ (Fig. 5.5); secondly, we plot the variation of local Nu and temperature along the solid-fluid interface on three different grids viz. 151×101, 301×201, and 451×301 (Fig. 5.6) for the parameters $Re = 800$, $k = 10$, and $b = 4h$. The overlap of the graphs on grids of size 301×201 and 451×301 clearly indicates grid independence of our computed data on grid of size 301×201. As such, all our computations have been carried out on 301×201 grid.

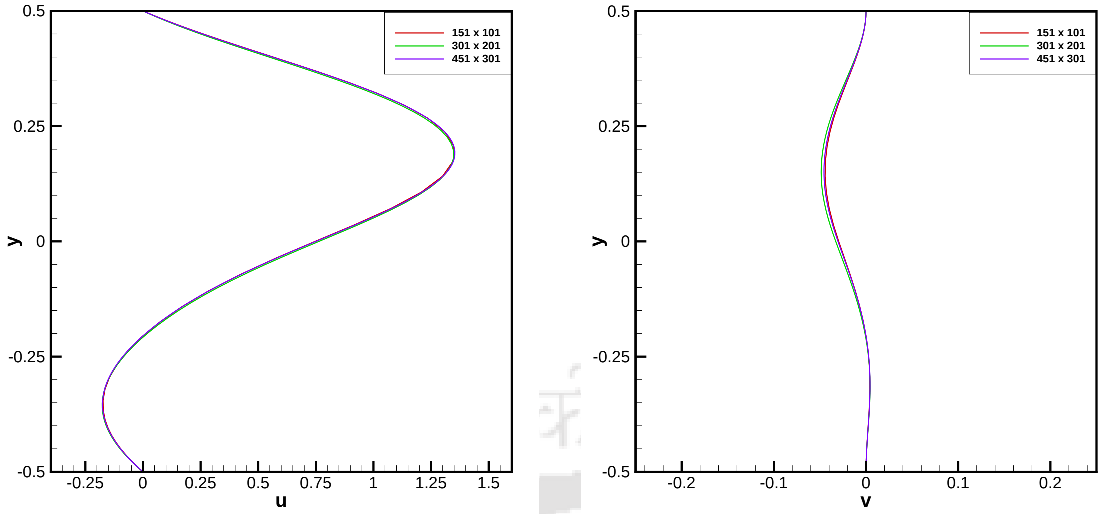

(a) u vs. y (b) v vs. y

Figure 5.5: Grid independence via u and v along the vertical centerline of the lower wall eddy on three different grids for $Re = 800$.

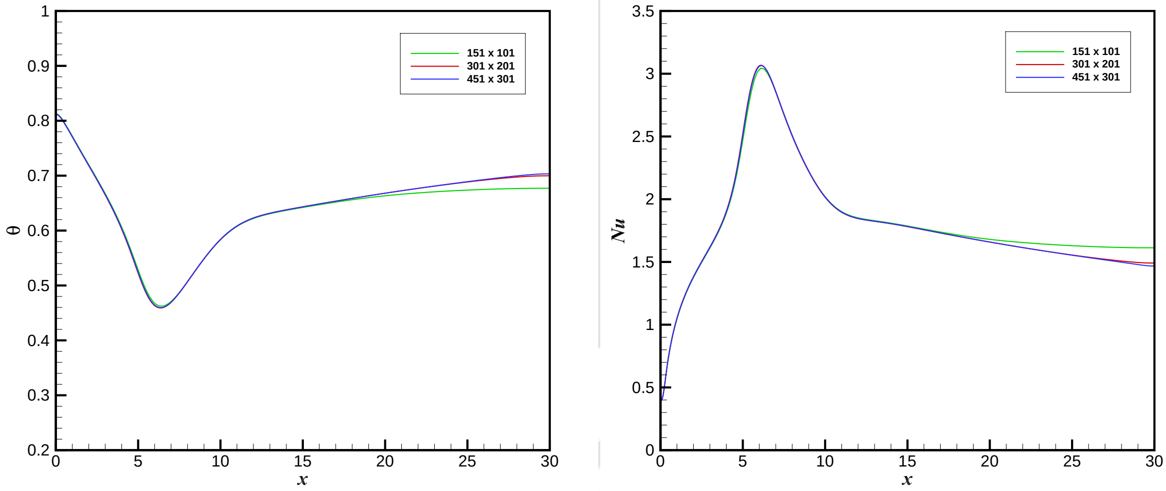

(a) Interface temperature. (b) Nusselt number.

Figure 5.6: Grid independence of computed data on three different grids with $Re = 800$, $k = 10$, $Pr = 0.71$, and $b = 4h$.

5.2.6 Results and discussion

In this section we present the results of our computations which have been carried out on a grid of size 301×201.

Influence of Reynolds number (Re)

In this section, we investigate the influence of Reynolds number, Re, on the heat transfer characteristics. To this end, the Re is varied while keeping the other parameters constant at $k = 10$, and $b = 4h$.

In figure 5.7 we plot the streamlines in the fluid region and show the effect of Re on the flow field. As one can see, with the increase in Re, the recirculation zone formed at the edge of the step grows in size. Another vortex starts forming at the top wall of the channel from $Re = 500$ onwards. The streamlines have been specifically plotted to have a better idea of the heat transfer phenomenon that would be discussed later on. Also, in figure 5.8 the velocity vector plots for different Re's are shown. From these plots the parabolic velocity profile at the inlet and the recirculation zones can be clearly observed along with the development of the vortex at the top wall from $Re = 500$ onwards. One can also see the flow becoming fully developed at the outlet as the parabolic velocity profile suggests thereat; the location from where the flow becomes fully developed moves downstream as Re increases. However, as is obvious from figure 5.8 the channel length $30H$ is enough to facilitate the flow to become fully-developed.

In the fluid region, we observe that the isotherms congregate near the reattachment point, and on moving downstream it spreads in the transverse direction (Fig. 5.9). Note that the reattachment point is nothing but a point on the interface up to which the recirculation zone spreads. This clustering of isotherms shifts downstream as Re increases, primarily because the reattachment location shifts with increasing Re (Figs. 5.9 (b)-(d)). Further, as a vortex also forms on the upper wall at higher Re's, the spread of temperature in the transverse direction is also reduced (Figs. 5.7(c),(d)).

In the solid region we observe that the temperature decreases in the vertical direction due to the cooling effect along the fluid-solid interface, with the lowest value of temperature occurring in the neighborhood of the reattachment point. To probe this phenomenon further, we plot a graph of the non-dimensional temperature, θ vs. y at the reattachment point for the different values of Re (Fig. 5.10). We can see that the temperature varies almost linearly in the slab, and non-linearly in the fluid. As mentioned above, the clustering of the isotherms indicating the formation of a thermal boundary layer is obvious from the figure.

In Figs. 5.11 (a) and 5.11 (b) we plot the variation of temperature and local Nu respectively, along the fluid-solid interface for different Re. The interface temperature decreases to the reattachment point and then rises as one moves downstream. With increase in Re the interface temperature decreases (Fig. 5.11 (a)), which implies that convective heat transfer increases with increasing Re at the interface due to increasing temperature differential. This fact can also be inferred from Fig. 5.11 (b), as Nu increases with increasing Re, as well as from the temperature contour values in the fluid region (Fig. 5.9). Along with these graphs we also show the recirculation regions near the step using exactly the same scale in the x-direction in the inset of the same figure; for a better visualization the scale in the y-direction has been magnified by a factor of four. One interesting observation comes out from figures 5.11(a), 5.11(b) is that the temperature along the interface is minimum at the reattachment point, and the convective heat transfer along the interface is maximum at the reattachment point.

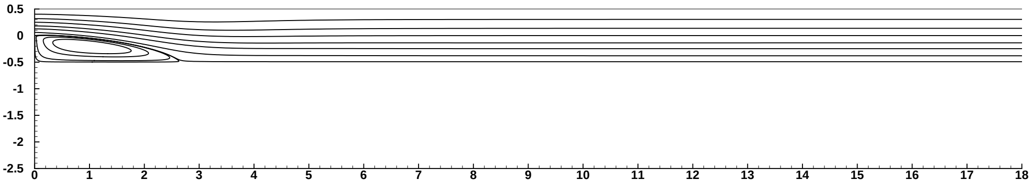

(a) $Re = 200$.

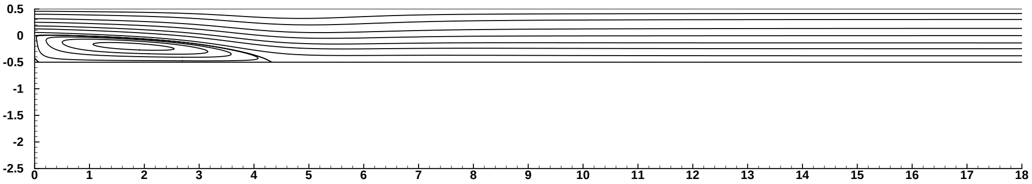

(b) $Re = 400$.

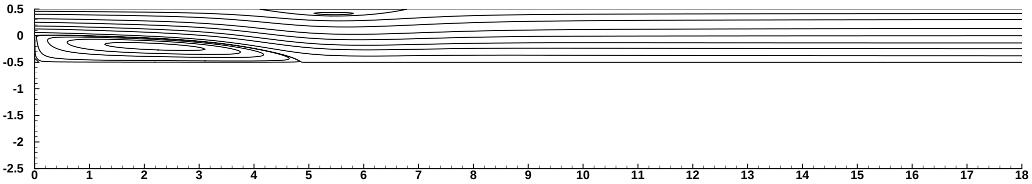

(c) $Re = 500$.

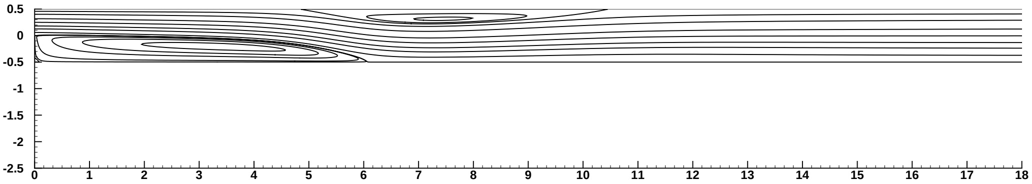

(d) $Re = 800$.

Figure 5.7: Streamlines for different Re with $k = 10$, $Pr = 0.71$ and $b = 4h$.

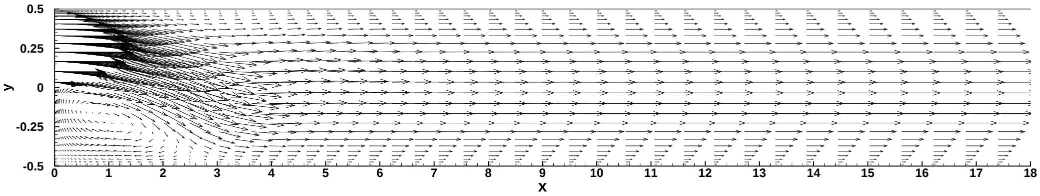

(a) $Re = 200$.

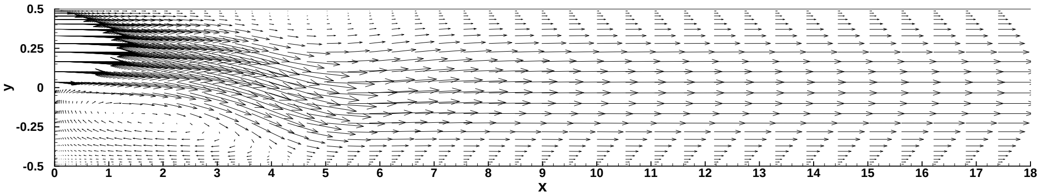

(b) $Re = 400$.

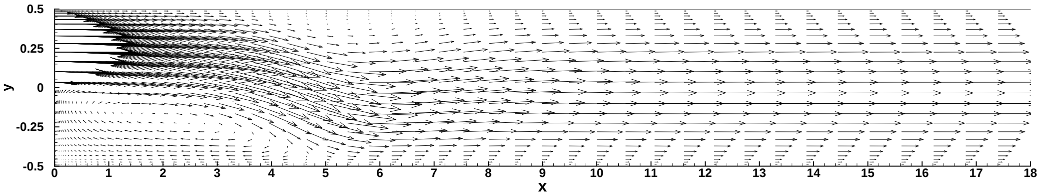

(c) $Re = 500$.

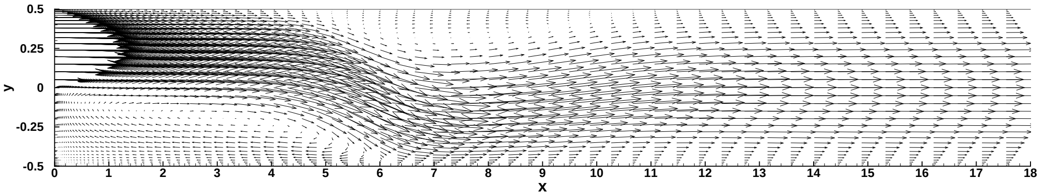

(d) $Re = 800$.

Figure 5.8: Velocity vectors (in magnitude) for different Re.

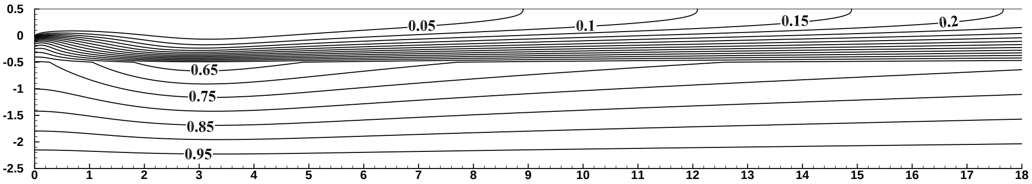

(a) $Re = 200$.

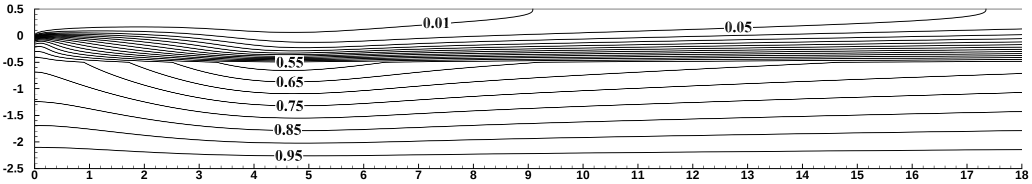

(b) $Re = 400$.

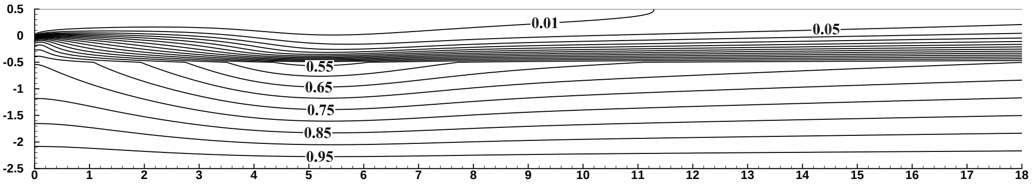

(c) $Re = 500$.

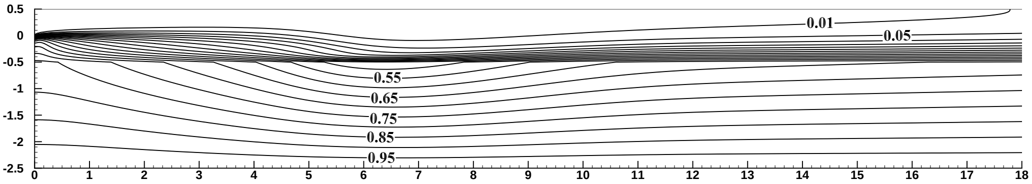

(d) $Re = 800$.

Figure 5.9: Isotherms for different Re with $k = 10$, $Pr = 0.71$ and $b = 4h$.

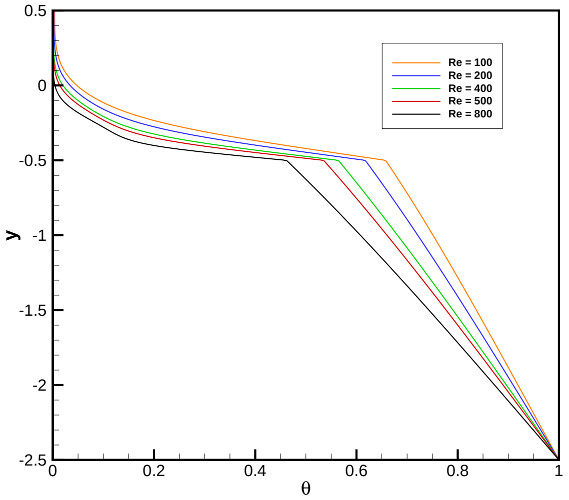

Figure 5.10: T vs y at the reattachment point for different Re.

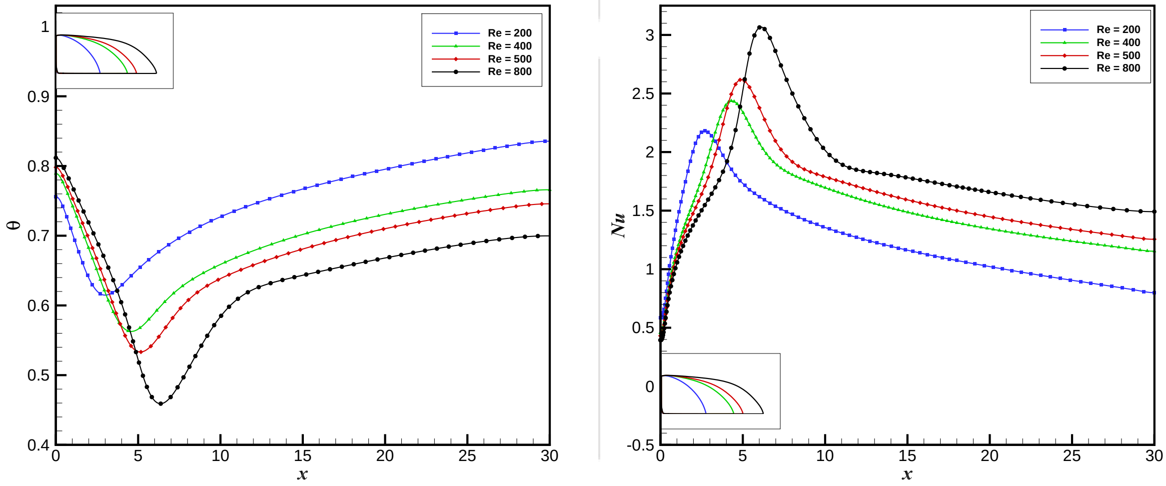

(a) Interface Temperature vs. x.

(b) Nu vs. x

Figure 5.11: Influence of Re on interface temperature and Nusselt number for $k = 10$, $Pr = 0.71$ and $b = 4h$. The recirculation region near the step is shown in the inset with the vertical scale magnified four times for better visualization.

Influence of conductivity ratio (k)

Here we study the influence of conductivity ratio (k) by varying it in the range $1 \leq k \leq 1000$. We also consider two values of Reynolds number ($Re = 200, 600$) while keeping the remaining parameters constant at $Pr = 0.71$ and $b = 4h$.

As seen from Figs. 5.12 and 5.13 the isotherms follow a similar pattern for both

$Re = 200$ and $Re = 600$. For $k = 1$ (Figs. 5.12(a) and 5.13(a)) the isotherms in the fluid region are loosely clustered near the reattachment zone, whereas in the solid region they are linear along the slab. As k increases to 10 (Figs. 5.12(b) and 5.13(b)), the temperature increases in the fluid as well as in the solid region, and the isotherms become clustered strongly in the neighborhood of the reattachment point. For $k > 10$ (Figs. 5.12(c)-(e) and Figs. 5.13(c)-(e)), there is little variation in the isotherms and thermal layer thickness in the fluid region, whereas temperature in the slab increases with k.

Influence of k on the temperature and local Nu along the interface are shown in Figs. 5.14 and 5.15 respectively. As k increases, the temperature along the interface also increases, and the temperature drop near the reattachment point is seen to smoothen out with increase in k. Also, as $k \to \infty$, the non-dimensional interface temperature approaches unity, i.e., the temperature becomes constant throughout the slab. The local Nusselt number varies inversely as the interface temperature, with a peak near the reattachment point. The near overlap of Nusselt number variation for $k = 500$ and $k = 1000$ indicates that there is little variation of Nu with increase in k. As observed in table 5.4, there is only a marginal increase in average Nusselt number $\overline{Nu}$ for $k \geq 100$.

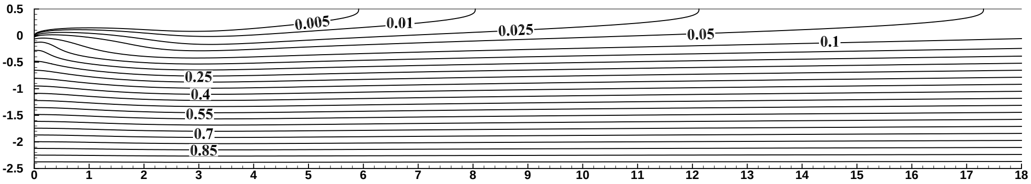

(a) $k = 1$.

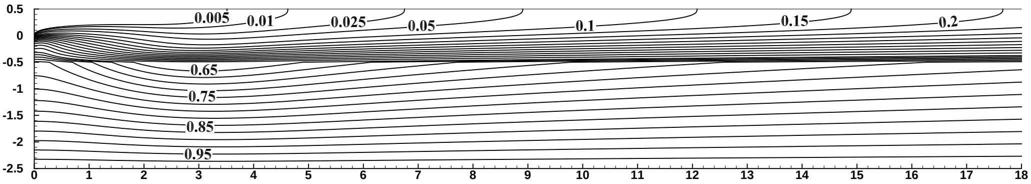

(b) $k = 10$.

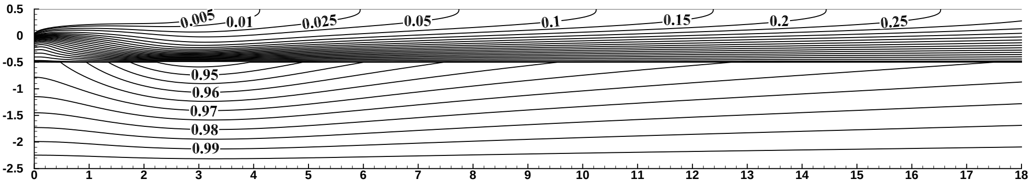

(c) $k = 100$.

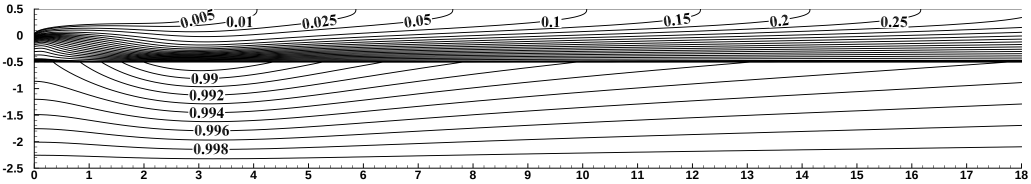

(d) $k = 500$.

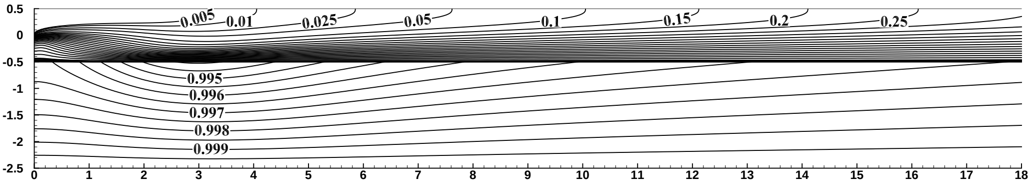

(e) $k = 1000$.

Figure 5.12: Isotherms for different k with $Re = 200$, $Pr = 0.71$ and $b = 4h$.

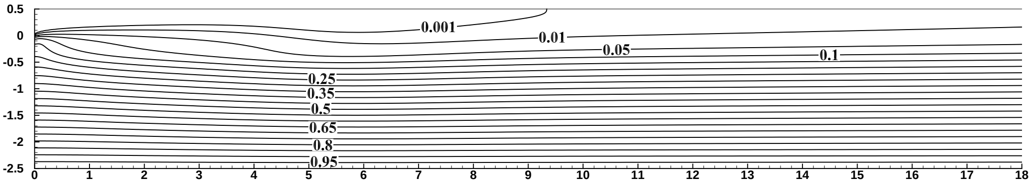

(a) $k = 1$.

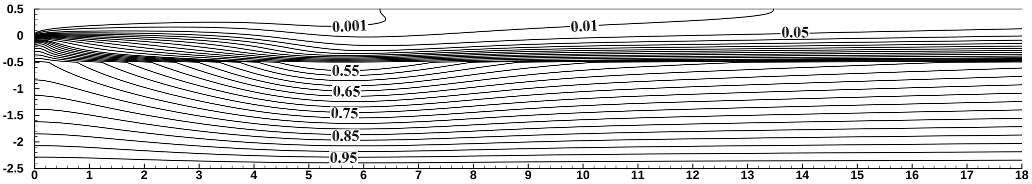

(b) $k = 10$.

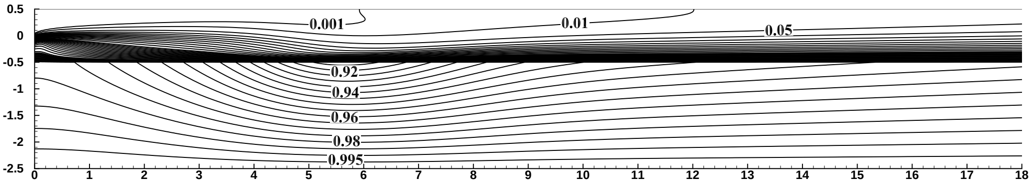

(c) $k = 100$.

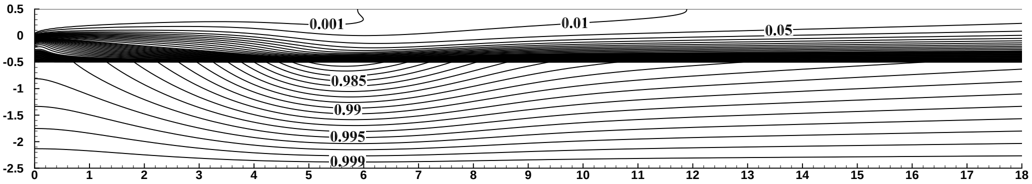

(d) $k = 500$.

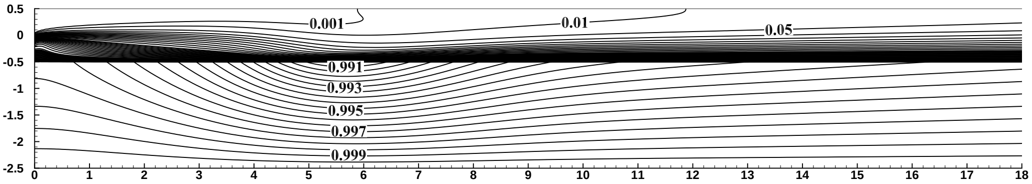

(e) $k = 1000$.

Figure 5.13: Isotherms for different k with $Re = 600$, $Pr = 0.71$ and $b = 4h$.

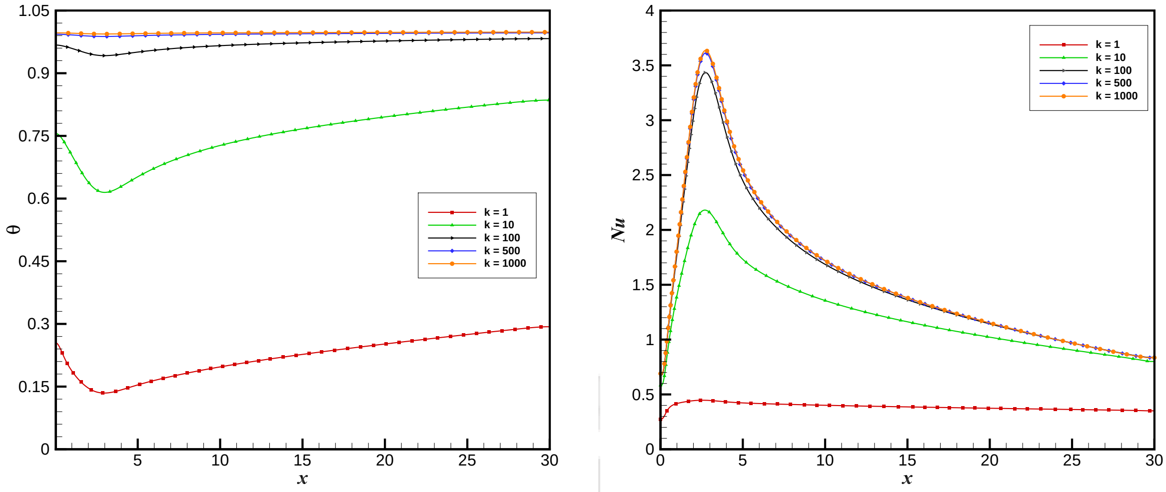

(a) Interface temperature vs. x.

(b) Nu vs. x.

Figure 5.14: Influence of k on interface temperature and Nusselt number for $Re = 200$, $Pr = 0.71$ and $b = 4h$.

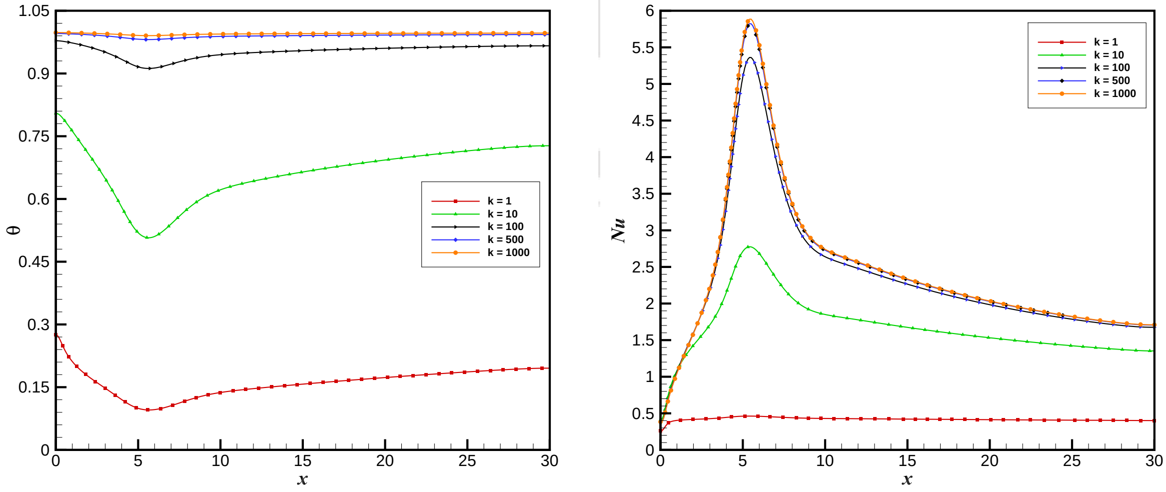

(a) Interface temperature vs. x.

(b) Nu vs. x.

Figure 5.15: Influence of k on interface temperature and Nusselt number for $Re = 600$, $Pr = 0.71$ and $b = 4h$.

Table 5.4: $\overline{Nu}$ for different values of k and $Re = 200$, 600 (with $Pr = 0.71$, and $b = 4h$).

k	Nu	
	$Re = 200$	$Re = 600$
1	0.3885286	0.4194439
10	1.2383312	1.6811163
50	1.5056371	2.2610267
100	1.5453093	2.3599576
500	1.5781064	2.4447293
800	1.5812241	2.4529496
1000	1.5822674	2.4556971

Influence of Prandtl number

Here we explore the influence of Prandtl number (Pr) on the heat transfer characteristics by varying it in the range $0.1 \leq Pr \leq 15$ and keeping the other parameters fixed at $Re = 200$, $k = 10$ and $b = 4h$. Fig. 5.16 shows the isotherms for various values of Pr viz. $Pr = 0.1$, 1, 5, 10 and 15.

When $Pr = 0.1$ (Fig. 5.16 (a)), the isotherms are evenly distributed in the domain and there is an increase in the temperature values in the fluid region as one moves downstream. As Pr increases (Fig. 5.16 (b)-(e)), the isotherms in the fluid region become progressively clustered near the fluid-solid interface; the thickness of the thermal boundary layer decreases indicating an increase in convective heat transfer (Fig. 5.17 (b)). For $Pr \geq 5$ (Fig. 5.16 (c)-(e)), the isotherms in the fluid region become disorderly at the inlet, owing to the dominance of the fluid's momentum diffusivity over its thermal diffusivity.

In the slab there is a slight non-linearity in the isotherms across the slab near the reattachment point for $Pr = 0.1$ (Fig. 5.16 (a)). This non-linearity becomes more pronounced as Pr increases (Fig. 5.16 (c)-(e)). A closer examination of the contour values in the solid region shows that temperature in the slab decreases with increase in Pr.

The temperature and local Nusselt number distribution along the fluid-solid interface are plotted in Fig. 5.14. With the exception of $Pr = 0.1$ (Fig. 5.17 (a)), the interface temperature distribution follows a similar pattern for the rest of the Pr values considered. This exception is due the fact that at $Pr = 0.1$, the flow at the inlet is largely unaffected by the entering fluid stream. Heat transfer rate increases with Pr as observed from Fig.

5.17 (b) as well as table 5.5.

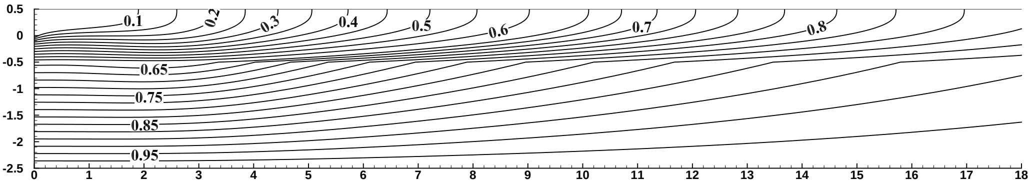

(a) $Pr = 0.1$

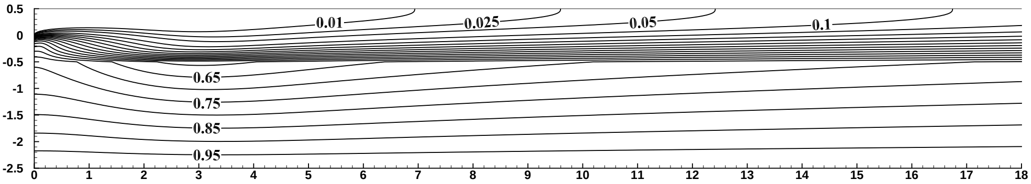

(b) $Pr = 1$

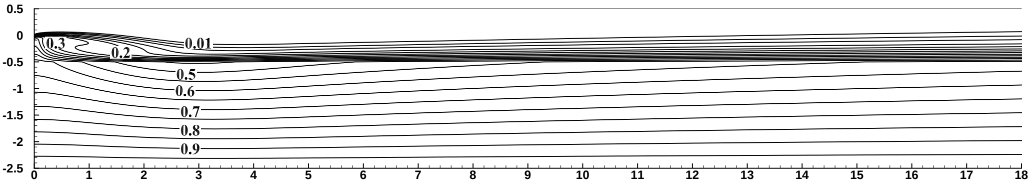

(c) $Pr = 5$

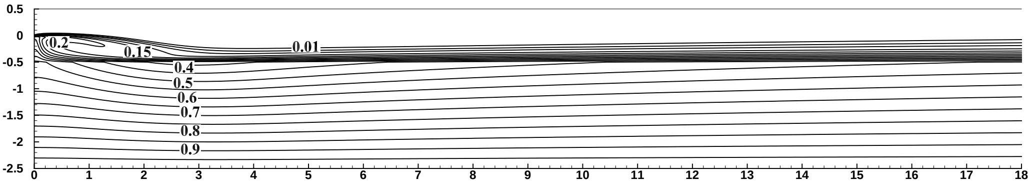

(d) $Pr = 10$

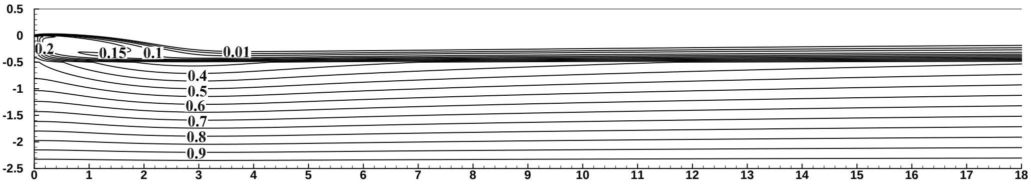

(e) $Pr = 15$

Figure 5.16: Isotherms for different Pr with $Re = 200$, $k = 10$ and $b = 4h$.

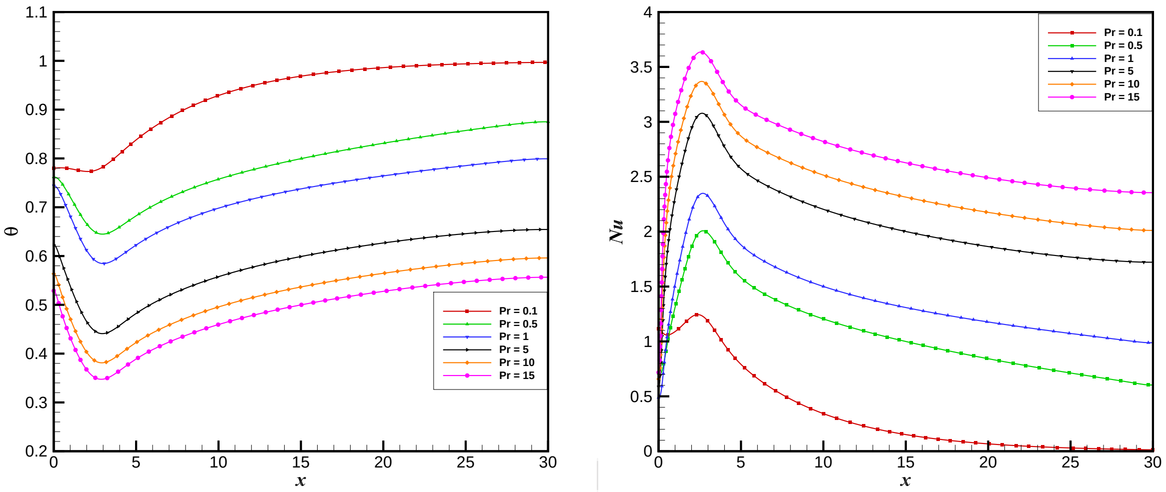

(a) Interface temperature vs. x. (b) Nu vs. x.

Figure 5.17: Influence of Pr on interface temperature and Nusselt number for $Re = 200$, $k = 10$ and $b = 4h$.

Table 5.5: Average Nusselt number ($\overline{Nu}$) for different Pr.

Pr	$\overline{Nu}$
0.1	0.3408129
0.5	1.0749647
0.71	1.2383312
1	1.3894813
5	2.0887445
10	2.3954021
15	2.7078314

Influence of slab thickness

Finally, we study the influence of slab thickness (b) on the heat transfer characteristics by varying it in the range $h \leq b \leq 6h$, and keeping the remaining parameters fixed at $Re = 800$, $Pr = 0.71$, and $k = 10$. Predictably, the isotherms in the fluid region remain unaffected by the change in slab thickness (Fig. 5.18). The increase in slab thickness allows a more even distribution of isotherms in the solid region. Consequently, the strength of convective heat transfer at the fluid-solid interface decreases with increased slab thickness. This is buttressed by the plot of temperature and local Nu along the interface (Fig. 5.19), as well as the values of $\overline{Nu}$ for the different slab thickness considered (table 5.6). Interestingly, as Re increases, there is a steeper decrease in average rate of convective heat transfer with slab thickness (Fig. 5.20).

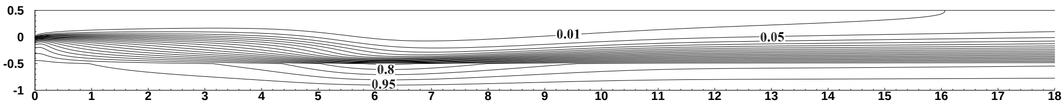

(a) $b = h$

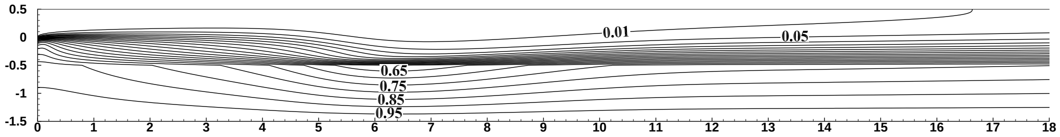

(b) $b = 2h$

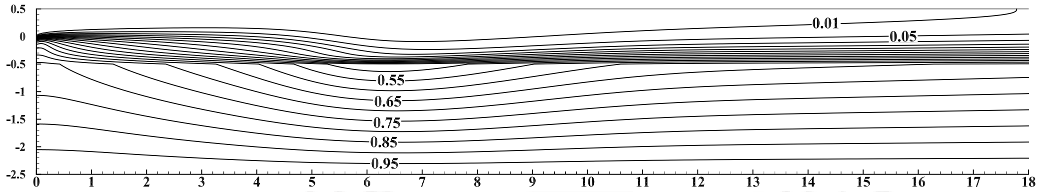

(c) $b = 4h$

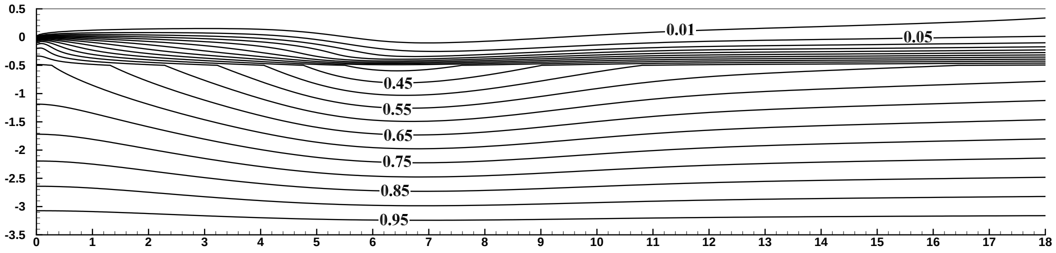

(d) $b = 6h$

Figure 5.18: Isotherms for different slab thickness with $Re = 800$, $Pr = 0.71$ and $k = 10$.

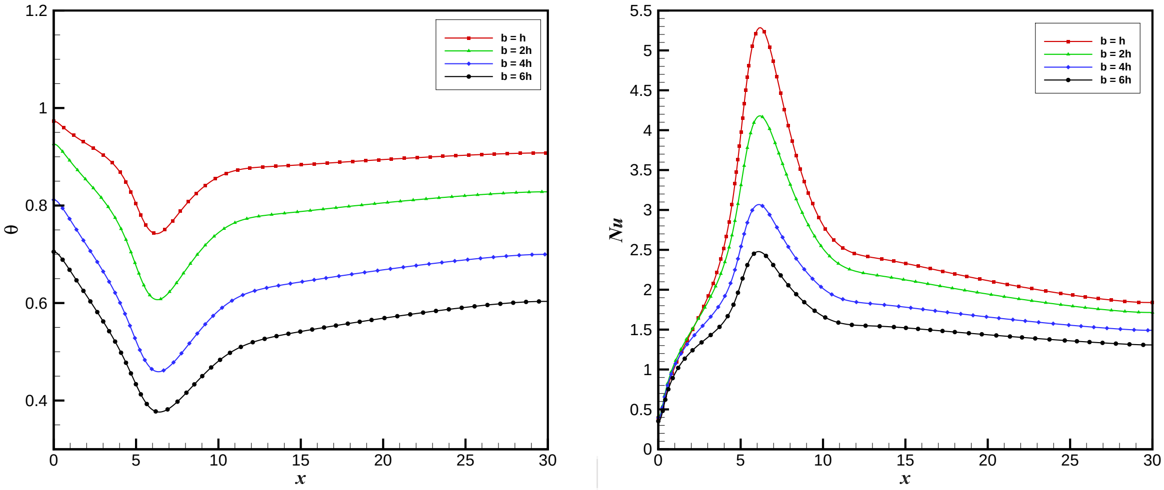

(a) Interface temperature vs. x. (b) Nu vs. x.

Figure 5.19: Influence of slab thickness b on interface temperature and Nusselt number for $Re = 800$, and $k = 10$.

Table 5.6: $\overline{Nu}$ for different slab thickness (b) and Re (with $k = 10$).

Re	$b = h$	$b = 2h$	$b = 4h$	$b = 6h$
200	1.4868902	1.3958636	1.2383312	1.1095782
400	1.9364963	1.7772362	1.5202996	1.3255717
600	2.2150757	2.0056801	1.6811163	1.4435785
800	2.4299484	2.1759032	1.7959799	1.5258996

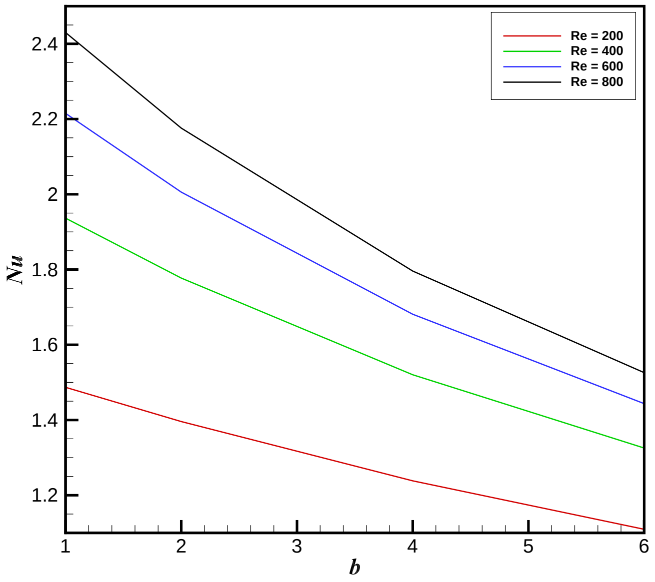

Figure 5.20: $\overline{Nu}$ vs b for different Re.

5.3 Conjugate Heat transfer in a suddenly expanding channel with large expansion ratios

Consider the flow of a 2D, viscous, Newtonian, and incompressible fluid of Prandtl number Pr in a long channel of width $h = 2\epsilon a(\epsilon << 1)$ which suddenly expands symmetrically, with right angles, into a long channel of width $H = 2a$ (Figure 5.21). A solid slab, the top wall of which is maintained at a constant uniform temperature T_W, of thickness b rests on the top of the channel. The length of the channel is taken as 40 times the channel width ($40a$), which allows the flow to become fully developed. Note that the parameter ϵ controls the expansion ratio ($= H/h$). For the present work two values of ϵ are chosen ($\epsilon = 0.1, 0.02$). Note that these two values of ϵ are chosen so that the flow patterns resulting from the present computations can be compared to the numerical results of Revuelta [132]. In figure 5.21, x_1 and x_2 denote the reattachment lengths, x_3 and x_4 mark the ends of the second recirculation zone which forms after $Re > Re_c$; V_1, V_2 and V_3 denote the recirculation eddies.

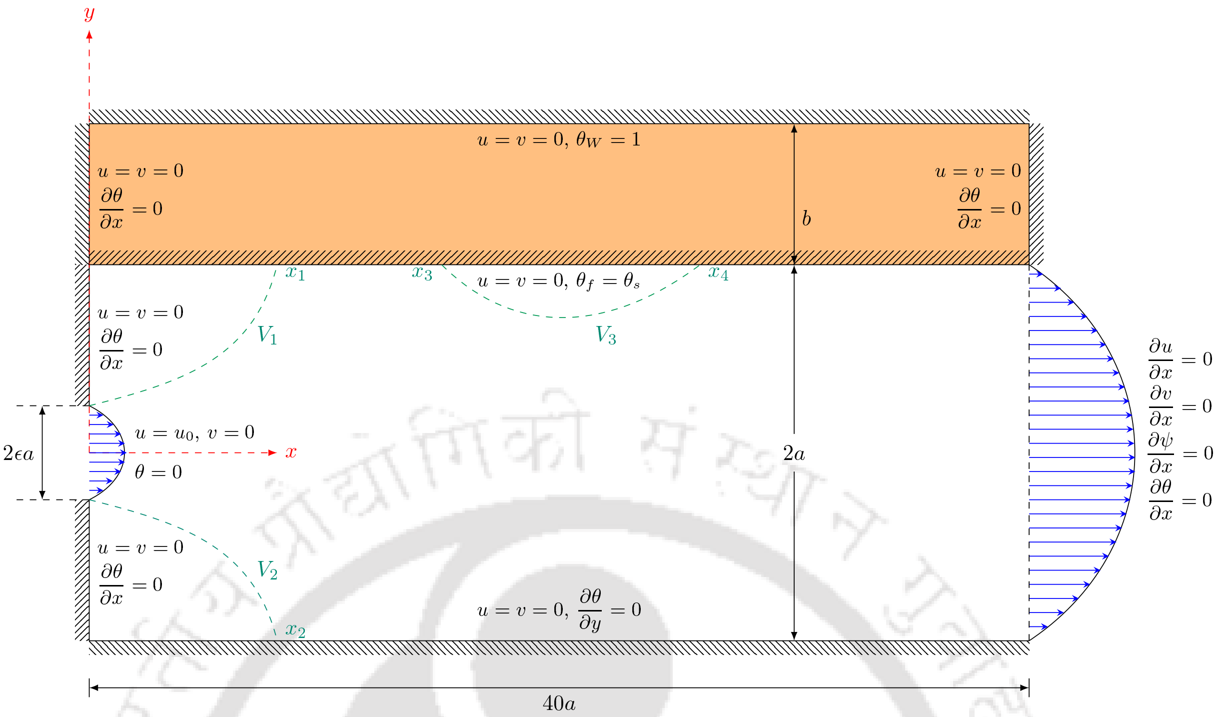

Figure 5.21: Schematic and boundary conditions for conjugate heat transfer on suddenly expanding channel.

The governing equations are given by (5.1) - (5.3). For this case, the Reynolds number is given by $Re = \dfrac{2U_{av}\epsilon a}{\nu}$, where U_{av} is the average flow velocity.The boundary conditions are given as follows: At the inlet, $u_0 = \sqrt{\dfrac{15}{16\epsilon}}\left[1 - \left(\dfrac{y}{\epsilon}\right)^2\right]$, $v = 0$, and $\theta = 0$. The streamfunction ψ at inlet is evaluated based on u_0. At the outlet, $\dfrac{\partial u}{\partial x} = \dfrac{\partial v}{\partial x} = \dfrac{\partial \theta}{\partial x} = 0$. At the top of the slab, $\theta = 1$. The bottom wall of the channel is adiabatic ($\dfrac{\partial \theta}{\partial y} = 0$), as are the vertical walls of the channel and the slab, i.e., $\dfrac{\partial \theta}{\partial x} = 0$ on the vertical walls.

At the interface of solid and fluid domain, the continuity in temperatures and heat fluxes are ensured by the following equations

$$\theta_f = \theta_s \tag{5.13}$$

$$k_f\left(\frac{\partial \theta_f}{\partial n}\right)_{wall} = k_s\left(\frac{\partial \theta_s}{\partial n}\right)_{wall} \tag{5.14}$$

where k_f, and k_s are the thermal conductivities of the fluid and the solid, respectively.

The local Nusselt number along the fluid-solid interface is given by

$$Nu(x) = -\left.\frac{\partial \theta}{\partial y}\right|_{wall} \tag{5.15}$$

and the average Nusselt number is given by

$$\overline{Nu} = \frac{1}{L}\int_0^L Nu(x)dx \tag{5.16}$$

where L is the length of the interface.

5.3.1 Grid generation

Previous studies of the flow phenomenon [132, 133] have shown that a relatively higher number of grid points are required for flow resolution near the inlet and near the top and bottom walls. To this end, we use the stretching functions given by the equations (5.9) and (5.10). Here, equation (5.9) gradually increases the density of grid points towards left, and equation (5.10) generates a centro-symmetric distribution of grid points with clustering near top and bottom walls, and near the interface. A sample of the grid used is shown in Figure 5.22 (a), and a magnified part of the grid is shown in Figure 5.22 (b).

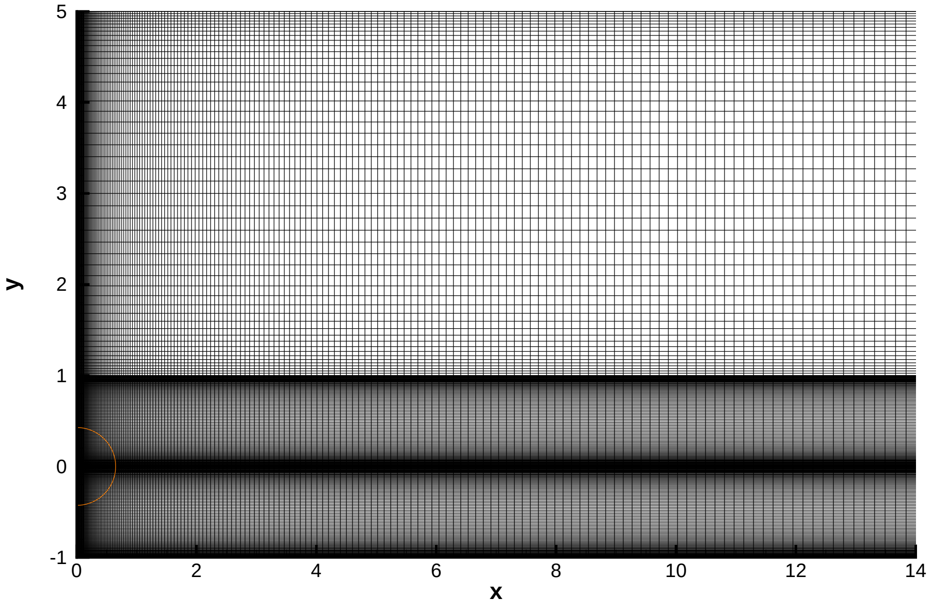

(a) Grid used with $\mu_1 = 0.99$ and $\mu_2 = 0.7$.

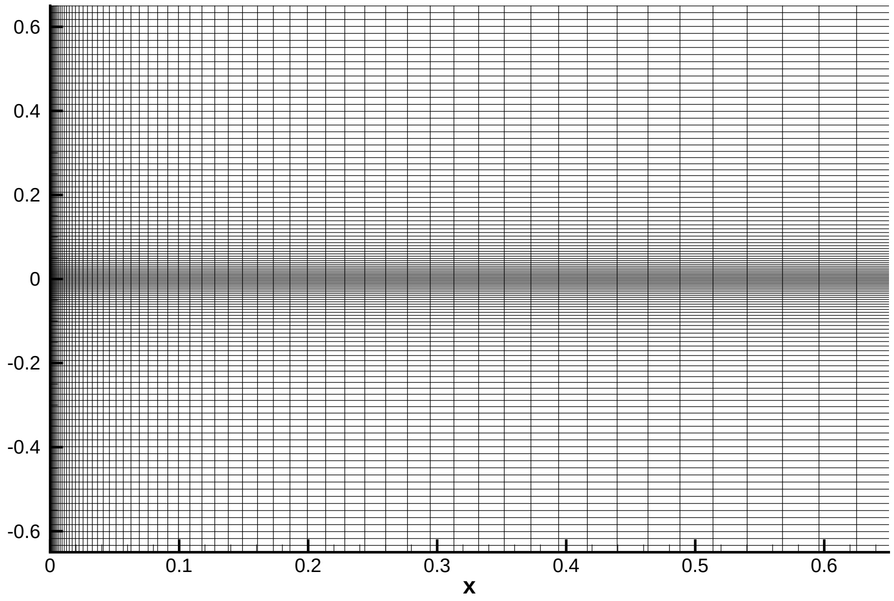

(b) Magnified part of the grid.

Figure 5.22: Mesh distribution.

5.3.2 Grid Independence

To establish grid independence of the presently computed data, we plot the graphs of local Nusselt number (Nu) vs. x and interface temperature vs. x for $Re = 35$, $Pr = 0.71$, $k = 10$, and $b = 4a$ for four different grids viz. 251×201, 281×221, 301×251, and

321 × 271. The near overlap of the graphs for grids 301 × 251 and 321 × 271 indicates that grid independence is achieved at grid size 301 × 251. Thus, all of our computations are performed on grid of size 301 × 251.

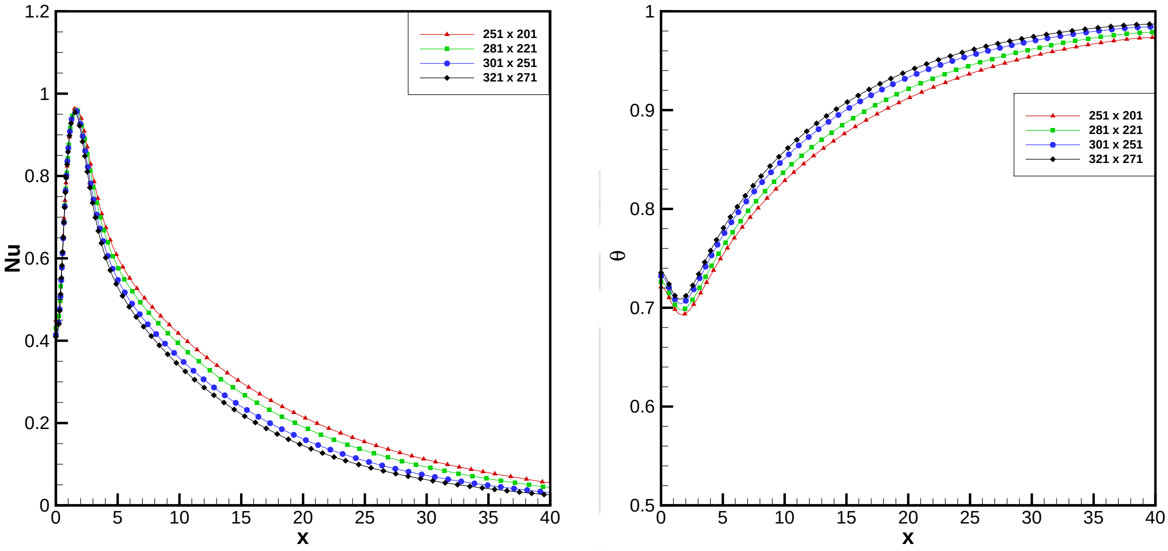

(a) Nu vs. x. (b) Interface temperature vs. x.

Figure 5.23: Grid independence study.

5.3.3 Results and Discussion

Flow Characteristics

Before embarking on the study of heat transfer characteristics, it is vital to understand the basic flow nature in a suddenly expanding channel. Figure 5.24 shows the streamlines for different values of Re ($35 \leq Re \leq 90$) and ϵ. The left column shows the streamlines for $\epsilon = 0.1$ and the right column for $\epsilon = 0.02$. As seen from the schematic (figure 5.21), V_1 and V_2 are the two symmetric recirculation eddies which exist for $Re < Re_c$, whereas the second recirculation eddy V_3 forms only when $Re > Re_c$; x_1 and x_2 mark the reattachment lengths for V_1 and V_2 respectively, x_3 and x_4 mark the ends of the second recirculation eddy V_3. A cursory glance reveals that the flow fields are quite similar for both expansion ratios, the notable difference being that the recirculation length decreases as the expansion ratio is increased for the same vale of Re. However one also needs to be cognizant of other subtle differences in the flow phenomenon.

The properties of the vortices V_1, V_2, and V_3 (figure 5.21) are tabulated in tables 5.7 and 5.8. Note that to the best of our knowledge, the properties of these vortices have been tabulated for the first time. Here, we notice the other significant difference between the flow phenomena for the two expansion ratios - the strengths of the vortices are also lower for the larger expansion ratio. As mentioned earlier in section 5.1, the 2D steady-state flow phenomena in a suddenly expanding channel contains two symmetric recirculation zones of equal size. With an increase in Re, the recirculation length also increases up to a critical Reynolds number Re_c, beyond which the flow loses its symmetry. The values of Re_c for $\epsilon = 0.1, 0.02$ are 40.6 and 43.5 respectively [132]. For $Re = 35, 40$, the flow is symmetric, i.e., $x_1 = x_2$, with the vortices V_1 and V_2 growing in size and strength as Re increases (figures 5.24 (a) - 5.24 (d)). For $Re > Re_c$, flow loses symmetry and the lower wall vortex V_2 grows in size (figures 5.24 (e) - 5.24 (h)). For $Re \geq 70$, a second vortex V_3 forms on the upper wall of the channel, whose size and strength increases as Re is increased (figures 5.24 (i) - 5.24 (n)). Meanwhile the lower wall vortex also grows in size and strength as Re increases. The evolution of the upper wall vortex V_1 vis-a-vis Re, however, is not as straightforward as that of V_2 and V_3 . This can be clearly noted from the variation of the recirculation length x_1 with Re in figure (5.26). V_1 reduces in size when $Re > Re_c$, and as seen from the figure, $x_1(Re = 50) < x_1(Re = 40)$. V_1 decreases further as Re is increased to 60. Note that at this point, the flow becomes asymmetric but the second vortex in the upper (V_3) has not formed yet. At $Re = 70$, as V_3 forms, the size of V_1 increases again till $Re = 90$. Although the size of V_1 fluctuates with Re, its strength increases with Re (tables 5.7 and 5.8). Thus, we see that two recirculation zones are formed in the upper wall of the channel. This has a direct effect on the isotherms and heat transfer rate as would be evident later on. Another interesting observation worth mentioning is that the flow becomes fully developed post-expansion at an earlier location for $\epsilon = 0.02$, as evidenced from the vector plots for $Re = 35, 90$ in figure 5.25. Note that the results presented in this section are in excellent agreement with that of Revuelta [132].

Table 5.7: Properties of the vortices for $\epsilon = 0.1$.

Re	x_1	x_2	x_3	x_4	$\psi_{mid}(x, y)$		
					V_1	V_2	V_3
35	2.252	2.252	–	–	0.301881 (0.71823,0.449124)	0.301881 (0.71823, -0.449124)	–
40	2.565	2.565	–	–	0.312786 (0.819972,0.449124)	0.312786 (0.819972,-0.449124)	–
50	1.8352	4.0435	–	–	0.321329 (0.785085,0.5)	-0.34961 (1.97737,-.24593)	–
60	1.8167	4.5009	–	–	0.329547 (0.8705,0.5335)	-0.390716 (2.58415,-0.159471)	–
70	1.8544	4.7055	4.9941	6.0575	0.335398 (0.96953, 0.55087)	-0.421593 (2.96487,-0.159741)	0.206094 (5.35142,0.8179)
80	1.90165	4.9058	4.3639	7.0406	0.339201 (1.05047,0.567706)	-0.446396 (3.20855,-0.159471)	0.213004 (5.69234, 0.601012)
90	1.9515	5.02219	4.34725	7.8399	0.34175 (1.13562, 0.60101)	-0.467175 (3.46379,-0.182092)	0.222616 (6.04482,0.466035)

Table 5.8: Properties of the vortices for $\epsilon = 0.02$.

Re	x_1	x_2	x_3	x_4	$\psi_{mid}(x, y)$		
					V_1	V_2	V_3
35	1.65394	1.65394	–	–	0.16495 (0.51397,0.38747)	-0.16495 (0.51397,-0.38747)	–
40	1.93081	1.93081	–	–	0.185166 (0.59597,0.387226)	-0.185166 (0.59597,-0.38722)	–
50	1.70104	3.18847	–	–	0.213901 (0.655215,0.44316)	-0.226059 (1.05047,-0.315806)	–
60	1.51989	3.63038	–	–	0.239036 (0.718238,0.5)	-0.29111 (1.97737,-0.097042)	–
70	1.50643	3.7242	3.50924	5.06292	0.262022 (0.75118,0.518995)	-0.347921 (2.23476,-0.063772)	0.104516 (4.29942,0.718055)
80	1.51216	3.73616	3.33646	5.76589	0.282005 (0.819972,0.537955)	-0.395458 (2.37079,-0.071261)	0.114238 (4.60137,0.44316)
90	1.52621	3.73505	3.25201	6.21042	0.29935 (0.855849,0.55684)	-0.435543 (2.37079,-0.063771)	0.127446 (4.70462,0.298696)

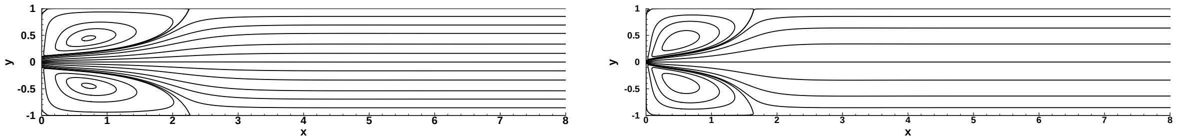

(a) $Re = 35$, $\epsilon = 0.1$ (b) $Re = 35$, $\epsilon = 0.02$

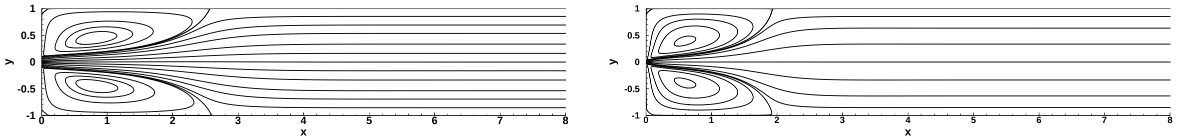

(c) $Re = 40$, $\epsilon = 0.1$ (d) $Re = 40$, $\epsilon = 0.02$

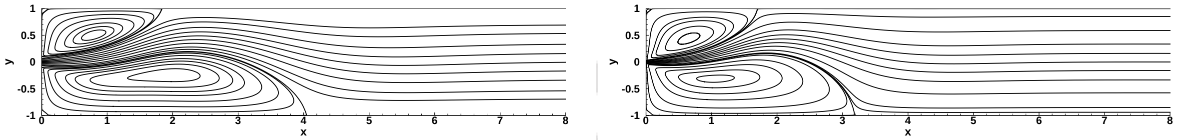

(e) $Re = 50$, $\epsilon = 0.1$ (f) $Re = 50$, $\epsilon = 0.1$

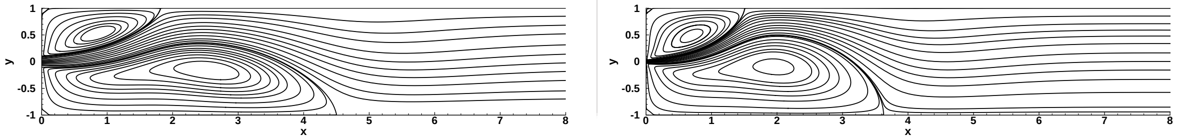

(g) $Re = 60$, $\epsilon = 0.1$ (h) $Re = 60$, $\epsilon = 0.02$

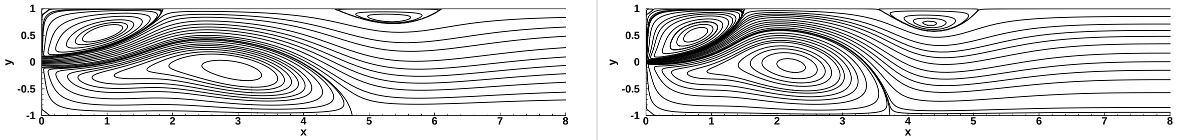

(i) $Re = 70$, $\epsilon = 0.1$ (j) $Re = 70$, $\epsilon = 0.02$

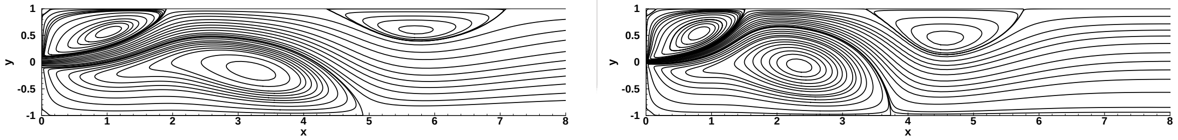

(k) $Re = 80$, $\epsilon = 0.1$ (l) $Re = 80$, $\epsilon = 0.02$

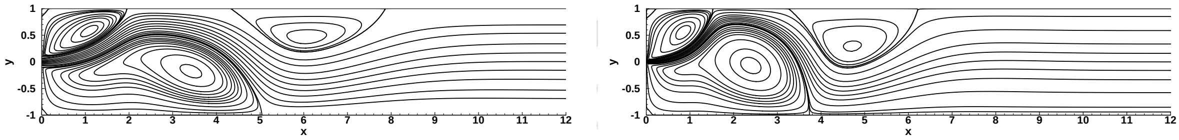

(m) $Re = 90$, $\epsilon = 0.1$ (n) $Re = 90$, $\epsilon = 0.02$

Figure 5.24: Streamlines for different values of Re with $\epsilon = 0.1$ (left) and $\epsilon = 0.02$ (right).

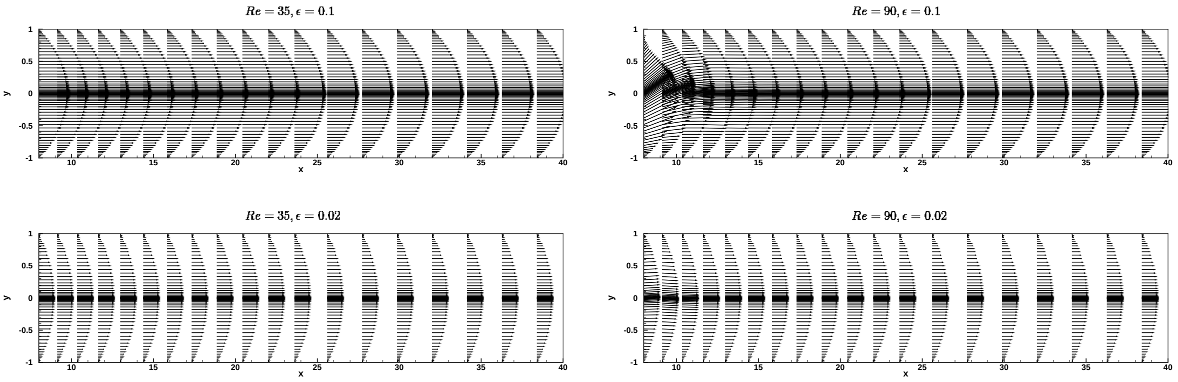

(a) (b)

Figure 5.25: Velocity vectors (in magnitude) for $Re = 35$, 90.

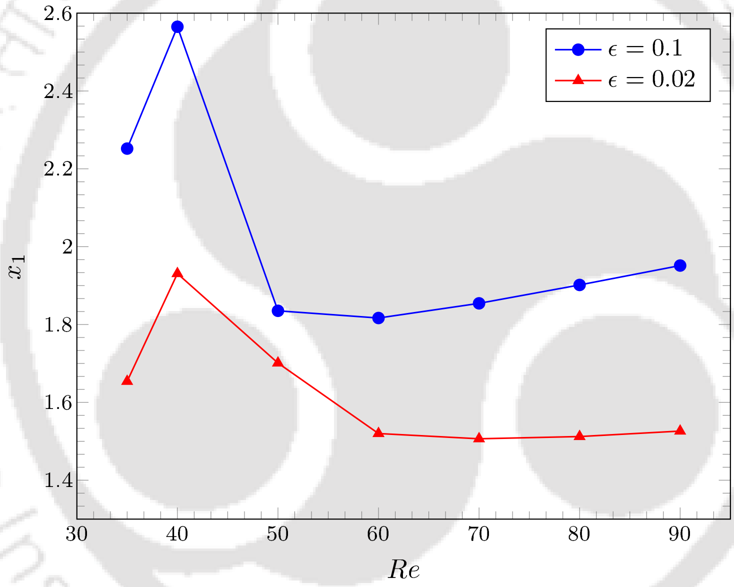

Figure 5.26: x_1 vs. Re for the two expansion ratios.

Heat transfer characteristics

In this section, we discuss the heat transfer characteristics in terms of isotherms and variation of Nusselt number. There are four different parameters for the present problem whose effect on heat transfer rate have to be examined, viz. Reynolds number (Re), conductivity ratio (k), Prandtl number (Pr), and slab thickness (b). To this end, each parameter is varied while keeping the others fixed. The effect of the expansion ratio (characterized by ϵ) is examined in conjunction with the other parameters. The isotherms for both values of ϵ are presented side-by-side in every section to better visualize its effect in tandem with the rest of the parameters.

Effect of Reynolds number Firstly, we discuss the effect of Re and ϵ by varying Re in the range $35 \leq Re \leq 90$. The other parameters are fixed at $k = 10$, $Pr = 0.71$, and $b = 4a$. Figure 5.27 shows the isotherms for $Re = 35, 50, 90$, the left column for $\epsilon = 0.1$ and the right column for $\epsilon = 0.02$. For the sake of brevity, isotherms for only three values of Re are shown.

As seen from figure 5.27, the isotherms are clustered near the reattachment point and they spread out as one moves farther downstream from the reattachment point. With an increase in Re, the reattachment length also changes, thereby shifting the location of this clustering of isotherms. Also, the isotherms are flattened with an increase in Re in the fluid region, with a thinning of the thermal boundary layer observed near the recirculation zone. This in turn reveals that the rate of heat transfer would be maximum in the recirculation zone (to be further confirmed by the plots of interface temperature and local Nusselt number). A careful observation of figures 5.27 (c) reveals that there is a slight non-linearity of the isotherms in the vicinity of the second recirculation zone, i.e., where V_3 is formed. In the solid region, the isotherms are non-linear near the interface, becoming linear as one moves away from the interface towards the top of the slab. With an increase in Re, the temperature in the solid region decreases near the interface, indicating a cooling effect due to the fluid flow. The isotherm patterns for both the expansion ratios considered here are similar, the notable difference being that for the case of $\epsilon = 0.1$, there is a more even distribution of the isotherms than for $\epsilon = 0.02$, owing to the fact that the flow after expansion becomes fully developed at an earlier location for $\epsilon = 0.02$. This in turn ensures a better overall rate of heat transfer (figure 5.29) for the lesser expansion ratio. Further, the location where the isotherms are clustered near the interface shifts upstream for the higher expansion ratio ($\epsilon = 0.02$) as the recirculation zones also shift upstream.

Figure 5.28 shows the comparative variation of interface temperature and local Nusselt number for $35 \leq Re \leq 90$ and $\epsilon = 0.1, 0.02$. We see that the plots of θ vs. x have a minima, and those of local Nu vs. x have a maxima in the recirculation zones. Only one minima and maxima are observed for $Re < Re_c$, and as $Re > R_c$ two maxima and minima are observed. They become more prominent from *Re* = 70 onwards as the second recirculation zone (V_3) forms on the top wall of the channel. For sudden expansion flows, there is a relatively better mixing of the fluid in the recirculation zones, which aids in convective heat transfer. Thus, we observe the maximum rate of heat transfer (and minimum temperature) in these recirculation zones. We also observe from figure 5.28 that for a particular value of *Re*, the lesser expansion ratio ($\epsilon = 0.1$) gives a greater rate of heat transfer. Also, for both the expansion ratios, as *Re* increases, the heat transfer rate also increases. Figure 5.29 shows the variation of average heat transfer rate w.r.t. *Re* for the two expansion ratios. The plot is similar for both expansion ratios, but as noted earlier, the lower expansion ratio ($\epsilon = 0.1$) promotes a better distribution of isotherms, thus ensuring a higher rate of overall heat transfer. The difference of nearly 50% in the heat transfer rates is solely a reflection of the effect of expansion ratio. This particular effect of the expansion ratio will be observed later on as well while studying the effects of the other parameters.

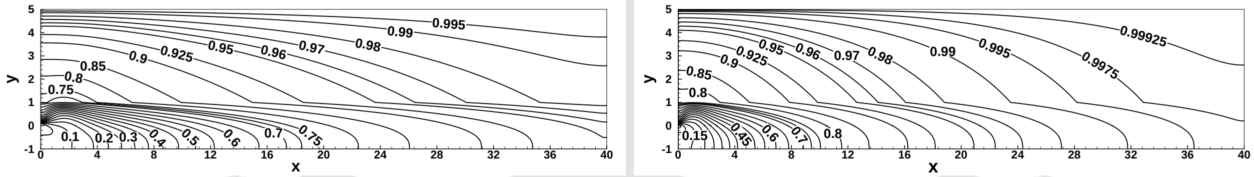

(a) $Re = 35$, with $\epsilon = 0.1$ (left) and $\epsilon = 0.02$ (right).

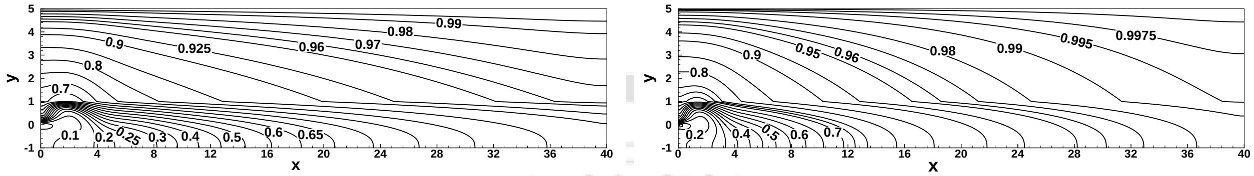

(b) $Re = 50$, with $\epsilon = 0.1$ (left) and $\epsilon = 0.02$ (right).

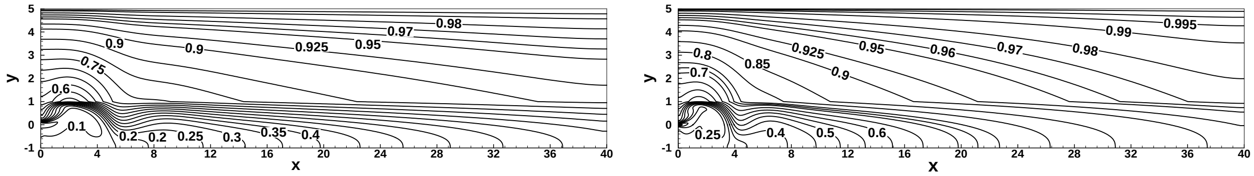

(c) $Re = 90$, with $\epsilon = 0.1$ (left) and $\epsilon = 0.02$ (right).

Figure 5.27: Isotherms for different *Re*, with $k = 10$, $b = 4a$, $Pr = 0.71$, and $\epsilon = 0.1$ (left) & $\epsilon = 0.02$ (right).

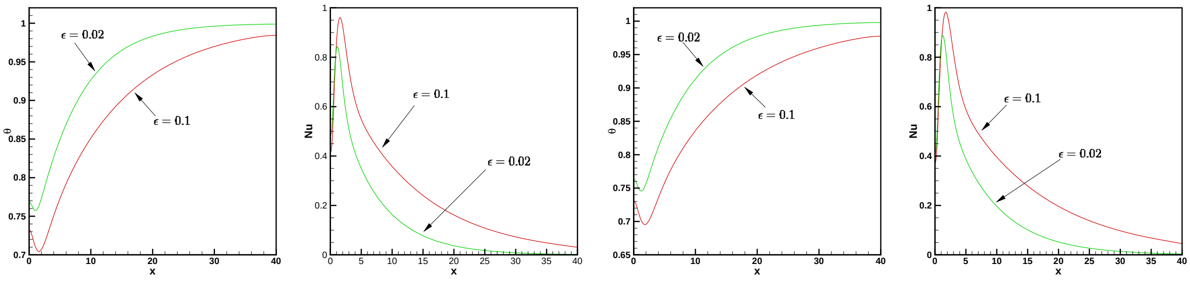

(a) $Re = 35$ (b) $Re = 40$

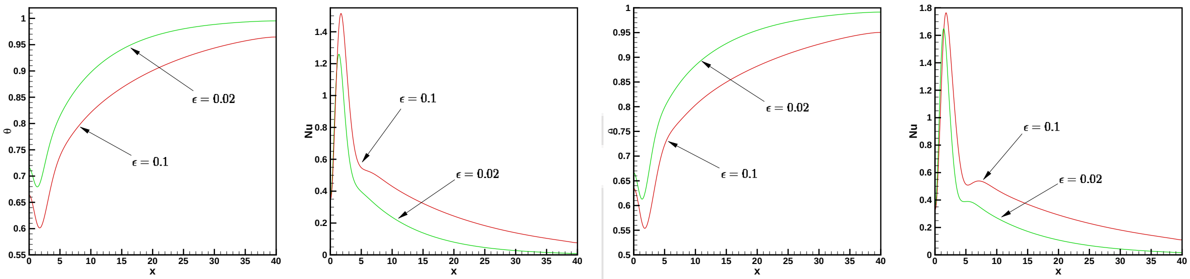

(c) $Re = 50$ (d) $Re = 60$

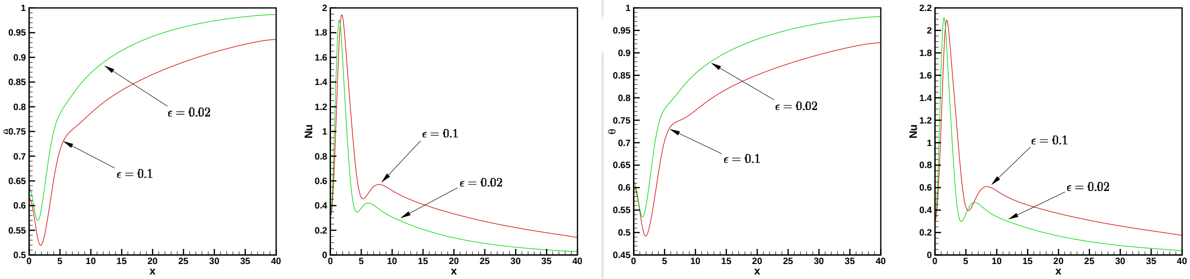

(e) $Re = 70$ (f) $Re = 80$

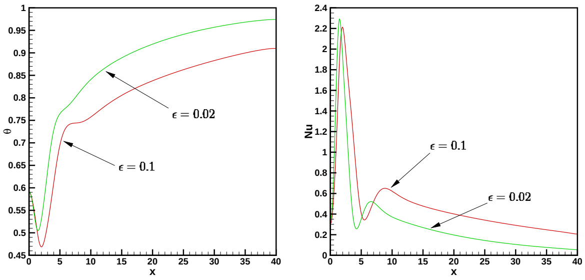

(g) $Re = 90$

Figure 5.28: Variation of interface temperature and local Nusselt number for different values of Re and ϵ.

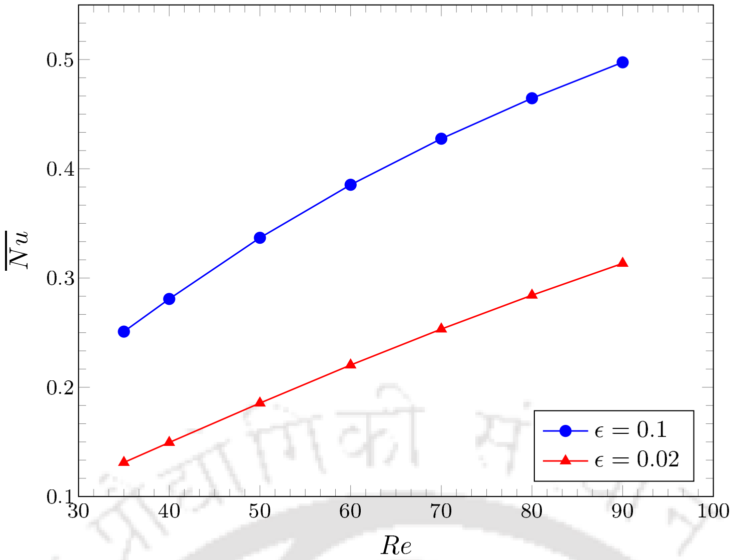

Figure 5.29: Variation of average Nusselt number with Re for $\epsilon = 0.1, 0.02$.

Effect of conductivity ratio Here, we discuss the effect of changing the material of the solid slab on heat transfer characteristics. This is achieved by varying the conductivity ratio (k) in the range $1 \leq k \leq 1000$, and keeping the other parameters fixed at $Re = 90$, $Pr = 0.71$, and $b = 4a$. Figure 5.30 shows the isotherms for different values of k, with the left column for $\epsilon = 0.1$ and the right for $\epsilon = 0.02$. As noted in the previous sections, two recirculation zones exist for $Re = 90$ and the isotherms are clustered near those reattachment points for all values of k. The isotherms are distributed in a similar pattern for both the expansion ratios. We see that for $k = 1$, the isotherms are loosely clustered near the reattachment zones, and they are linear along the slab as one moves away from the reattachment zones. In the fluid region, as k increases to 100 the isotherms become strongly clustered near the reattachment zones. However, a further increase in k only has a slight effect on the isotherms and thermal boundary layer thickness in the fluid region. Increasing k implies an increase in the thermal conductivity of the solid slab in this case. Thus, increasing k aids in heat conduction within the slab, and as evidenced from the contour values in figure 5.30 the temperature in the slab rises with k, which in turn effects the linearity of the isotherms. As k increases, the non-linearity of the isotherms in the slab also increases along the length of the channel.

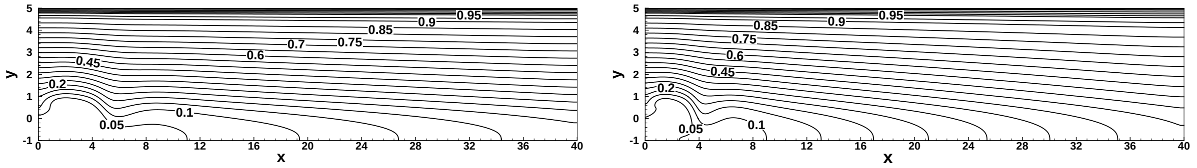

(a) $k = 1$

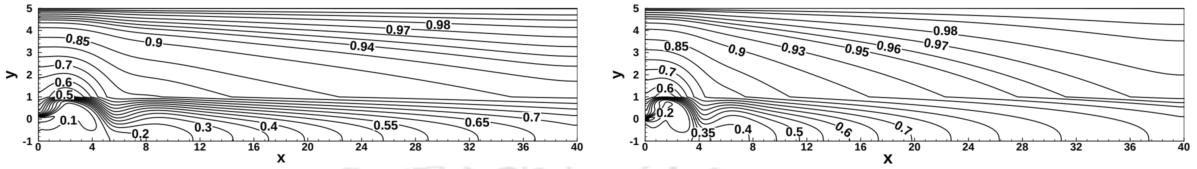

(b) $k = 10$

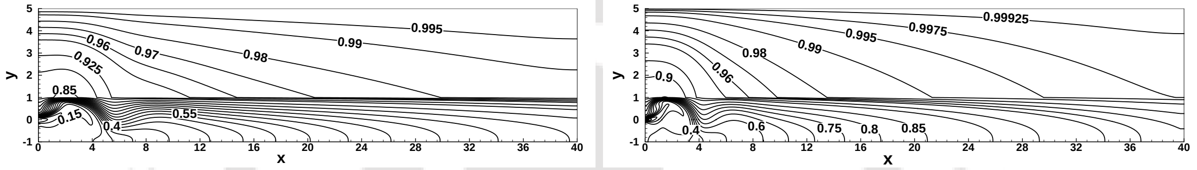

(c) $k = 50$

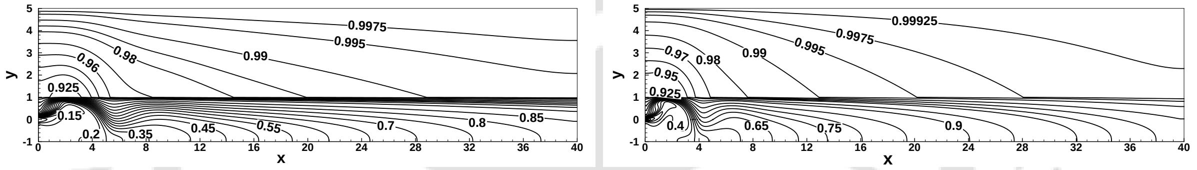

(d) $k = 100$

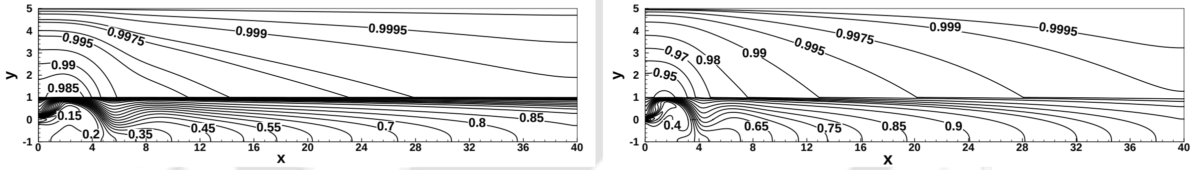

(e) $k = 500$

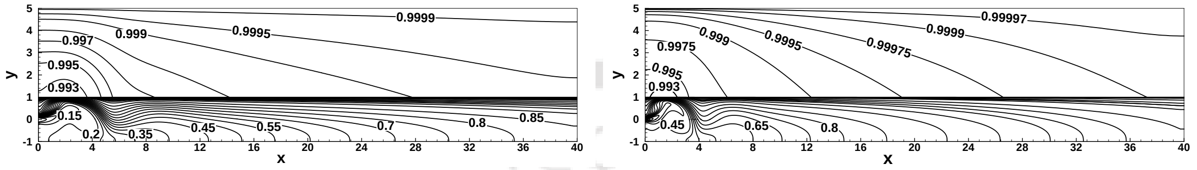

(f) $k = 1000$

Figure 5.30: Isotherms for different k with $\epsilon = 0.1$ (left) & $\epsilon = 0.02$ (right), and $Re = 90$, $Pr = 0.71$, $b = 4a$

Figure 5.31 shows the variation of interface temperature and local Nusselt number for the two expansion ratios - the left column (figures 5.31 (a) and 5.31 (c)) for $\epsilon = 0.1$, and the right column (figures 5.31 (b) and 5.31 (d)) for $\epsilon = 0.02$. With an increase in the conductivity ratio, the temperature along the fluid-solid interface also increases, and the local minima in the temperature near the reattachment zones smoothen out with an increase in k. As $k \to \infty$, the temperature becomes constant throughout the slab. The variation of local Nusselt number follows a pattern inverse to the interface temperature. The near overlap of the Nusselt number variation for $k > 100$ indicates that there is little increase in Nu (i.e., heat transfer rate) with k. This is also glimpsed from figure 5.32 which plots the variation of average Nusselt number w.r.t. k for both the expansion ratios. As noted in section 5.3.3, the reduction in $\overline{Nu}$ that is seen in figure 5.32 is attributed to the expansion ratio only.

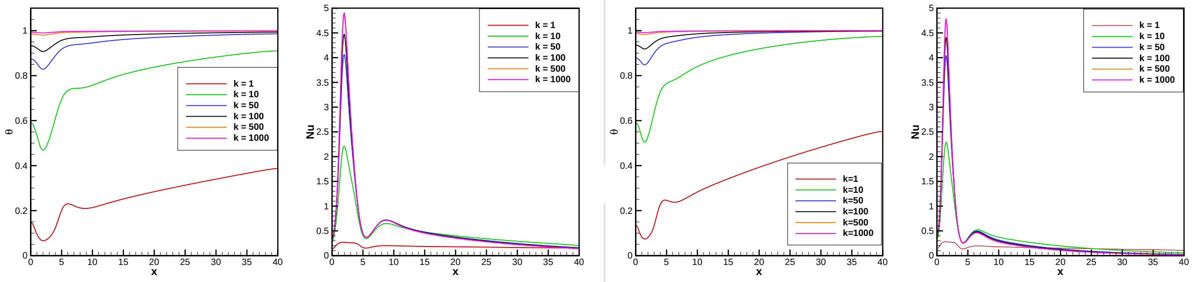

(a) $\epsilon = 0.1$ (b) $\epsilon = 0.02$

Figure 5.31: Variation of temperature and local Nusselt number along the interface w.r.t. conductivity ratio for (a) $\epsilon = 0.1$, and (b) $\epsilon = 0.02$

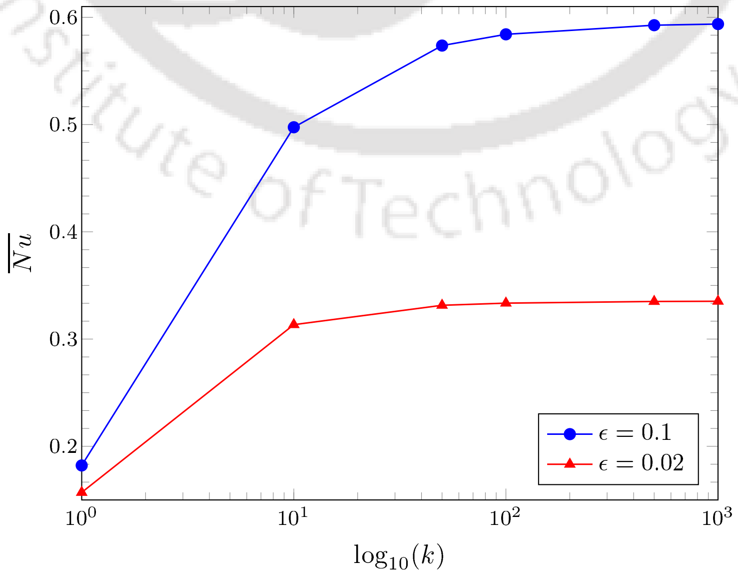

Figure 5.32: Variation of average Nusselt number with k for $\epsilon = 0.1, 0.02$

Effect of Prandtl number In this section, we examine the effect of Prandtl number (Pr) on the heat transfer characteristics by varying it in the range $0.1 \leq Pr \leq 20$, and keeping the other parameters fixed at $Re = 40$, $k = 10$, and $b = 4a$.

Figure 5.33 shows the isotherms for different values of Pr, the left column for $\epsilon = 0.1$ and the right for $\epsilon = 0.02$. At lower values of Pr, the thermal diffusivity dominates the momentum diffusivity, thus allowing heat to diffuse at a faster rate than velocity or momentum. This is reflected in the isotherms shown in figures 5.33 (a) and 5.33 (b). As the Prandtl number increases, the isotherms in the fluid region become clustered near the fluid-solid interface, and there is a reduction in the thermal boundary layer thickness. For $Pr \geq 5$, the inlet fluid plays a significant role in the heat transfer characteristics. As the momentum diffusivity dominates thermal diffusivity for high values of Pr, the inlet fluid inhibits the diffusion of heat in the fluid region along the channel. Thus we observe that the isotherms are clustered near the inlet of the channel. This effect is more pronounced for $Pr = 10, 20$ (figures 5.33 (e) and 5.33 (f)). The thickness of the thermal boundary layer also reduces significantly, indicating an increase in the rate of convective heat transfer. In the solid region, the isotherms are seen to be non-linear for low values of Pr (figures 5.33 (a) - 5.33 (c)). This non-linearity vanishes for the higher values of Pr, barring the region near the recirculation zone. A closer look at the contour values in the solid region reveals that the temperature in the slab decreases with an increase in Pr.

Figure 5.34 shows the variation of temperature and local Nusselt number along the interface w.r.t. Pr for (a) $\epsilon = 0.1$ and (b) $\epsilon = 0.02$. The plots of temperature and Nu follow a similar pattern for all values of Pr, except for $Pr = 0.1$ as the flow at the inlet remains largely unaffected by the incoming fluid stream. The plots are also similar for both values of ϵ, the peak in the plot of local Nu occurring near the recirculation zone. The increase in convective heat transfer rate with Pr, as observed earlier with the thinning of the thermal boundary layer, is confirmed by these plots, as well as the plot of average Nusselt number (figure 5.35). This graph also shows a near 50% reduction in heat transfer rate as the expansion ratio increases.

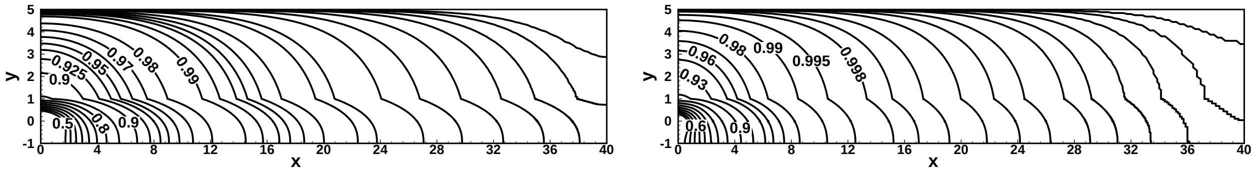

(a) $Pr = 0.1$

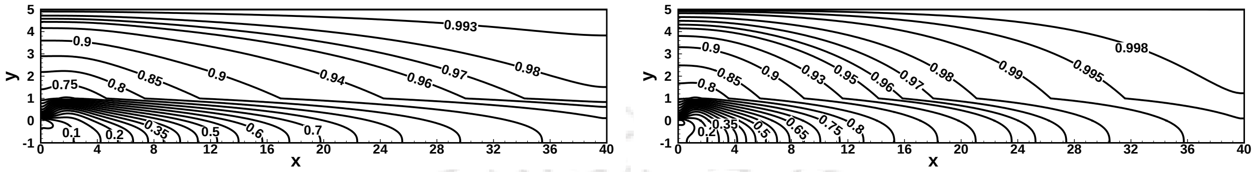

(b) $Pr = 0.71$

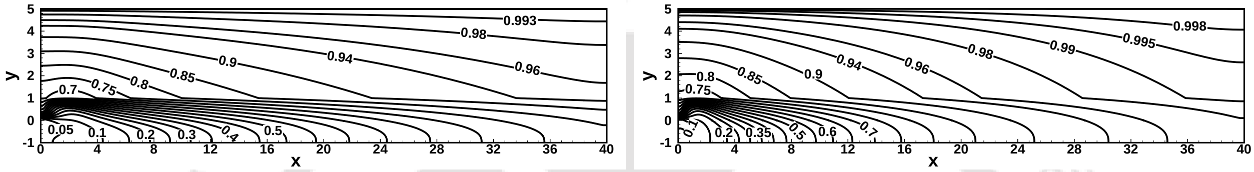

(c) $Pr = 1$

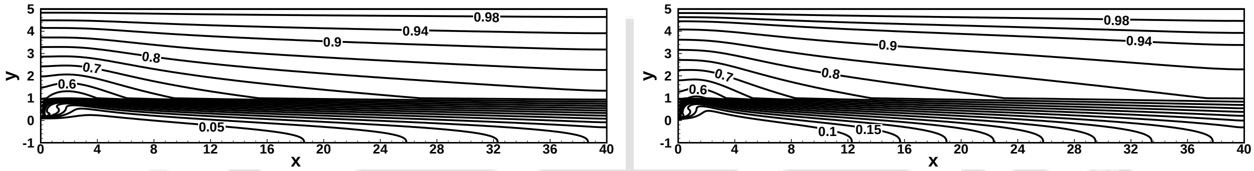

(d) $Pr = 5$

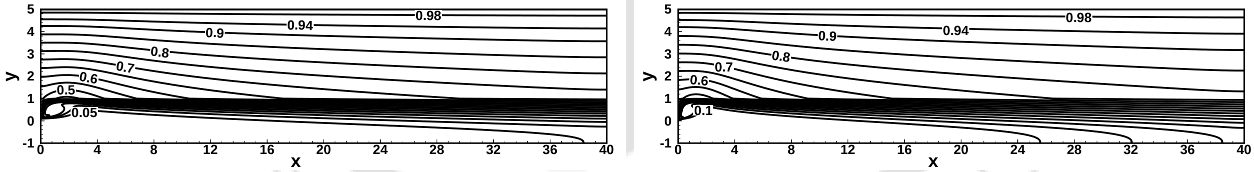

(e) $Pr = 10$

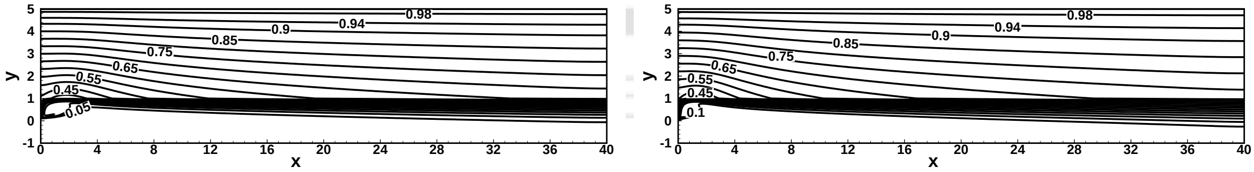

(f) $Pr = 20$

Figure 5.33: Isotherms for different Pr with $\epsilon = 0.1$ (left) & $\epsilon = 0.02$ (right), and $Re = 40$, $b = 4a$, $k = 10$

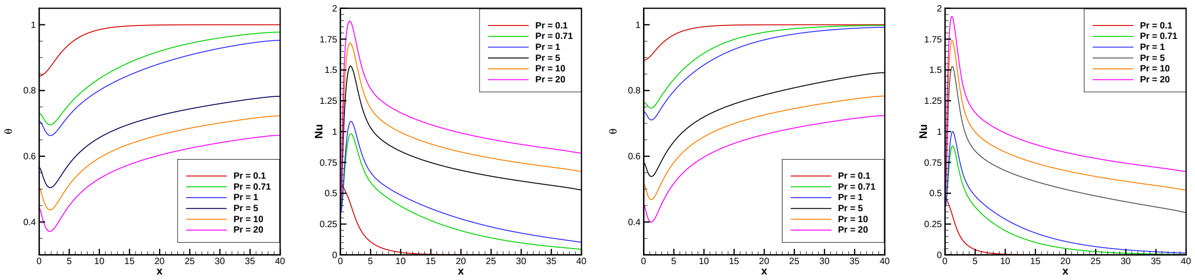

(a) $\epsilon = 0.1$ (b) $\epsilon = 0.02$

Figure 5.34: Variation of temperature and local Nusselt number along the interface w.r.t. Prandtl number for (a) $\epsilon = 0.1$, and (b) $\epsilon = 0.02$

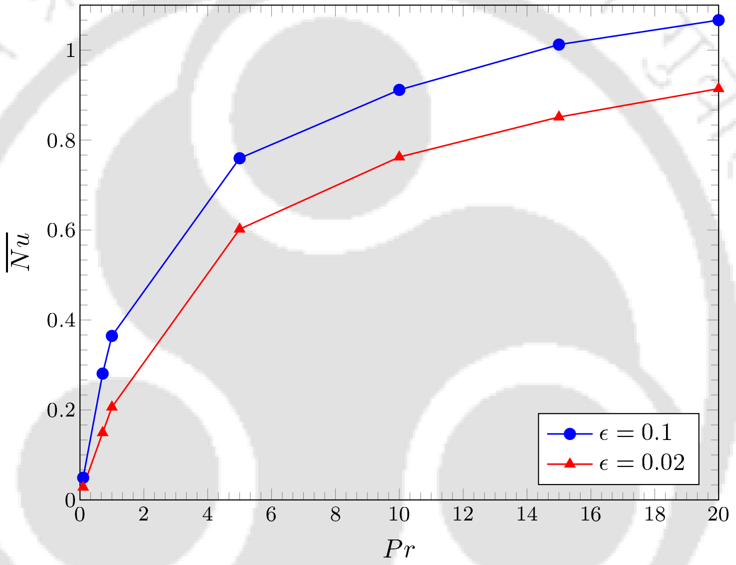

Figure 5.35: Variation of average Nusselt number with Pr for $\epsilon = 0.1, 0.02$

Effect of slab thickness Lastly, we study the effect of changing slab thickness (b) on the isotherms and heat transfer characteristics. This is achieved by varying the slab thickness in the range $h \leq b \leq 6h$, and keeping the rest of the parameters fixed at $Re = 50$, $Pr = 0.71$, and $k = 10$.

Figure 5.36 shows the isotherms for different values of b, with the left column for $\epsilon = 0.1$ and the right for $\epsilon = 0.02$. As expected, the effect of b on isotherms is mostly observed in the solid region. There is a subtle change in the isotherms in the fluid region as well, which can be observed from a closer look at the temperature contour values. As the slab thickness increases, the interface temperature decreases (figure 5.36), since there is a more even distribution of temperature in the solid region. With an increase in slab thickness, the thermal resistance of the slab also increases, which consequently has an adverse effect on the heat conduction in the slab. Thus, it is seen that the heat transfer rate is maximum for the lowest value of b (figure 5.37). Figure 5.38 shows the variation of average Nusselt number with slab thickness for different values of Re and ϵ. It is interesting to note that as Re increases there is a steeper decrease in $\overline{Nu}$ with b. This is true for both values of ϵ, and as observed in previous sections, there is a reduction in overall heat transfer rate of approximately 50% when the expansion ratio is increased.

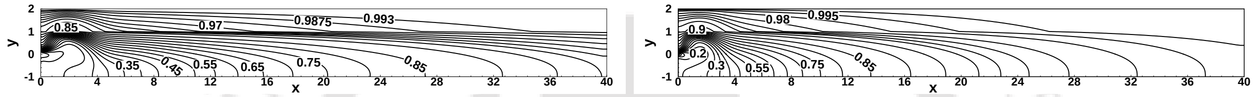

(a) $b = a$

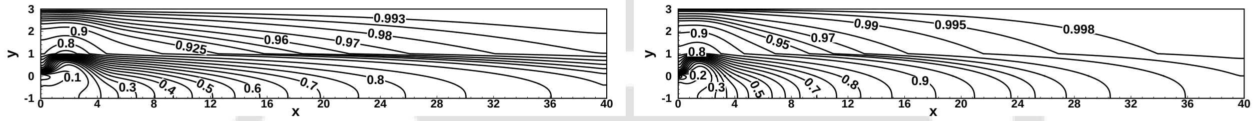

(b) $b = 2a$

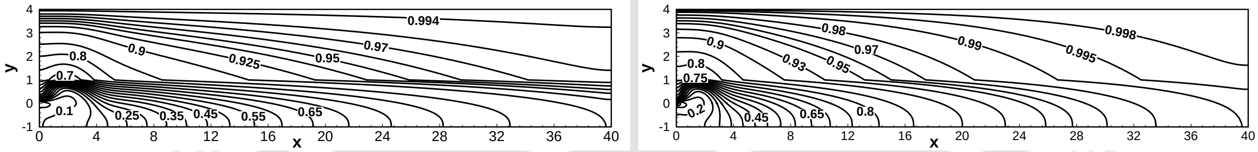

(c) $b = 3a$

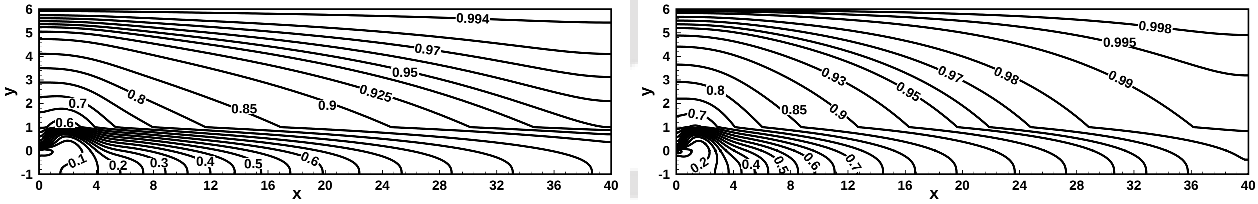

(d) $b = 5a$

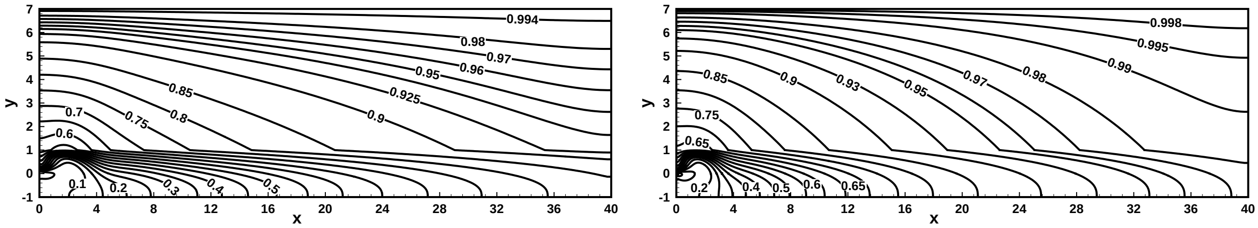

(e) $b = 6a$

Figure 5.36: Isotherms for different b with $\epsilon = 0.1$ (left) & $\epsilon = 0.02$ (right), and $Re = 50$, $Pr = 0.71$, $k = 10$

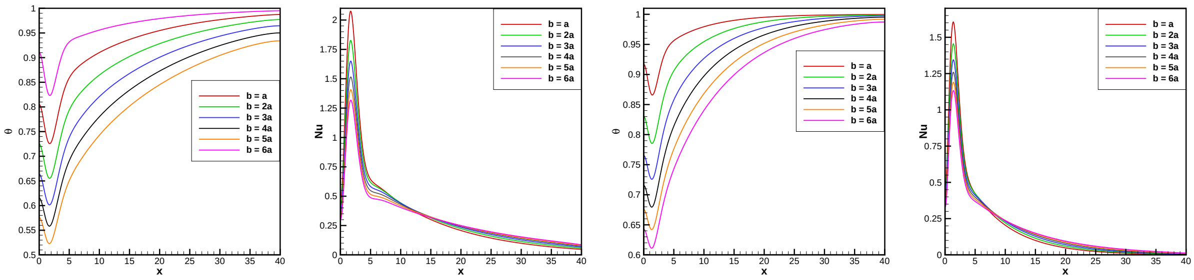

(a) $\epsilon = 0.1$ (b) $\epsilon = 0.02$

Figure 5.37: Variation of temperature and local Nusselt number along the interface w.r.t. slab thickness for (a) $\epsilon = 0.1$, and (b) $\epsilon = 0.02$

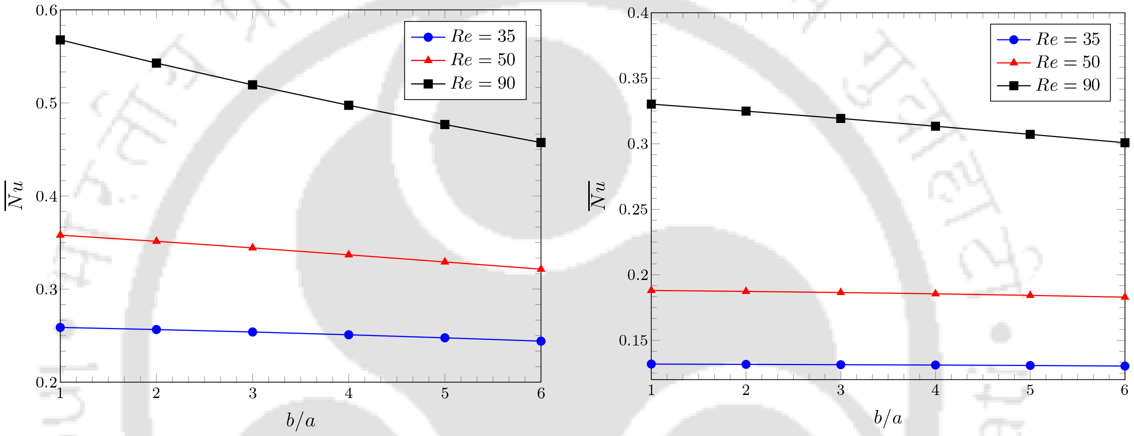

(a) $\epsilon = 0.1$ (b) $\epsilon = 0.02$

Figure 5.38: Variation of average Nusselt number w.r.t. slab thickness and *Re* for (a) $\epsilon = 0.1$, and (b) $\epsilon = 0.02$

5.4 Conclusions

In this chapter we have simulated steady state conjugate heat transfer in suddenly expanding flows. Two commonly encountered geometries were considered - flow in a backward facing step, and flow in a symmetric channel with large expansion ratios. Although the flow phenomena for the BFS configuration, and to some extent flow in a symmetric channel have been investigated over the years, the additional phenomenon of conjugate heat transfer has remained underutilized. The numerical approach used is a combination of a high order FD scheme on compact non-uniform stencil for the ψ-v form of the N-S equations and an HOC scheme for the energy equations. To the best of our knowledge, such an approach towards studying conjugate heat transfer hasn't been adopted previously.

The heat transfer characteristics, in general, are similar for both the cases considered. We systematically studied the effect of Reynolds number (Re), conductivity ratio (k), Prandtl number (Pr), and slab thickness (b) on the heat transfer characteristics. In general, it was observed that in the fluid region, the isotherms congregate in the neighborhood of the reattachment point and on moving downstream it spread in the transverse direction. With an increase in Re this clustering shifts downstream, as the reattachment location shifts downstream with increasing Re. In the solid slab, the temperature decreases in the vertical direction, with the lowest temperature value occurring in the neighborhood of the reattachment point. Convective heat transfer along the fluid-solid interface increases with increasing Re as seen clearly from the graph of local Nusselt number (Nu) along the interface. More significantly, it was seen that the interface temperature is minimum and the convective heat transfer along the interface is maximum at the reattachment point(s).

The influence of conductivity ratio, k, was studied for the range $1 \leq k \leq 1000$ for two different Re in the case of CHT in BFS flow. The flow physics followed a similar pattern for both values of the Re's, with little variation in the isotherms and thermal layer thickness in the fluid beyond $k = 10$. In the slab, however, the temperature was seen to increase with k. Also, as $k \to \infty$, the temperature becomes constant throughout the slab. Convective heat transfer was observed to increase with k, but only to a certain extent ($k = 100$), and there was only a marginal increase for $k > 100$.

The effect of increasing the Prandtl number (Pr) was observed mainly in the inlet of the channel as the relatively greater value of momentum diffusivity inhibits heat diffusion in the channel downstream. In the solid region, at low values of Pr, the isotherms are non-linear, and except in the region near the recirculation zones this non-linearity vanishes with increase in Pr. Also, the temperature in the slab was seen to decrease with increasing Pr.

Lastly, while examining the effect of slab thickness (b), it was observed that heat transfer rate decreased with increase in b owing to the increase in thermal resistance of the slab. Further, with an increase in Re the net heat transfer rate was seen to decrease at a steeper rate with increasing slab thickness.

In case of the symmetric channel, two values of expansion ratios were considered. The expansion ratio plays a significant role in the flow physics thereby affecting the heat transfer characteristics as well. Flow characteristics were briefly discussed, and properties of the recirculation eddies tabulated for the benefit of future researchers. It was observed that overall the net heat transfer rate decreases nearly by 50% as the expansion ratio is increased. This is due to the fact that as the expansion ratio increases, the flow becomes fully developed at an earlier location for $\epsilon = 0.02$. Thus, the core fluid penetrates a greater distance for $\epsilon = 0.1$ which in turn ensures a more even heat distribution, and consequently a higher rate of heat transfer.

CHAPTER 6

FORCED CONVECTION OVER A DIAMOND CYLINDER IN UNIFORM FLOW

6.1 Introduction

Bodies immersed in fluid flow can be characterized as being streamlined or blunt/bluff, depending on its overall shape and structure. A bluff body can be defined as a body that, as a result of its shape, has separated flow over a substantial part of its surface [35]; any body, which when kept in fluid flow, the fluid does not touch the whole boundary of the object. Roshko [135] defined a bluff body as one that resulted in a wide extent of separated flow and is associated with significant drag force as well as vortex-shedding. Flow past bluff bodies is commonly found in nature and engineering applications, for instance flow past an airplane, a submarine, an automobile, or wind blowing past a high-rise building. Thus, over the years, massive research efforts have been undertaken to gain a comprehensive understanding of the fluid flow and heat transfer phenomena past bluff bodies of various cross-sectional geometries. Although much effort has been devoted to analyzing the complex flow physics and thermo-fluid transport phenomenon for a variety of cross-sections (circular, rectangular, square, and elliptical), most of the literature deals with circular geometry. A thorough review of this topic can be found in the works of Williamson [166], and the books of Zdravkovich [176, 177].

It is well known that, in general, beyond a critical Reynolds number flow around slender cylindrical bodies exhibits periodic vortex shedding as a result of the Bénard–von Kármáan instability which then leads to alternate vortex structures known as the von Kármáan vortex street. This phenomena is responsible for fluctuating forces on the body that may cause structural vibrations, acoustic noise emissions, and at times, resonance, which would trigger the failure of structures [97]. Examples of such cylindrical structures in engineering applications include skyscrapers, towering structures, long-spanned bridges, and wires. The frequency associated with the periodic wake, the forces and moment acting on the body, as well as the heat transfer parameters, are a strong function of the body shape and size, Reynolds number of the flow, and the angle of attack [129]. Thus, from an engineering point of view, it is crucial to investigate flow around slender bodies with different shapes.

A square cylinder aligned with all four sides 45^0 to the incoming flow, i.e., with an angle of incidence $\alpha = 45^0$ is commonly referred to as a diamond cylinder. The length scale for such a cylinder is $\sqrt{2}$ times the side of the cylinder. Compared to circular, or square cylinders at zero incidence, it is only in recent years that the diamond configuration has generated interest in the scientific community.

Zaki et.al. [175] presented numerical ($Re \leq 250$) and experimental ($1000 \leq Re \leq 10000$) results for flow past a freely rotatable square cylinder. Sohankar et al. [146] performed 2D finite-volume computations to investigate the flow around a fixed and an inclined square cylinder (angle of incidence, $\alpha = 0^0 - 45^0$) in the laminar vortex-shedding regime ($45 \leq Re \leq 200$). This study explored the effects of boundary conditions, streamwise extents of the domain, angle of incidence, and blockage, β on the flow. Ranjan et.al. [129] used a finite volume method on unstructured grids to investigate flow and heat transfer around a square cylinder at incidence ($\alpha = 0^0 - 45^0$) for $Re = 60 - 150$. They analyzed the dependence of Strouhal number (St), force coefficients (drag and lift), moment coefficient and average Nusselt number on Reynolds number (Re), and angle of incidence (α) for a fixed blockage ratio. Moussaoui et.al. [116] carried out an MRT-Lattice Boltzmann simulation of forced convection heat transfer over a diamond cylinder placed in a differentially horizontal channel for $Re \leq 300$. Yoon etl.al. [171] carried out a numerical investigation to study the effects of Re and angle of incidence α on the characteristics of flow past a square cylinder immersed in cross freestream. They obtained the critical Reynolds number (Re_c) for periodic vortex shedding at each angle of incidence using Stuart–Landau equation, and Re_c for $\alpha = 45^0$ was determined to be 39.

Sohankar and Najafi [145] conducted a numerical investigation to study the control of vortex shedding, heat transfer and the reduction of oscillatory forces from a perforated square cylinder at incidence for $100 \leq Re \leq 200$. Vijaybabu et.al. [161] employed a lattice Boltzmann method to study 2D unsteady flow and heat transfer around a permeable diamond-shaped cylinder placed in an infinite stream of fluid. They reported the formation of twin recirculation regimes behind the cylinder. Kumar et.al. [92] employed a stabilized finite element formulation to investigate the initial separation of laminar boundary layer for steady flow around square cylinders at 4^0 incidence for $Re = 6-8.2$, and identified three distinct separation regimes. In a subsequent work [93], they focused on understanding the physics of the secondary separation phenomenon. Recently, Alam et.al. [1] numerically studied the flow topology, heat transfer, and forces for a square cylinder at $Re = 150$ by altering the corner radius. As functions of the normalized corner radius (varied from $0-1$) and angle of incidence (varied from $0^0 - 45^0$), they identified four major flow patterns.

In a recent work, Jiang [67] carried out a numerical investigation to study three-dimensional (3D) wake transition for flow past a diamond cylinder. Detailed 3D direct numerical simulations (DNS) showed that the wake becomes three-dimensional at $Re_{cr} \sim 121$ and is represented by mode A with global vortex dislocations for $Re = Re_{cr} - 150$. For $Re = 160 - 210$, a mode swapping between modes A and B takes place. With the increase in Re, the mode B structures are destabilised by the streamwise vortices of mode A, and consequently the probability of occurrence of mode A with global vortex dislocations decreases monotonically. For $Re \geq 220$, the wake is dominated by increasingly disordered mode B structures.

The literature review thus far shows that increasing efforts are paid to understand the flow structure past a diamond cylinder. However, the study of forced convection heat transfer phenomena has received comparatively less attention. This study focuses on the forced convection aspect of flow past a diamond cylinder in uniform free stream for $Re = 80$, 100, and 120, where the working fluid is taken to be air (Prandtl number, $Pr = 0.71$). The numerical approach is a combination of a recently developed compact scheme by Kumar and Kalita [95] for the unsteady ψ-v form of the N-S equations, and an

HOC scheme developed by Kalita et.al. [81] for the temperature equation. As in chapter 3, a body fitted Cartesian grid is used for our computations. New insights into the heat transfer phenomena are provided in terms of streamlines, isotherms, vorticity contours, and fast Fourier transform (FFT) plots.

This chapter is organized as follows: In section 6.2 the problem schematic, boundary conditions, and governing equations are presented. In section 6.3 we discuss the discretization procedure of the governing equations. This section has two subsections, 6.3.1 which discusses the generation of a body fitted Cartesian grid for the problem, and 6.3.2 which discusses the solution of algebraic system of equations resulting from discretization of the governing equations. In the next section, i.e., section 6.4, we simulate forced convection over a circular cylinder as a validation exercise. Comparison of relevant parameters with well established results in the literature is presented in this section. In section 6.5 we present the results for the simulation of forced convection over a diamond cylinder, and finally in section 6.6 we conclude this chapter.

6.2 The problem

Consider a heated horizontal diamond cylinder of characteristic length D placed in a uniform free stream (figure 6.1). The free stream velocity is U_0 and the fluid Prandtl number (Pr) is taken to be 0.71. The surface of the cylinder is maintained at a constant temperature of T_s, whereas the free stream has a temperature T_∞. It is assumed that the temperature difference $\Delta T (= T_s - T_\infty)$ has a negligible effect on the fluid properties.

The non-dimensional incompressible N-S and energy equations in the biharmonic form are given by

$$Re\left[\frac{\partial}{\partial t}(\nabla^2\psi)\right] - \left(\frac{\partial^4\psi}{\partial x^4} + 2\frac{\partial^4\psi}{\partial x^2\partial y^2} + \frac{\partial^4\psi}{\partial y^4}\right) = Re\left[\frac{\partial\psi}{\partial y}\left(\frac{\partial^3\psi}{\partial x^3} + \frac{\partial^3\psi}{\partial x\partial y^2}\right) - \frac{\partial\psi}{\partial x}\left(\frac{\partial^3\psi}{\partial x^2\partial y} + \frac{\partial^3\psi}{\partial y^3}\right)\right] \tag{6.1}$$

$$\frac{\partial\theta}{\partial t} + u\frac{\partial\theta}{\partial x} + v\frac{\partial\theta}{\partial y} = \frac{1}{RePr}\left(\frac{\partial^2\theta}{\partial x^2} + \frac{\partial^2\theta}{\partial y^2}\right) \tag{6.2}$$

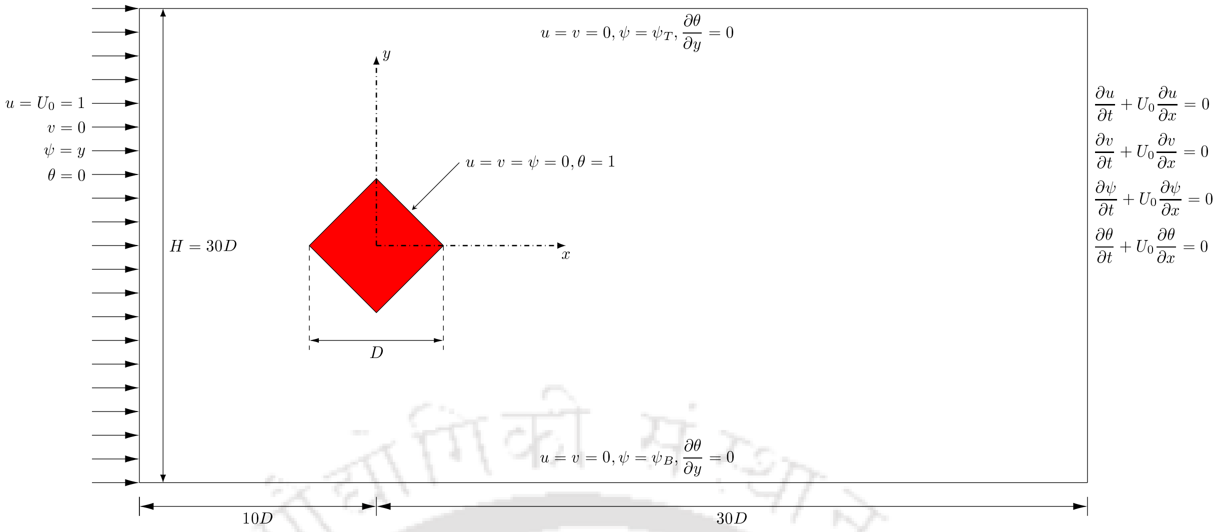

Figure 6.1: Schematic and boundary conditions for forced convection over a diamond cylinder

where $Re = \dfrac{U_0 D}{\nu}$ is the Reynolds number, and $Pr = \dfrac{\nu}{\alpha}$ is the Prandtl number. Here, the following non-dimensional variables have been utilized.

$$x^* = \frac{x}{D}, \quad y^* = \frac{y}{D}, \quad u^* = \frac{u}{U_0}, \quad v^* = \frac{v}{U_0}, \quad \theta = \frac{T - T_\infty}{\Delta T}$$

In our computaions, we have set $D = 1$. Note that the asterisks in equations (6.1) and (6.2) have been dropped for convenience.

Figure 6.1 shows the prescribed boundary conditions in terms of the non-dimensional quantities. The inlet is located upstream at a distance of $10D$ from the center of the cylinder, and the outlet is located downstream at a distance of $30D$ from the center of the cylinder. At the inlet, uniform flow has been prescribed ($u = 1, v = 0, \psi = y, \theta = 0$), whereas convective boundary conditions are imposed at the outlet, i.e., $\dfrac{\partial \phi}{\partial t} + U_0 \dfrac{\partial \phi}{\partial x} = 0$ where ϕ represents either u, v, ψ, or θ. At the upper and lower confining walls, boundary conditions simulating a frictionless wall $\left(\dfrac{\partial u}{\partial y} = v = 0, \psi = \psi_T, \psi_B\right)$ and zero heat flux $\left(\dfrac{\partial \theta}{\partial y} = 0\right)$ have been used. Here, the subscripts T and B denote 'Top' and 'Bottom' respectively. On the surface of the cylinder, $\theta = 1$ and $u = v = \psi = 0$.

Nusselt number is the quantitative parameter indicating heat transfer. The local Nusselt number is given by

$$Nu = -\frac{\partial \theta}{\partial n} \tag{6.3}$$

where n is the direction normal to the cylinder surface.

The surface-average Nusselt number is given by

$$\overline{Nu}_s = \frac{1}{A}\int_S Nu\, dS \tag{6.4}$$

where A is the surface area of the cylinder, and the integral is evaluated over the surface of the cylinder. For the numerical integration, we use Simpson's $\frac{1}{3}^{rd}$ rule on nonuniform grids (see equation (3.19) in chapter 3).

Another important non-dimensional parameter is the Strouhal number (St) which is given by

$$St = \frac{fD}{U_0} \tag{6.5}$$

where f is the frequency of vortex shedding.

6.3 Discretization and Numerical procedure

In section 2.3 of chapter 2 we described in brief the scheme developed by Kumar and Kalita [95] for the unsteady biharmonic form of the N-S equations. We use this scheme for equation (6.1) in combination with the HOC scheme developed by Kalita et.al. [80] (described in section 2.2) for the temperature equation (6.2).

The velocities u and v can be approximated by solving the tri-diagonal systems resulting from the following equations (see Kumar and Kalita [95]) through Thomas algorithm [10]

$$\frac{y_b}{2k}u_{i,j+1} - 2u_{i,j} + \frac{y_f}{2k}u_{i,j-1} = \frac{3\left(\psi_{i,j+1} - \psi_{i.j-1}\right)}{2k} - \frac{3(y_f - y_b)}{2k}\left[\frac{\psi_{i,j+1}}{y_f} + \frac{\psi_{i,j-1}}{y_b} - \left(\frac{1}{y_f} + \frac{1}{y_b}\right)\psi_{i,j}\right] \tag{6.6}$$

$$\frac{x_b}{2h}v_{i+1,j} - 2v_{i,j} + \frac{x_f}{6h}v_{i-1,j} = \frac{3\left(\psi_{i-1,j} - \psi_{i+1,j}\right)}{2h} + \frac{3(x_f - x_b)}{2h}\left[\frac{\psi_{i+1,j}}{x_f} + \frac{\psi_{i-1,j}}{x_b} - \left(\frac{1}{x_f} + \frac{1}{x_b}\right)\psi_{i,j}\right]. \tag{6.7}$$

6.3.1 Grid generation

In this section, we describe in brief the procedure used to generate a body fitted Cartesian grid for the simulation of forced convection over a diamond cylinder. The grid is generated in such a way that the geometry of the diamond cylinder passes through the grid points. The procedure to accomplish this is as follows:

1. First a square block is created (block 1 in figure 6.2), where we generate the grid for the diamond geometry by distributing the points along x- and y- axis with uniform spacing.
2. Then the neighboring blocks, i.e., blocks 2-9 in figure 6.2, generated by using different stretching functions according to the computation requirement, are assembled. During this task, it must be ensured that continuity of the grid lines in each direction of the overall computational domain is maintained.

Figure 6.3 (a) shows the representative grid around block 1 generated by using the procedure outlined above, and figure 6.3 (b) shows a close-up view of the grid inside the blue box.

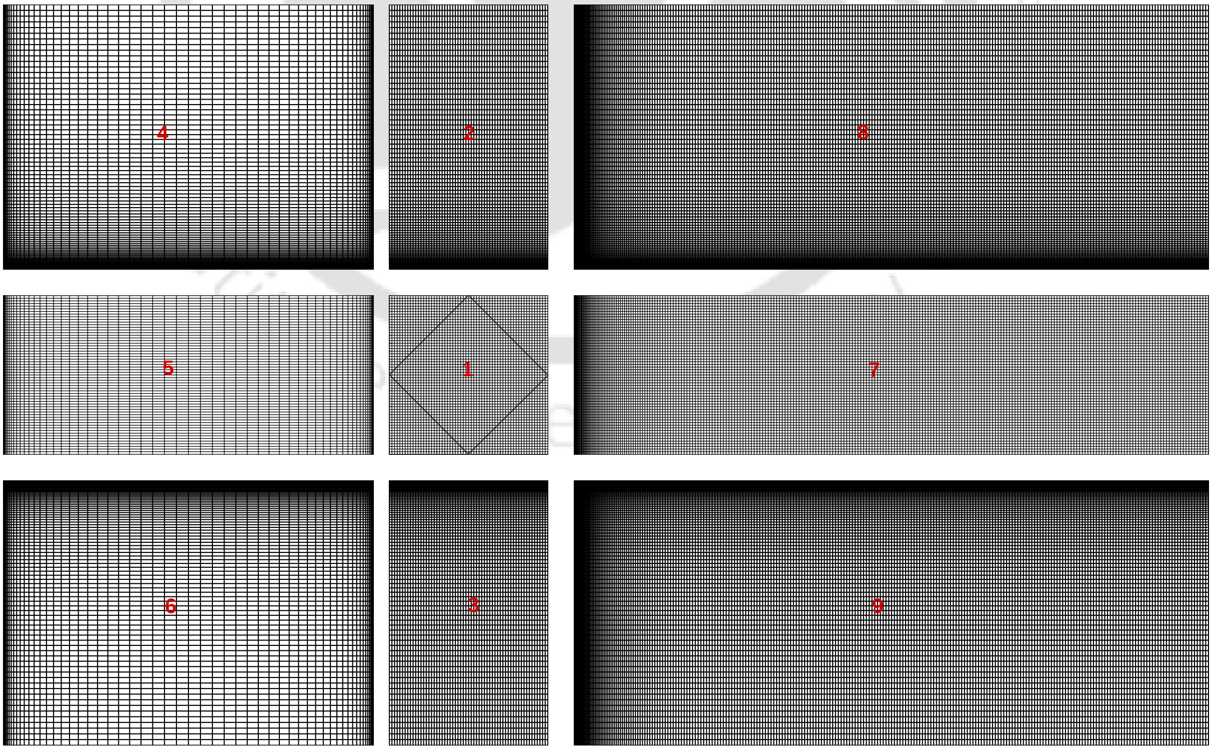

Figure 6.2: Grid used for the diamond cylinder

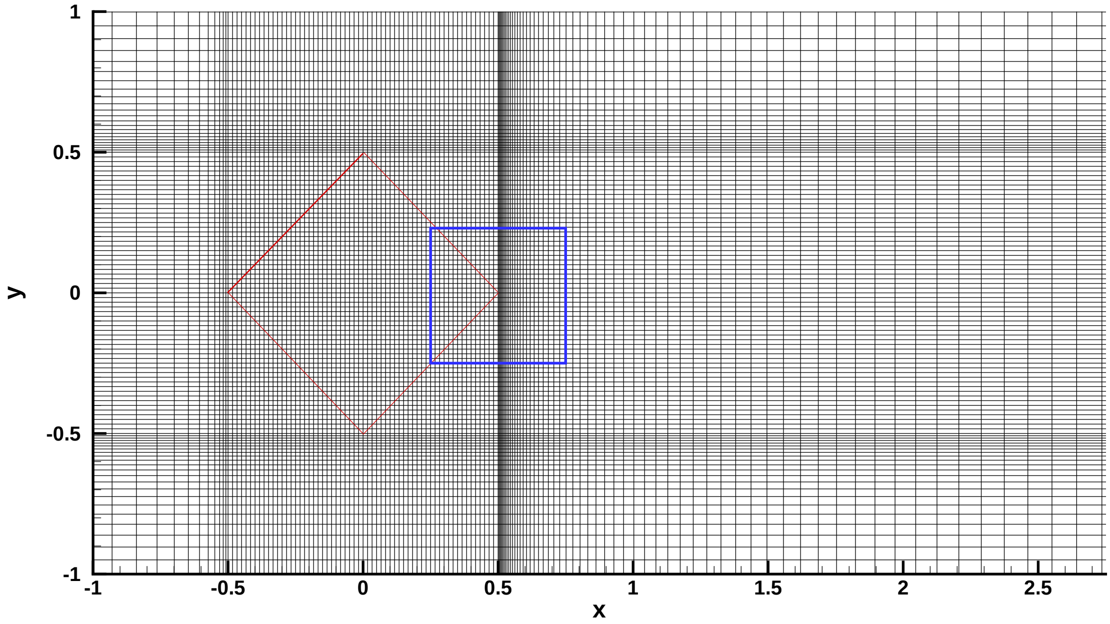

(a) Representative grid.

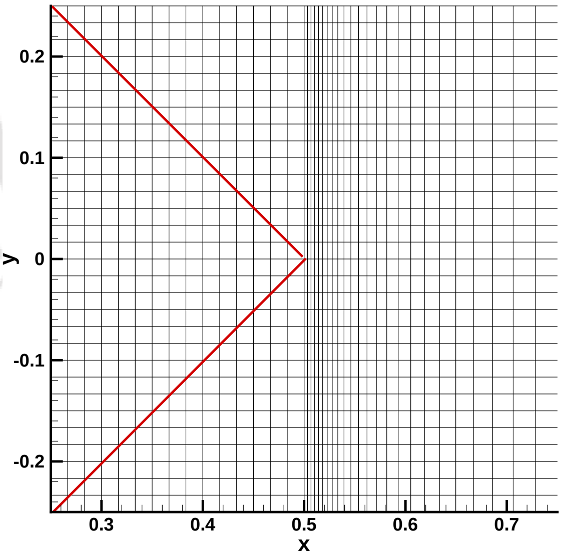

(b) Close-up view of the grid inside the blue box.

Figure 6.3: Representative grid and close-up view of the grid used for diamond cylinder.

6.3.2 Solution of system of equations

We now discuss the solution of system of equations resulting from the discretization of the governing equations. The system of equations resulting from applying the scheme (2.31) to equation (6.1), and the scheme (2.2) to equation (6.2) can be written as

$$A_1\boldsymbol{\psi} = f(Re, \boldsymbol{\psi}^n, \boldsymbol{u}^n, \boldsymbol{v}^n, \boldsymbol{u}^{n+1}, \boldsymbol{v}^{n+1}) \tag{6.8}$$

$$A_2\boldsymbol{\theta} = f(Re, Pr, \boldsymbol{\theta}^n, \boldsymbol{\theta}^{n+1}, \boldsymbol{u}^{n+1}, \boldsymbol{v}^{n+1}) \tag{6.9}$$

where for a grid size of $m \times n$, the coefficient matrices A_1, A_2 are of order mn and ψ^n, θ^n, u^n, v^n, u^{n+1}, v^{n+1}, θ^{n+1} are vectors with mn components. Here the coefficient matrices A_1 and A_2 are asymmetric because of nonuniformity of the grid. The computation of transient state forced convection problems governed by equations (6.1) and (6.2) requires an inner-outer iteration procedure. After initializing u, v, ψ, and θ with appropriate boundary conditions, (6.8) is solved for discrete values of ψ. Once ψ is computed, the velocities u, v can be computed from the third-order approximations (6.6) and (6.7) by employing Thomas algorithm [10] for tridiagonal system of equations. Then θ can be calculated from (6.9). This constitutes one outer iteration or time step.

Note that equation (6.8) contains the $(n+1)^{th}$ time level values of u and v, which is available only when the streamfunction values are known at $(n+1)^{th}$ time level. Here, we follow local linearization technique for which the algorithm is as follows:

1. Initialize $\boldsymbol{\psi}^{n+1}$, $\boldsymbol{u}^{n+1}$, $\boldsymbol{v}^{n+1}$ and $\boldsymbol{\theta}^{n+1}$ (with $\boldsymbol{\psi}^n$, $\boldsymbol{u}^n$, $\boldsymbol{v}^n$, $\boldsymbol{\theta}^n$).

2. Set $\boldsymbol{\psi}^{n+1}_{\text{old}} = \boldsymbol{\psi}^n$, $\boldsymbol{\theta}^{n+1}_{\text{old}} = \boldsymbol{\theta}^n$.

3. Compute $\boldsymbol{\psi}^{n+1}$ using equation (6.8).

4. Compute $\boldsymbol{u}^{n+1}$ and $\boldsymbol{v}^{n+1}$ using equations (6.6) and (6.7).

5. Compute $\boldsymbol{\theta}^{n+1}$ using equation (6.9).

6. If max $|\boldsymbol{\psi}^{(n+1)} - \boldsymbol{\psi}^{(n+1)}_{\text{old}}|<$ tolerance limit, then stop; else repeat step 2-6 until convergence.

The inner iterations involve solving matrix equations (6.8) and (6.9) at each time step by iterative solvers. We have used bicongugate gradient stabilized (BiCGStab) method with preconditioning, where Incomplete LU decomposition is used as a preconditioner. Preconditioning was particularly useful for $Re \geq 100$ where we have used the Lis library [105]. The inner iterations were stopped when the Euclidean norms of the residual vectors $\boldsymbol{r}_1 = \boldsymbol{f} - A_1\boldsymbol{\psi}$ and $\boldsymbol{r}_2 = \boldsymbol{b} - A_2\boldsymbol{\theta}$ arising out of equations (6.8)-(6.9) fell below 0.5×10^{-9}. All of our computations were carried out on a Intel core i7 based PC with 16 GB RAM.

6.4 Code Validation - Forced convection over a circular cylinder at low Reynolds numbers

In order to validate our code, we simulate forced convection over a horizontal circular cylinder at low Reynolds numbers. As will be seen shortly, the results from the present computation are an excellent match with well established results in the literature.

As in the previous section, the grid for the case of circular cylinder is generated in such a way that the circular geometry passes through the grid points (see Kumar and Kalita [95, 96]). Note that the computational domain as well as the boundary conditions for this case is the same as shown in figure 6.1. The only difference is that the diamond cylinder has been replaced by a circular cylinder of characteristic length (diameter) D.

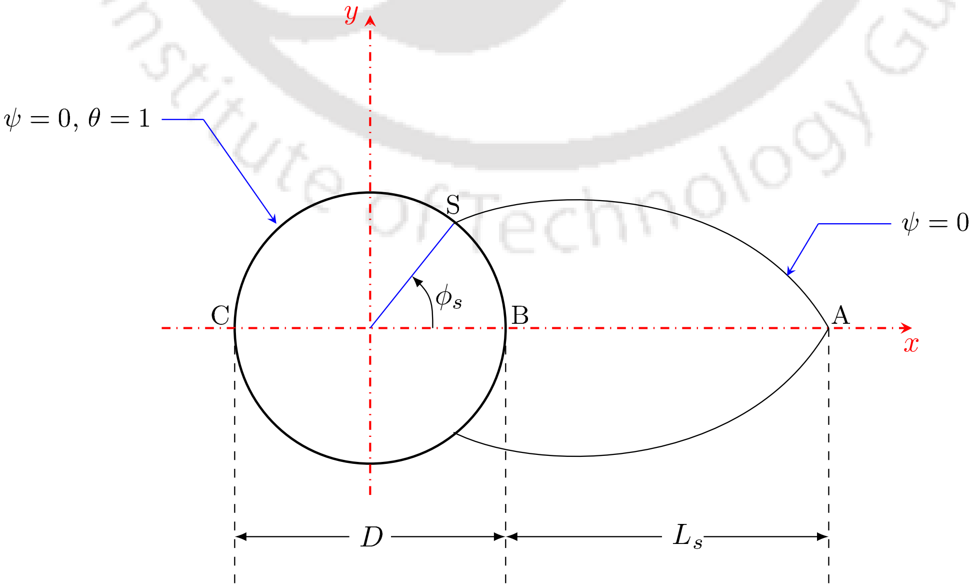

Figure 6.4: Schematic of wake-bubble geometry for the circular cylinder

Figure 6.4 shows the typical wake-bubble geometry of the flow. Points A, B, and C denote wake stagnation point, back stagnation point, and front stagnation point respectively. Point S is the separation point, ϕ_s is the separation angle, and L_s is the eddy length.

Table 6.1: Comparison of eddy length (L_s)

Re	L_s			
	Present	Biswas and Sarkar [24]	Takami and Keller [152]	Dennis and Chang [39]
15	1.16	1.189	1.162	–
20	1.884	1.865	1.844	1.88
30	3.156	3.226	3.223	–
35	3.689	3.793	–	–
40	4.583	4.424	4.650	4.69

Table 6.2: Comparison of separation angle (ϕ_s)

Re	L_s			
	Present	Biswas and Sarkar [24]	Takami and Keller [152]	Dennis and Chang [39]
15	39^0	38.57^0	38.6^0	–
20	42^0	43.64^0	43.65^0	43.7^0
30	48^0	49.29^0	49.6^0	–
35	50.99^0	51.35^0	–	–
40	53.99^0	53.10^0	53.55^0	53.8^0

Table 6.3: Comparison of surface averaged Nusselt number ($\overline{Nu_s}$)

Re	$\overline{Nu_s}$			
	Present	Biswas and Sarkar [24]	Jafroudi and Yang [64]	Apelt and Ledwich [12]
15	2.39332	2.1809	2.176	2.193
20	2.63401	2.4483	2.433	–
30	3.15940	2.8877	2.850	–
35	3.36211	3.0772	–	–
40	3.48791	3.2351	3.2	3.255

For this comparison exercise, simulations are carried out for *Re* = 15, 20, 30, 35, and 40. Previous works (Takami and Keller [152], Dennis and Chang [39], Apelt and Ledwich [12], Jafroudi and Yang [64],) have shown that the flow is steady for these values of *Re*'s. In the present case steady-state has been reached through time marching. The values of eddy length (L_s), separation angle (ϕ_s), and surface averaged Nusselt number ($\overline{Nu_s}$) from the present computation have been compared with well established results in

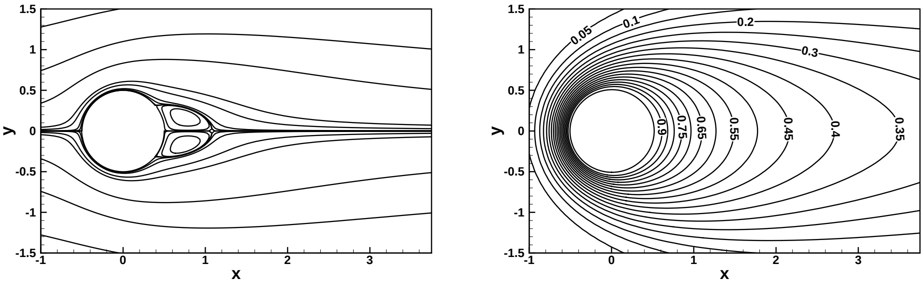

(a) Streamlines (left) and Isotherms (right) for $Re = 15$

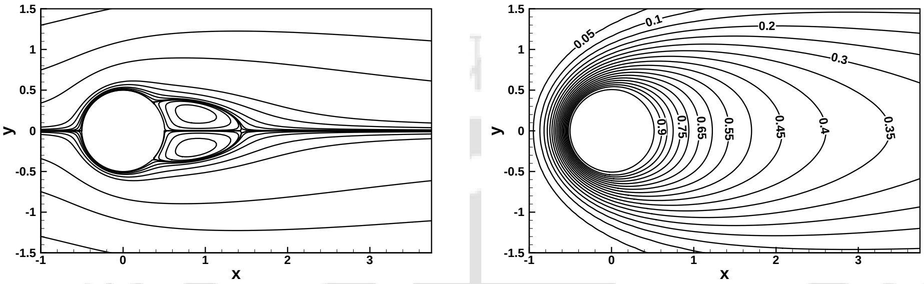

(b) Streamlines (left) and Isotherms (right) for $Re = 20$

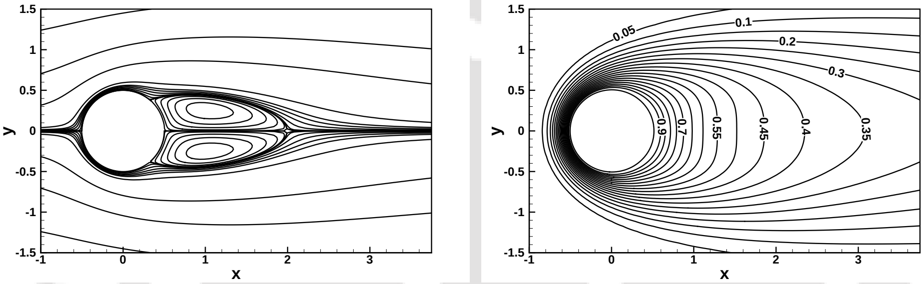

(c) Streamlines (left) and Isotherms (right) for $Re = 30$

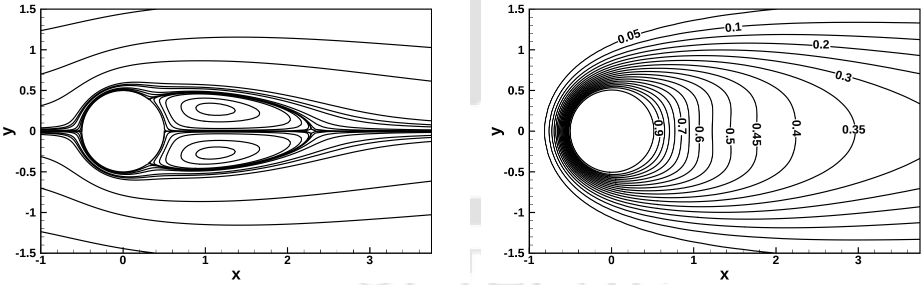

(d) Streamlines (left) and Isotherms (right) for $Re = 35$

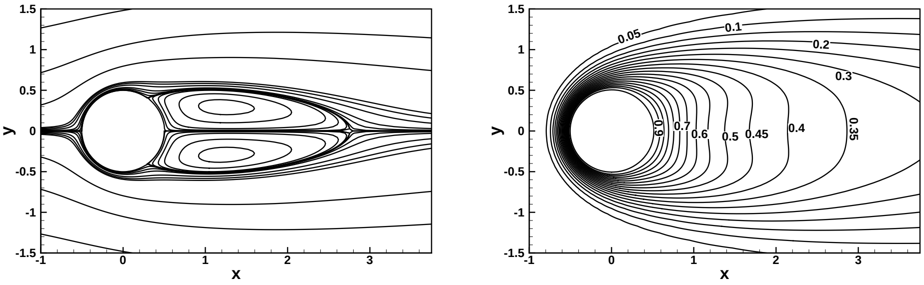

(e) Streamlines (left) and Isotherms (right) for $Re = 40$

Figure 6.5: Streamlines and Isotherms for different Reynolds numbers.

tables 6.1, 6.2, and 6.3 respectively. Figures 6.5 (a)-(e) show the streamlines and isotherms for $Re = 15 - 40$. One can clearly see the increase in the eddy length, L_s, with an increase in Re. Also, the increase in convective heat transfer is evident from the flattening of the isotherms and thinning of thermal boundary layer in figures 6.5 (a)-(e), as well as from the values of $\overline{Nu_s}$ in table 6.3.

6.5 Results and Discussion

In this section, we present the results for our computations, which were carried out for $Re = 80$, 100, and 120 with $Pr = 0.71$. All our computations have been carried out on a grid of size 391×241.

Before we present the streamlines, isotherms, and vorticity contours, we present a comparison of the Strouhal number, St for the three values of Re in table 6.4. As we can see the present values are a good match with established values, especially the recent work of Jiang [67].

Table 6.4: Comparison of Strouhal number (St)

Re	St			
	Present	Jiang [67]	Sohankar et.al. [146]	Yadav et.al. [170]
80	0.16236	0.1643	–	–
100	0.17313	0.1757	0.1788	0.1811
120	0.1812	0.18408	–	–

Figure 6.6 shows the evolution of streamlines for $Re = 120$ at different instants of non-dimensional time t. The flow goes through various stages until the commencement of periodic vortex shedding. For the sake of brevity, the time evolution of the flow for only one Re is shown, but all the Re's chosen in this study exhibit similar flow evolution; only the duration of different stages vary for each Re. In the initial stages, the flow remains symmetric about the x- axis, and two symmetrical vortices appear on the surface of the cylinder. With time, the wake grows in size and strength (see figures 6.6 (a)-6.6(d)). At a certain time, the wake loses its symmetry, and waviness starts to appear in the streamlines (figures 6.6 (e), 6.6 (f)). Moments later, the vortices behind the cylinder start oscillating gradually (figures 6.6(g)-6.6(l)), and vortex shedding starts leading to the development of von Kármáan vortex street. Note that figures 6.6 (j) - 6.6 (l) represent a typical vortex

shedding cycle; these are half a vortex shedding cycle apart, and figure 6.6 (k) is a mirror image of figure 6.6 (j) and 6.6 (l). A magnified view of these figures in the vicinity of the cylinder is provided in figure 6.9 (a). Figures 6.9 (b) and 6.9 (c) show the corresponding vorticity contours and isotherms respectively.

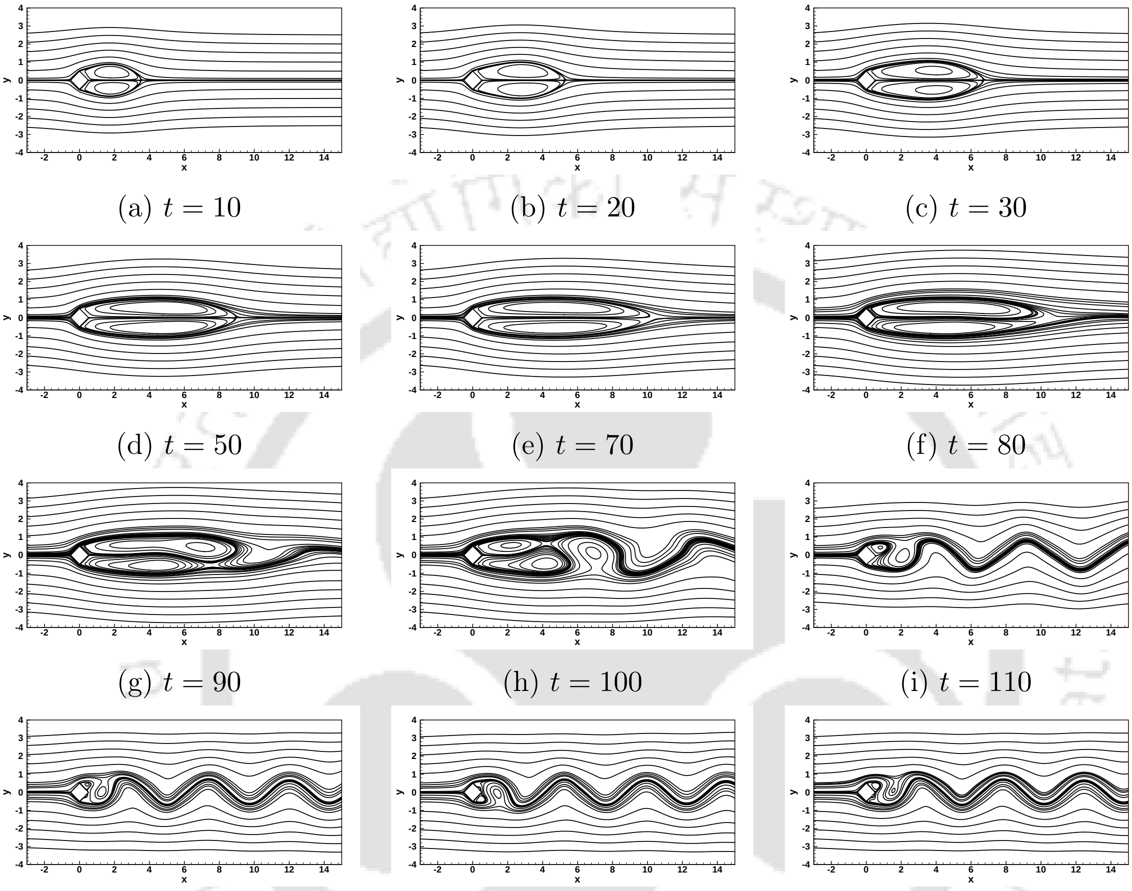

(a) $t = 10$ (b) $t = 20$ (c) $t = 30$

(d) $t = 50$ (e) $t = 70$ (f) $t = 80$

(g) $t = 90$ (h) $t = 100$ (i) $t = 110$

(j) $t = 158$ (k) $t = 161$ (l) $t = 164$

Figure 6.6: Streamline evolution for $Re = 120$

Figures 6.7 and 6.8 show the vorticity contours and isotherms respectively at different instants of non-dimensional time t. These contour plots are for the same values of t for which the streamlines have been shown in figure 6.6. The vortex shedding phenomena for one vortex shedding cycle can be clearly seen in figures 6.7 (j) - 6.7 (l). Note that the vorticity values are post-processed.

The instantaneous isotherms also depict vortex shedding (figures 6.8 (h) - 6.8 (l)). Note that the vorticity contours are structurally similar to the corresponding isotherms, which implies that the shedding vortices carry the heat away with them from the heated cylinder. The core of the vortex contains most of the heat, and the heat gets diffused into

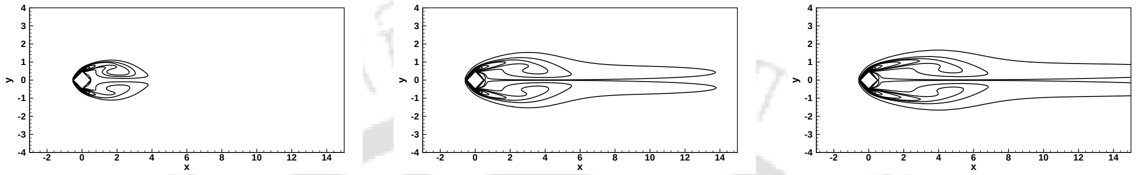

(a) $t = 10$ (b) $t = 20$ (c) $t = 30$

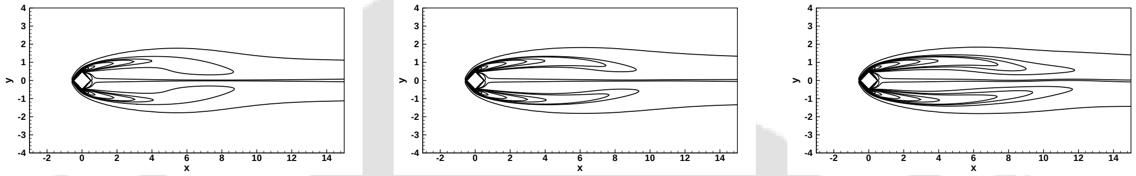

(d) $t = 50$ (e) $t = 70$ (f) $t = 80$

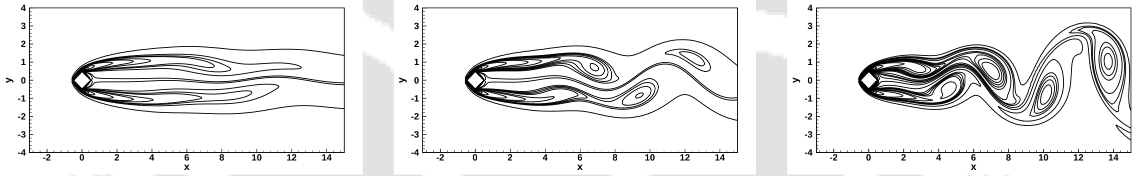

(g) $t = 90$ (h) $t = 100$ (i) $t = 110$

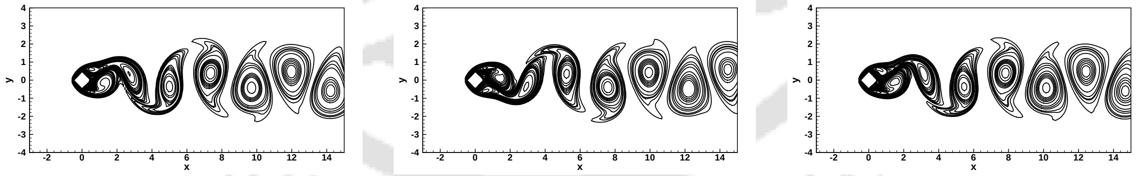

(j) $t = 158$ (k) $t = 161$ (l) $t = 164$

Figure 6.7: Vorticity contours at different times for $Re = 120$

the free stream as the vortices are convected away from the cylinder. One of the ways to demonstrate this is to carry out a Fast Fourier Transform (FFT) of the transverse component of velocity and temperature at different locations downstream of the cylinder. Figure 6.10 shows the FFT of the y-velocity v at four different locations viz. $x = 5$, $x = 10$, $x = 15$, and $x = 20$ for $Re = 120$. The primary frequency f_P is the vortex shedding frequency. One can observe that the value of f_P remains same in all the locations. However the amplitude decreases as one moves from $x = 5$ to $x = 20$. This shows the diffusion of energy downstream of the cylinder.

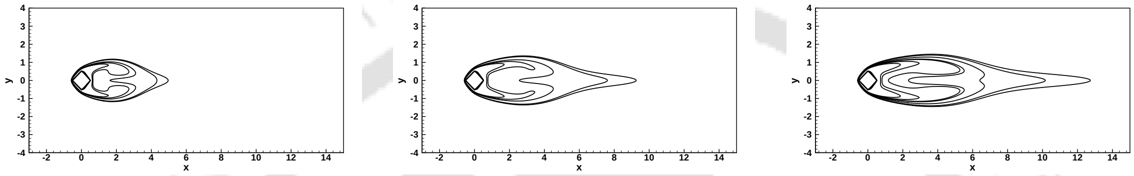

(a) $t = 10$ (b) $t = 20$ (c) $t = 30$

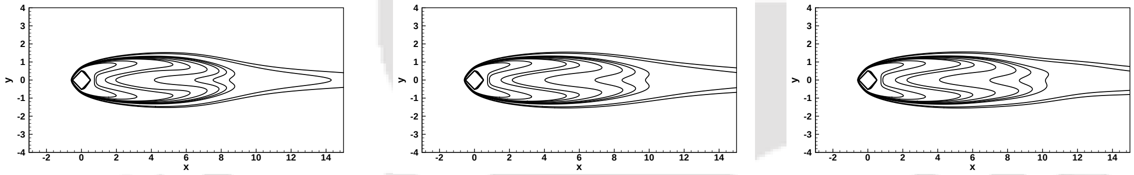

(d) $t = 50$ (e) $t = 70$ (f) $t = 80$

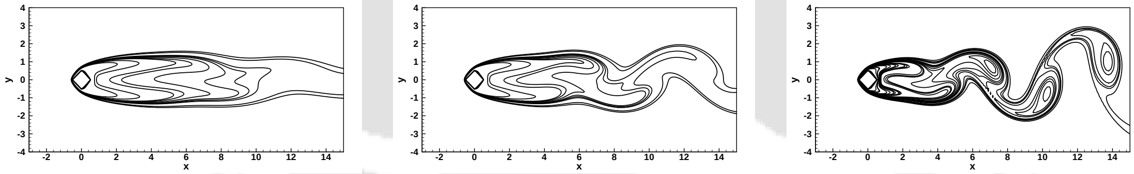

(g) $t = 90$ (h) $t = 100$ (i) $t = 110$

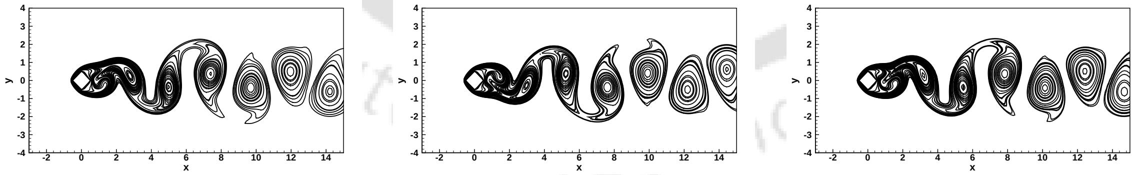

(j) $t = 158$ (k) $t = 161$ (l) $t = 164$

Figure 6.8: Isotherms at different times for $Re = 120$

Figure 6.11 shows the instantaneous isotherms in the wake of the cylinder. We can observe that the hot fluid is captured in the core of the shed vortices, as can be seen from the existence of local maxima of the contour values at the vortex centers. Also, one can see the heat being diffused into the free stream in the far wake.

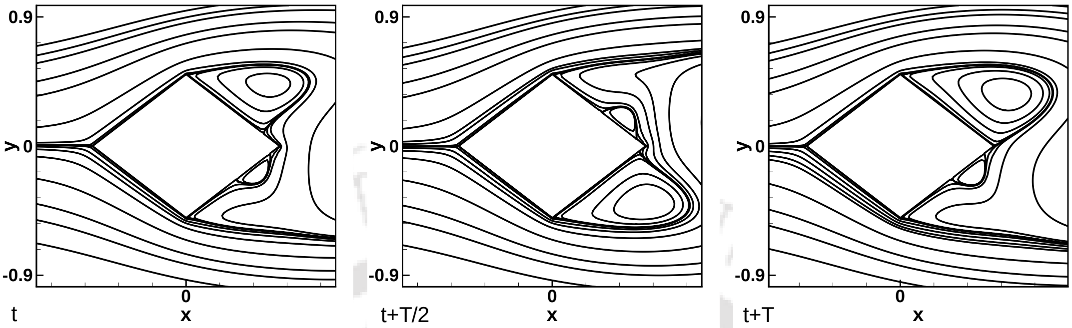

(a) Magnified view of streamlines

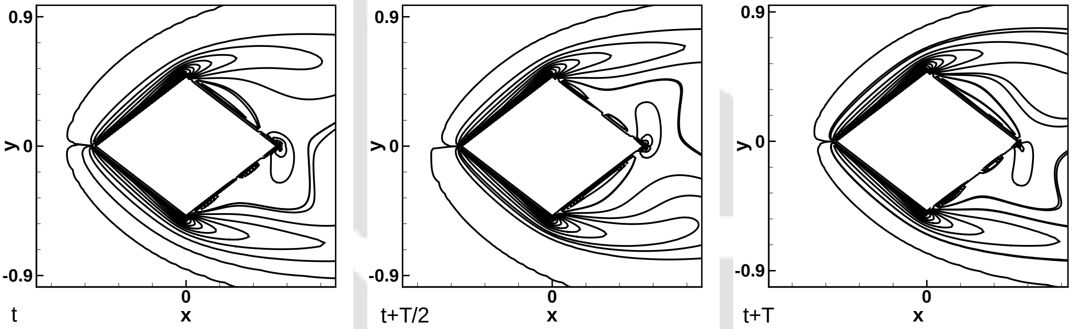

(b) Magnified view of vorticity

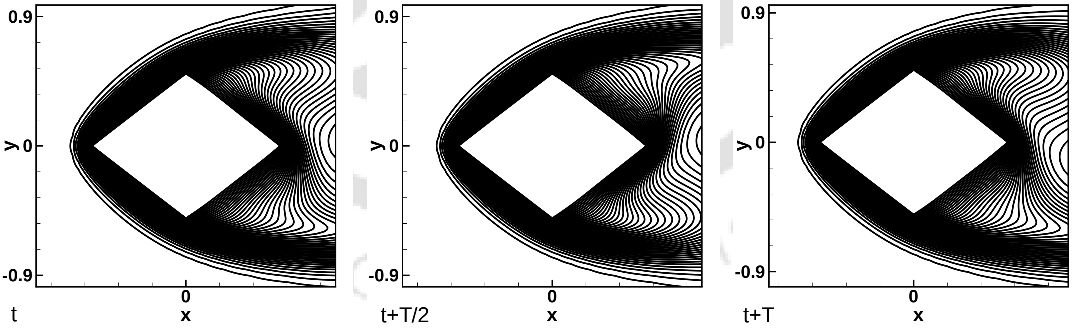

(c) Magnified view of isotherms

Figure 6.9: Magnified view of (a) streamlines (b) vorticity and (c) isotherms of a complete shedding cycle in the vicinity of the cylinder.

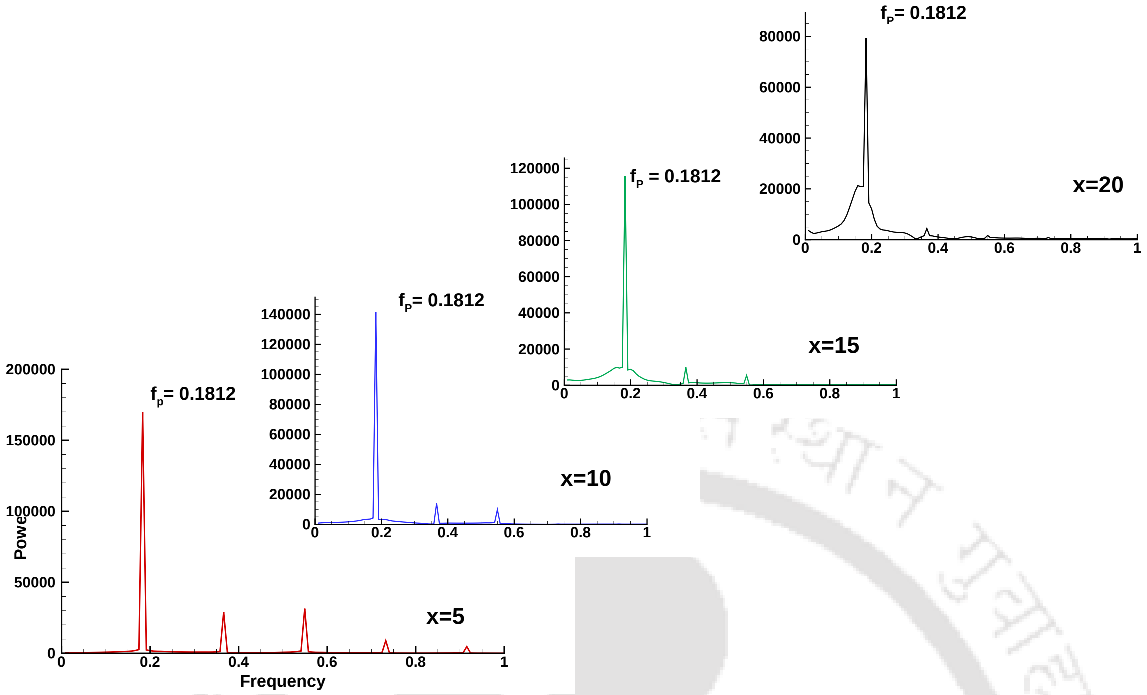

Figure 6.10: Fast Fourier Transform of transverse component of velocity for $Re = 120$ at $x = 5,10,15,$ and 20.

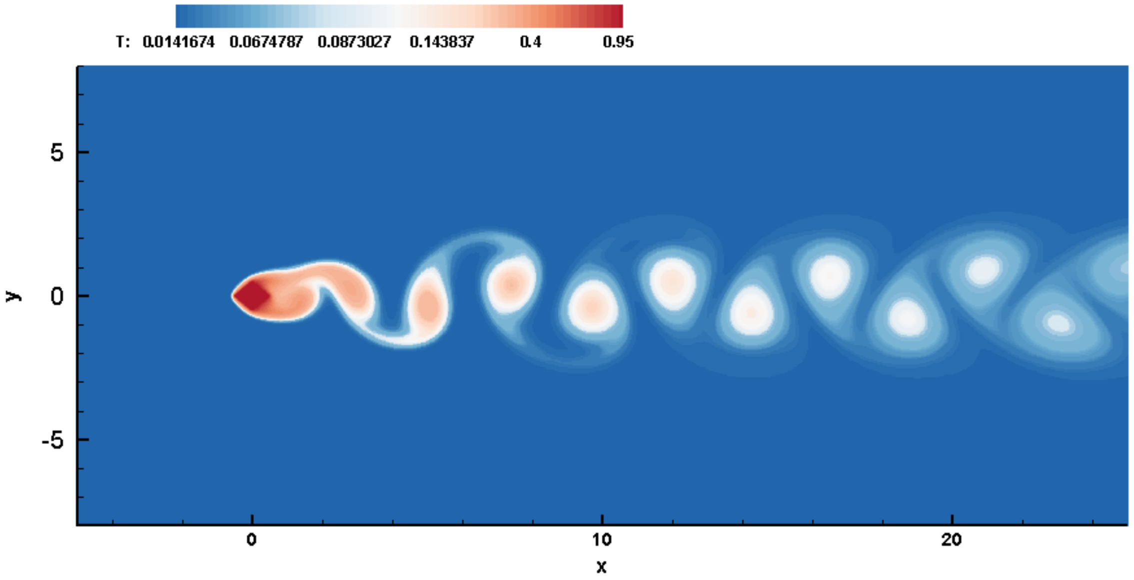

Figure 6.11: Instantaneous isotherms for $Re = 120$.

Figure 6.12 shows the variation of the surface average Nusselt number $\overline{Nu}_s$ with time for (a) $Re = 80$ (b) $Re = 100$ and (c) $Re = 120$. There is a sharp drop in $\overline{Nu}_s$ in the beginning of the flow, then there is a steady decline in the value of $\overline{Nu}_s$ till around $t = 35$, after which the value of $\overline{Nu_s}$ remains nearly constant for most of the flow duration. As expected, there is an increase in the heat transfer rate with Re, indicated by an increase in $\overline{Nu_s}$. The interesting part about the plots Nusselt number is that $\overline{Nu_s}$ shows a periodic variation after a certain time. This periodicity commences from the moment of vortex shedding. Clearly, as the Re increases, sooner the fluctuation happens. This periodicity is shown in the inset of figures 6.12 (b) and 6.12 (c). Note that the frequency of this fluctuation is greater for the higher value of Re. A plausible explanation for this phenomena can be gleaned from an FFT plot of the Nusselt number. Let us consider the FFT of $\overline{Nu_s}$ for $Re = 100$, as shown in figure 6.13. The primary frequency here is 0.34642, which is $\approx 2 \times St$ for $Re = 100$. As mentioned previously, the isotherms and vorticity contours are struturally similar owing to the fact that the shed vortices convect the heat from the cylinder downstream. Vorticity values alternate between positive and negative, whereas the temperature always remains positive. Thus, it can be expected that the frequency of isotherms being shed would be twice the vortex shedding frequency. The FFT of $\overline{Nu_s}$ corroborates this fact. The periodicity of $\overline{Nu_s}$ seen in figure 6.12 commences from the moment of vortex shedding.

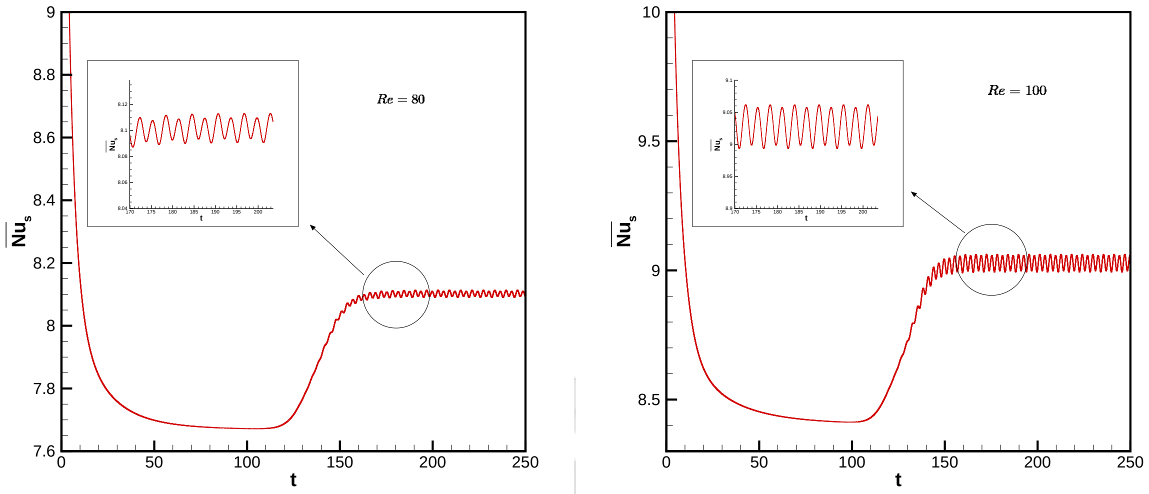

(a) $Re = 80$ (b) $Re = 100$

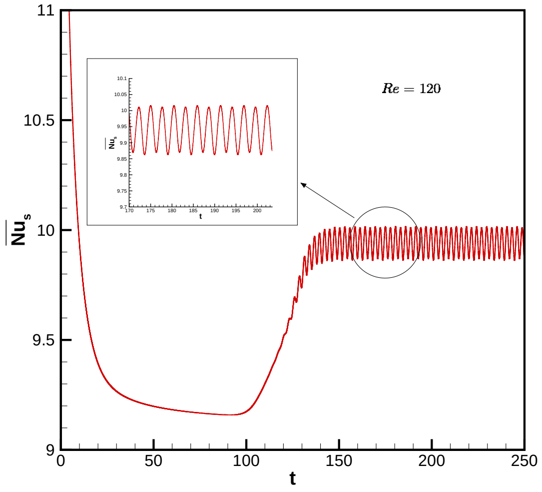

(c) $Re = 120$

Figure 6.12: Time history of $\overline{Nu_s}$ for (a) $Re = 80$, (b) $Re = 100$, and (c) $Re = 120$.

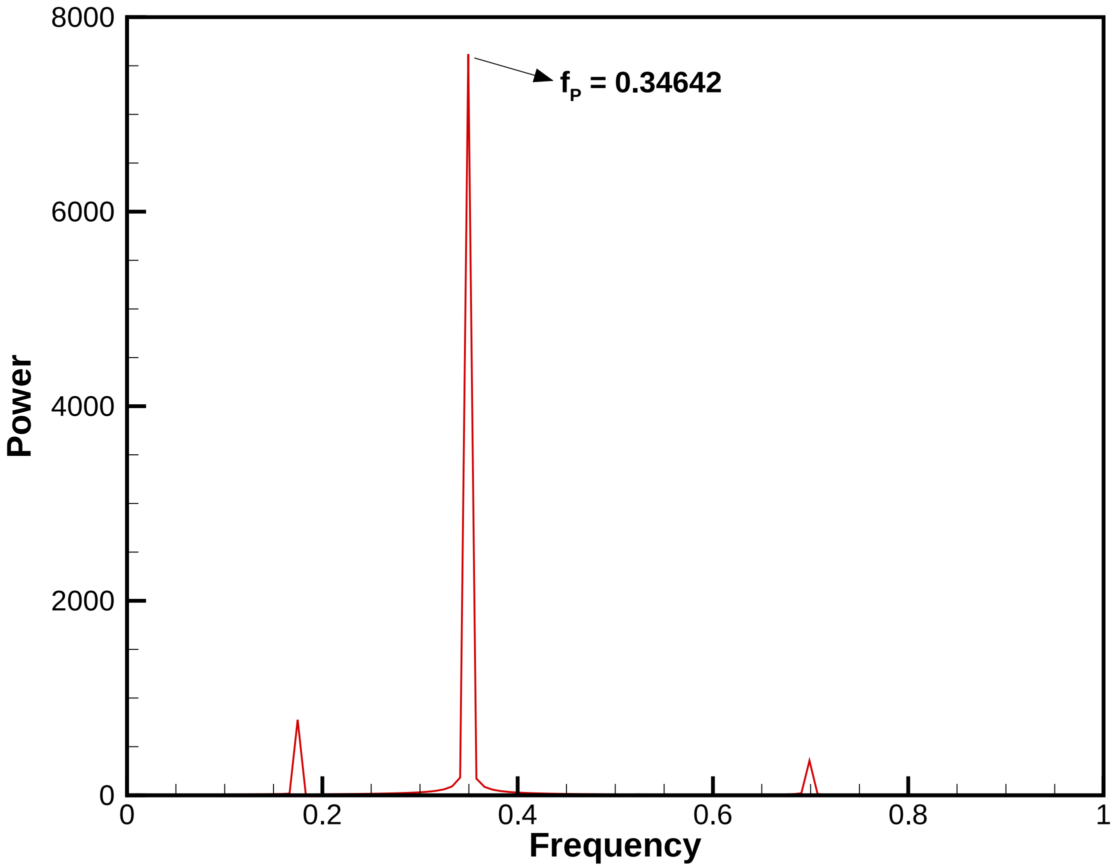

Figure 6.13: FFT of $\overline{Nu_s}$ for $Re = 100$.

6.6 Conclusions

In this chapter we have simulated forced convection over a heated diamond cylinder in a uniform free stream. The working fluid was taken as air with $Pr = 0.71$, and computations were performed for three values of Reynolds numbers ($Re = 80$, 100, 120). The numerical approach used was a combination of a compact finite difference scheme developed by Kumar and Kalita [95] for the transient ψ-v form of the N-S equations, and the HOC scheme of Kalita et.al. [81] for the temperature equation. Similar to the approach adopted in chapter 3, a body fitted Cartesian grid was used in the computations.

Firstly, we validated our code by simulating steady state forced convection over a circular cylinder for $15 \leq Re \leq 40$. The comparison exercise carried out for the values of separation angle (ϕ_s), wake length (L_s), and surface average Nusselt number ($\overline{Nu_s}$)

showed that the present results were in excellent agreement with well established results in the literature.

Then we computed forced convection over a diamond cylinder, and presented our results in terms of streamlines, isotherms, and vorticity (calculated in post-processing) contours. We showed the time evolution of streamlines for $Re = 120$, and described in brief the various stages up to periodic vortex shedding. The plots of isotherms and vorticity contours were nearly identical owing to the fact that the shed vortices convect the heat away from the cylinder. The core of the vortices hold most of the heat, and in the far wake of the cylinder the heat from the vortices are diffused into the free stream. This observation was also inferred from an FFT plot of the y- velocity taken at four different locations. The variation of surface average Nusselt number with time showed an interesting phenomenon previously unreported (to the best of our knowledge); after remaining nearly constant, $\overline{Nu_s}$ showed a periodic variation after a certain time for $Re = 100, 120$. This periodicity commenced sooner for $Re = 120$, and its frequency was also higher for $Re = 120$.

CHAPTER 7

CONCLUSIONS

7.1 Observations and Remarks

This dissertation is concerned with the application of compact/HOC schemes on nonuniform grids to heat and mass transfer problems of varying complexity. An overwhelming majority of researchers have applied compact/HOC schemes solely to fluid flow problems, ignoring the heat and mass transfer phenomena widely prevalent in nature and engineering applications. Moreover, even when applied to heat and mass transfer problems, the use of grid transformation while dealing with complex geometries presents certain disadvantages such as increase in computational time and complexity, and the computations are prone to errors. This work not only provides the contours for the application of compact and HOC schemes to heat and mass transfer problems but also presents a viable alternative to grid transformation when dealing with problems having non-rectangular geometries. In the following paragraphs the work done in thesis is described briefly, and relevant comments are made thereafter.

Firstly, we investigated natural convection around heated bodies of different shapes embedded in a square enclosure using the ψ-v form of the N-S equations. We reconstructed a recent scheme developed by Kumar and Kalita [94], and a fourth order compact scheme developed by Kalita et.al. [80] for the energy equation. Probably for the first time, a body fitted Cartesian grid has been used for the computations for such studies, thus avoiding the need for grid transformation and also gaining significant computational simplicity.

Computations were carried out for $10^3 \leq Ra \leq 10^7$ for both cases of circular as well as diamond cylinder. In the case of the circular cylinder, we further established the existence of secondary vortices at the four corners of the enclosure for $10^3 \leq Ra \leq 10^6$, and at all positions of the cylinder. We verified that these secondary corner vortices as well as other vortices reported in the literature are non-spurious by observing the changes in sign of the pressure gradient along the surfaces. Note that these secondary corner vortices have not been reported in any previous study in the literature. Lastly, we have provided a brief comparison of the flow structure and heat transfer characteristics on a circular cylinder vis a vis its diamond cylinder counterpart under the same conditions prescribed on the boundaries.

Secondly, we numerically investigated the problem of double diffusive natural convection in a vertical porous annulus by applying a reconstructed compact HOC scheme on non-uniform grids. We have also proposed a novel approach to explicitly approximate the velocities. Using the Darcy model, we investigated the influence of aspect ratio (A), radius ratio (κ), Lewis number (Le), buoyancy ratio (N), and thermal Rayleigh number (Ra) on the flow. Note that for the range of parameters for which numerical results are available, our simulations are extremely close both in terms of contour plots and the values of Nusselt and Sherwood numbers. While earlier studies concentrated on the description of the steady-state flow, for a certain range of parameters we have reported the transient flow as well. Extensive simulations for various parameters were carried out to discern a clearer picture of heat and mass transfer characteristics.

Next, we have investigated steady state conjugate heat transfer in suddenly expanding flow using the combination of a high order finite scheme on compact non-uniform stencil for the ψ-v form of the N-S equations and an HOC scheme for the energy equations. Two geometries were considered in this study - a backward facing step (BFS), and a symmetric channel with large expansion ratios. While establishing new benchmark results for the BFS flow case, we also arrived new insights into the heat transfer phenomena for flow in a suddenly expanding channel. To the best of our knowledge, the ψ-v approach used in this work for investigating conjugate heat transfer hasn't been used previously.

Finally, simulations were carried out to study forced convection over a diamond cylinder placed in a uniform free stream using a transient scheme [95] for the unsteady ψ - v

form of the N-S equations. Validation of the code was carried out for the case of forced convection over a circular cylinder in a uniform free stream at low Reynolds numbers. The present results were an excellent match with well established numerical and experimental results. For the case of diamond cylinder, we were able to capture different modes of flow structures previously unreported in the literature. In addition, we have also carried out Fast Fourier Transform (FFT) analysis to establish the veracity of the modes. We have again demonstrated the use of body fitted cartesian grids as a viable alternative for computing fluid flow and heat transfer phenomena over bluff bodies.

The above discussion clearly establishes the achieving of all the objectives set out at the beginning of this thesis. It has also opened up a host of other interesting research possibilities which can be listed in a nutshell as follows:

7.2 Scope for future work

1. Two of the problems considered in this thesis involved bluff bodies which were symmetric about either x- or y- axis. Simulation of heat and mass transfer problems associated with asymmetric bluff bodies such as inclined elliptic cylinder, airfoil with different angle of attack promises to be an intriguing area of research.

2. This thesis has used the Darcy model to simulate double-diffusive natural convection in a vertical porous annulus. Including Soret and Dufour effect in addition to using the Darcy-Brinkman-Forchheimer model presents a unique opportunity to develop an HOC scheme to deal with such problems.

3. This work presented ways to deal with problems involving natural and forced convection over bluff bodies. Thus, simulation of mixed convection over bluff bodies is the next logical choice in the application of compact and HOC schemes to heat and mass transfer problems. The biharmonic form of the N-S equations for mixed convection problems can be written as

$$Re\left[\frac{\partial}{\partial t}(\nabla^2\psi)\right] + Re[v\nabla^2 u - u\nabla^2 v] = \frac{\partial^4\psi}{\partial x^4} + 2\frac{\partial^4\psi}{\partial x^2\partial y^2} + \frac{\partial^4\psi}{\partial y^4} - Ri\frac{\partial\theta}{\partial x} \tag{7.1}$$

where $Ri = \dfrac{Gr}{Re^2}$ is the Richardson number, and Gr is the Grashof number. Efforts are currently underway to develop a high order compact scheme to numerically solve mixed convection problems governed by equation (7.1)

4. Some compact and HOC schemes exist for the 3D biharmonic form of the N-S equations and convection-diffusion type equations in nonuniform grids. It would be interesting to see if the body-fitted grid framework could be extended to 3D heat and mass transfer problems. The biharmonic form of the unsteady N-S equations for 3D incompressible viscous flows is given by

$$\frac{\partial}{\partial t}(\nabla^2 \boldsymbol{\Psi}) + [(\nabla \times \boldsymbol{\Psi}) \cdot \nabla]\nabla^2 \boldsymbol{\Psi} - (\nabla^2 \boldsymbol{\Psi} \cdot \nabla)(\nabla \times \boldsymbol{\Psi}) = \frac{1}{Re}\nabla^4 \boldsymbol{\Psi} \tag{7.2}$$

where $\boldsymbol{\Psi}$ is the 3D streamfunction vector, given by $\mathbf{u} = \nabla \times \boldsymbol{\Psi}$, $\mathbf{u} = (u, v, w)$ is the velocity vector, and Re is the Reynolds number.

Altas et.al. [6] had proposed a compact finite difference scheme for numerically solving steady-state 3D biharmonic equations of the form

$$\nabla^4 \phi(x, y, z) = f(x, y, z) \tag{7.3}$$

Each of the three components of equation (7.2) can be put in the following form

$$\frac{1}{Re}\nabla^4 \phi = \frac{\partial}{\partial t}(\nabla^2 \phi) + f(x, y, z) \tag{7.4}$$

which is exactly of the form (7.3) except for the time derivative term. Kalita and Gupta [82] had proposed that following the approach utilized for developing a compact high order scheme for the transient 2D biharmonic form of the N-S equations, a high order compact scheme for the 3D version could be developed as well.

Additionally, Kalita [75] had developed a spatially fourth order accurate and temporally second order accurate super compact high order scheme for 3D convectionreaction-diffusion equations of the form

$$a\frac{\partial\phi}{\partial t}-\nabla^2\phi+c(x,y,z,t)\frac{\partial\phi}{\partial x}+d(x,y,z,t)\frac{\partial\phi}{\partial y}+e(x,y,z,t)\frac{\partial\phi}{\partial z}+f(x,y,z,t)\phi=g(x,y,z,t) \tag{7.5}$$

Following the approach of combining the biharmonic form of the N-S equations with the energy equation for heat transfer problems outlined in this work, one can also strive to extend this approach to 3D heat and mass transfer problems. The major challenge would be utilize body-fitted Cartesian grids for flow configurations involving non-rectangular bluff bodies.

BIBLIOGRAPHY

[1] M. M. Alam, T. Abdelhamid, and A. Sohankar. Effect of cylinder corner radius and attack angle on heat transfer and flow topology. *International Journal of Mechanical Sciences*, 175:105566, 2020.

[2] F. Alavyoon. On natural convection in vertical porous enclosures due to prescribed fluxes of heat and mass at the vertical boundaries. *International Journal of Heat and Mass Transfer*, 36(10):2479 – 2498, 1993.

[3] F. Alavyoon, M. Yoshio, and K. Shigeo. On natural convection in vertical porous enclosures due to opposing fluxes of heat and mass prescribed at the vertical walls. *International Journal of Heat and Mass Transfer*, 37(2):195 – 206, 1994.

[4] N. Alleborn, K. Nandakumar, H. Raszillier, and F. Durst. Further contributions on the two-dimensional flow in a sudden expansion. *Journal of Fluid Mechanics*, 330:169–188, 1997.

[5] Z. Alloui, L. Dufau, H. Beji, and P. Vasseur. Multiple steady states in a porous enclosure partially heated and fully salted from below. *International Journal of Thermal Sciences*, 48(3):521 – 534, 2009.

[6] I. Altas, J. Erhel, and M. M. Gupta. High accuracy solution of three-dimensional biharmonic equations. *Numerical Algorithms*, 29(1):1–19, 2002.

[7] A. Altawallbeh, N. Saeid, and I. Hashim. Magnetic field effect on natural convection in a porous cavity heating from below and salting from side. *Advances in Mechanical Engineering*, 5:183079, 2013.

[8] A. Altawallbeh, N. Saeid, and I. Hashim. Numerical solution of double-diffusive natural convection in a porous cavity partially heated from belowand partially salted from the side. *Journal of Porous Media*, 16(10):903–919, 2013.

[9] A. Amahmid, M. Hasnaoui, M. Mamou, and P. Vasseur. Boundary layer flows in a vertical porous enclosure induced by opposing buoyancy forces. *International Journal of Heat and Mass Transfer*, 42(19):3599 – 3608, 1999.

[10] D. M. Anderson and S. H. Davis. Two-fluid viscous flow in a corner. *Journal of Fluid Mechanics*, 257:1–31, 1993.

[11] J. D. Anderson and J. Wendt. *Computational Fluid Dynamics*, volume 206. Springer, 1995.

[12] C. Apelt and M. Ledwich. Heat transfer in transient and unsteady flows past a heated circular cylinder in the range $1 \leq R \leq 40$. *Journal of Fluid Mechanics*, 95(4):761–777, 1979.

[13] B. Armaly, F. Durst, J. Pereira, and B. Schönung. Experimental and theoretical investigation of backward-facing step flow. *Journal of Fluid Mechanics*, 127:473–496, 1983.

[14] R. Arun Kumar and G. Rajesh. Physics of vacuum generation in zero-secondary flow ejectors. *Physics of Fluids*, 30(6):066102, 2018.

[15] A. Bahloul, M. A. Yahiaoui, P. Vasseur, R. Bennacer, and H. Beji. Natural convection of a two-component fluid in porous media bounded by tall concentric vertical cylinders. *Journal of Applied Mechanics*, 73(1):26–33, 05 2005.

[16] I. Barton. A numerical study of flow over a confined backward-facing step. *International Journal for Numerical Methods in Fluids*, 21(8):653–665, 1995.

[17] F. Battaglia, S. J. Tavener, A. K. Kulkarni, and C. L. Merkle. Bifurcation of low reynolds number flows in symmetric channels. *AIAA Journal*, 35(1):99–105, 1997.

[18] H. Beji, R. Bennacer, R. Duval, and P. Vasseur. Double-diffusive natural convection in a vertical porous annulus. *Numerical Heat Transfer, Part A: Applications*, 36(2):153–170, 1999.

[19] M. Ben-Artzi, J.-P. Croisille, and D. Fishelov. A high order compact scheme for the pure-streamfunction formulation of the Navier-Stokes equations. *Journal of Scientific Computing*, 42(2):216–250, 2010.

[20] M. Ben-Artzi, J.-P. Croisille, D. Fishelov, and S. Trachtenberg. A pure-compact scheme for the streamfunction formulation of Navier-Stokes equations. *Journal of Computational Physics*, 205(2):640–664, 2005.

[21] S. Benissaad and N. Ouazaa. Analytical and numerical study of double diffusive natural convection in a confined porous medium subjected to heat and mass fluxes. *Journal of Porous Media*, 15(10):909–926, 2012.

[22] M. Benzeghiba, S. Chikh, and A. Campo. Thermosolutal convection in a partly porous vertical annular cavity. *Journal of Heat Transfer*, 125(4):703–715, 2003.

[23] G. Biswas, M. Breuer, and F. Durst. Backward-facing step flows for various expansion ratios at low and moderate Reynolds numbers. *Journal of Fluids Engineering*, 126(3):362–374, 2004.

[24] G. Biswas and S. Sarkar. Effect of thermal buoyancy on vortex shedding past a circular cylinder in cross-flow at low reynolds numbers. *International Journal of Heat and Mass Transfer*, 52(7-8):1897–1912, 2009.

[25] S. Biswas and J. C. Kalita. Moffatt eddies in the driven cavity: a quantification study by an HOC approach. *Computers & Mathematics with Applications*, 76(3):471–487, 2018.

[26] M. Bourich, A. Amahmid, and M. Hasnaoui. Double diffusive convection in a porous enclosure submitted to cross gradients of temperature and concentration. *Energy Conversion and Management*, 45(11):1655 – 1670, 2004.

[27] M. Bourich, M. Hasnaoui, and A. Amahmid. Double-diffusive natural convection in a porous enclosure partially heated from below and differentially salted. *International Journal of Heat and Fluid Flow*, 25(6):1034 – 1046, 2004.

[28] M. Bourich, M. Hasnaoui, and A. Amahmid. A scale analysis of thermosolutal convection in a saturated porous enclosure submitted to vertical temperature and horizontal concentration gradients. *Energy Conversion and Management*, 45(18-19):2795–2811, 2004.

[29] F. Cao, Y. Ge, and H.-W. Sun. Partial semi-coarsening multigrid method based on the HOC scheme on nonuniform grids for the convection–diffusion problems. *International Journal of Computer Mathematics*, 94(12):2356–2372, 2017.

[30] D. R. Chenoweth and S. Paolucci. Natural convection in an enclosed vertical air layer with large horizontal temperature differences. *Journal of Fluid Mechanics*, 169:173–210, 1986.

[31] W. Cherdron, F. Durst, and J. H. Whitelaw. Asymmetric flows and instabilities in symmetric ducts with sudden expansions. *Journal of Fluid Mechanics*, 84(1):13–31, 1978.

[32] T. Chiang and T. W. Sheu. A numerical revisit of backward-facing step flow problem. *Physics of Fluids*, 11(4):862–874, 1999.

[33] K. Chida. Surface temperature of a flat plate of finite thickness under conjugate laminar forced convection heat transfer condition. *International Journal of Heat and Mass Transfer*, 43(4):639 – 642, 2000.

[34] W. K. Chiu, C. J. Richards, and Y. Jaluria. Experimental and numerical study of conjugate heat transfer in a horizontal channel heated from below. *Journal of Heat Transfer*, 123:688 – 697, 2001.

[35] N. R. Council. *Twenty-First Symposium on Naval Hydrodynamics.* The National Academies Press, Washington, DC, 1997.

[36] A. K. De and A. Dalal. A numerical study of natural convection around a square, horizontal, heated cylinder placed in an enclosure. *International Journal of Heat and Mass Transfer*, 49(23-24):4608–4623, 2006.

[37] G. de Vahl Davis. Natural convection of air in a square cavity: A bench mark numerical solution. *International Journal for Numerical Methods in Fluids*, 3:249 – 264, 05 1983.

[38] D. Deka and S. Sen. A new transformation free generalized (5,5)HOC discretization of transient Navier-Stokes/Boussinesq equations on nonuniform grids. *International Journal of Heat and Mass Transfer*, 171:120821, 2021.

[39] S. Dennis and G.-Z. Chang. Numerical solutions for steady flow past a circular cylinder at Reynolds numbers up to 100. *Journal of Fluid Mechanics*, 42(3):471–489, 1970.

[40] S. Dennis and J. Hudson. Compact h^4 finite-difference approximations to Operators of Navier-Stokes Type. *Journal of Computational Physics*, 85(2):390 – 416, 1989.

[41] D. Drikakis. Bifurcation phenomena in incompressible sudden expansion flows. *Physics of Fluids*, 9(1):76–87, 1997.

[42] F. Durst, A. Melling, and J. Whitelaw. Low Reynolds number flow over a plane symmetric sudden expansion. *Journal of Fluid Mechanics*, 64(1):111–128, 1974.

[43] F. Durst, J. Pereira, and C. Tropea. The plane symmetric sudden-expansion flow at low reynolds numbers. *Journal of Fluid Mechanics*, 248:567–581, 1993.

[44] S. Dutta and J. C. Kalita. Heat and mass transfer characteristics of double-diffusive natural convection in a porous annulus: A higher-order compact approach. *Heat Transfer*, 51(1):140–169, 2022.

[45] S. Dutta, P. Kumar, and J. C. Kalita. Streamfunction-velocity computation of natural convection around heated bodies placed in a square enclosure. *International Journal of Heat and Mass Transfer*, 152:119550, 2020.

[46] S. Dutta, P. Kumar, and J. C. Kalita. ψ - v computation of steady-state conjugate heat transfer in backward-facing step flow. *Heat Transfer*, 50(6):5714–5743, 2021.

[47] E. Erturk. Numerical solutions of 2-D steady incompressible flow over a backward-facing step, part I: High Reynolds number solutions. *Computers & Fluids*, 37(6):633 – 655, 2008.

[48] R. Fearn, T. Mullin, and K. Cliffe. Nonlinear flow phenomena in a symmetric sudden expansion. *Journal of Fluid Mechanics*, 211:595–608, 1990.

[49] A. G. Fedorov and R. Viskanta. Three-dimensional conjugate heat transfer in the microchannel heat sink for electronic packaging. *International Journal of Heat and Mass Transfer*, 43(3):399–415, 2000.

[50] T. Gao, J. Liang, and M. Sun. Symmetric/asymmetric separation transition in a supersonic combustor with single-side expansion. *Physics of Fluids*, 29(12):126102, 2017.

[51] D. K. Gartling. A test problem for outflow boundary conditions - flow over a backward-facing step. *International Journal for Numerical Methods in Fluids*, 11(7):953 – 967, 1990.

[52] M. Ghil, J.-G. Liu, C. Wang, and S. Wang. Boundary-layer separation and adverse pressure gradient for 2-D viscous incompressible flow. *Physica D: Nonlinear Phenomena*, 197(1):149 – 173, 2004.

[53] J. P. Guerrero and R. Cotta. Benchmark integral transform results for flow over a backward-facing step. *Computers & fluids*, 25(5):527–540, 1996.

[54] M. M. Gupta. High accuracy solutions of incompressible Navier-Stokes equations. *Journal of Computational Physics*, 93(2):343 – 359, 1991.

[55] M. M. Gupta and J. C. Kalita. A new paradigm for solving Navier-Stokes equations: streamfunction-velocity formulation. *Journal of Computational Physics*, 207(1):52 – 68, 2005.

[56] M. M. Gupta and J. C. Kalita. New paradigm continued: Further computations with streamfunction-velocity formulations for solving Navier-Stokes equations. *Communications in Applied Analysis*, 10(4):461–490, 2006.

[57] M. R. Hajmohammadi and S. S. Nourazar. Conjugate forced convection heat transfer from a heated flat plate of finite thickness and temperature- dependent thermal conductivity. *Heat Transfer Engineering*, 35(9):863–874, 2014.

[58] T. Hawa and Z. Rusak. Viscous flow in a slightly asymmetric channel with a sudden expansion. *Physics of Fluids*, 12(9):2257–2267, 2000.

[59] T. Hawa and Z. Rusak. The dynamics of a laminar flow in a symmetric channel with a sudden expansion. *Journal of Fluid Mechanics*, 436:283–320, 2001.

[60] N. Himrane, D. Ameziani, M. El Ganaoui, and H. Ragueb. Some insights on unsteady double diffusive natural convection of porous medium in vertical open-ended cylinder. *Arabian Journal for Science and Engineering*, 44(2):1379–1392, 2019.

[61] J. D. Hofman. *Numerical Methods for Engineers and Scientists*. CRC Press, 2001.

[62] D. B. Ingham and I. Pop. *Transport in Porous Media III*. Elsevier, 2005.

[63] A. Ja and A. Cheddadi. Numerical investigation of buoyancy balance effect on thermosolutal convection in a horizontal annular porous cavity. *The European Physical Journal E*, 42(9):1–12, 2019.

[64] H. Jafroudi and H. Yang. Steady laminar forced convection from a circular cylinder. *Journal of Computational Physics*, 65(1):46–56, 1986.

[65] S. Jahangeer, M. Ramis, and G. Jilani. Conjugate heat transfer analysis of a heat generating vertical plate. *International Journal of Heat and Mass Transfer*, 50(1-2):85–93, 2007.

[66] D. Jaiswal and J. C. Kalita. Novel high-order compact approach for dynamics of spiral waves in excitable media. *Applied Mathematical Modelling*, 77:341–359, 2020.

[67] H. Jiang. Three-dimensional wake transition of a diamond-shaped cylinder. *Journal of Fluid Mechanics*, 918, 2021.

[68] G. Jilani, S. Jayaraj, and M. Adeel Ahmad. Conjugate forced convection-conduction heat transfer analysis of a heat generating vertical cylinder. *International Journal of Heat and Mass Transfer*, 45(2):331 – 341, 2002.

[69] K. Johannsen. On the validity of the Boussinesq approximation for the Elder problem. *Computational Geosciences*, 7(3):169–182, 2003.

[70] B. John, P. Senthilkumar, and S. Sadasivan. Applied and theoretical aspects of conjugate heat transfer analysis: a review. *Archives of Computational Methods in Engineering*, 26(2):475–489, 2019.

[71] G. Juncu. Unsteady conjugate heat/mass transfer from a circular cylinder in laminar crossflow at low Reynolds numbers. *International Journal of Heat and Mass Transfer*, 47(10):2469 – 2480, 2004.

[72] G. Juncu. Conjugate heat/mass transfer from a circular cylinder with an internal heat/mass source in laminar crossflow at low Reynolds numbers. *International Journal of Heat and Mass Transfer*, 48(2):419–424, 2005.

[73] G. Juncu. Unsteady conjugate forced convection heat/mass transfer from a finite flat plate. *International Journal of Thermal Sciences*, 47(8):972 – 984, 2008.

[74] J. C. Kalita. Effects of clustering on the simulation of incompressible viscous flows. *Engineering Applications of Computational Fluid Mechanics*, 1(1):36–48, 2007.

[75] J. C. Kalita. A super-compact higher order scheme for the unsteady 3D incompressible viscous flows. *Computational and Applied Mathematics*, 33(3):717–738, 2014.

[76] J. C. Kalita and P. Chhabra. An improved (9,5) higher order compact scheme for the transient two-dimensional convection–diffusion equation. *International Journal for Numerical Methods in Fluids*, 51:703 – 717, 2006.

[77] J. C. Kalita, D. C. Dalal, and A. K. Dass. Fully compact higher-order computation of steady-state natural convection in a square cavity. *Physial Review E*, 64:066703, Nov 2001.

[78] J. C. Kalita, D. C. Dalal, and A. K. Dass. A class of higher order compact schemes for the unsteady two-dimensional convection-diffusion equations with variable convection coefficients. *International Journal for Numerical Methods in Fluids*, 38:1111 – 1131, 2002.

[79] J. C. Kalita and A. K. Dass. Higher order compact simulation of double-diffusive natural convection in a vertical porous annulus. *Engineering Applications of Computational Fluid Mechanics*, 5(3):357–371, 2011.

[80] J. C. Kalita, A. K. Dass, and D. C. Dalal. A transformation-free HOC scheme for steady convection–diffusion on non-uniform grids. *International Journal for Numerical Methods in Fluids*, 44(1):33–53, 2004.

[81] J. C. Kalita, A. K. Dass, and N. Nidhi. An efficient transient Navier-Stokes solver on compact nonuniform space grids. *Journal of Computational and Applied Mathematics*, 214:148–162, Apr. 2008.

[82] J. C. Kalita and M. M. Gupta. A streamfunction–velocity approach for 2D transient incompressible viscous flows. *International Journal for Numerical Methods in Fluids*, 62(3):237–266, 2010.

[83] J. C. Kalita and S. Sen. The (9,5) HOC formulation for the transient navier–stokes equations in primitive variable. *International Journal for Numerical Methods in Fluids*, 55(4):387–406, 2007.

[84] L. Kalla, M. Mamou, P. Vasseur, and L. Robillard. Multiple solutions for double diffusive convection in a shallow porous cavity with vertical fluxes of heat and mass. *International Journal of Heat and Mass Transfer*, 44(23):4493 – 4504, 2001.

[85] P. R. Kanna and M. K. Das. Conjugate forced convection heat transfer from a flat plate by laminar plane wall jet flow. *International Journal of Heat and Mass Transfer*, 48(14):2896 – 2910, 2005.

[86] S. J. Karabelas. Conformal cartesian grids for symmetric bodies: A novel boundary fitted grid method. *Journal of Applied & Computational Mathematics*, 4(4):1–15, 2015.

[87] R. Karvinen. Some new results for conjugated heat transfer in a flat plate. *International Journal of Heat and Mass Transfer*, 21(9):1261–1264, 1978.

[88] M. V. Karwe and Y. Jaluria. Numerical Simulation of Thermal Transport Associated With a Continuously Moving Flat Sheet in Materials Processing. *Journal of Heat Transfer*, 113(3):612–619, 08 1991.

[89] B. Kim, D. Lee, M. Ha, and H. Yoon. A numerical study of natural convection in a square enclosure with a circular cylinder at different vertical locations. *International Journal of Heat and Mass Transfer*, 51(7-8):1888–1906, 2008.

[90] J. Kim and P. Moin. Application of a fractional-step method to incompressible Navier-Stokes equations. *Journal of Computational Physics*, 59(2):308–323, 1985.

[91] J. Kramer, R. Jecl, and L. Škerget. Boundary domain integral method for the study of double diffusive natural convection in porous media. *Engineering Analysis with Boundary Elements*, 31(11):897–905, 2007.

[92] D. Kumar, K. Sourav, S. Sen, and P. K. Yadav. Steady separation of flow from an inclined square cylinder with sharp and rounded base. *Computers & Fluids*, 171:29–40, 2018.

[93] D. Kumar, K. Sourav, P. K. Yadav, and S. Sen. Understanding the secondary separation from an inclined square cylinder with sharp and rounded trailing edges. *Physics of Fluids*, 31(7):073607, 2019.

[94] P. Kumar and J. C. Kalita. A transformation-free $\psi - v$ formulation of the Navier-Stokes equations on compact nonuniform grids. *Journal of Computational and Applied Mathematics*, 2019.

[95] P. Kumar and J. C. Kalita. An efficient ψ-v scheme for two-dimensional laminar flow past bluff bodies on compact nonuniform grids. *International Journal for Numerical Methods in Fluids*, 92(12):1723–1752, 2020.

[96] P. Kumar and J. C. Kalita. A comprehensive study of secondary and tertiary vortex phenomena of flow past a circular cylinder: A cartesian grid approach. *Physics of Fluids*, 33(5):053608, 2021.

[97] A. Kumar De and A. Dalal. Numerical simulation of unconfined flow past a triangular cylinder. *International Journal for Numerical Methods in Fluids*, 52(7):801–821, 2006.

[98] R. Kupferman. A central-difference scheme for a pure stream function formulation of incompressible viscous flow. *SIAM Journal on Scientific Computing*, 23(1):1–18, 2001.

[99] P. Lax and B. Wendroff. Systems of Conservation Laws. *Communications on Pure and Applied Mathematics*, 13(2):217–237, 1960.

[100] A. Lehtinen and R. Karvinen. Analytical solution for a class of flat plate conjugate convective heat transfer problems. *Frontiers in Heat and Mass Transfer*, 2(4), 2011.

[101] P. LeQuéré. Accurate solutions to the square thermally driven cavity at high rayleigh number. *Computers & Fluids*, 20(1):29 – 41, 1991.

[102] W. Li, Z. Chi, R. Kan, J. Ren, and H. Jiang. Experimental investigation of heat transfer dependency on conjugate and convective thermal boundary conditions in pin fin channel. In *Turbo Expo: Power for Land, Sea, and Air*, volume 56710, page V05AT10A013. American Society of Mechanical Engineers, 2015.

[103] D. Lin. Unsteady natural convection heat and mass transfer in a saturated porous enclosure. *Wärme-und Stoffübertragung*, 28(1-2):49–56, 1993.

[104] M. Lindstedt and R. Karvinen. Conjugated heat transfer from a uniformly heated plate and a plate fin with uniform base heat flux. *International Journal of Heat and Mass Transfer*, 107:89 – 95, 2017.

[105] Lis: Library of iterative solvers for linear systems. `http://www.ssisc.org/lis/`.

[106] A. Luikov, V. Aleksashenko, and A. Aleksashenko. Analytical methods of solution of conjugated problems in convective heat transfer. *International Journal of Heat and Mass Transfer*, 14(8):1047–1056, 1971.

[107] J. Luo and E. H. Razinsky. Conjugate heat transfer analysis of a cooled turbine vane using the V2F turbulence model. *Journal of Turbomachinery*, 129(4):773–781, 2007.

[108] R. J. MacKinnon and R. W. Johnson. Differential-equation-based representation of truncation errors for accurate numerical simulation. *International Journal for Numerical Methods in Fluids*, 13(6):739–757, 1991.

[109] M. Mamou, P. Vasseur, and E. Bilgen. Multiple solutions for double-diffusive convection in a vertical porous enclosure. *International Journal of Heat and Mass Transfer*, 38(10):1787 – 1798, 1995.

[110] M. Marcoux, M.-C. Charrier-Mojtabi, and M. Azaiez. Double-diffusive convection in an annular vertical porous layer. *International Journal of Heat and Mass Transfer*, 42(13):2313 – 2325, 1999.

[111] A. Mojtabi and M.-C. Charrier-Mojtabi. Double-diffusive convection in porous media. In K. Vafai, editor, *Handbook of Porous Media*, pages 269 – 320. Taylor & Francis, 2005.

[112] S. Mondal and P. Sibanda. Effects of buoyancy ratio on unsteady double-diffusive natural convection in a cavity filled with porous medium with non-uniform boundary conditions. *International Journal of Heat and Mass Transfer*, 85:401 – 413, 2015.

[113] T. Mondal, A. Guha, and M. Kumar Das. Analysis of conjugate heat transfer for a combined turbulent wall jet and offset jet. *Journal of Heat Transfer*, 138(5), 2016.

[114] M. Mosaad. Laminar forced convection conjugate heat transfer over a flat plate. *Heat and Mass Transfer*, 35:371 – 375, 1999.

[115] F. Moukalled and S. Acharya. Natural convection in the annulus between concentric horizontal circular and square cylinders. *Journal of Thermophysics and Heat Transfer*, 10(3):524–531, 1996.

[116] M. Moussaoui, M. Jami, A. Mezrhab, and H. Naji. MRT-Lattice Boltzmann simulation of forced convection in a plane channel with an inclined square cylinder. *International Journal of Thermal Sciences*, 49(1):131–142, 2010.

[117] D. A. Nield and A. Bejan. *Convection in Porous Media*. Springer, New York, 4 edition, 2013.

[118] S. K. Pandit. On the use of compact streamfunction-velocity formulation of steady Navier-Stokes equations on geometries beyond rectangular. *Journal of Scientific Computing*, 36(2):219–242, 2008.

[119] S. K. Pandit, J. C. Kalita, and D. Dalal. A transient higher order compact scheme for incompressible viscous flows on geometries beyond rectangular. *Journal of Computational Physics*, 225(1):1100–1124, 2007.

[120] S. K. Pandit, J. C. Kalita, and D. Dalal. A fourth-order accurate compact scheme for the solution of steady Navier–Stokes equations on non-uniform grids. *Computers & Fluids*, 37(2):121–134, 2008.

[121] G. Pareschi, N. Frapolli, S. S. Chikatamarla, and I. V. Karlin. Conjugate heat transfer with the entropic lattice Boltzmann method. *Phys. Rev. E*, 94:013305, Jul 2016.

[122] S. Patel, M. Min, and T. Lee. A spectral-element discontinuous Galerkin thermal lattice Boltzmann method for conjugate heat transfer applications. *International Journal for Numerical Methods in Fluids*, 82(12):932–952, 2016.

[123] M. P. Paulraj, R. K. Parthasarathy, J. Taler, D. Taler, P. Oclon, and A. Vallati. Numerical investigation of conjugate heat transfer from laminar wall jet flow over a shallow cavity. *Heat Transfer Research*, 49(12), 2018.

[124] T. Perelman. On conjugated problems of heat transfer. *International Journal of Heat and Mass Transfer*, 3(4):293–303, 1961.

[125] A. Pozzi and M. Lupo. The coupling of conduction with forced convection over a flat plate. *International Journal of Heat and Mass Transfer*, 32(7):1207–1214, 1989.

[126] P. Rajesh Kanna and M. K. Das. Conjugate heat transfer study of two-dimensional laminar incompressible offset jet flows. *Numerical Heat Transfer, Part A: Applications*, 48(7):671–691, 2005.

[127] P. Rajesh Kanna and Manab Kumar Das. Conjugate heat transfer study of backward-facing step flow - A benchmark problem. *International Journal of Heat and Mass Transfer*, 49(21):3929 – 3941, 2006.

[128] M. Ramšak. Conjugate heat transfer of backward-facing step flow: A benchmark problem revisited. *International Journal of Heat and Mass Transfer*, 84:791 – 799, 2015.

[129] R. Ranjan, A. Dalal, and G. Biswas. A numerical study of fluid flow and heat transfer around a square cylinder at incidence using unstructured grids. *Numerical Heat Transfer, Part A: Applications*, 54(9):890–913, 2008.

[130] R. K. Ray. A transformation-free HOC scheme for incompressible viscous flow past a rotating and translating circular cylinder. *Journal of Scientific Computing*, 46(2):265–293, 2011.

[131] J. N. Reddy and D. K. Gartling. *The Finite Element Method in Heat Transfer and Fluid Dynamics*. CRC press, 1 edition, 1994.

[132] A. Revuelta. On the two-dimensional flow in a sudden expansion with large expansion ratios. *Physics of Fluids*, 17(2):028102, 2005.

[133] A. Revuelta Bayod, A. L. Sánchez Pérez, and A. Liñán Martínez. Confined axisymmetric laminar jets with large expansion ratios. *Journal of Fluid Mechanics*, 456:319–352, 2002.

[134] A. Rips, K. Shoele, and R. Mittal. Heat transfer enhancement in laminar flow heat exchangers due to flapping flags. *Physics of Fluids*, 32(6):063603, 2020.

[135] A. Roshko. Perspectives on bluff body aerodynamics. *Journal of Wind Engineering and Industrial Aerodynamics*, 49(1):79–100, 1993.

[136] Z. Rusak and T. Hawa. A weakly nonlinear analysis of the dynamics of a viscous flow in a symmetric channel with a sudden expansion. *Physics of fluids*, 11(12):3629–3636, 1999.

[137] M. Sankar, Y. Park, and J. Lopez. Double-diffusive convection from a discrete heat and solute source in a vertical porous annulus. *Transport in Porous Media*, 91:753 – 775, 2012.

[138] M. Seddiq, M. Maerefat, and M. Mirzaei. Modeling of heat transfer at the fluid-solid interface by lattice Boltzmann method. *International Journal of Thermal Sciences*, 75:28–35, 2014.

[139] S. Sen. A new family of (5,5)CC-4OC schemes applicable for unsteady Navier–Stokes equations. *Journal of Computational Physics*, 251:251–271, 2013.

[140] S. Sen. Fourth order compact schemes for variable coefficient parabolic problems with mixed derivatives. *Computers & Fluids*, 134-135:81–89, 2016.

[141] S. Sen and J. C. Kalita. A 4OEC scheme for the biharmonic steady Navier–Stokes equations in non-rectangular domains. *Computer Physics Communications*, 196:113–133, 2015.

[142] S. Sen, J. C. Kalita, and M. M. Gupta. A robust implicit compact scheme for two-dimensional unsteady flows with a biharmonic stream function formulation. *Computers & Fluids*, 84:141–163, 2013.

[143] G. L. Sleijpen and H. A. van der Vorst. An overview of approaches for the stable computation of hybrid BiCG methods. *Applied Numerical Mathematics*, 19(3):235 – 254, 1995. Iterative Methods for Linear Equations.

[144] G. D. Smith. *Numerical Solution of Partial Differential Equations: Finite Difference Methods (Oxford Applied Mathematics and Computing Science Series)*. Clarendon Press, 3 edition, 1985.

[145] A. Sohankar and M. Najafi. Control of vortex shedding, forces and heat transfer from a square cylinder at incidence by suction and blowing. *International Journal of Thermal Sciences*, 129:266–279, 2018.

[146] A. Sohankar, C. Norberg, and L. Davidson. Low-Reynolds-number flow around a square cylinder at incidence: study of blockage, onset of vortex shedding and

outlet boundary condition. *International Journal for Numerical Methods in Fluids*, 26(1):39–56, 1998.

[147] J. Sohn. Evaluation of FIDAP on some classical laminar and turbulent benchmarks. *International Journal for Numerical Methods in Fluids*, 8(12):1469–1490, 1988.

[148] W. Spotz and G. Carey. Formulation and experiments with high-order compact schemes for nonuniform grids. *International Journal for Numerical Methods in Heat and Fluid Flow*, 8(3):288 – 303, 1998.

[149] K. Srinivasan and S. G. Rubin. Segmented multigrid domain decomposition procedure for incompressible viscous flows. *International Journal for Numerical Methods in Fluids*, 15(11):1333–1355, 1992.

[150] J. Strikwerda. High-order accurate schemes for incompressible viscous flow. *International Journal for Numerical Methods in Fluids*, 24:715 – 734, 1997.

[151] R. Sugavanam, A. Ortega, and C. Choi. A numerical investigation of conjugate heat transfer from a flush heat source on a conductive board in laminar channel flow. *International Journal of Heat and Mass Transfer*, 38(16):2969–2984, 1995.

[152] H. Takami and H. B. Keller. Steady two-dimensional viscous flow of an incompressible fluid past a circular cylinder. *The Physics of Fluids*, 12(12):II–51, 1969.

[153] F. E. Teruel and E. Fogliatto. Numerical simulations of flow, heat transfer and conjugate heat transfer in the backward-facing step geometry. *Mecanica Computacional*, 32(6):3265 – 3278, 2013.

[154] J. F. Thompson, Z. U. Warsi, and C. W. Mastin. *Numerical Grid Generation: Foundations and Applications.* Elsevier North-Holland, Inc., 1985.

[155] Z. F. Tian and P. Yu. An efficient compact difference scheme for solving the streamfunction formulation of the incompressible Navier-Stokes equations. *Journal of Computational Physics*, 230(17):6404–6419, 2011.

[156] E. F. Toro. *Riemann Solvers and Numerical Methods for Fluid Dynamics: A Practical Introduction.* Springer, 3 edition, 2009.

[157] O. V. Trevisan and A. Bejan. Natural convection with combined heat and mass transfer buoyancy effects in a porous medium. *International Journal of Heat and Mass Transfer*, 28(8):1597 – 1611, 1985.

[158] O. V. Trevisan and A. Bejan. Mass and heat transfer by high Rayleigh number convection in a porous medium heated from below. *International Journal of Heat and Mass Transfer*, 30(11):2341 – 2356, 1987.

[159] K. Vafai. *Handbook of Porous Media*. Taylor and Francis, New York, 2 edition, 2005.

[160] M. Venkatachalappa, Y. Do, and M. Sankar. Effect of magnetic field on the heat and mass transfer in a vertical annulus. *International Journal of Engineering Science*, 49(3):262–278, 2011.

[161] T. Vijaybabu, K. Anirudh, and S. Dhinakaran. LBM simulation of unsteady flow and heat transfer from a diamond-shaped porous cylinder. *International Journal of Heat and Mass Transfer*, 120:267–283, 2018.

[162] E. Vishnuvardhanarao and M. K. Das. Study of conjugate heat transfer from a flat plate by turbulent offset jet flow. *Numerical Heat Transfer, Part A: Applications*, 53(5):524–542, 2007.

[163] M. Vynnycky, S. Kimura, K. Kanev, and I. Pop. Forced convection heat transfer from a flat plate: the conjugate problem. *International Journal of Heat and Mass Transfer*, 41(1):45 – 59, 1998.

[164] F. M. White. *Fluid Mechanics*. Tata McGraw Hill, 2008.

[165] P. Williams and A. Baker. Numerical simulations of laminar flow over a 3D backward-facing step. *International Journal for Numerical Methods in Fluids*, 24(11):1159–1183, 1997.

[166] C. H. Williamson. Vortex dynamics in the cylinder wake. *Annual Review of Fluid Mechanics*, 28(1):477–539, 1996.

[167] A. Xu, L. Shi, and T. S. Zhao. Accelerated lattice Boltzmann simulation using GPU and OpenACC with data management. *International Journal of Heat and Mass Transfer*, 109:577 – 588, 2017.

[168] H. Xu, Z. Luo, Q. Lou, S. Zhang, and J. Wang. Lattice Boltzmann simulations of the double-diffusive natural convection and oscillation characteristics in an enclosure with Soret and Dufour effects. *International Journal of Thermal Sciences*, 136:159–171, 2019.

[169] H. Xu, T. Wang, Z. Qu, J. Chen, and B. Li. Lattice Boltzmann simulation of the double diffusive natural convection and oscillation characteristics in an enclosure filled with porous medium. *International Communications in Heat and Mass Transfer*, 81:104–115, 2017.

[170] P. K. Yadav, K. Sourav, D. Kumar, and S. Sen. Flow around a diamond-section cylinder at low Reynolds numbers. *Physics of Fluids*, 33(5):053611, 2021.

[171] D.-H. Yoon, K.-S. Yang, and C.-B. Choi. Flow past a square cylinder with an angle of incidence. *Physics of fluids*, 22(4):043603, 2010.

[172] H. S. Yoon, M. Y. Ha, B. S. Kim, and D. H. Yu. Effect of the position of a circular cylinder in a square enclosure on natural convection at Rayleigh number of 10^7. *Physics of Fluids*, 21(4):047101, 2009.

[173] P. X. Yu and Z. F. Tian. Compact computations based on a stream-function–velocity formulation of two-dimensional steady laminar natural convection in a square cavity. *Physical Review E*, 85(3):036703, 2012.

[174] P. X. Yu and Z. F. Tian. A compact streamfunction-velocity scheme on nonuniform grids for the 2D steady incompressible Navier-Stokes Equations. *Computers & Mathematics with Applications*, 66(7):1192–1212, Oct. 2013.

[175] T. Zaki, M. Gad-El-Hak, et al. Numerical and experimental investigation of flow past a freely rotatable square cylinder. *Journal of Fluids and Structures*, 8(7):555–582, 1994.

[176] M. M. Zdravkovich. *Flow around circular cylinders: Volume 1: Fundamentals*, volume 1. Oxford university press, 1997.

[177] M. M. Zdravkovich. *Flow around circular cylinders: Volume 2: Applications*, volume 2. Oxford university press, 2003.

[178] F.-Y. Zhao, D. Liu, and G.-F. Tang. Free convection from one thermal and solute source in a confined porous medium. *Transport in Porous Media*, 70(3):407–425, 2007.

[179] F.-Y. Zhao, D. Liu, and G.-F. Tang. Natural convection in a porous enclosure with a partial heating and salting element. *International Journal of Thermal Sciences*, 47(5):569–583, 2008.

[180] F.-Y. Zhao, D. Liu, and G.-F. Tang. Natural convection in an enclosure with localized heating and salting from below. *International Journal of Heat and Mass Transfer*, 51(11-12):2889–2904, 2008.